TESIS DE LA UNIVERSIDAD DE ZARAGOZA

2016

60

Javier Gracia Garza

Micromegas for the search of solar axions in CAST and low-mass WIMPs in TREX-DM

Departamento
Física Teórica

Director/es
García Irastorza, Igor

ISSN 2254-7606

Prensas de la Universidad
Universidad Zaragoza

ISSN 2254-7606

Universidad Zaragoza
1542

Tesis Doctoral

MICROMEGAS FOR THE SEARCH OF SOLAR AXIONS IN CAST AND LOW-MASS WIMPS IN TREX-DM

Autor

Javier Gracia Garza

Director/es

García Irastorza, Igor

UNIVERSIDAD DE ZARAGOZA

Física Teórica

2015

Micromegas for the search of solar axions in CAST and low-mass WIMPs in TREX-DM

memoria presentada por
Javier Gracia Garza
para optar al grado de doctor
en Física

Laboratorio de Física Nuclear y Astropartículas
Área de Física Atómica, Molecular y Nuclear
Departamento de Física Teórica

Universidad de Zaragoza

October 28, 2015

Contents

Part I

Phenomenology and properties of Micromegas detectors

Chapter 1

The physics and evolution of gaseous detectors

Contents

1.1 Introduction

Particle detectors are instruments that use the induced signals (e.g., ionization, scintillation, Cherenkov radiation, phonons, acoustic heat, etc.) produced by the interaction of the incoming particles with the matter making the detector to get physical information about the event (e.g., energy, momentum, trajectory, particle identification, timing, etc.). This chapter focuses on particle detection with gaseous detectors in ionization mode. The ionization mechanisms and the physics principles of operation of these detectors are described. The great evolution of the gaseous detectors over the last decades is reported, focusing on the latest developments of micro-pattern gaseous detectors, specially on the Micromegas technology, which is one of the most widely used readout archictectures and the fundamental tool of this *Thesis* work.

1.2 Interaction of particles in gaseous media

1.2.1 Interaction of photons

The main interaction mechanisms of photons are: photoelectric effect, Compton scattering, coherent scattering and pair production. A photon beam is characterized by the fact that although its intensity decreases while passing through a material, the energy of the photons not removed from the beam is not degraded.

The statistical probability of undergoing one or another process (defined by the interaction cross-section) depends on the photon energy, and the density and atomic number of the target material. As an example, figure 1.1 shows the interaction cross-sections of the different processes in argon. At low energies, the dominant process is the photoelectric effect. Above around 100 keV, the dominant process is the Compton scattering, which is surpassed by the pair production mechanism at energies slightly above the energy threshold for this process (1.022 MeV). Other interaction mechanisms at high energies are photonuclear reactions, such as (γ, n) or (γ, p), pion production and others, which are not considered in this study.

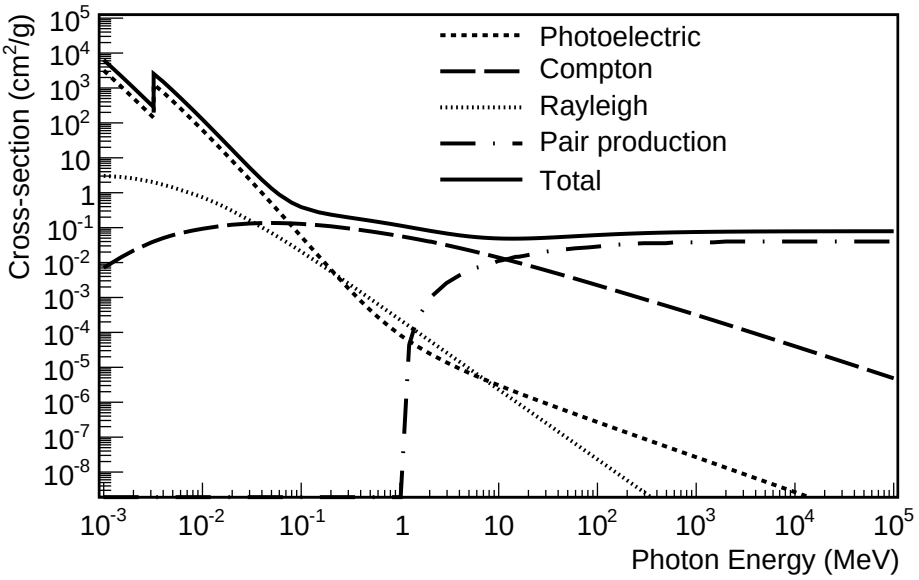

Figure 1.1: Interaction cross-sections as a function of the photon energy in argon. A sharp increase in the photoelectric cross-section can be observed at 3.19 keV, when the electrons of the Argon K-shell become available for this process. Curves generated using data of the NIST Standard Reference Database [1].

Photoelectric effect

The photoelectric effect consists on the absorption of a photon of energy E_γ by an atom, making it unstable. To return to a stable state, an electron from one of the bound atomic shells is emitted. The process is only allowed if E_γ is greater than the binding energy E_{shell} of the most loosely electron of the atom. The kinetic energy of the emitted electron, or photoelectron, is

$$E_e = E_\gamma - E_{shell} \tag{1.1}$$

The photoelectric cross-section is the addition of all the contributions of the energetically allowed atomic shells. When the energy of the incident photon rises above the binding energy of one shell, the electrons of that shell become available for the photoelectric effect. This results in a sharp increase in the photoelectric cross-section (see figure 1.1), the so-called shell edges: K-edge, L-edge, etc. This phenomenon is also observed in figure 1.3 as a sharp decrease in the mean free path at, for instance, 3.2 keV in argon, and 33 keV and 5 keV in xenon, corresponding to the K and L-shells respectively. Atomic shell data is tabulated in [2]. Above the K-shell binding energy, the photoelectric cross-section with this shell represents more than about 80% of the total photoelectric cross-section.

Photoelectric cross-section rapidly increases with the atomic number Z of the material (larger electron density on the medium), and decreases with the energy of the photon energy. The K-shell

photoelectric cross-section is given by

$$\sigma_{pe} = \frac{32\sqrt{2}\pi}{3}\alpha^4 Z^5 r_e^2 \left(\frac{m_e c^2}{E_\gamma}\right)^{7/2} \tag{1.2}$$

where r_e is the classical radius of the electron, α is the fine structure constant and m_e is the electron mass. This formula is valid while $E_\gamma < m_e c^2$, i.e., below about 511 keV.

When an electron of an inner shell is knocked off by the incident photon, a vacancy is created in the atomic shell to which the electron belonged. The atom must return to its stable state by filling this vacancy with an outer shell electron, which can be done by two different mechanisms: fluorescence and Auger transition.

Fluorescence. The vacancy is filled by an outer shell electron, emitting a photon with energy equal to the difference of the two energy levels. The emitted photon is in the x-ray energy range and can interact in the gas detection medium (leading to full incident photon energy reconstruction), or escape from the gas (leading to the so-called *escape peak*).

Auger transition. The vacancy is filled by an outer shell electron, but the energy difference between atomic levels is transferred to an electron of the same atom. If this energy is larger than its binding energy, the electron is ejected from the atom. This electron is called Auger electron.

As in the atomic relaxation process a vacancy gives rise to another vacancy, returning to the atomic stable state can involve more than one transition. The fraction of atomic relaxation through the fluorescence mechanism (fluorescence yield) is roughly proportional to Z. The fluorescence yield in Helium is negligible; in Neon it is 4.3% [3]; in argon, the K-shell fluorescence yield is 13.5%, while in Xenon it is 88.9% [4]. The L-shell fluorescence for argon is negligible, while in xenon it is around 10% [5].

In order to illustrate the interaction mechanisms described above, a calibration spectrum measured with a CAST Micromegas detector is shown in figure 1.2. The calibration is done by blocking the alpha particles emitted by a ^{241}Am source with an aluminum foil. The peaks labeled as *X-rays* and *Gamma* correspond to full energy absorption of the photons emitted by the ^{241}Am source. These gammas are able to produce photoelectric effect in the aluminum foil and in the materials making the detection system. The aluminum fluorescence gives rise to the 1.5 keV peak. The relaxation of the copper atoms (making for example the Micromegas readout) and iron produce the emission of 8.0 and 6.4 keV photons respectively by means of their K-shell fluorescence transition. These x-rays can be absorbed in the argon gas by photoelectric effect. The excited argon atoms relax by emitting either a 3.2 keV Auger electron or a 3.2 keV fluorescence x-ray. In the first case, the full energy is absorbed in the sensitive volume, giving rise to the photopeaks at 8.0 and 6.4 keV. In the latter case, two phenomena can occur: the 3.2 fluorescence x-ray is absorbed in the gas, or it escapes the detection volume. In the former situation, the events contribute to the 8.0 and 6.4 peaks (though in two separated charge clusters). In the last situation, only the photoelectrons ionize the gas, producing the small bumps at 4.8 and 3.2 keV, respectively.

Compton scattering

Compton scattering is the inelastic scattering of photons on free or loosely bounded electrons at rest. In the process, the Compton scattered photon transfers energy to the atomic electron (Compton electron). From conservation of energy and momentum it is possible to derive the shift between incident and scattered photon

$$\Delta\lambda = \frac{h}{m_e c}\left(1 - cos\theta\right) \tag{1.3}$$

where m_e is the electron mass, h is the Planck constant, and θ is the angle between incident and scattered photons. The maximum energy transfer to the medium occurs at θ =180°, producing the characteristic Compton edge in the energy spectra of gamma ray sources. Different scattered angles contribute to the so-called Compton continuum, which is apparent in figure 1.2.

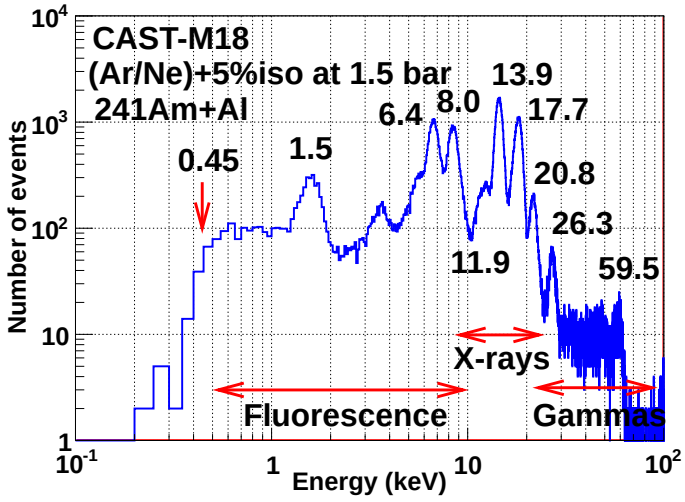

Figure 1.2: Energy spectra generated by the strips of a CAST Micromegas detector when the detector was illuminated by a ^{241}Am source covered by an aluminum foil. Apart from the gammas and x-rays emitted by the source, fluorescence of copper (8 keV), iron (6.4 keV) and aluminum (1.5 keV) are present. The energy threshold is situated around 450 eV.

The differential cross-section of the Compton scattering is accurately described by the Klein-Nishina formula

$$\frac{d\sigma_c}{d\Omega} = \frac{r_e^2}{2}\left[\frac{1+cos^2\theta}{(1+\alpha(1-cos\theta))^2}\right]\left[1+\frac{4\alpha^2 sen^4(\theta/2)}{(1+cos^2\theta)(1+\alpha(1-cos\theta))}\right] \tag{1.4}$$

where r_e is the classical electron radius and $\alpha = h\nu/m_e c^2$, being ν the frequency of the incident photon. Below x-ray energies, the scattering process between free electrons and photons can be elastic or coherent. This scattering process is called **Thomson scattering**. At these energies, quantum effects are negligible and the cross-section can be calculated using concepts of classical electromagnetism. It is found that the cross-section of the process does not depend on the photon energy $\sigma_{th} = 8\pi r_e^2/3$. Another coherent scattering is the so-called **Rayleigh scattering**, which occurs when the wavelength of the incident photon is larger than the target atomic radius. In these coherent processes, the energy transfer to the detection medium is negligible, and the atoms do not become excited. Therefore, they have no interest for particle detection.

Pair production

Pair production is the conversion of a photon into an electron-positron pair. The process must occur in the presence of a third body, such as a nucleus, to ensure momentum conservation. The energy threshold for this process corresponds to two electron rest masses, i.e., 1.022 MeV. The pair production cross-section increases $\propto Z^2$. The third reaction partner can also be an electron (the so-called triplet pair production), being the energy threshold in this case 2.04 MeV. However, the cross-section for this process is much lower than for pair production in nucleus. Besides, there are few natural sources that emit γ-rays above this energy, so this process is not of much interest for particle detection in low energy physics.

1.2.2 Photon attenuation

The passage of photons through matter is described by the total attenuation coefficient μ_t. Consider a beam of mono-energetic photons penetrating a layer of material at position x_0 with intensity

$N(x_0)$. Photons interacting in the material are removed from the beam, so after a distance dx, the intensity of the beam is

$$dN = N(x_0 + dx) - N(x_0) = -\mu_t N(x_0) dx \tag{1.5}$$

where the total attenuation coefficient is

$$\mu_t = \sigma_t n = \sum_i \sigma_i n = \sum_i \mu_i \tag{1.6}$$

where σ_i is the individual cross-section of the k process, μ_i is the associated attenuation coefficient, and n is the number density of the medium $n = N_A \rho / A$, being N_A the Avogadro constant and A the molar mass. Thus, the beam attenuation over a distance x along the propagation axis is

$$N(x) = N(x_0) e^{-\mu_t x} \tag{1.7}$$

The intensity of the photon beam after a distance $\lambda_t = 1/\mu_t$ is reduced by a factor e. This distance is the total photon mean free path in the target material. Figure 1.3 shows the dependence of the total mean free path with the energy for argon at different pressures (left) and for different gaseous media (right). Figure 1.4 shows the interaction point distribution of x-rays of different energies as simulated with *Geant4* in Ar+2%iC$_4$H$_{10}$ at 1.4 bar (i.e., CAST-Micromegas nominal conditions).

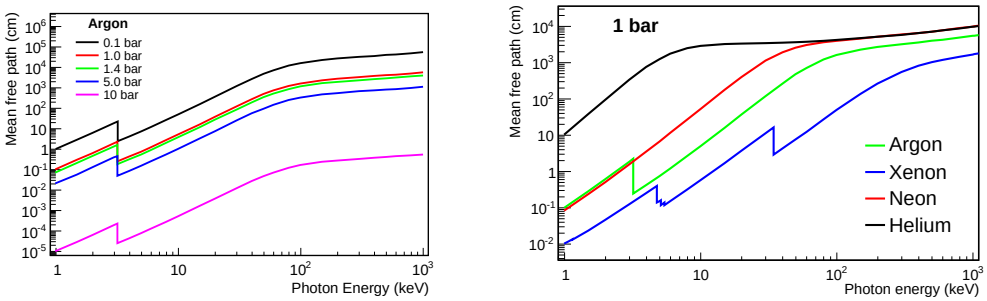

Figure 1.3: Left: Mean free path as a function of the photon energy for Ar at different pressures. Right: Photon mean free path for different noble gases: Xe, Ar, Ne and He. Curves generated using the computer application called XCOM [1].

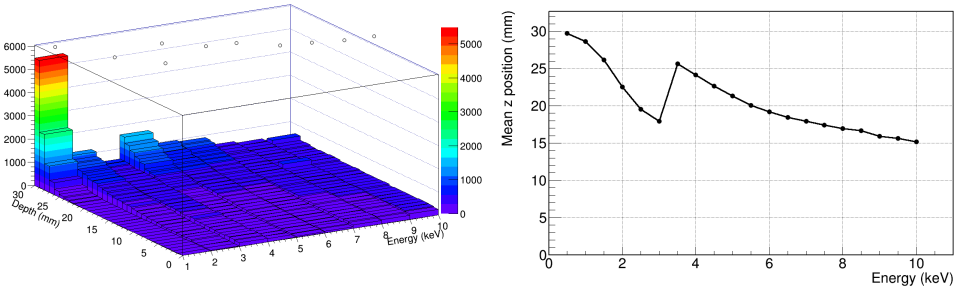

Figure 1.4: Interaction point of x-rays of different energies as simulated with Geant4 *in Ar+2%iC$_4$H$_{10}$ at 1.4 bar. The x-rays penetrate the detector volume from the x-ray window placed at 30 mm from the origin. The mean interaction point along the drift axis is represented on the right panel.*

1.2.3 Interaction of charged particles

When charged particles pass through a medium, the interactions they undergo result in a reduction of their energy. Heavy and light charged particles behave quite differently. The former experience stronger Coulomb forces of nuclei than the latter. Heavy particles do not change their initial direction, but electrons result deflected by the interactions. Heavy charged particles (such as alpha particles, ions or muons) and electrons are treated separately in this study.

Heavy charged particles

The primary modes in which heavy charged particles loss energy are:

1. **Inelastic collisions**: Coulomb interactions with atomic electrons of the medium.
2. **Breemstrahlung**: decelerating charged particles emit electromagnetic radiation that may ionize the medium. This energy loss mechanism only becomes significant for particles with energies well above its rest mass.

Nuclear interactions may also contribute to the energy loss, but for practical purposes it can be neglected. In case of electrons or muons, this is always true as they do not feel the strong interaction. For α-particles or ions this is also valid if their energy is not high enough to penetrate to the vicinity of the nucleus, where the short range nuclear forces are felt.

The stopping power: the Bethe-Bloch formula. The rate at which a charged particle losses its energy while it passes through a material is known as the stopping power. The mean rate of energy loss is well described by the Bethe-Bloch formula

$$-\frac{dE}{dx} = 4\pi N_A r_e^2 m_e c^2 \rho \frac{Z}{A}\frac{z^2}{\beta^2}\left[\frac{1}{2} ln\left(\frac{2m_e c^2\beta^2\gamma^2 W_{max}}{I^2}\right) - \beta^2 - \frac{\delta(\beta\gamma)}{2} - \frac{C}{Z}\right] \tag{1.8}$$

where

r_e	classical electron radius	z	charge of incident particle
m_e	electron mass	β	v/c of the incident particle
N_A	Avogadro's number	γ	$1/\sqrt{1-\beta^2}$
I	mean excitation potential	δ	density correction
Z	atomic number of material	C	shell correction
A	atomic weight of material	W_{max}	max. E transfer in single collision
ρ	density of gas		

An extensive interpretation of this formula is done for example in [6], where the range of validity of the different terms are also discussed. The energy loss dependence on the particle energy is illustrated in figure 1.5, where the different loss regions are apparent.

The energy loss depends on the gas composition through the term Z/A, the gas density ρ and the mean excitation potential I. The dependence on the incident particle is accounted for through the charge z and its velocity β. The energy loss dependence on the kind of particle is illustrated on the left of figure 1.6, and can be used for particle identification.

At very low energies, $0.005 < \beta\gamma < 0.05$ there is no satisfactory theory, so one has to rely on the phenomenological formulae developed by Andersen and Ziegler. For even more slowly particles, the stopping power is well described by the Lindhard approach, being proportional to β [7]. At low energies (below $\beta\gamma \sim 0.1$), the shell correction term C/Z takes into account the atomic binding neglected in the quantum mechanical calculation of the original Bethe-Bloch formula.

Above $\beta\gamma \sim 0.1$, the energy loss decreases as $1/\beta^2$. At $\beta\gamma \sim \mathcal{O}(1)$, particles produce the minimum ionization of the media per unit length. The minimum ionization value is about 1-2 MeVcm^{2}g^{-1}, and it is only slightly dependent on Z. Particles with energy close to this minimum are called minimum ionizing particles, or MIPs. The differential energy loss of minimum ionizing particles in several gases is shown in Table 1.1, expressed in keV/cm.

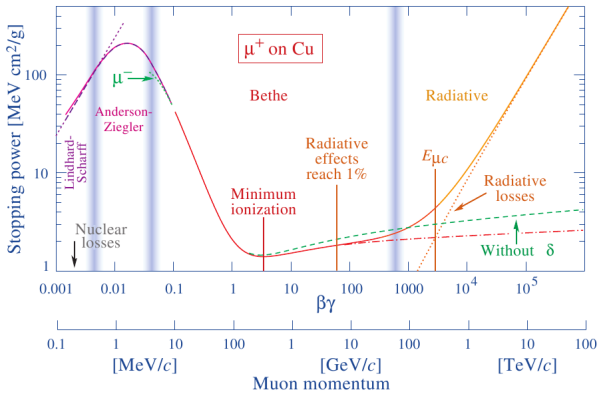

Figure 1.5: Left: stopping power of positive muons in copper as a function of the muon momentum, extracted from [6].

At higher particle energies ($10 \lesssim \beta\gamma \lesssim 1000$), the energy loss increases with energy as $\ln(\beta\gamma)$, related with the increase in distant collisions due to the particle electric field extension (the so-called relativistic rise region). At higher ($\beta\gamma$) values, the media becomes polarized, limiting the field extension, which saturates the energy loss (the so-called Fermi plateau). This saturation is taken into account through the **density effect** correction introduced via the δ term in equation 1.8.

The physical meaning of the Bethe-Bloch energy loss is the following: a high-energy charged particle looses energy at decreasing rate until it reaches the energy at which it produces the minimum ionization per unit length. Afterwards, it keeps loosing energy at higher and higher rates towards the end of its track, until it reaches the so-called Bragg peak. This fact has great practical implications for radiation therapy. The stopping power as a function of the residual energy (or the path length) of the incident particle is known as the Bragg curve (see figure 1.6). A real example of the Bragg curve is shown on figure 1.7 for an α particle track read-out by a Micromegas detector in Ar+2% iC_4H_{10} at 1 bar. For comparison, figure 1.8, shows a minimum ionizing cosmic particle crossing the gaseous chamber.

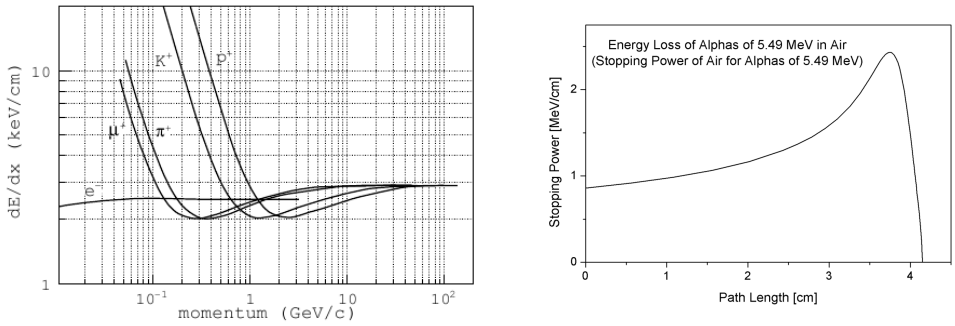

Figure 1.6: Left: stopping power in argon at normal conditions as a function of the particle momentum for several particles, extracted from [8]. Right: the Bragg curve for 5.9 MeV alpha particles in air, extracted from [9].

Electrons

Due to the low electron mass, relativistic effects need to be taken into account when computing their energy loss by inelastic collisions. The Bethe-Bloch formula must be modified to account for

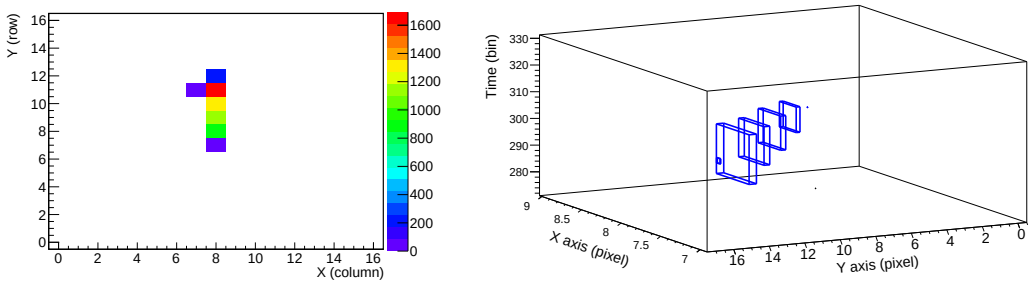

Figure 1.7: An example of an α track recorded by a pixelized Micromegas detector in Ar + 2% iC_4H_{10} at 1 bar (∼1 cm/bin). The charge collection distribution is shown in the xy plane (left) and in 3D (right). The charge collected in each pixel is represented in a color scale of arbitrary ADC units (left), and in the box size (right). The Bragg peak at the end of the track is observed.

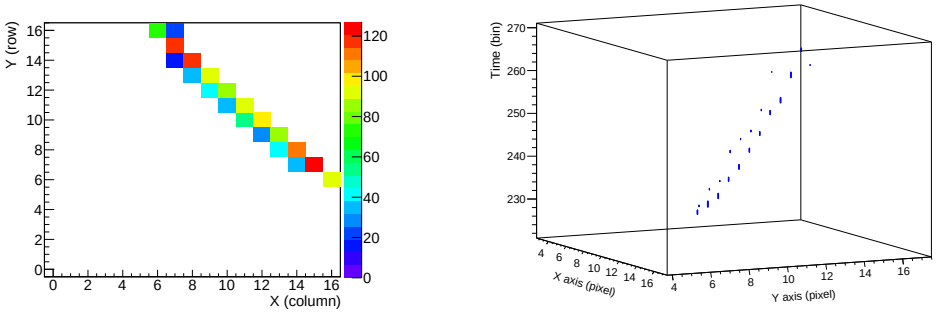

Figure 1.8: Two-dimensional and three-dimensional view of a cosmic event crossing the gas chamber read-out by a pixelized Micromegas detector in Ar+2% iC_4H_{10} at 1 bar (∼1 cm/bin).

the fact that the incident and atomic electron mass is identical. The stopping power for electrons then becomes

$$-\frac{dE}{dx} = 2\pi N_A r_e^2 m_e c^2 \rho \frac{Z}{A}\frac{1}{\beta^2}\left[ln\left(\frac{\tau^2(\tau+2)}{2(I/m_e c^2)}\right) + 1 - \beta^2 + \frac{\frac{1}{8}\tau^2 - (2\tau+1)ln2}{(\tau+1)^2} - \frac{\delta}{2} - 2\frac{C}{Z}\right] \quad (1.9)$$

where τ is the kinetic energy of the particle in units of $m_e c^2$.

The stopping power for electrons in lead is shown on the left of figure 1.9. As shown in the figure, radiative energy losses by Breemstrahlung become significant at relatively low energies. The critical energy at which the radiative and collisional energy losses become equivalent is called *critical energy* E_c. The critical energy has been parameterized in [6] as

$$E_c \simeq \frac{a}{Z+b}\ \text{MeV} \quad (1.10)$$

where for solids: $a = 610$, $b = 1.24$; and for gases: $a = 710$, $b = 0.92$. For example, the critical energy in argon is about 37 MeV. Even if this energy is much lower than the energies at which radiative losses become significant for heavy charged particles, it is still too high to be considered in this study.

Range of charged particles

The range of a charged particle is defined as the distance they travel before loosing (almost) all its energy. The range of charged particles in the gas media is of relevance for detector design and

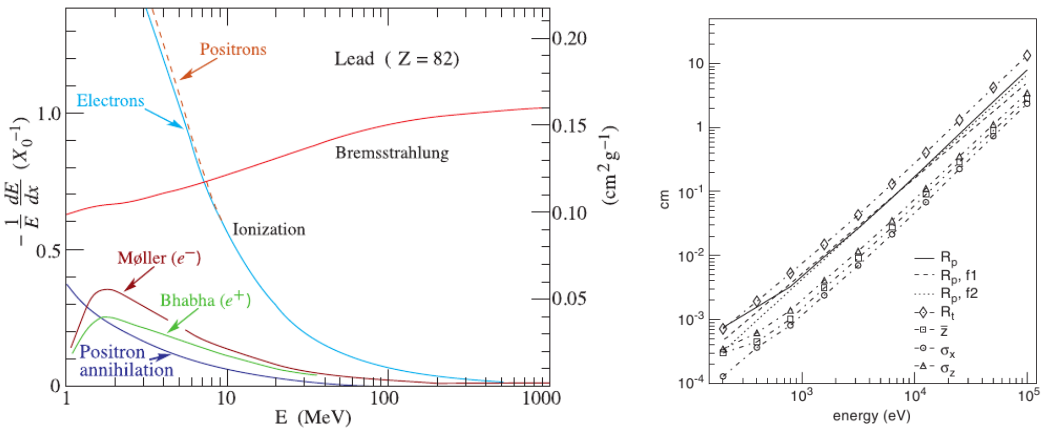

Figure 1.9: Left: stopping power of electrons as a function of their energy in lead, extracted from [6]. Right: electron range in argon at standard conditions as a function of the incident energy.

physical interpretation of the results. Due to the statistical nature of the interactions between charged particles and the stopping material, the range of a particle shows a statistical fluctuation around a mean value. This fact is knows as **range straggling**.

Heavy charged particle are barely deviated from their incident path, so they follow straight line tracks in a gaseous medium. However, the scattering probability at large angles for electrons is high, so they follow random trajectories, covering on average a distance R_p (practical range). The mathematical computation of the electron range is a complex issue. However, there exist several empirical or semi-empirical models to compute it. Some parameterizations of R_p as a function of the electron energy are given in [10]:

$$R_p = \begin{cases} 3.872 \cdot 10^{-3} \cdot \frac{A}{Z} \cdot E[\text{keV}]^{1.492} & \text{mg/cm}^2 & 0.3 < E < 10\text{keV} \\ 6.97 \cdot 10^{-3} \cdot E[\text{keV}]^{1.6} & \text{mg/cm}^2 & 10 < E < 50\text{keV} \\ 0.71 \cdot E[\text{MeV}]^{1.72} & \text{g/cm}^2 & E < \mathcal{O}(100)\text{keV} \end{cases} \tag{1.11}$$

As shown in figure 1.9 (right), these parameterization fit the simulated and experimental data with high accuracy. For example, the range of electrons of few keV in argon at NTP conditions is of the order of hundreds of μm.

A parameterization of the range of α-particles in air is given in [11]:

$$R^{air} = \begin{cases} e^{1.61\sqrt{E}} & \text{mm} & E < 4\text{MeV} \\ (0.05E + 2.85)E^{3/2} & \text{mm} & 4 < E < 15\text{MeV} \end{cases} \tag{1.12}$$

Knowing the range of a particle in a medium, the range of that particle in a second medium can be expressed as

$$\frac{R_1}{R_2} = \frac{\rho_2}{\rho_1}\left(\frac{A_1}{A_2}\right)^{1/2} \tag{1.13}$$

where ρ_i and A_i with $i = 1, 2$ is the density and mass number of the media.

1.3 Phenomenology of gaseous detectors

1.3.1 Charge generation

In the previous section, we have seen the different ionization mechanisms of the atoms and molecules in a gas medium. Photons give rise to electrons ejected from the gas molecules, usually accompanied by Auger electrons and fluorescence x-rays. Heavy charged particles and electrons loose their

energy through inelastic collisions with the gas molecules. These collisions normally result in the production of electron-ion pairs and excited states of the gas atoms, which relax to its fundamental state through fluorescence emission and Auger transitions, contributing to the total ionization of the gas medium. Another de-excitation mechanism contributing to the ionization yield is the Penning transfer[1] between gas molecules. However, collisions with complex molecules (such as typical hydrocarbon *quenchers*) can also activate rotational and vibrational modes of the molecules, which do not contribute to the ionization yield.

Therefore, the different contributions to the ionization of the medium are:

1. **Primary ionization:** electron-ion pairs generated directly by the collision of the incident charged particle with the gas molecules.
2. **Secondary ionization:** a fraction of the primary electrons (denominated δ-rays) are expelled with high enough energy to produce substantial secondary ionization. Penning transfers contribute also to the secondary ionization.

This process continues until the energy of the ejected electrons is lower than the ionization potential of the gas atoms. Above a few tens of eV, the total number of electron-ion pairs created is proportional to the absorbed energy. The ionization phenomena and the relation between the absorbed energy and the number of electron-ion pairs is the subject of this section.

Primary and secondary ionization

The ionization collisions occur randomly along the track of the charged particle. The distribution of the number of ionizing collisions k in a segment s of the track follows Poissonian statistics [12]

$$P(k) = \frac{(s/\lambda)^k}{k!}\, e^{-s/k} \tag{1.14}$$

where $\lambda = 1/(N_e\sigma_I)$ is the mean free path, i.e., the mean distance between charge clusters; being N_e the electron density of the gas and σ_I the ionization cross-section. The number of primary electrons per unit length is $n_p = 1/\lambda$, which depends on the particle type and energy and in the gas mixture. In some cases (about 34% in Argon at normal conditions for minimum ionizing particles), the ejected electrons have enough energy to further ionize the medium. The total number of electrons per unit length n_T is typically 2-3 times larger than n_p (see Table 1.1).

The probability of a charged particle to produce an electron with energy E or larger follows an approximate $1/E^2$ dependence (Rutherford scattering law). The long tail of the distribution implies that although large energy transfers are rare they do occur, increasing substantially the differential energy loss. As an example, in 1 cm of argon at NTP, there exist 1% probability of producing electrons with energy of 1 keV or larger, and less than 0.1% of producing electrons with energy above 10 keV.

Mean energy per electron-ion pair

As we have seen, not all the energy absorbed in the medium is invested in the ionization of the medium. Part of the incoming energy is lost in other excitation channels, such as scintillation, or vibration and rotation of the gas molecules. Experimentally, it is found that above a few tens of eV, the mean number of electron-ion pairs, N_e, is proportional to the absorbed energy as

$$N_e = E_0/W \tag{1.15}$$

where W is the mean energy to create an electron-ion pair in a certain gas. Experiments have found that the ratio of W values measured with α and β sources is approximately the unity for noble gases, while small deviations are reported for complex hydrocarbons. It has also been found

[1] In some gas mixtures (so-called Penning mixtures), an excited state A^* ionizes a gas molecule B, producing a free electron: $A^* + B \rightarrow A + B^+ + e^-$. This reaction can occur if the ionization potential of B is lower than the excitation potential of A. It contributes to increase the ionization yield and the gas gain. Penning mixtures are not treated in this thesis as they were not used in the work here reported.

Gas	ρ (mg/cm^3)	$dE/dx\|_{min}$ keV cm^{-1}	n_p cm^{-1}	n_T cm^{-1}	I_{exc} eV	I_{ion} eV	W (eV) eV	F
He	0.166		4.8	7.8	19.8	24.5	45	0.17
Ne	0.84	1.45	13	50	16.7	21.6	30	0.17
Ar	1.66	2.53	25	106	11.6	15.7	26	0.23
Xe	5.50	6.87	41	312	8.4	12.1	22	0.17
CH_4	0.67	1.61	37	54	8.8	12.6	30	0.26
CO_2	1.84	3.35	35	100	7.0	13.8	34	0.33
iC_4H_{10}	2.49	5.67	90	220	6.5	10.6	26	0.26
CF_4	3.78	6.38	63	120	10.0	16.0	54	

Table 1.1: Gas properties at normal temperature and pressure: $dE/dx|_{min}$, n_p, n_T: differential energy loss, primary and total number of electron-ion pairs per cm of minimum ionizing particles; I_{exc}, I_{ion}: lowest excitation and ionization energies; W: mean energy for electron-ion pair creation; and F: measured Fano factor. Values extracted from [12, 8, 6].

that the W factors are independent of the deposited energy (above a few keV for β particles, and above few MeV for α particles.) These facts allow to determine the deposited energy through the number of electron-ion pairs generated in the gas.

Some W values for common gases are listed on Table 1.1. The W dependence on the gas composition is complex. In general, it increases with the ionization potential I_{ion} and with the probability of the gas molecules to undergo non-ionizing mechanisms, such as the promotion to excited, vibrational, and rotational modes. As an example, the fraction of the deposited energy invested into ionization I_{ion}/W in argon is 60%, while in i-butane is about 40%.

In a gas mixture of the compounds A and B, the final W_{AB} value can be calculated as the weighted average of the individual gases

$$\frac{1}{W_{AB}} = \frac{C_A\sigma_A}{W_A} + \frac{C_B\sigma_B}{W_B} \tag{1.16}$$

where C_i and σ_i are the concentrations and ionizing cross-sections of the individual gases. In Penning mixtures, the W value is lower due to the contribution to the ionization through Penning transfers.

The Fano factor

Two identical charged particles depositing an energy E_0 in a gas will not necessarily produce the same number of electron-ion pairs, as the inelastic collisions are governed by probabilities. In the case of independent ionizing collisions, the number of primary electrons N_e will fluctuate according to Poissonian statistics with variance $\sigma_{N_e} = N_e$. However, the energy loss in the inelastic collisions with the gas molecules is not purely statistical. The ionizing collisions are not independent as the number of ways an atom can be ionized is limited by the discrete electronic levels. Thus, the primary electron creation is not a fully Poissonian process, but it shows a reduced variance, accounted for by the Fano factor F [13]:

$$\sigma_{N_e} = FN_e \tag{1.17}$$

The Fano factor depends on the gas composition and the nature and energy of the ionizing particle. Table 1.1 shows some values of the Fano factor for various common gases measured with low energy electrons. The fluctuation in the number of primary electron-ion pairs is the first contribution to the energy resolution of a gaseous detector. The fact that an atom can only become ionized in a certain number of ways, results in a better energy resolution than predicted by purely statistical considerations. The lower limit to the relative energy resolution, $R = \sigma_E/E$, imposed by this fluctuation is called the **Fano limit**, or intrinsic energy resolution, and it is given by:

$$R(\%\ \text{FWHM}) = 2.35\sqrt{\frac{W}{E}F} \tag{1.18}$$

Note that R increases $\propto 1/\sqrt{N_e}$ since $\sigma_e \propto \sqrt{N_e}$ and $E \propto N_e^{-1}$. The intrinsic energy resolution of any gaseous filled detector can be estimated at any energy using the tabulated values. For example, in argon at 5.9 keV (the energy of the ^{55}Fe source main x-rays with which the Micromegas detectors of CAST are calibrated), the intrinsic energy resolution is 7.5% FWHM, equivalent to 0.44 keV.

1.3.2 Charge transport

Drift velocity

A free electron in a gas scatters isotropically with the gas atoms with a mean instantaneous velocity u. When an electric field is applied, the electron is accelerated between collisions at a rate given by $(e/m)E$. The resulting mean drift velocity is then:

$$v_d = \frac{e\tau}{m} \cdot E \tag{1.19}$$

where the mean time between collisions is $\tau(E) = 1/(N\sigma_s u)$. Here, N is the molecular density of the gas, σ is the scattering cross-section and u is the mean instantaneous velocity. The total energy of the drifting electron is

$$mu^2/2 = \varepsilon = \varepsilon_E + (3/2)k_B T \tag{1.20}$$

where ε_E is the energy picked up by the electron between collisions, in which a fraction λ is lost. Over a distance x, there will be an equilibrium between the energy lost by collisions and the energy gained by the electric field. The mean number of collisions over x is $n = (x/v_d)(1/\tau)$, i.e., the time the electron takes to cover the distance x weighted by the mean time between collisions τ. This results in the equilibrium equation

$$\frac{x}{u\tau}\lambda\varepsilon_E = eEx \tag{1.21}$$

For many gases, the relation $\varepsilon_E \gg (3/2)k_B T$ is satisfied so the the thermal energy term can be neglected in equation 1.20. In this case, one obtains an approximate expression for the drift and instantaneous velocity:

$$\begin{aligned} v_d^2 &= \frac{eE}{mN\sigma_s}\sqrt{\frac{\lambda}{2}} \\ u^2 &= \frac{eE}{mN\sigma_s}\sqrt{\frac{2}{\lambda}} \end{aligned} \tag{1.22}$$

Note that both σ_s and λ depend on the electron energy ε and on the molecule electronic structure. High drift velocities require low σ and large λ values. Some heavy noble gases (Ar, Kr and Xe) and light molecular gases (e.g., CH_4 or CF_4) show a dip in the cross-section at a few tenths of eV (Ramseur effect). If the electron energy remains around this dip, large drift velocities are obtained. In pure noble gases, the energy of drifting electrons can only be dissipated through inelastic scatterings: ionization or excitation. These processes have energy thresholds of several eV, so the electrons mainly suffer elastic scatterings with very low energy losses. In this case, the electrons quickly pick up energy and get out of the Ramseur dip, leading to low drift velocities. On the other hand, molecular gases have rotational and vibrational levels at lower energies. This fact implies that the fractional energy loss in this gases is larger. The energy of drifting electrons is kept in around the Ramseur minimum and large drift velocities are achieved.

Therefore, electron drift velocities are highly dependent on the gas composition. The addition of small quantities of molecular gases can change significantly the available energy levels and thus the velocity of drifting electrons. As an example, the dependence of the drift velocity with the electric field for some argon mixtures is shown in figure 1.10 as computed by the Magboltz program [14].

The model studied before relies on the approximation of a single mean instantaneous velocity u, while a more realistic treatment requires considering the distribution of velocities around its mean value. The importance of gaseous detectors in particle physics has motivated the study of the drift properties of several gas mixtures. A compilation of such measurements can be found for example in references [15, 16, 17, 18].

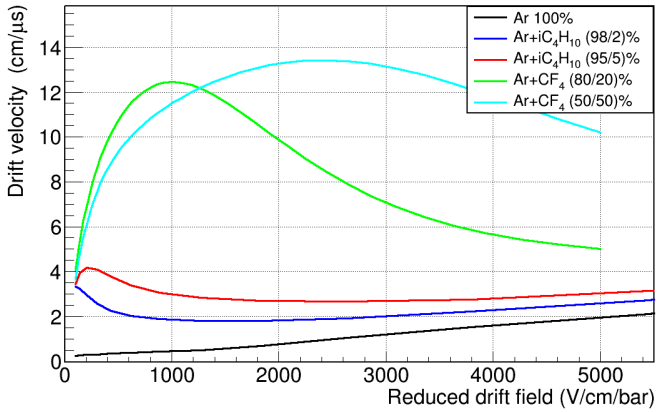

Figure 1.10: Dependence of the drift velocity of electrons with the reduced drift field as calculated by Magboltz in various argon mixtures.

Diffusion

Drifting electrons do not follow exactly the electric field lines, but they experiment diffusion along them as a result of the random scattering they suffer. Here, I briefly discuss this process, while the reader is referred to other detailed works for more information, as for example [12]. Until 1967, electron diffusion in gases was considered to be isotropic. However, it was found experimentally that longitudinal and transversal diffusion can be significantly different. A point-like cloud of electrons drifting in the z-direction with a velocity v_d due to the external field E presents at time t a Gaussian density distribution

$$n(r) = \left(\frac{1}{\sqrt{4\pi D_L t}}\right)\left(\frac{1}{\sqrt{4\pi D_T t}}\right)^2 \exp\left(-\frac{(x+y)^2}{4D_T t} - \frac{(z-v_d t)^2}{4D_L t}\right) \tag{1.23}$$

where $r^2 = x^2 + y^2 + (z - v_d t)^2$, with D_T and D_L representing the transversal and longitudinal diffusion constants respectively. The diffusion constants can be determined by the spread of the electron cloud after a given drift length: a highly pixelized readout allows to measure the mean squared deviation of the lateral diffusion, while the longitudinal can be determined from the measurement of the drift velocity and the spread of arrival times of primary charges. The mean squared deviation of the electron cloud after a drift length L can be written in terms of the diffusion coefficients as

$$\begin{aligned} \sigma_t &= D_T\sqrt{L} \\ \sigma_l &= D_L\sqrt{L} \end{aligned} \tag{1.24}$$

where D_T and D_L are usually expressed in units of $\mu m/\sqrt{cm}$. As an example, figure 1.11 shows the longitudinal and transversal coefficients for some argon-based mixtures computed with Magboltz. It is convenient to keep this coefficients as low as possible, since they limit the accuracy of particle tracking or reduce the rejection capabilities of gaseous detectors. As the figure shows, the addition of molecular gases to pure noble gases can reduce both transversal and longitudinal diffusion about a factor 10.

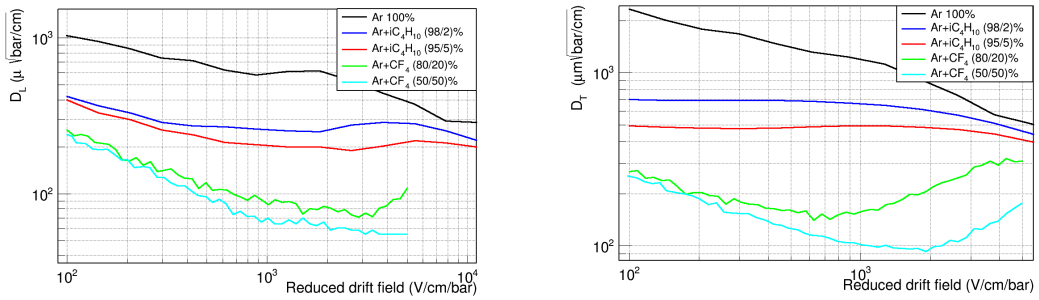

Figure 1.11: Dependence of the longitudinal and transversal diffusion coefficients with the reduced drift field as calculated by the Magboltz program in various argon mixtures.

Electron attachment

Drifting electrons can be absorbed in the gas by electronegative components of the gas mixture or by impurities. The molecules with larger electron affinities are halogenides (*e.g.* CF_4) and oxygen. A gas mixture with significant electron attachment will present, for example, a reduced energy resolution or a deterioration in the imaging capabilities of the detector. The attachment is usually produced by impurities present in the gas in the form of air, water or halogen-containing compounds. Electron attachment can be reduced by curing the vessel leaks and reducing the known outgassing components inside it. A continuous flow of clean gas is also desirable, as well as baking-out and pumping of the detector chamber. The different electron attachment processes are studied in detail in [21]. The attachment coefficients have been measured in several compounds, some of which can be found for example in [22, 23, 24].

1.3.3 Charge amplification

The signal induced in an electrode by the primary electrons is not large enough to be distinguished from electronic noise when detected by the electronics coupled to the sensitive electrodes[2]. Therefore, particle detection in gaseous media relies on the avalanche multiplication of the primary charges, a process discovered by J. Townsend at the beginning of the XX century.

A requisite for the avalanche multiplication is the presence of large enough electric field to accelerate the primary electrons above the threshold of inelastic collisions. When this occurs, the gas molecules become excited or ionized, producing more electron-ion pairs, a process that can repeat several times. As electrons drift much faster than ions, the geometric distribution of the charges adopt a drop-like shape: electrons move fast to the front of the charge cloud, while ions slowly move to the back of the cloud. The multiplication factor of the number of electrons is called the gas gain, G, which depends on the gas composition and pressure, and on the field strength.

In noble gases, the relaxation of the excited states occur through the emission of photons, typically in the IR-UV energy range. In organic compounds with vibrational and rotational excitation levels, the relaxation can well occur through non-radiative processes. UV photons can produce photoelectrons in the gas molecules or the electrodes, which in turn, can develop new avalanches. At high bias voltages it can result in continuous discharge and breakdown of the detector, limiting the gas gain. However, the addition to the gas of molecular compounds with absorption bands in the UV range allows to reach higher gains. These molecular gases are called quenching gases or quenchers.

[2] Although alpha particles and heavy nuclei could produce a large enough charge density to be detected

The multiplication factor

Even though, theoretically, the multiplication factor could be increased without limit by increasing the electric field, physically, this is not the case. The limit on the multiplication factor is due to the effect of space charge (the charges in the amplification region modify the electric field in such a way that multiplication saturates) and is about $G \sim 10^8$, known as **Raether limit**. However, it is found empirically that the maximum achievable gain before breakdown is about two orders of magnitude lower.

The distance an electron travels until the next ionization defines the mean free path, which depends on the density of electrons in the gas and on the cross-section. The inverse of this quantity is the **first Townsend coefficient** α, a measurement of the number of ionizations per unit length. The dependence of α with the electric field is shown in figure 1.12 for an argon-based mixture. The number of electrons n will grow on a drift path dx by

$$dn = n(x)\ \alpha(E(x))\ dx \tag{1.25}$$

with $\alpha(E(x))$ the first Townsend coefficient at the electric field $E(x)$ experienced by the electrons in the path dx. The amplification $G = n/n_0$ of the number of electrons in a path from x_0 and x_1 is

$$G = \frac{n}{n_0} = \exp\left(\int_{x_0}^{x_1} \alpha(E(x))dx\right) \tag{1.26}$$

where the integral is done over the path of the electron that developed the avalanche. In the case of a uniform field, like in a parallel plate detector or Micromegas, the gain is simply $G = e^{\alpha x}$, with x the amplification gap. The Raether limit of 10^8 corresponds to about $\alpha x \sim 20$. The goal of any detector is to achieve stable operation before the spark breakdown. High gain detectors are of special interest for low-energy searches, as lower energy thresholds can be reached. The parameter α has been parameterized in various theoretical models. In the Rose and Korff model [25], α is

$$\frac{\alpha}{P} = Ae^{-BP/E} \tag{1.27}$$

with empirical constants A and B depending on the gas. Meanwhile, in the Diethorn approximation [26], α is proportional to E, and it is an accurate model above a few tens of kV/cm.

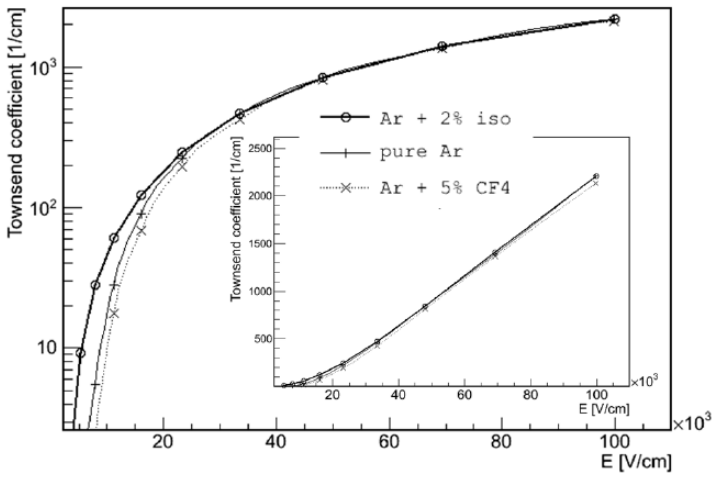

Figure 1.12: Townsend coefficient versus electric field, extracted from [27].

Gain fluctuations

The number of final electrons after the avalanche multiplication of a single electron fluctuates. This fluctuation affects the precision with which the detector measures, for example, the energy

deposition or the track of an ionizing particle. If $n_0 \gg 1$ and if all the n_0 avalanches develop independently the *central limit theorem* applies and the amplification factor $G = n/n_0$ is the mean of a Gaussian distribution with variance S^2,

$$S^2 = n_0\sigma^2 \tag{1.28}$$

where σ^2 is the variance of the single avalanche size distribution, also called single electron response or simply gain distribution. The shape of the gain distribution depends on the strength of the electric field. It is useful to define the so-called *relaxation parameter* χ to distinguish between the regimes at moderate and high fields

$$\chi = \alpha(E(x))\, x_0 \tag{1.29}$$

where α^{-1} is the mean free path for ionization, and $x_0 = U_i/E$ is the distance that an electron of nearly initial null energy has to travel before being able to ionize the gas, with U_i the ionization potential of the gas.

At moderate fields $x_0 \ll \alpha$ and $\chi \sim 0$, while at high fields $\chi \to 1$. In the low field regime (below few tens of kV/cm), the probability per unit path length of an electron to ionize a gas molecule does not depend on the history of the electron. The distribution for single-electron amplification follows an exponential distribution (Yule-Furry law)

$$p_N = \frac{1}{\bar{N}} e^{-N/\bar{N}} \tag{1.30}$$

where $\bar{N} = G$. The variance of the distribution is $\sigma^2 = \bar{N}^2$. This distribution indicates that the most probable gain values are small, but large fluctuations in single avalanches do occur. On the other hand, at high fields x_0 becomes comparable to the ionization mean free path (χ approaches 1), an ionization occurs approximately every x_0, so the fluctuations are reduced. As a result, the most probable gain value shifts towards the mean gain, and a maximum arises in the gain distribution, which approach remarkably well (see, for example [28]) the Polya distribution [29] given by

$$p(m, N) = \frac{m^m}{\Gamma(m)} \frac{1}{\bar{N}} \left(\frac{N}{\bar{N}}\right)^{m-1} e^{-m\frac{N}{\bar{N}}} \tag{1.31}$$

where $\bar{N} = G$ and $b = m^{-1}$ is the relative variance of the distribution $\sigma^2 = \bar{N}^2 b$. An analytical expression for the relative variance of the gain distribution in arbitrary electric field configurations is given by [30]:

$$b = \frac{4e^{-2\chi} - 4e^{-\chi} + 1}{4e^{-\chi} - 2e^{-2\chi} - 1} \tag{1.32}$$

which decreases with the electric field through the $\chi(E)$ dependence, and typically assume values between at 0.2-0.9 in most gases operated at 20-100 kV/cm. The shape of the Polya distribution is shown in figure 1.13 for several values of the relative variance. The maximum of the gain distribution occurs at $\bar{N}(m-1)/m$.

In the gaussian regime, the contribution to the energy resolution according to equation 1.28 is $S^2 = n_0\bar{N}^2 b$, which by convolution with the Fano limit contribution (equation 1.18) results in a relative energy resolution of

$$R(\%\ \text{FWHM}) = 2.35\sqrt{\frac{W}{E}(F+b)} \tag{1.33}$$

As an example, the limit to the intrinsic energy resolution at 5.9 keV in Ar+iC$_4$H$_1$0 (98/2 %) of a 50 μm gap Micromegas detector operated at 60 kV/cm is about 11% FWHM, very close to the best values achieved by a detector of the Micromegas type [31, 274].

Besides from statistical fluctuations, some other geometrical and operational parameters influence the avalanche process and can negatively contribute to the energy resolution. Some of these effects are the electronic noise, electron transmission from the conversion to the amplification regions, attachment, geometrical imperfections, edge effect or space charge effect at high particle rates.

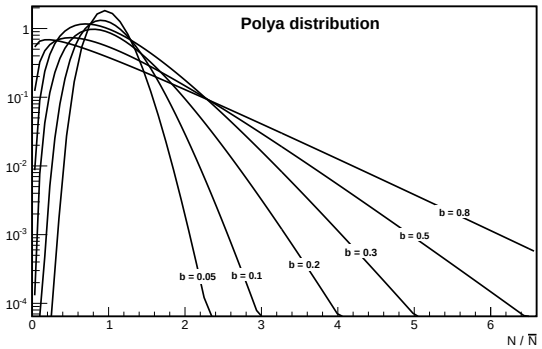

Figure 1.13: Polya distributions for several values of the relative variance b.

1.4 Signal induction

In the avalanche process, a large number of electron-ion pairs are generated in the gas. These charges drift in the amplification region in antiparallel directions towards their corresponding electrode. The current on the electrodes are generated by this movement, due to the instantaneous change of electrostatic flux lines ending on them. The instantaneous electric current $i(t)$ generated by a moving charge q in the vicinity of an electrode is computed by the Shockley-Ramo's theorem [33, 34]:

$$i(t) = q\ \mathbf{v(t)} \cdot \mathbf{E_W} \tag{1.34}$$

where $\mathbf{v(t)}$ is the velocity of the moving charge and $\mathbf{E_W}$ is the weighted field, defined as the electric field which would exist at the electron's position with the electrode biased to 1 volt and all other conductors grounded.

The currents induced by electrons and ions in an electrode have very different characteristic times since electrons are around 10^3 times faster than ions. However, the total charge generated in the electrode is the same for both electrons and ions: $Q = \int_0^t i(t)dt$. As an example, in figure 1.14 the signal induced in a Micromegas electrode by electrons and ions is shown.

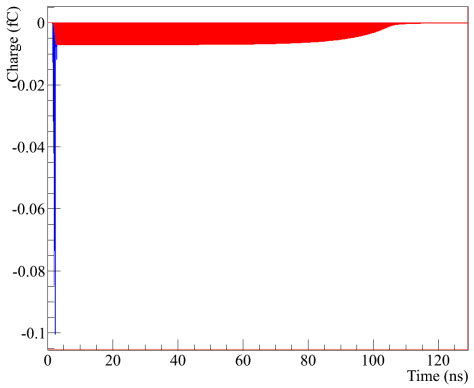

Figure 1.14: Simulated electric current induced in a Micromegas electrode by electrons (blue) and ions (red). Extracted from [35].

In the last years there have been developments to reduce the sparks rate in a high intensity particle flux, since they enlarge the dead time of the detector. These developments are based in the

introduction of a high resistivity layer covering the anode electrode to absorb the sparks. In this case, the electric fields show a time dependence and the signal induction is more complex. This is studied in detail in [36], where equivalent equations to 1.34 can be found for resistive detectors.

1.5 From wired to micro-patterned gaseous detectors

The invention of the **Multi-Wire Proportional Chamber** (MWPC) in 1968 by G. Charpack *et. al.* [37] revolutionized the field of instrumentation in particle physics. The traditional Geiger-Müller counters and the old imaging detectors (bubble or cloud chambers) were not capable to address the needs of high energy particle physics. Higher rates and accurate particle trajectory determination required the use of fully-electronic readouts. The MWPC is a gaseous chamber with an anode plane made of parallel closely-spaced wires, acting as independent proportional counters. The cathode can also be wired, allowing to measure the 2D position of the avalanche. MWPCs provide information about particle trajectory, momentum and charge so they quickly became widely used in particle and high energy physics. The **drift chamber** [38] was developed to measure the track position along the field direction. This is accomplished by measuring the drift time of the primary electrons, and requires an auxiliary detector to determine the time of passage of the ionizing particle through the drift volume.

The **Time Projection Chamber** (TPC) [39] invented in the late 1970s by D. R. Nygren combines the xy-positioning provided by the MWPC and the z information of the drift chamber. The combination of MWPCs and TPCs lead to many discoveries in particle physics and many new applications in the industry. However, for some applications these devices are limited in position resolution and trigger rate. The wires cannot easily be placed significantly closer than $p = 1$ mm, what limits the position resolution ($\sigma \sim p/\sqrt{12}$). Besides, the rate capabilities are limited by the ion back-flow as the ions are slowly evacuated from the active volume. These difficulties along with the need of covering larger and larger areas (i.e., more wires) required passing from hand-made instrumentation to the electronic era.

The breakthrough occurred in 1988 when A. Oed used microelectronics technology to developed the Micro Strip Gas Counters (MSGC) [40]. It consists of alternating cathode and anode strips printed on an insulating support with an electric field high enough to produce electron multiplication. Even though MSGCs suffered from aging and discharges, the fast evacuation of the ions allow to operate the detector at rates 100 times higher than classic MWPCs, with about 10 times better spatial resolution (∼100 μm). This detector has few applications nowadays, but it inspired many other amplification structures. These devices were the first of a new kind of detectors known as **Micropattern Gaseous Detectors** (MPGDs), which share the use of microelectronic and photolitographic techniques. Nowadays, TPCs equipped with micropatterned amplification structures at the end-plates are successfully used in many experiments, ranging from rare event searches, such as dark matter searches, to high energy physics at colliders or neutrino oscillation experiments.

Other amplification architectures followed the invention of MSGCs, such as Pixel and Microdot readouts [41, 42], where the strips are replaced by dots or pixels. However, the most popular structures currently in use are based on the GEM and Micromegas architectures, for Gas Electron Multiplier invented in 1996 by Sauli [43], and MICRO-MEsh GAseous Structure introduced by I. Giomataris in 1954 [44], respectively.

Other novel detector geometries and technologies have been developed since then. It is worth remarking two of them: InGrid and resistive detectors. The InGrid detectors [45] consist on a Micromegas grid precisely fixed by means of insulating pillars in a silicon chip by wafer post-processing technology. InGrid integrates the pixelated CMOS technology and an electron-amplifying structure to produce a very compact, precise and high-granularity device with impressive tracking capabilities. An InGrid detector was installed in CAST in 2014 in order to probe its performance as a low-background detector (see section 4.8.4). On the other hand, aging effects caused by discharges are an important issue in high-luminosity experiments. To deal with this effect, some development on micropattern gaseous detectors have included a resistive layer over the anode electrodes to absorb the sparks [46].

The invention of different micropattern gaseous detector schemes provide a huge variety of applications, offering outstanding spatial resolution, high rate capability, operational stability, radiation hardness, and large cost-effective sensitive areas. These and other developments concerning the application, study and production of microppattern gas-avalanche detectors are actively under investigation by the RD-51 Collaboration [47].

For more information about GEM and other novel concepts in electron-multiplying technologies, the reader is referred to [48]. However, the Micromegas technology is studied here with some detail. First, we describe the Micromegas structure and main manufacturing processes. After reviewing the Micromegas principle of operation, its main properties are listed, and illustrated with examples.

1.6 The Micromegas technology

The Micromegas is an amplification gaseous structure developed at Saclay in 1995 by Y. Giomataris *et al.* [44], conceived as a new approach to overcome the limitations of the MSGC. It consists in a parallel-plate electron-multiplication structure in combination with a conversion-drift region. The amplification gap is formed by a micro-mesh grid fixed by insulating pillars over the anode. This region is typically of $\sim$100 μm with electric fields of about 100 kV/cm, while the conversion region can range from few mm to some meters with moderate electric fields (about 100-1000 V/cm). The operation principle of Micromegas is simple: ionizing radiation produce free electrons in the conversion region, which are drifted towards the amplification gap. The electrons pass through the mesh holes due to the shape of the field lines and an avalanche is produced for every electron in the amplification gap. The moving charges between the mesh and the anode induce the signals at the electrodes that are conveniently read-out. The large ratio between amplification and drift fields allows a high electron transmission from the conversion to the amplification region and a fast evacuation of the ions, avoiding charge space effect that could produce gain fluctuations in high rate environments.

Micromegas detectors are being used in many high energy and nuclear physics R&D projects or experiments, such as COMPASS [49], NA48 [50], n-TOF[51], T2K [52], CLAS-12 [53], ATLAS muon tracking system [54]. Besides, they are also being applied in rare event searches, as discussed in section 1.7.

1.6.1 Micromegas design and fabrication

The manufacturing process has evolved since their invention. In the first prototypes, the micromesh and the anode plane were build separately over supporting frames that were lately screwed together. Gold-coated anode strips (5 μm thick, 50 μm width and 200 μm pitch) are printed over an insulating substrate. Standard lithographic techniques are applied to a photoresisitive film to develop the insulating pillars, which are then glued to a frame and mounted on the strip surface, defining a precise (2%) gap. The micromesh (3 μm thick, with 17 μm openings every 25 μm) was made in nickel using the electroforming technique and then glued on a supporting frame. The two frames were then screwed together and the application of the voltage in the micromesh stretched it over the insulating pillars.

A new method for making the micromesh was developed combining chemical etching techniques and high precision photolithography over a kapton foil copper-plated in both sides [55]. It consists in applying a photoresistive film on two faces of copper clad. Then, the lithographic etching is applied over both sides, where the masks have the mesh holes pattern and the pillars pattern respectively. Finally, copper and kapton are chemically etched, configuring the mesh and the pillars, which are mounted on top of the anode pads.

However, these production procedures required screwing the mesh and strips frames and delicate manual handling. In order to avoid this and achieve better parallelism and feasibility, new manufacturing techniques were developed: the bulk [56] and microbulk [57] technologies. They are characterized by the fact that the readout plane and the micromesh form a single structure.

Bulk technology. In the bulk Micromegas technology, the usual electroformed mesh is replaced by a woven wire mesh (tenths of μm thick), which are very robust to stretching and handling and are industrially produced, existing in inexpensive large rolls in many materials. The schematics of the fabrication procedure is shown in figure 1.15. The whole detector is made in one single piece. The support base material, the copper strips, the photo-imageable polymide film and the mesh are laminate together. Then, the photoresistive film is etched by photolitographic methods producing the pillars (see figure 1.16). The industrial assembly process allows to produce large and stable bulk Micromegas modules at low-cost.

The amplification gap in bulk detectors ranges typically between 128 μm to 256 μm, showing quite high gain before the spark limit ($2{\cdot}10^4$ in Ar + 5% iC_4H_{10}), an ion-induced signal risetime of about 100ns (dependent on the gap size), gas gain uniformity and energy resolution better than 20% FWHM at 5.9 keV.

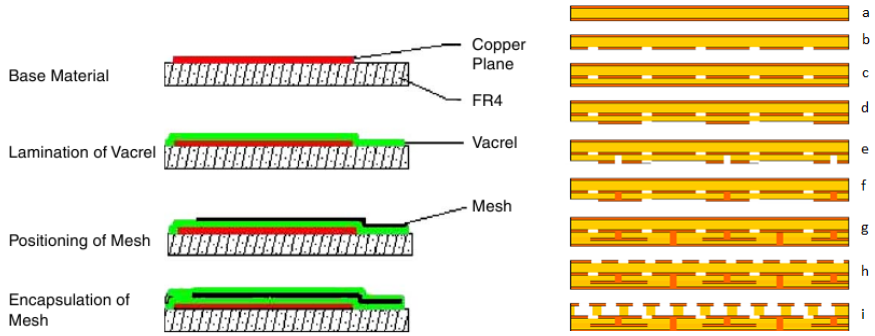

Figure 1.15: Schematics of the fabrication procedure of the bulk (left) and microbulk (right) Micromegas. The process is described in the text.

Microbulk technology. The schematics of the manufacturing process of microbulk Micromegas with 2D readout is shown in figure 1.15. The base material is a kapton foil of 50 μm thickness with 5 μm copper layers in both sides ((a) in the figure). The interconnection of the readout pads requires adding two Cu-coated kapton back-layers, although the connection in one direction can currently be done at the pads level. The readout pads are constructed by means of standard photolithography (b). Then, a single-side Cu-coated kapton foil is attached to the pads side (c), which is etched to make the readout line connections in one direction (d). The kapton etching (e) and copper filling (f) produces the vias to the readout lines. The second layer of Cu-coated kapton is attached and the readout lines in the other direction and the vias are constructed equivalently (g). Finally, the mesh holes are produced by photochemical methods (h) and the kapton is etched to produce the pillars (i). The kapton pillars are produced below the mesh copper, avoiding dead spaces. The mesh holes pattern of a microbulk Micromegas detector are shown in figure 1.16.

This technique achieves the highest precision in the gap homogeneity and flatness, which allows to achieve energy resolutions as good as 11.2% FWHM at 5. keV in Ar + 5% iC_4H_{10} [57], or better than 2% FWHM at 5.5 MeV in 2% and 5% argon-isobutane mixtures. The gain energy resolution of microbulk Micromegas in different argon and xenon gas mixtures at different pressures has been extensively studied for example in [18, 19, 20].

1.6.2 Micromegas properties

Some of the fundamental features of bulk and microbulk Micromegas detectors used in CAST and TREX-DM experiments have been measured within this work. These results are shown in subsequent chapters. Here, we simply discuss qualitatively the most relevant properties of Micromegas detectors and their dependencies:

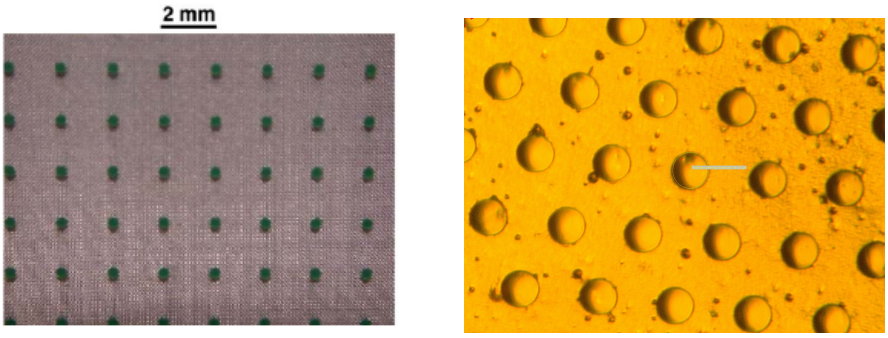

Figure 1.16: A bulk detector where the 400 µm diameter pillars spaced every 2 mm are visible (left, extracted from [56]) and the mesh holes pattern of a microbulk detector (right).

1. **Electron transmission:** the electron transmission or transparency of the mesh is the fraction of initial electrons that pass from the conversion region to the amplification gap through the mesh holes. The absolute measurement of this fraction cannot be done, so the results are normalized. The transparency depends on the detector geometry and on the ratio of amplification and drift fields. It is fundamental that Micromegas detectors are operated at the plateau of maximum electron transmission, where the full electron cloud is transmitted through the mesh. For a given amplification field, this maximum is reached at moderate drift fields. In very large drift field configurations, many lines end up at the mesh, reducing the electron transmission. In low drift field configurations, free electrons drift very slowly so recombination and attachment processes become too important to achieve high transmission.
2. **Gain:** the gain is the multiplication factor of the electrons in the amplification gap. The electron multiplication process is described in section 1.3.3. This quantity can be measured provided the total energy deposition and the W factor of the gas are known. In Micromegas detectors, the maximization of the gain is obtained by simple substitution of equation 1.27 in equation 1.26 and differentiation. The gain depends on the gap size, bias voltage, pressure and gas mixture. In the Rose and Korf model, the amplification gap that maximizes the multiplication factor is $d_{max} = BP/V$, where P is the gas pressure, V the bias voltage and B a gas parameter. With gaps around d_{max}, the gain fluctuations due to mechanical defects, atmospheric or temperature variations are minimized. The existence of this maximum is demonstrated in [58] by studying the variation of the gain with pressure, what is expected to be equivalent to the gap variation.
3. **Energy resolution:** it is the accuracy with which the energy of an event is determined. The energy resolution of an ideal gaseous detector is given by equation 1.33. In practice, one needs to include two more terms: δ_n coming from the electronic noise and δ which accounts for any other issue, like spatial inhomogeneities or pressure and temperature fluctuations. It can be then described as $R \propto (W/E_0(F+b) + \delta^2 + \delta_n^2)^{1/2}$. The energy resolution depends on the ratio of amplification and drift fields: it is optimized at the maximum of the electron transmission, experimenting a degradation beyond the plateau. It also depends on the amplification field: it is degraded at values close to the spark limit due to the increased fluctuations of the gas gain, and at very low gains, it also degrades because electronic noise becomes comparable to the signal size.
4. **Position resolution:** it is the accuracy of the coordinate determination of an event. Micromegas have the potential of achieving excellent position resolution due to the high granularity of the readout and the small avalanche gap. The position resolution is normally measured as the difference between the centroid measured by the Micromegas and the extrapolation to the Micromegas of a reference measurement when irradiated by a perpendicular and collimated beam. Alternatively, it is measured as the difference between two

Micromegas situated back-to-back. Position resolutions as good as 36 μm and 24 μm have been achieved with Micromegas of 250 μm and 500 μm respectively [59] in argon-based mixtures. Position resolution is limited by the electron diffusion in the drift gap. In order to estimate the best achievable position resolution a Micromegas with 100 μm was operated in a fast low-diffusion gas like CF_4:iC_4H_{10} (80:20), achieving a spatial resolution of 14 μm.

5. **Time resolution:** the accuracy on the time determination in Micromegas detectors can be theoretically expressed as: $\sigma_t = 1.28t/\ln G$ [48]. Here, t is the time in which electrons are collected ($\sim$1 ns) and G is the detector gain ($\sim 10^4$), giving a theoretical time resolution of about 0.1 ns. In practice, this is difficult to achieve because the resolution is dominated by the drift times of the primary electrons and fast enough amplifiers require operating the detector at too high gains. However, with the deposition of a CsI photocathode on the mesh and by illuminating with UV light, time resolutions as good as 0.5 ns are achieved [48].

1.7 The T-REX project

The T-REX project (TPCs for Rare Event search Experiments) [60], developed in the University of Zaragoza, aims to apply TPCs with novel micropattern structure concepts in experiments searching for rare events, like axion, dark matter or double beta decay experiments. These searches are characterized by the extremely low counting rates expected. The T-REX project goal is to merge the ultra low-background know-how (passive and active shielding, selection of radiopure materials and event discrimination) with the enhanced features that a gaseous TPC provides. In particular, a TPC instrumented with a highly granular readout provides the topological information of the event, allowing for powerful background suppression and signal identification. The main task concerns the development and study of the latest Micromegas readout planes in order to meet the requirements posed by the different rare event searches. In this context, the T-REX activity during the last years includes the characterization of novel Micromegas readouts, especially those of microbulk type, study and improvement of their radiopurity, simulation, development of discrimination algorithms, and the construction and test of demonstrating prototypes. The three fundamental applications are: the low background x-ray detectors of the CAST experiment for axion searches, the R&D studies of Micromegas readouts for dark matter within the TREX-DM project and for double beta decay within the NEXT collaboration. The two first applications are the issue of this work.

Part II

Search of solar axions in CAST with Micromegas detectors: limit on the $a\gamma\gamma$ coupling in the 2012 ^4He phase and the new vacuum phase.

Chapter 2

Axion physics: theory and experiments

Contents

2.1 Introduction

The Standard Model (SM) is the most successful theory of particle physics to date. The experimental observations show that the theory describes with high precision the interaction of the elementary constituents of matter. The recent discovery of the Higgs boson closes the search for the matter content predicted by the theory. Despite its great success, it is inherently an incomplete theory as it does not provide a satisfactory explanation for many basic phenomena of the Universe (e.g., gravitational force, the nature of dark matter and dark energy, the neutrino mass, or the matter/antimatter asymmetry), or it does not explain some features of the theory itself (e.g, the hierarchy problem, or the high number of free parameters).

One of the problems belonging to the last category is the fact that the CP symmetry seems not to be violated in the strong interactions (*strong CP problem*), even if the theory contains a CP violating term. Experimentally, no such violation has been observed, implying that the coefficient of this term is unnaturally very close to zero, which requires a high degree of fine tunning.

The PQ[1] mechanism [61, 62], proposed in 1977, is the most compelling solution to the long-standing strong CP problem of Quantum Chromodynamics (QCD). A consequence of this mechanism is the existence of a weakly interacting, pseudoscalar neutral particle with very low, but not vanishing mass: the axion [63, 64].

Besides, axions and other more generic axion-like pseudoscalar particles that arise in some extensions of the SM (e.g., string theory [65]) are, along with the Weakly Interacting Massive Particles (WIMP) of supersymmetric theories, the most attractive dark matter candidates. Their interest relies in the fact that both WIMPs and axions were not proposed to solve the dark matter problem of the Universe, but they may naturally solve it.

The astrophysical and cosmological arguments that constrain the phase space available for the axion existence are briefly reviewed in this chapter, along with some possible positive hints coming from astrophysical observations. The diverse axion detection techniques used to look for axions are summarized, and the current and projected sensitivities of the leading experiments in the field are shown.

2.2 QCD and axions

In the 1960s, a great number of particles classified as hadrons were discovered in particle accelerators. It was Gell-Mann and Yuval Ne'eman who proposed and scheme to classify these hadrons by mass, spin and charge in the so-called *eightfold way* [66]. Afterwards, it was realized that this group structure could be reproduced by the existence of three flavours of more elemental fractionally charged particles, the quarks. All the experiments looking for these fractionally charged particles failed, suggesting that quarks were just a mathematical tool with no physical correspondence in the real world.

However, in order to explain the kinematics of high energy hadron collisions, the parton model was invoked by Feynman in 1969 [67], in which partons are real elementary particles. The controversy between the approaches of Gell-Mann and Feynman finished when experiments conducted in SLAC in 1969, verified that partons behaved as point-like real particles. The discovery of asymptotic freedom [68] and the use of perturbative methods of quantum field theory allowed to make precise predictions, which have been verified with high precision in a huge body of experimental observations. The use of computational methods allowed to verify the confinement of quarks and gluons inside hadrons, although a mathematical proof is still lacking.

QCD is the theory that describes the fundamental interaction between quarks and gluons which make up the hadrons. QCD is a non-abelian gauge theory with symmetry group $SU(3)$. The analog to the electric charge of electromagnetism is the property called color, which it is conserved. The eight gauge bosons of QCD, corresponding to the generators of $SU(3)$, are the force carriers of the strong interactions: the gluons. They are the analog to the photon of quantum electrodynamics, whose symmetry group is $U(1)$.

2.2.1 The $U(1)_A$ problem

The development of QCD theory and experiments in the 1970s made clear the presence of a shortcoming. The QCD Lagrangian density for N flavours is

$$\mathcal{L}_{QCD} = \sum_{n=1}^{N} \overline{\psi_n}(i\gamma^\mu D_\mu - m_n)\psi_n - \frac{1}{4} G^a_{\mu\nu} G^{\mu\nu}_a \tag{2.1}$$

where the first term describes the quark fields ψ_n and the second the gluon self-interaction, being $G^a_{\mu\nu}$ the gluon field tensor with $a = 1, ...8$. The quark mass of flavour n is m_n. The covariant derivative is defined as $D_\mu = \partial_\mu - ieA^a_\mu T^a = \partial_\mu - ieA_\mu$, being g de coupling constant and T^a the generators of the $SU(3)$ group rotations of the quark fields in the color space.

[1] after R. D. Peccei and H. R. Quinn

The QCD Lagrangian is invariant under $SU(3)$ transformations corresponding to the color conservation in strong interactions. Besides, in the limit of vanishing quark masses $m_n \longrightarrow 0$, the system has an additional global symmetry: $U(N)_V \times U(N)_A$, i.e., the system is invariant under flavour and chirality transformations. In practice, only m_u and m_d are approximately zero ($m_{u,d} \ll \Lambda_{QCD}$). Thus, we expect QCD to be approximately $U(2)_V \times U(2)_A$ invariant. Indeed, it is observed experimentally that QCD is $U(2)_V = SU(2)_V \times U(1)_V$ invariant. The associated conserved quantity under $SU(2)_V$ is isospin, which adequately describes the organization of hadrons in multiplets of the similar mass (e.g., singlets: Λ^0, doublets: (p,n), triplets: (Σ^+,Σ^0,Σ^-), quartets: (Δ^{++}, Δ^+, Δ^0, Δ^-), etc.). Meanwhile, $U(1)_V$ conserves the baryon number.

On the other hand, $U(2)_A = SU(2)_A \times U(1)_A$ symmetry of QCD is not observed in nature. When the vacuum state does not posses a symmetry of the Lagrangian, it is said that the symmetry is spontaneously broken. If the symmetry is exact the consequence is the existence of a massless boson, a Nambu-Goldstone (NG) boson. If the symmetry is only approximate, a massive particle arises, a pseudo-NG boson. The NG bosons associated with the breakdown of $SU(2)_A$ are the pions. The breaking of the $U(1)_A$ symmetry should produce a NG boson, whose expected mass is less than $\sqrt{3}m_\pi$. However, there are no signs of such a light particle in the hadronic spectrum. The η particle has the correct quantum numbers, but it is largely too heavy. The lack of a pseudoscalar NG candidate for the spontaneous breaking of the $U(1)_A$ symmetry is called the $U(1)_A$ problem of QCD [69], which threatened for some time the robustness of the theory.

2.2.2 Solution of the $U(1)_A$ problem

The resolution of the $U(1)_A$ problem of QCD was possible thanks to the realization by 't Hooft [70] that non-abelian gauge theories have a rich vacuum structure. The complexity of the vacuum structure makes that an infinite number of degenerate states that cannot be continuously transformed into one another minimize the action. Thus, the correct vacuum configuration of QCD is the superposition of an infinite number of degenerate states labeled by the number n

$$|\theta\rangle = \sum_{n=-\infty}^{\infty} e^{-in\theta}|n\rangle \tag{2.2}$$

where θ is an arbitrary number of the theory $0 < \theta < 2\pi$ that must be measured. The state $|\theta\rangle$ is usually named «the θ-vacuum». The effect of this vacuum state is the anomalous breaking of the $U(1)_A$ symmetry [71], which is not longer a true symmetry of QCD. By appropriate means, the effect of the θ-vacuum can be recast in a single non-perturbative term to be added to the QCD Lagrangian

$$\mathcal{L}_\theta = \theta \frac{g^2}{32\pi^2} G^a_{\mu\nu} \tilde{G}^{\mu\nu}_a \tag{2.3}$$

where $G^a_{\mu\nu}$ is the field strength tensor and $\tilde{G}^{\mu\nu}_a$ its dual. When the electroweak sector is taken into consideration, a second term proportional to $G^a_{\mu\nu}\tilde{G}^{\mu\nu}_a$ arises in the theory

$$\mathcal{L}_{weak} = \arg(\det M) \frac{g^2}{32\pi^2} G^a_{\mu\nu} \tilde{G}^{\mu\nu}_a \tag{2.4}$$

where M is the diagonalized quark mass matrix. Putting Eqs. 2.3 and 2.4 together the additional term to the QCD Lagrangian is

$$\mathcal{L}_{\bar{\theta}} = \mathcal{L}_\theta + \mathcal{L}_{weak} = \bar{\theta} \frac{g^2}{32\pi^2} G^a_{\mu\nu} \tilde{G}^{\mu\nu}_a \tag{2.5}$$

where $\bar{\theta} = \theta + \arg(\det M)$. The addition of $\mathcal{L}_{\bar{\theta}}$ to the QCD Lagrangian solves the $U(1)_A$ problem, but a new problem arises. The $\mathcal{L}_{\bar{\theta}}$ term is not invariant under CP transformations. However, the CP violation has never been observed experimentally in QCD.

2.2.3 The EDMN and the strong CP problem

The most sensitive way of looking for CP violation in QCD is the measurement of the permanent Electron Dipole Moment of the Neutron (EDMN), denoted by d_n. A non-vanishing value of d_n means the violation of CP symmetry in strong interactions. A neutron is a neutral particle with substructure, as it is proven by the fact of its non-vanishing magnetic dipole moment (MDMN) [72]. Thus, the neutron can be conceived as an object with moving electric charges inside it. An electric dipole moment can only exists in a particle if the charge distribution inside it is not symmetric. In figure 2.1, a model of a neutron without (left) an with (right) EDMN is sketched.

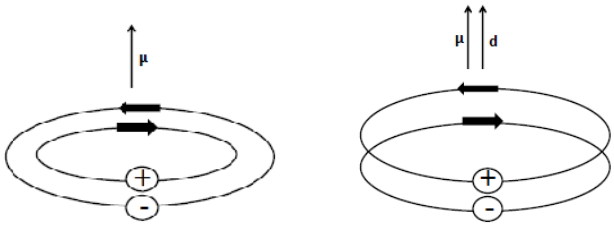

Figure 2.1: A neutron model with vanishing (left) and no-vanishing (right) EDMN. The electric and magnetic dipole moments are denoted respectively by d and μ.

While a neutron with non-vanishing EDMN is invariant under charge conjugation transformation, it is not under parity and time reversal transformations. The effect of applying these transformations in our neutron model are shown in figure 2.2. It is straightforward to observe that the system is neither invariant under CP transformations. The same conclusion is derived considering that CPT symmetry holds for all physical phenomena [73, 74]. The fact that a non-vanishing EDMN would produce time reversal violation in the system, implies that CP symmetry must come also violated.

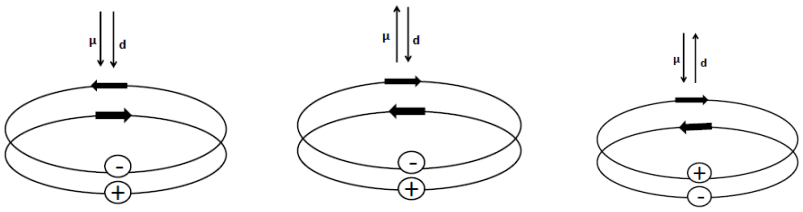

Figure 2.2: Charge conjugation (left), parity (middle) and time reversal (right) transformations effect on a neutron model. The electric and magnetic dipole moments are denoted respectively by d and μ.

The relation between EDMN and the $\bar{\theta}$ parameter is [75, 76, 77]

$$d_n \approx \frac{e\bar{\theta}m_q}{m_n} \tag{2.6}$$

where m_q is the reduced quark mass given by $m_q = m_u m_d/(m_u + m_d)$ and m_n is the neutron mass. The most sensitive measurements of EDMN set a bound $|d_n| < 2.9 \times 10^{-26}$ e×cm (90% CL) [78], corresponding to a limit of $\bar{\theta} < 10^{-10}$. The smallness of $\bar{\theta}$ is not forbidden, but it results very unnatural. Even more if we consider that $\bar{\theta}$ arises as the combinations of two separate and independent effects: the vacuum structure of QCD, and electroweak effects involving quark masses. This fact implies either that both parameters are extremely small or that they are fine-tunned to a exceptional degree. The unnatural smallness of $\bar{\theta}$ is a long-standing problem of QCD referred to as strong CP problem. Or, in other words, why the strong interactions seem to not violate CP when the theory contains a term that allows it.

2.2.4 The Peccei-Quinn Solution and axions

The most appealing solution to the strong CP problem was proposed by Peccei and Quinn in 1977 [61, 62]. Their original idea is to promote the $\bar{\theta}$ parameter into a dynamical variable, which due to its classical potential relaxes to zero. This is accomplished by the addition of a new global chiral $U(1)$ symmetry, usually named $U(1)_{PQ}$, which is spontaneously broken at a scale f_a. Shortly thereafter, Weinberg and Wilczek realized that due to the spontaneous symmetry breaking of $U(1)_{PQ}$ there should be a new non-massless pseudo-Nambu-Goldstone boson, the axion [63, 64]. The resulting contribution to the Lagrangian is

$$\mathcal{L}_a = \frac{a}{f_a}\xi\frac{g^2}{32\pi^2}G_a^{\mu\nu}\tilde{G}^a_{\mu\nu} \tag{2.7}$$

where a is the axion field and ξ is a model-dependent constant. Combining this term with the previously discussed $\bar{\theta}$ term in Equation 2.5 and the remaining axion terms we have

$$\mathcal{L}_a = -\frac{1}{2}\partial^\mu a\partial_\mu a + \mathcal{L}_{int}\Big[\frac{\partial^\mu a}{f_a};\psi\Big] + \left(\frac{a}{f_a}\xi + \bar{\theta}\right)\frac{g^2}{32\pi^2}G_a^{\mu\nu}\tilde{G}^a_{\mu\nu} \tag{2.8}$$

where the first term accounts for the axion kinetic energy, the second term accounts for the axion field interactions and the last term accounts for the axion potential energy. In this way, the $\bar{\theta}$ parameter has promoted to a dynamic variable, and the axion field acquires an effective potential of the form

$$V_{eff} \sim \cos\left(\bar{\theta} + \frac{a}{f_a}\xi\right) \tag{2.9}$$

whose minimization with respect to the axion field occurs at the axion field expectation value $\langle a\rangle$

$$\langle a\rangle = -\frac{f_a}{\xi}\bar{\theta} \tag{2.10}$$

for which the coeffient of the $G^a_{\mu\nu}\tilde{G}^{\mu\nu}_a$ term cancels, dynamically solving the strong CP problem. Moreover, expanding the axion field around the vacuum expectation value gives the axion a mass

$$m_a^2 = \left\langle\frac{\partial^2 V_{eff}}{\partial a^2}\right\rangle = -\frac{\xi}{f_a}\frac{g^2}{32\pi^2}\frac{\partial}{\partial a}\left\langle G_b^{\mu\nu}\tilde{G}^b_{\mu\nu}\right\rangle\Big|_{\langle a\rangle=-\bar{\theta}f_a/\xi} \tag{2.11}$$

This mechanism is valid for any value of the $U(1)_{PQ}$ breaking scale, f_a, so *a priori*, the axion mass is also arbitrary.

Summarizing, the strong CP problem is restored by the Peccei-Quinn mechanism introducing a spontaneously broken global symmetry and its associated massive pseudo-Nambu-Goldstone boson, whose detection would definitely validate the theory.

2.3 Axion interactions and models

Searching for the axion requires to know about their properties and how it interacts with ordinary matter. The properties that characterize the axion are its mass m_a and its coupling to other particles, g_{ai}, which depend on the only free parameter of the theory: the arbitrary breaking scale f_a of the $U(1)_{PQ}$ symmetry. Axions interact with gluons and photons in all theoretical models, although there are models in which they also couple with fermions, like electrons and neutrons. In basis of the couplings of axions with matter one can derive the coefficient that relates m_a and f_a, or conceive the experimental techniques for the axion detection.

2.3.1 Axion couplings

Coupling to gluons

The axion coupling with gluons is governed by equation 2.7. The fact that both neutral pions and axions are bosons with the same quantum numbers allows for the mixing of their propagating states. The mass and interaction strength of the interaction are usually expressed in terms of the scaling factor f_π/f_a, where $f_\pi = 92$ MeV is the pion decay constant. By appropriate algebraic methods one finds that in first approximation $m_a f_a \approx m_\pi f_\pi$, where $m_\pi = 135$ MeV is the π^0 mass. Going into more detail

$$m_a = \left(\frac{z}{(1+z+w)(1+z)}\right)^{1/2} \frac{f_\pi m_\pi}{f_a} \sim 6.0 \text{ eV} \left(\frac{10^6 \text{ GeV}}{f_a}\right) \tag{2.12}$$

where the nominal values for $z = m_u/m_d = 0.56$ and $w = m_u/m_s = 0.029$ have been assumed [79, 80].

Coupling to photons

The two-photon interaction with axions is of fundamental interest for most of the experimental searches. The contribution to the $a\gamma\gamma$ interaction is illustrated on the right of figure 2.3. The Lagrangian that describes the interaction is given by

$$\mathcal{L}_{int} = -\frac{1}{4} g_{a\gamma} F_{\mu\nu} \tilde{F}^{\mu\nu} a = g_{a\gamma} \vec{E} \vec{B} a \tag{2.13}$$

where $F_{\mu\nu}$ is the electromagnetic field-strength tensor, $\tilde{F}_a^{\mu\nu}$ its dual, and $\vec{E}$ and $\vec{B}$ the electric and magnetic fields respectively. Thus, photons can oscillate into axions and the other way around, a processes known as Primakoff and inverse-Primakoff effect. The coupling constant is given by

$$g_{a\gamma} = \frac{\alpha}{2\pi f_a} \left| \frac{E}{N} - \frac{2\,(4+z+w)}{3\,(1+z+w)} \right| = \frac{\alpha}{2\pi f_a} \left| \frac{E}{N} - 1.92 \pm 0.08 \right| \tag{2.14}$$

where α is the fine structure constant. Therefore, the actual value of the coupling constant $g_{a\gamma}$ relies on the model-dependent ratio E/N, where E and N are the electromagnetic and color anomaly of the axial current associated with the axion field. In the two most widely accepted axion models (see Section 2.3.2) the ratio $E/N = 0$ (hadronic models, e.g., KSVZ model [81]) and $E/N = 8/3$ (gran unified theories, e.g., DFSZ model [82, 83]), but more generally, E/N can take a broad range of values, and for a fixed f_a, so can $g_{a\gamma}$ [84]. On the left of figure 2.4, the model-favored «axion-lines» in the $g_{a\gamma} - m_a$ plane are shown.

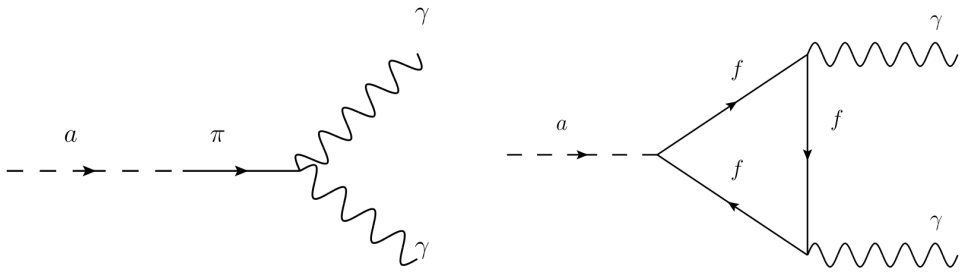

Figure 2.3: Feynman diagram of the $a\gamma\gamma$ coupling. On the left, the coupling is mediated by the axion-pion mixing, while on the right the interaction is mediated by fermions.

The life-time of the axions is governed by the decay $a \longrightarrow \gamma\gamma$. The decay rate is given by [85]

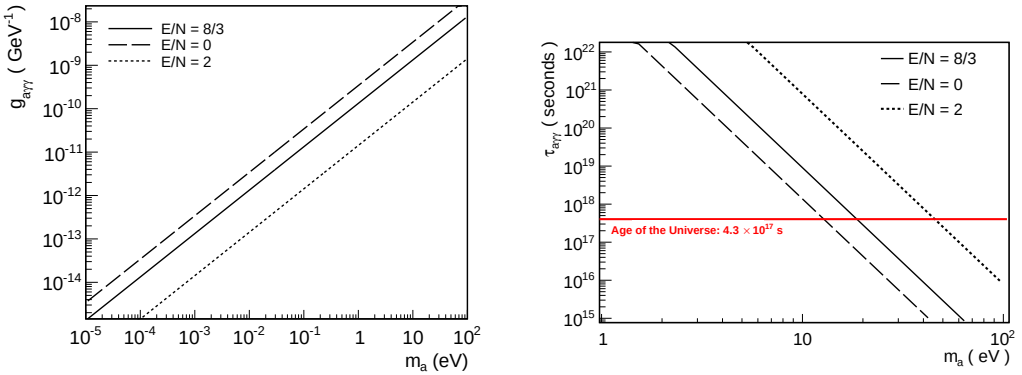

Figure 2.4: Left: coupling constant of axion to photons as a function of the axion mass for some usual values of the E/N parameter in the different axion models. Right: dependence of the $a \longrightarrow \gamma\gamma$ decay time with the axion mass for different E/N parameters.

$$\Gamma_{a\longrightarrow\gamma\gamma} = \frac{g_{a\gamma\gamma}^2 m_a^3}{64\pi} = \frac{m_a^3 \alpha^2}{256\pi^3 f_a^2}\left(\frac{E}{N} - \frac{2\,(4+z+w)}{3\,(1+z+w)}\right)^2 \approx 1.1\times 10^{-24}\left(\frac{m_a}{\mathrm{eV}}\right)^5 s^{-1} \tag{2.15}$$

where the second expression uses Equation 2.14, and the numerical expression assumes the model in which $E/N = 0$. The dependence of the axion decay time with its mass is shown on the right of figure 2.4. Note that only if $m_a \gtrsim 20$ eV the axion decays faster than the age of the Universe, 4.3×10^{17} s

Coupling to fermions

The interaction of axions with fermions has the structure

$$\mathcal{L}_{aff} = \frac{g_{aff}}{2m_f}\bar{\Psi}_f \gamma^\mu \gamma_5 \Psi_f \partial_\mu a \tag{2.16}$$

where Ψ_f and m_f are the fermion field and mass, respectively. Here, the coupling is usually expressed as $g_{aff} \equiv C_f m_f / f_a$, being C_f a model dependent numerical coefficient. There are models that contemplate the coupling of axions to electrons at tree level ($C_e \neq 0$), while in other models they only interact through higher order loop corrections (see Section 2.3.2.2). The difference is of great importance for evaluating the astrophysical effects of the axion and justifies a distinction when setting bounds in the $(g_{a\gamma}, m_a)$ plane.

The coupling of axions to nucleons arises from two similar contributions [86]: the tree-level coupling of axions with quarks, and the axion-pion mixing. This means that even in those models in which the tree-level coupling with quarks is forbidden (as it is the case of KSVZ model), there is still a contribution to the coupling with nucleons of the same order that in those models that present both contributions.

2.3.2 Axion models

For all axion couplings, the larger the f_a scale, which in principle is unconstrained, the smaller the mass and weaker becomes the interaction strength. Historically, we distinguish between two generic models characterized by the size of f_a. Models with small f_a lead to high axion masses and couplings, denominated «visible axions». On the other hand, large f_a values lead to tiny axion masses and its interactions with Standard Model particles are then highly suppressed, denominated «invisible axions».

2.3.2.1 Visible axions

Weinberg and Wilczek [63, 64] demonstrated that the implication of the $U(1)_{PQ}$ symmetry proposed by Peccei-Quinn was the existence of a light pseudoscalar, originally named visible or PQWW axion. In this axion model it was assumed that the breakdown scale of the $U(1)_{PQ}$ symmetry was of the order of the weak scale, $f_a \approx f_{weak} \approx 250$ GeV. The minimal ingredient for including the $U(1)$ symmetry in the SM is the existence of two orthogonal Higgs doublets, Φ_1 and Φ_2, which allow for invariant $U(1)_{PQ}$ transformations. In this model, the axion is the common phase to Φ_1 and Φ_2

$$\Phi_1 = \frac{v_1}{\sqrt{2}} \begin{pmatrix} 1 \\ 0 \end{pmatrix} e^{ixa/f_a} \qquad \Phi_2 = \frac{v_2}{\sqrt{2}} \begin{pmatrix} 0 \\ 1 \end{pmatrix} e^{ia/xf_a} \tag{2.17}$$

where $v_1/\sqrt{2}$ and $v_2/\sqrt{2}$ are the Higgs vacuum expectation values and x its ratio, with $f_a = \sqrt{v_1^2 + v_2^2} = \left(\sqrt{2}G_F\right)^{-1/2} = v \approx 250$ GeV. Substituting this f_a value into the numerical expression of equation 2.12 give rise to an axion mass $m_a \approx 24$ keV. This axion model has been ruled out after intensive searches, like the non-observation of the process $K^+ \longrightarrow \pi^+ + a$. Indeed, the expected branching ratio [87] is

$$BR(K^+ \longrightarrow \pi^+ + a) \gtrsim 3 \cdot 10^{-5} \tag{2.18}$$

which it is much higher than the experimental bound [88]

$$BR(K^+ \longrightarrow \pi^+ + \text{nothing}) \lesssim 3.8 \cdot 10^{-8} \tag{2.19}$$

Although alternative models with $f_a \approx f_{weak}$ were proposed they have been extensively excluded by experiments.

2.3.2.2 Invisible axions

As stated before, the PQ mechanism works for every value of f_a, so after experimentally ruling out visible axions, models with $f_a \gg f_{weak}$ were proposed. The resulting axions are much lighter, very weakly coupled to ordinary matter and very long lived ($\tau_{a\gamma\gamma} \sim f^5$, see equation 2.15). The minimal ingredient of these models is a complex scalar field σ, being the axion its phase

$$\sigma = \frac{f_a}{\sqrt{2}} e^{ia/f_a} \tag{2.20}$$

This field acquires a vacuum expectation value, spontaneously breaking the PQ symmetry. Basically, two type of models have been proposed differing in whether they couple to fermions at tree level or not.

KSVZ axions

The KSVZ model was proposed by Kim [81], and Shifman, Vainstein and Zakharov [199] in 1979. In this model the vacuum expectation value of the σ field is $\langle\sigma\rangle = f_a \gg f_{weak}$, and a new heavy quark Q with $M_Q \sim f_a$ is introduced in the theory, which is the only field that posses tree-level coupling with ordinary quarks and leptons. Due to this property they are usually called *hadronic axion models*, and the interaction of axions with quarks or electrons is suppressed. Diverse implementations of the model provide different axion properties, expressed in terms of the E/N ratio, which is proportional to the new exotic quark electric charge. The standard KSVZ model generates a neutral quark and thus, $E/N = 0$, although E/N can typically range between 0 and 6.

The drawback of the model is the lack of physical motivation for a new heavy quark.

DFSZ axions

This model was proposed by Dine, Fischler, Srednicki [83], and Zhitnitski [82] in 1980-81 in the contexts of Gran Unified Theories. Like visible axion models, it also requires the existence of at least two Higgs fields Φ_1 and Φ_2, whose interaction with the σ field induce the tree-level coupling of axions with quarks and leptons. In this model $E/N = 8/3$.

KSVZ and DFSZ are the more generic axion models, but other implementations exist.

2.4 Axion-like particles

In order to overcome the limitations of the SM many theoretical proposals have been advocated. Two of the most appealing are string theory and supersymmetry. This theoretical frameworks provide new heavy ($m \gtrsim 100$ GeV), weakly interacting particles (usually coined WIMPs, Weakly Interacting Massive Particles), which are natural candidates to account for the dark matter of the Universe, the most well-known of which is the neutralino (see part III on this *Thesis*). Although there is no clear evidence of their existence, the detection of these particles may be at reach of the current multi-TeV proton collisions at the Large Hadron Collider (LHC), and of the current or planned multi-ton underground WIMP experiments.

Most of the SM extensions also predict the existence of many very light (sub-eV) weakly-coupled particles, named WISPs (Weakly Interacting Slim Particles), which can also naturally constitute the total or partial amount of dark matter (DM) of the Universe. Given the rich particle structure of the SM there is no reason to think that the "dark sector" structure is simpler, so both WIMPs and WISPs could coexist. The most prominent examples of WISPs are axions and axion-like particles (ALPs), but many other exist (hidden photons, gravitinos, light moduli fields, etc.). As axions do, the more general category of ALPs usually emerge as pseudo Nambu-Goldstone bosons associated to the breakdown of global symmetries (like lepton number [90] or the R-symmetry in supersymmetric theories [91]), but also arise as string compactifications of the extra dimensions in string theory [65, 92].

From the phenomenological point of view, the most important property shared between QCD axions and ALPs is that both present coupling to two photons, opening the door to its hypothetical detection in the presence of high electromagnetic fields (see section 2.6 for a review of the main detection techniques). However, there is a fundamental difference: while axions' mass and couplings are determined by the f_a parameter, ALPs properties are much less constrained. Their masses and couplings are independent parameters, resulting in a great enlargement of their available parameter space. On the top of figure 2.5 it is shown the axion parameter space, illustrating the limits imposed by astrophysics and cosmology and current or foreseeable experiments. On the bottom of figure 2.5 the available parameter space for ALPs together with experimentally excluded regions (see section 2.6 for a review on the experimental constrains), bounds from astrophysical and cosmological observations or considerations.

2.4.1 Axions and ALPs as dark matter candidates

As mentioned before, ALPs (and axions) can account for the totality or a faction of the DM of the universe, whose existence is very strongly supported by experimental observations. Any DM candidate must be electrically neutral, do not couple via the strong or weak forces with ordinary matter and their mean life must be comparable with the age of the universe. Many ALPs satisfy these conditions, being natural candidates for dark matter.

Dark matter axions could have been formed in the early Universe either thermally or non-thermally. For small enough f_a parameters (i.e., $f_a \lesssim 10^8$ GeV, large axion masses and coupling strengths) axions thermalize in the early Universe and they would contribute to the hot dark matter (HDM) of the Universe. HDM axions would have an effect in the large-scale structure formation. The measurements of the cosmic microwave background (CMB) of *WMAP-7* places an upper bound on the axion mass $m_a \lesssim 0.9$ eV. The recent Planck measurements of the CMB

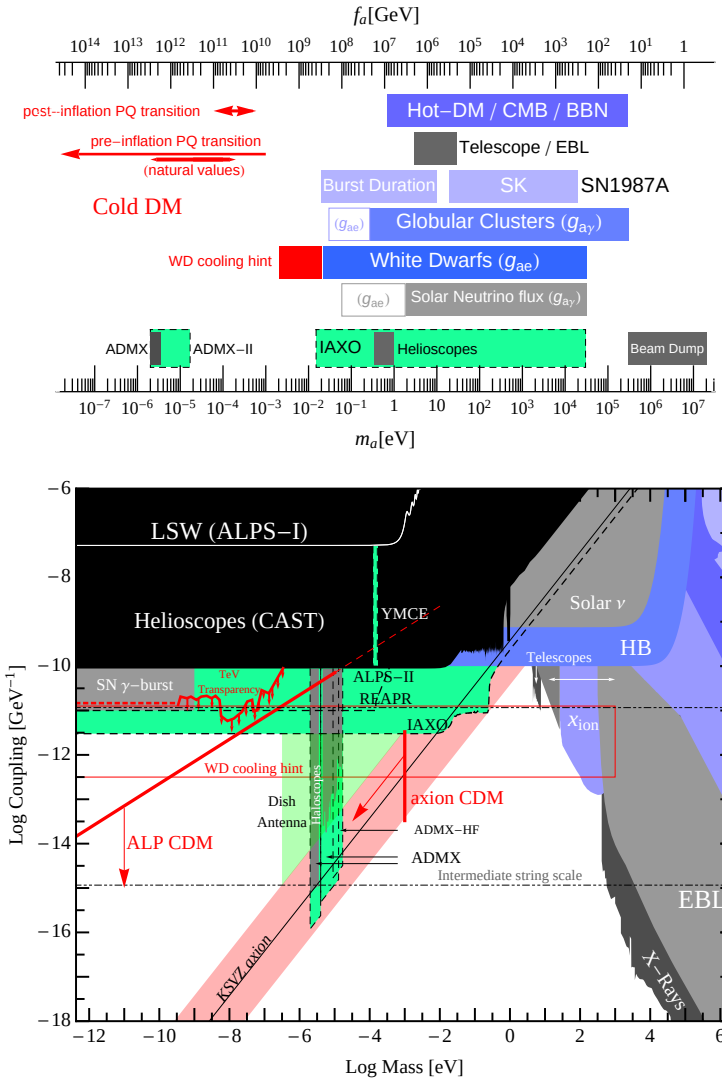

Figure 2.5: Axions (top) and ALPs (bottom) parameter space. The color code is: experimentally excluded regions (dark green), expected sensibility of future experiments (light green), constrains from astronomical observations (gray) and astrophysical or cosmological arguments (blue). In red, hints from astronomic observations and regions where ALPs could account for the totality of the Dark Matter of the universe. Extracted from [93]. An explanation of the labeled regions is given in the text.

constrains the axion mass, providing a limit $m_a \lesssim 1.01$ eV (95% CL). The inclusion of other data sets, particularly the matter power spectrum released by the Sloan Digital Sky Survey (SDSS-DR7) and the Hubble parameter measured by the Hubble Space Telescope (HST), constrains the axion mass to $m_a \lesssim 0.72$ eV (95% CL) [94]. Axions with masses above this bound would produce too much HDM.

On the other side, the effect that axion decays would have during the Big Bang Nucleosynthesis (BBN), particularly affecting the cosmic deuterium abundance, impose axions to have masses $m_a < 300$ keV [95]. These limits are shown on the figure 2.5, where can be appreciated that while HDM QCD axions are very disfavored by observations, there is still some room for HDM ALPs provided the coupling constant is $g_{a\gamma} \lesssim \mathcal{O}(10^{-13})$ GeV^{-1} [96].

Axions with large f_a posses low enough couplings not to thermalize in the early universe.

Axions can be produced by the so-called *vacuum realignment mechanism*. At temperatures above the breakdown scale of the PQ symmetry the axion is massless and the axion field assumes a value characterized by the misalignment angle, $-\pi < \theta_0 < \pi$ [97],

$$a_0 = \theta_0 \frac{\alpha\xi}{2\pi g_{a\gamma}} \tag{2.21}$$

As the Universe cools down and its temperature becomes $T < \Lambda_{QCD}$ the axion acquires mass: the axion field relaxes to its CP conserving minimum, around which it oscillates. These coherent oscillations correspond to non-relativistic axion particles [92] that can thus contribute to the Cold Dark Matter (CDM). The axion energy density Ω_a accounts for the total non-baryonic mass density when it saturates the observed value $\Omega_{\rm nbm}h^2 = 0.1186 \pm 0.0020$ (68% CL) [98].

$$\frac{\Omega_a}{\Omega_{\rm nbm}} \sim \kappa_a \theta_0^2 \left(\frac{f_a}{5\times 10^{11}\ {\rm GeV}}\right)^{1.184} \simeq \kappa_a \theta_0^2 \left(\frac{12\ \mu{\rm eV}}{m_a}\right)^{1.184} \tag{2.22}$$

where κ_a is a numerical factor ranging roughly between 0.5 and a few. Therefore, the ratio is unity for axions mass of around 10−100 μeV ($f_a \sim 5\times 10^{11}$ GeV) in case $\theta_0 \sim \mathcal{O}(1)$. Note that,unless θ_0 is sufficiently small, very light axions would produce more CDM than the experimentally observed (a phenomenon coined *overclosure* of the universe). Somewhat larger axion masses (up to the meV scale [99]) are also possible with the appropriate values of the free parameters in equation 2.22.

So far, we have considered that the PQ phase transition occurs before inflation, but it could have happened after it. In this case, θ_0 is randomly distributed in the $-\pi < \theta_0 < \pi$ range and thus, the vacuum realignment contribution to the axion energy density reads

$$\frac{\Omega_{a,VR}}{\Omega_{nbm}} \sim \left(\frac{40\ \mu{\rm eV}}{m_a}\right)^{1.184} \tag{2.23}$$

Furthermore, the decay of cosmic strings and domain walls into axions [100] suppose a new production mechanism and an additional contribution to Ω_a, which is ofter bigger than that of equation 2.22, leading to smaller preferred values of f_a (and larger m_a). There is no consensus on whether this contributions are dominant, but some estimations suggest $m_a \sim \mathcal{O}(100)$ μeV for axions accounting for the total amount of DM.

If the PQ symmetry is broken after the end of inflation, axions would constitute the 100% of CDM in a narrow range of masses given by $m_a = (71 \pm 2)\mu{\rm eV}(\alpha_{\rm dec}+1)^{6/7}$, where $\alpha_{\rm dec} = \Omega_{a,{\rm strings+walls}}/\Omega_{a,{\rm tot}}$ [101].

2.5 ALPs constrains from cosmology and astrophysics

2.5.1 Constrains from stellar evolution

ALPs would be an additional contribution to the total energy loss of a star, which in the absence of physics beyond the standard model, is mainly attributed to photons and neutrinos escaping from the plasma. The effect of ALPs in the evolution of a star is to shorten their burning process and thus reducing their lifetime. Here, we review some of the bounds imposed by this effect based on the reference [85]. On the top of figure 2.5, the constrains for the QCD axions are shown in terms of the axion mass, also including the models in which axions couple to electrons, which are typically further constrained. The same is shown for generic ALPs on the bottom of figure 2.5 in the $m_{ALP} - g_{a\gamma}$ plane.

- **Solar age:** the current phase of the Sun imposes that the axion luminosity does not exceed the photon luminosity, $L_a < g_{10}^2 1.85\times 10^{-3} L_{\rm Sun}$, setting a limit $g_{a\gamma} < 2.3\times 10^{-9}$ GeV^{-1}.
- **Helioseismology:** the effect of axion losses modify the sound-speed profile of the Sun and implies different concentrations of Helium in the core of the star. Helioseismology provides a limit $g_{a\gamma} \lesssim 1\times 10^{-9}$ GeV^{-1} [102].

- **Solar neutrino flux:** axion emission requires an increased nuclear burning rate and the temperatures are also higher. This fact implies an enhanced solar ^{8}B neutrino flux. The measurement of the ^{8}B neutrino flux allows to bound the coupling constant to photons to $g_{a\gamma} \lesssim 5 \times 10^{-10}$ GeV^{-1} [103], which can be further extended if one considers also the axion-electron coupling.
- **Globular Cluster stars:** the most stringent astrophysical limit to the $g_{a\gamma}$ of generic ALPs comes from Horizontal Branch (HB) stars in Globular Cluster (GC). A GC is a spherical collection of stars gravitationally bounded that formed at around the same time. HB stars are burning helium, whose consumption rate would be accelerated by the loss of energy in form of ALPs, implying a reduction of the HB lifetime. This phenomenon would lead to a reduction of the R ratio, defined as the ratio of HB stars with respect to Red Giant stars. However, the R ratio is compatible with the null hypothesis (no axions), imposing the long-standing limit $g_{a\gamma} < 10^{-10}$ GeV^{-1} [104]. A recent study that analyzes the dependence of the $g_{a\gamma}$ with the Helium mass fraction provides the bound $g_{a\gamma} < 0.66 \times 10^{-10}$ GeV^{-1} at 95% CL [105], which is the most stringent limit in a wide axion mass range. However, the higher than expected R parameter has been interpreted as a possible hint for an ALP coupled to photons with $g_{a\gamma} = 0.29 - 0.57 \times 10^{-10}$ GeV^{-1} [106].

  In the DFSZ models, an additional argument is used to further constrain the axion properties: axions may delay the start of helium burning producing brighter stars. Red Giant Brach (RGB) stars posses a degenerate helium core and thus processes involving axion-electron couplings are higher in these stars that in HB stars. Measurements of the RGB stars luminosity allows to set a limit in the DSFZ model of $g_{aee} < 3 \times 10^{-13}$ GeV^{-1} that corresponds to $m_a < 9$ meV$/\cos^2\beta$ and $g_{a\gamma}\cos^2\beta < 1.2 \times 10^{-12}$ GeV^{-1}, where $\cos\beta$ is related with the ratio of the two Higgs vacuum expectation values given in equation 2.17 [107].
- **White-Dwarf cooling:** After the helium burning phase, low mass stars can promote to white dwarfs: a very dense stellar remnant made out of electron-degenerate matter, which firs cools down by neutrino emission and afterwards by emission of photons from its surface. The comparison between observations and expected white-dwarf luminosity sets a limit corresponding to $g_{aee} < 1.3 \times 10^{-13}$ GeV^{-1} (95% CL), which is the most restrictive bound on the axion-electron coupling. In terms of its coupling to photons, the limit is $m_a < 5$ meV$/\cos^2\beta$ [108].
- **SN1987A, burst duration:** very massive stars can undergo core collapse when the nuclear burning force is not large enough to compensate gravitational attraction. The result is a very dense object (even neutrinos are trapped), a proto-neutron star, whose explosion releases an extremely energetic burst of radiation (of the order of the Sun emission over its entire life) in some seconds: a supernova (SN). Axion-nucleon breemstrahlung would be an additional channel for the energy loss of a SN, accelerating the cooling process and thus reducing the burst duration. For very small or null coupling g_{aN} the burst duration is maximum as there is no anomalous energy loss. The burst duration decreases as g_{aN} grows up, given the additional channel for energy loss. When the mean free path of axions becomes lower than the SN characteristic size, axions start to get trapped, ending with the maximum burst duration for high enough g_{aN}, when all axions are trapped. This process is illustrated in figure 2.6.

  In 1987 Supernova, a burst of neutrinos was observed by three different observatories: 24 anti-neutrinos were observed by Kamiokande II (11), IMB (8), and Baksan (5) in a burst lasting around 13 seconds, which it is in good agreement with theoretical expectations. In spite of the low statistics, this agreement can be used to constrain the g_{aN} coupling to a range $3 \times 10^{-10} \lesssim g_{aN} \lesssim 3 \times 10^{-7}$, which translates into the bound on the axion mass $m_a \lesssim 16$ meV. However, the uncertainties in supernova dynamics and ALP production in such a dense medium forces to take this limit with some caution.
- **SN1987, absence of gamma-ray signal:** the axions emitted by a SN would be converted to x-rays in the magnetic field of the Milky Way, leading to a potential gamma-ray excess in coincidence with the neutrino detection. The absence of such a signal in the Gamma-Ray

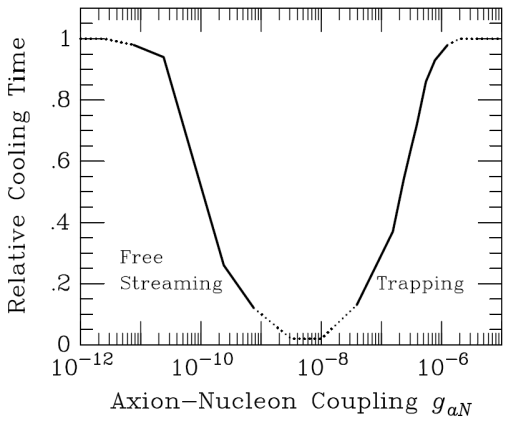

Figure 2.6: Relative duration of a SN neutrino burst as a function of the axion-nucleon coupling. Free streaming *axions have mean free paths long enough escape from the core of the neutron star, while in the* trapping *region axions are confined. Extracted from [85].*

Spectrometer (GRS) of the Solar Maximum Mission (SMM) is recently used in [109] to set an upper bound of $g_{a\gamma} \lesssim 5.3 \times 10^{-12}$ GeV^{-1} at 95% CL for $m_a \lesssim 4.4 \times 10^{-10}$ eV.

- **Existence of Cepheid stars:** Some stars in the mass range $\sim 8 - 12 M_\odot$ are known to go through a blue loop stage in their evolution. This stage is required for the existence of Cepheid stars. A recent work shows that a sufficiently large $g_{a\gamma}$ would eliminate the blue loop phase of these stars, matching the observation of less blue stars than expected. This fact provides a very stringent limit of $g_{a\gamma} < 0.8 \times 10^{-10}$ GeV^{-1} [110], but also interpretable as a hint of the ALP existence.

2.5.2 Constrains from ALP decay

- **EBL:** if the photons produced by ALP decay could produce observational effects, particularly one would observe a peak at energy $E = m_a/2$ in the photon spectra, somehow affected by redshift. So far, the Extragalactic Background Light (EBL) has not revealed any significative feature in the spectrum, so the decay rate of the ALP must be obscured by other gamma sources, placing a limit on the $m_a - g_{a\gamma}$ plane labeled *EBL* in figure 2.5 [111].
- **Telescope:** dark matter is aggregated around galaxies and other large-scale structures, where its decay may produce visible light above the background for sufficiently high couplings. The absence of such a signal allows to exclude the region labeled as *Telescopes* in figure 2.5 [112].
- **X-rays**: the same argument applies for the x-ray spectra measured in the context of sterile neutrinos. The properly scaled limit to the ALP is shown in figure 2.5, labeled *X-rays* [113].

Astronomical and cosmological observations provide an excellent insight in the axion/ALP physics. Although no positive signal has been observed so far, the parameter space has been significantly constrained, and some unexplored regions are very well motivated from the dark matter point of view, as the so-called *classic axion window*, $m_a \sim 10^{-3} - 10^{-5}$ eV (although, as stated before, much lower axions masses are also possible in the so-called *anthropic axion window*. Besides, there are some appealing astronomical observations that could be explained by the existence of ALPs. These hints are reviewed below.

2.5.3 ALPs hints

There are some troublesome astrophysical phenomena that could be explained by the existence of ALPs. However, one should take with caution the ALP interpretation of unexplained astronomical

observations because they can be probably due to experimental systematics or more conventional physics. However, while these observations remain unaccounted for with standard physics, they suppose an additional physical motivation for exploring favored regions of the ALP parameter space.

Cooling of White-Dwarfs

The cooling rate of White-Dwarf (WD) stars is predicted by stellar evolution models. The possible emission of ALPs from WD stars would accelerate this process, specially in models with coupling to electrons (like non-hadronic axion models) given that the axio-breemstrahlung is the dominant process in such an environment. These reasoning leads to the constrains shown before in section 2.5, but recent measurements suggest a non-standard energy loss in the WD luminosity function compatible with a typical axion model of the following properties [114]

$$g_{aee} \sim 10^{-13}\ \text{GeV}^{-1} \qquad g_{a\gamma} \sim 10^{-12}\ \text{GeV}^{-1} \qquad m_a \sim \mathcal{O}(10^{-3})\ \text{eV} \tag{2.24}$$

This promising axion region is quoted *WD cooling hint* in figure 2.5 (top), and could be within reach of planned experiments. Although it has been claimed that current data does not support a statistically significant anomalous WD cooling [115], independent observational data of two pulsating WDs [116, 117] are best fitted with an extra cooling process.

Cooling of Horizontal branch stars

The higher than expected R parameter measured in globular clusters suggests an additional channel for the cooling of HB stars. This discrepancy (at 1σ level) has been interpreted as a possible hint for an ALP coupled to photons with $g_{a\gamma} = 0.29 - -0.57 \times 10^{-10}$ GeV^{-1} [106].

Cooling of Red Giants

The brighter than expected observation of the RGB stars in the M5 globular cluster can be understood with an anomalous energy loss channel provided by an axion with $g_{ae} \sim (1-2) \times 10^{-13}$ GeV^{-1} [118].

Cooling of neutron stars

Another hint comes from the observation of a faster cooling rate of a neutron star in Cassiopeia A, interpreted in terms of an axion with coupling to neutrons at a level of $g_{an} \sim 4 \times 10^{-10}$ GeV^{-1} [119]. This hint is, however, marginal due to the uncertainties in the neutron stars cooling mechanisms.

Blue loop anomaly

Stars with masses around 10 times larger than the Sun go through a red-blue-red phase in their helium burning phase. The observation of less blue (hot) stars than expected can be interpreted in terms of an anomalous cooling process. In particular, the existence of an axion with $g_{a\gamma} \sim 8 \times 10^{-11}$ GeV^{-1} could solve the puzzle.

TeV transparency

Distant astrophysical TeV gamma ray emitters (like active galactic nuclei, AGN) have been observed by HESS and MAGIC observatories. This observation was unexpected since the e^+e^- pair production via interaction with the EBL was thought to make the universe opaque to these gamma rays. Of course, if the EBL is less dense or the source spectra is softer than previously believed the puzzle is solved without new physics. Alternatively, the photon conversion into ALPs in the magnetic fields present around the gamma sources and their reconversion to photons in the Milky Way (or in the intergalactic magnetic fields) can also explain the apparent transparency of the

Universe. In figure 2.5 (bottom), the required ALP properties are shown in the $m_a - g_{a\gamma}$ plane labeled as *TeV Transparency*. The required ALP masses and couplings are roughly:

$$g_{a\gamma} \gtrsim 10^{-12}\ \text{GeV}^{-1}; \qquad m_a \lesssim 10^{-7}\ \text{eV} \tag{2.25}$$

Although this region is somehow constrained by the burst duration of SN1987A (see section 2.5) and by the blazar observation performed by the HESS collaboration [120], it is just below the current best constrains over that ALP mass set by CAST, and it is within the reach of planned and future experiments, like ALPS-II and IAXO.

Soft x-ray excess in Galaxy Clusters

The soft x-ray excess observed in Galaxy Clusters could be attributed to the axion-photon conversion of the Cosmic Axion Background (CAB) in the magnetic fields of the clusters [121]. In particular, high statistical significance in the soft x-ray excess has been observed in the Coma cluster, imposing constrains in the ALP mass and coupling to photons [122]

$$10^{-11} \gtrsim g_{a\gamma} \gtrsim 10^{-13}\sqrt{\frac{0.5}{\Delta N_{eff}}}\ \text{GeV}^{-1}; \qquad m_a \lesssim 10^{-12}\ \text{eV} \tag{2.26}$$

where ΔN_{eff} is the effective number of extra neutrinos.

It is worth pointing out that many of the hints for ALPs reported above overlap in some region of the $g_{a\gamma} - m_a$ plane. Moreover, other hints for the existence of ALPs have been observed: the probable observation of the so-called caustic rings (particular structure of DM galactic halos) [123] can be generated by the Bose-Einstein condensate that CDM ALPs can form [124]; and the observation of a unexpected 3.55 keV x-ray line from galaxy clusters that has been attributed to the decay of a 7.1 keV mass ALP [125].

2.6 Direct searches for axions and ALPs

Most of the experimental approaches to the search for axions and ALPs rely on their $a\gamma\gamma$ coupling. This coupling leads to the Primakoff conversion of photons into axions in the presence of magnetic fields. Depending on the source of this magnetic field we distinguish between different type of experiments: *light-shinning through a wall (LSW)* experiments or look for axions produced in the laboratory, *haloscopes* experiments look for axions making the DM halo of our galaxy, and *helioscope* experiments look for axions generated in the Sun plasma. The incoming flux of axions must be converted back to photons in order to produce measurable effects. The photon regeneration can occur in the electric field of a nucleus (see underground type of searches below) or in a laboratory magnetic field, being this option the preferred one as it offers more sensitivity. In this section, we review the three main detection techniques mentioned before and the current or planned experiments. Finally, we will briefly describe other type of searches, some of which are still in an incipient phase or not so sensitive as the dominant techniques.

2.6.1 LSW experiments

The LSW technique [126] looks for axions purely generated in a laboratory. It is based on the use of an intense laser beam traversing a strong magnetic field, which triggers the $\gamma \longrightarrow ALP$ conversion of a small fraction of the incident photons. Then, a "wall" blocks the laser beam, while the converted ALPs can traverse it and re-converted to photons in a second magnetic field. Over typical $\mathcal{O}$(m) magnet lengths, the coherence on the axion conversion probability $P_{a\gamma}$ is maintained up to ALP masses in the meV range. A conceptual sketch of the simplest LSW technique is show in figure 2.7 (left).

The advantage of these experiments is that they are less model-dependent than the rest of searches since they do not rely on astronomical or cosmological assumptions. However, the axion-photon conversion process must occur twice, so the expected number of photons is $N_\gamma^{out} \propto N_\gamma^{in}(g_{a\gamma}BL)^4\varepsilon_{det}$. This fact penalize the sensitivity of these searches. The strategies to achieve higher sensitivities are: increasing the intensity of the laser beam, the intensity of the magnetic field or the length of the magnets. Different experiments of these type have been conducted or are currently running (BMV, BFRT, GammeV), the most sensitive of which are ALPS-I with a limit of $g_{a\gamma} < 6.5 \times 10^{-8}$ GeV^{-1} for $m_a \lesssim$ meV [127], and OSQAR with a limit of $g_{a\gamma} < 5.7 \times 10^{-8}$ GeV^{-1} [128] for axion masses below ∼0.3 meV.

These limits are well above the bounds set by astronomical observations or helioscopes, but the introduction of optical resonator cavities [129], though technologically challenging, can lead to unprecedented bounds on $g_{a\gamma}$. Two resonantly-enhanced experiments are planned (ALPS-II and REAPR) with projected sensitivities of the order of $g \sim 10^{-11}$ GeV^{-1} for axion masses below the meV, thus partially exploring the region of the parameter space motivated by the TeV transparency of the Universe.

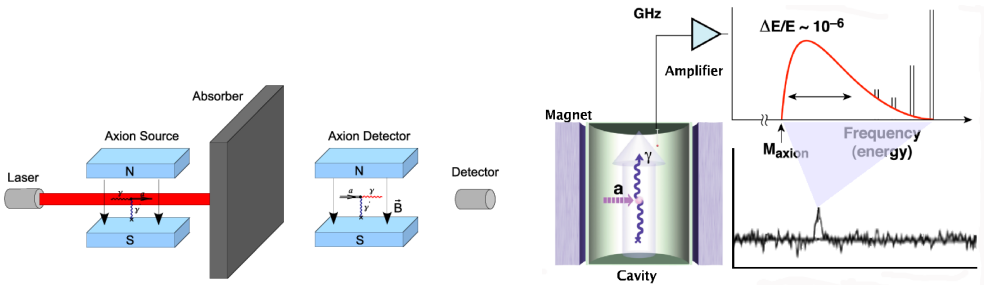

Figure 2.7: Conceptual illustration of the light-shinning-through-wall (left) and haloscope (right)techniques for axion/ALP detection.

2.6.2 Haloscope experiments

Haloscope experiments look for ALPs composing the DM of the Universe by means of its resonant conversion into photons via the Primakoff effect in the presence of a strong magnetic field. The detection principle is shown in figure 2.7 (right). As explained in Section 2.4.1, CDM axions, whose kinetic energy is much smaller than their mass, are expected in the $10^{-6} - 10^{-3}$ eV range ($\sim 10^{12} - 10^{14}$ cm^{-3}), so the regenerated photon is expected in the microwave range . The parameters of the resonant cavity must be tuned to change its resonant frequency, as the conversion is coherent only when the frequency matches the axion mass ($\nu = m_a c^2/h$). Changing the resonant frequency allows to scan over a range of axion masses. The expected signal is thus an excess of events for a given resonant frequency (somehow broadened due to axion distribution of velocities in the halo).

The most sensitive experiment up to date of this type is Axion Dark Matter Experiment (ADMX) [130] (running since 1987), a 1 m long, 0.5 m diameter 8 T superconducting solenoid magnet, which has excluded QCD axions in a narrow range of axion masses around the μeV (see figure 2.5). Note that haloscopes are sensitive to the product of two, a priori, free parameters $\rho_{a,DM}g_{a\gamma}^2$, so the limits on the coupling are derived under a particular assumption on the density of the DM axions, usually taken as the total CDM density.

The upgrades of ADMX, ADMX-II and ADMX-HF, will further improve the sensitivity, increase the scanning rate, and most importantly, it will extend the search for higher axions masses, up to $\sim 10^{-5}$ eV (see figure 2.5). The experimental challenge now is how to extend the mass scan in both directions. Proposals towards larger axion masses use higher frequency microwave cavities (YMCE [131]) or optical interferometers, while smaller axion masses (also possibly making the CDM in the anthropic axion window, see Section 2.4.1) could be within reach by measuring in

the radio regime (WISPDMX [132]) or employing LC-circuits [133]. Other possibility to extend the low mass search is using objects that provide at the same time large volumes and magnetic fields like TOKAMAKs or stellarators [132] or a spherically shaped dish antenna [134], whose projected sensitivity is shown in figure 2.5. In this context, the Center for Axion and Precision Physics Research (CAPP), funded by the Institute for Basic Science (IBS) in Korea, will explore the dark-matter axion by means of a microwave experiment of large volume, very high magnetic field and high quality microwave cavity.

2.6.3 Helioscope experiments

Helioscopes look for axions or ALPs generated in the Sun, an idea originally conceived by P. Sikivie in 1983 [135], and further developed in 1989 by K. van Bibber, P. M. McIntyre, D. E. Morris and G. G. Raffelt [136]. The technique is based on the axion production via Primakoff effect in the large electromagnetic fields of the the solar plasma. However, for non-hadronic axions other production mechanisms exist (see next Chapter). The advantage of this type of search is that is less model dependent than haloscope searches, since it only relies on well studied solar physics. Due to their large mean free path axions can escape from the Sun and travel unimpeded to the Earth, with energies in the keV range. In the Earth they can be transformed back to x-rays (of the same energy than the incident axions) by means of a intense magnetic field pointing to the Sun core. The helioscope technique is illustrated in figure 2.8. The basic requirements for these searches are a powerful magnet and x-ray detectors. More details on the parameters that drive the sensitivity of an axion helioscope are presented in next section.

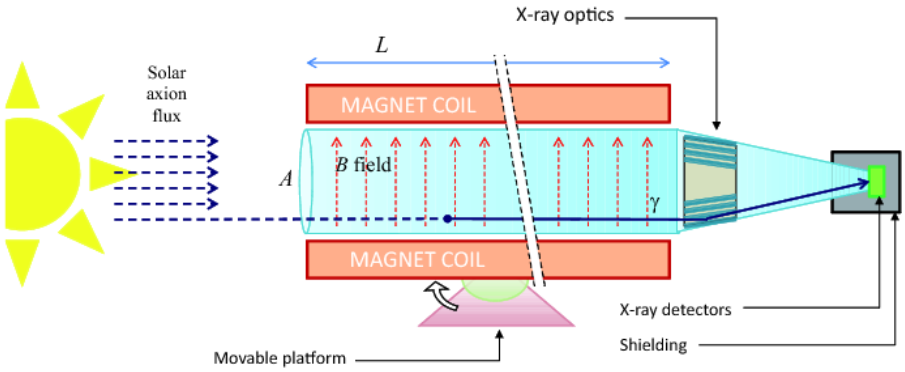

Figure 2.8: Sketch of the axion helioscope detection principle. The Sun is the axion source, reconverted to photons in a laboratory magnetic field pointing to the Sun. Photons are focused to low background x-ray detectors by means of x-ray optics.

An advantage of helioscopes with respect to haloscopes is that the probability of axion conversion is coherent up to relatively large axion mases ($\mathcal{O}(10^{-2})$ eV), and thus the expected signal is independent of the axion mass. The coherence condition can be restored in a narrow mass range by means of a buffer gas at a certain pressure [136], allowing to extend the search up to $\sim$ eV in several pressure steps.

The first implementation of this technique was conducted with a static magnet in the Brookhaven National Laboratory in 1992 [137], excluding $g_{a\gamma} > 3.9 \times 10^{-9}$ GeV^{-1} (3σ C.L.) for $m_a < 0.11$ eV. The second attempt was carried out in 1998 by The Tokyo Axion Helioscope, already with a moving magnet. From the absence of a signal they placed the limit $g_{a\gamma} < 6.0 \times 10^{-10}$ GeV^{-1} (95% C.L.) for $m_a < 0.03$ eV [138].

The third and latest generation of an axion helisocope is The CERN Axion Solar Telescope (CAST) experiment [139], which is where this thesis has been developed. CAST uses a 9.3 m long, 9 T prototype dipole magnet for the LHC. The experiment started taking data in 2003, and still today is the most sensitive solar axion search. From the non-observation of a x-ray excess

during the vacuum phase (2003-2004), the upper bound is $g_{a\gamma} < 8.8 \times 10^{-11}$ GeV^{-1} (95% CL) for $m_a < 0.02$ eV [140, 141]. The phase that utilized ^{4}He as a buffer gas (2005-2006) probed masses in the range 0.02 eV $< m_a <$ 0.64 eV with an average limit of $g_{a\gamma} < 2.3 \times 10^{-10}$ GeV^{-1} (95% CL) [142], while the ^{3}He phase (2008-2011) set an upper limit $g_{a\gamma} < 3.3 \times 10^{-10}$ GeV^{-1} (95% CL) averaged on the 0.64 eV $< m_a <$ 1.17 eV [143, 144]. These results, shown in figure 2.5, are the most stringent limits for a wide range of masses, surpassing the astrophysical constrain imposed by HB stars. A more detailed explanation of the solar axion detection using helioscopes is given in chapter 3, while the CAST Experiment is described in detail in chapter 4.

In addition to the three main experimental approaches described before, there are other searches that have already or are planning to give limits to the $a\gamma\gamma$ coupling, usually as by-products of experiments looking for something else. Some examples of these techniques are the following: *laser polarization experiments*, looking for changes in the polarization of laser photons traversing a magnetic field [145, 146]. Although the PVLAS collaboration claimed to have found an anomalous signal in 2006 that could be interpreted using axions [147], it was soon found to be an experimental artifact and was also excluded by other searches. Also limits on the $g_{a\gamma}$ ($\sim 10^{-9}$ GeV^{-1}) and g_{aee} ($\sim 10^{-12}$ GeV^{-1}) couplings have been set as by-products of underground WIMP searches [148, 149, 150, 151] based on Bragg scattering in a crystal lattice (an idea originally proposed by E. A. Paschos and K. Zioutas [152]), or axio-electric effect in solid state detectors [148] or liquid nobel gases [153, 154], using as axion sources both the Sun and the DM halo. ALPs have also been searched in beam-dump and collider experiments [155] or nuclear transitions mediated by axion emission (e.g., [156]). On the other hand, the Cosmic Axion Spin Precession Experiment (CASPEr) will search for experimental signatures of the energy shift oscillations (with a frequency m_a) produced by the coupling of axion-like particles with gluons and fermions. This search would achieve extraordinary sensitivity to axions with masses below 10^{-6}–10^{-7} eV [157]. New theoretical ideas are implying weakly-coupled long-range spin-dependent interactions (fifth-force) mediated by the exchange of new light bosons, like ALPs. These ALPs are planned to be searched using high precision nuclear magnetic resonance (NMR) by the Axion Resonant InterAction Detection Experiment (ARIADNE), reaching high sensitivity in the *classic axion window* mass range [158].

Chapter 3

Detection of solar axions with helioscopes

Contents

3.1 Introduction

The detection of solar axions with an helioscope is based in two basic theoretical inputs. First, the Primakoff production of solar axions in the core of the Sun; and secondly, the axion to photon conversion in a laboratory magnetic field by the inverse Primakoff effect (see figure 3.1). The expected number of photons to be observed by the x-ray detectors rely only in the theoretical axion flux and in the conversion probability.

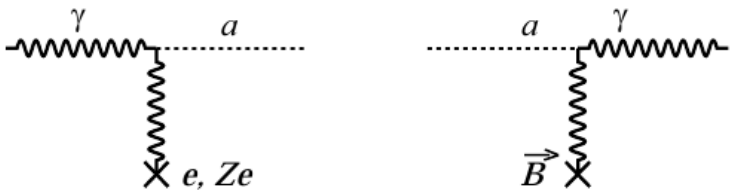

Figure 3.1: The Primakoff effect triggered by the electric fields generated by electrons and nuclei, like in the Sun (left); and the inverse Primakoff effect in the presence of an external magnetic field, like the generated in a laboratory magnet.

3.2 Solar axion flux

The core of the Sun is a dense plasma well described by the Standard Solar Model, and turns out to be a plentiful source of axions due to the presence of many free electrons, nuclei and strong electromagnetic fields.

The theoretical calculation of the axion flux depends only on the solar model and the axion couplings. As stated before, Primakoff effect is allowed in both hadronic (KSVZ) and non-hadronic (DFSZ) axion models, while processes involving the axion-electron coupling only occur at tree level for the last type of models. These processes, usually called *BCA processes*, are atomic axio-recombination and axio-deexcitation, axio-Bremsstrahlung, and axio-Compton scattering. The

Feynman diagrams of the most relevant axion production mechanisms are shown in figure 3.2 (top).

Despite axio-electron driven production mechanisms are dominant in non-hadronic axion models (see figure 3.2, bottom), solar axion bounds usually rely only on the Primakoff production, covering thus more generic classes of axion and ALPs. Nevertheless, it is worth remarking that BCA processes in the Sun produce axions with much lower mean energy (energy spectrum peaking at ∼1 keV) than those produced by the Primakoff effect (peaking at around 3 keV). This fact, may have important observational consequences and implications for the experimentalists.

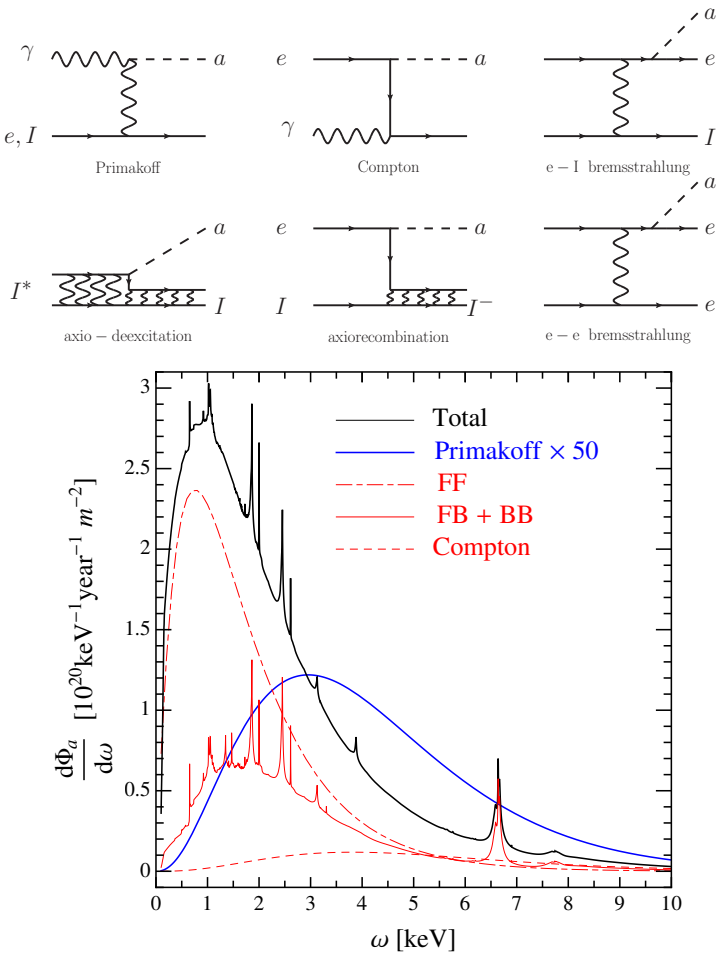

*Figure 3.2: Top: Feynman diagram of the Primakoff effect (top left) and axion production mechanisms in non-hadronic axion models. Bottom: contributions to the differential solar axion flux. In red, the processes involving axion-electron coupling (for $g_{ae}=10^{-13}$ GeV^{-1}): atomic recombination and deexcitation (*FB+BB*, solid), Bremsstrahlung (*FF*, dot-dashed) and Compton (dashed). In blue, the Primakoff flux for $g_{a\gamma}=10^{-12}$ GeV^{-1}. Figures extracted from [159].*

.

In stars, the Primakoff production of axions occurs with the electromagnetic fields of electrons and nuclei by virtue of equation 2.13. Their charge distribution $\rho(\vec{r})$ generates a Coulomb electric field $\vec{E}(\vec{r})$, in which the incident photons can convert to axions. In a non-relativistic plasma, where $T \ll m_e$, we can neglect the recoil energy of the sources of the electric field. In this approximation, the energy of the photon and axion energy are the same, $E_\gamma = E_a$, and the interaction is favored at zero degrees between the direction of the incident photon and outcoming axion.

The differential cross-section of the process for a incident photon of momentum $\vec{k}_\gamma$ is [160]

$$\frac{d\sigma_{\gamma\to a}}{d\Omega} = \frac{g_{a\gamma}^2\alpha}{8\pi}\frac{\left|\vec{k}_\gamma \times \vec{p}_a\right|}{\left|\vec{q}\right|^4}\left|F(\vec{q})\right|^2 \tag{3.1}$$

where $\vec{q} = \vec{k}_\gamma - \vec{p}_a$ is the momentum tranfer, and $F(\vec{q})$ is the form factor of the charge distribution, defined as $F(\vec{q}) = \int d^3\vec{r}\rho(\vec{r})e^{-i\vec{q}\vec{r}}$.

For a point-like particle of Ze charge, the form factor is simply $F^2 = Z^2$, independently of the momentum transfer. However, in the presence of moving charges, like in the solar plasma, one has to consider non negligible screening effects, which produce the modification of the classic Coulomb potential $1/r \to e^{-\kappa r}/r$. The screening effect reduces the axion production cross-section by an effective factor [160]

$$\left|F_{eff}(\vec{q})\right|^2 = Z^2\frac{\left|\vec{q}\right|^2}{\left|\vec{q}\right|^2 + \kappa^2} \tag{3.2}$$

Note that the screening effect is significant if $\kappa \gtrsim |\vec{q}|$. The inverse of κ is the so-called Debye-Hückel radius. Beyond this radius, the contribution to the Primakoff production of axions is significantly cut-off, resulting in an overall reduction of the solar axion flux. The parameter κ is given by

$$\kappa^2 = \frac{4\pi\alpha}{T}(n_e + \sum_j Q_j^2 n_j) \tag{3.3}$$

where n_e is the number density of electrons in the medium

$$n_e = N_A\ \rho_e \sum_j \frac{Z_j}{W_j} \tag{3.4}$$

being Z_j and W_j the atomic number and weight respectively; and n_j the number density of the ion with charge Q_j.

In order to compare the momentum transfer $|\vec{q}|$ with the κ parameter in the solar center we follow this reasoning: photons in a plasma obey the dispertion relation $E_\gamma^2 = k_\gamma^2 + \omega_{pl}^2$, which can be interpreted as if the photon acquires an effective mass m_γ,

$$m_\gamma \equiv \omega_{pl} = \sqrt{\frac{4\pi\alpha n_e}{m_e}}. \tag{3.5}$$

The momentum transfer in the case $E_\gamma \gg m_\gamma$, and $E_\gamma \gg m_a$ is

$$|\vec{q}| = \left|\vec{k}_\gamma - \vec{p}_a\right| = \left|\sqrt{E^2 - m_\gamma^2} - \sqrt{E^2 - m_a^2}\right| \approx \frac{|m_\gamma^2 - m_a^2|}{2E} \tag{3.6}$$

According to the Standard Solar Model, in the core of the Sun the plasma frequency $\omega_{pl} = 0.3$ keV, and the plasma temperature is T=1.3 keV, producing an effective photon mass much larger than typical axion masses. Therefore, the axion mass can be neglected in equation 3.6, simplifying it to $|\vec{q}| \approx m_\gamma^2/2E$, which for standard values of the Sun leads to values $|\vec{q}| \approx 35$ eV. The Standard Solar Model value for κ is around 94 keV, which means that Primakoff production of axions is notably reduced by screening effects in the core of the Sun. The same holds for HB stars, where $\kappa \approx 27$ keV and $|\vec{q}| \approx 0.23$ keV.

The integration of $d\sigma/d\Omega$ gives the transition rate of a photon of energy E into an axion of the same energy [161]

$$\Gamma_{\gamma\to a} = \frac{g_{a\gamma}^2 T\kappa^2}{32\pi}\left[\left(1 + \frac{\kappa^2}{4E^2}\right)\log\left(1 + \frac{4E^2}{\kappa^2}\right) - 1\right] \tag{3.7}$$

In order to calculate the total axion flux at Earth it is necessary to combine the production rate $\Gamma_{\gamma\to a}$ with the Bose-Einsten photon distribution in the solar plasma ($e^{E/T} - 1$). Integrating over the Sun volume and over photon energies, the axion flux per unit area at the Earth is [141]

$$\Phi_a = \frac{R_\odot^3}{4\pi D^2} \int_0^1 dr 4\pi r^2 \int_{w_{pl}}^\infty dE \frac{4\pi k_\gamma^2}{(2\pi)^3} \frac{dk_\gamma}{dE} \frac{2\Gamma_{\gamma\to a}}{e^{E/T}-1} \tag{3.8}$$

where $r = R/R_\odot$ is a radial variable normalized to the solar radius $R_\odot$, and D is the Earth-Sun distance. The lower limit in the energy integral comes from the aforemenitioned photon dispertion relation in the approximation of vanishing recoil energy of the electric field sources. Note that this calculation is not appropriate for photon energies below $w_{pl} = 0.3$ keV.

The Sun can be seen as a point-like source of a parallel axion beam in first approximation, though it is more realistic to consider the flux dependence on the solar radius, as T, ω_{pl} and $\Gamma_{\gamma\to a}$ are position dependent. The dependence of the solar axion luminosity with the axion energy and solar radius in units of $R_\odot$ is shown on the right of figure 3.3. The flux of axions as a function of the axion energy (for an arbitrary $g_{a\gamma} = 10^{-10}$ GeV^{-1}) is shown in figure 3.3 (left) for several values of the solar radius r. Note that most of the axion flux is originated within the $0.25R_\odot$ of the Sun. Details on the calculations can be found in [141].

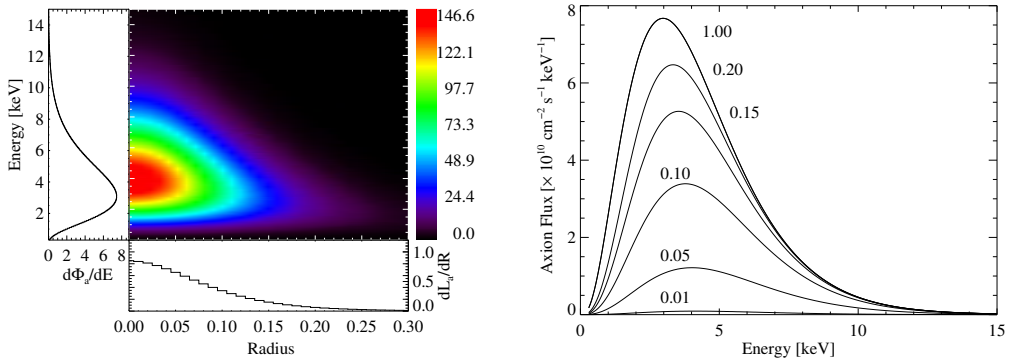

Figure 3.3: Left: contour plot of the solar axion luminosity as a function of the dimensionless $r = R/R_\odot$ variable and the axion energy. Right: axion energy spectrum generated by the solar plasma within a volume defined by the radius r. Extracted from [141].

.

Taking into account the current solar models, the total axion flux at Earth Φ_a, and the amount of energy emitted by the Sun in form of axions L_a due to the Primakoff production mechanisms are

$$\begin{aligned} \Phi_a &= g_{10}^2 3.75 \cdot 10^{11} \text{cm}^{-2}\text{s}^{-1} \\ L_a &= g_{10}^2 1.85 \cdot 10^{-3} L_\odot \end{aligned} \tag{3.9}$$

where $L_\odot$ is the total photon luminosity of the Sun and $g_{10} \equiv g_{a\gamma}/(10^{-10})\text{GeV}^{-1}$. An accurate analytic parametrization of the solar axion flux spectrum in the most relevant energy range is

$$\frac{d\Phi_a}{dE_a} = g_{10}^2\, 6.02 \cdot 10^{10}\, E_a^{2.481}\, e^{-E_a/1.205} \quad \text{cm}^{-2}\text{s}^{-1}\text{keV}^{-1} \tag{3.10}$$

where E_a is expressed in keV. The mean axion energy of the distribution is $\langle E_a \rangle = 4.2$ keV, while the most expected axion energy is $E_a = 3$ keV.

3.3 Probability of axion conversion

The axions arriving to the Earth must be reconverted into observable x-rays in the presence of laboratory magnetic fields. In [162], Raffelt and Stodolsky showed that this conversion is efficient only when the polarization plane of the outcoming photon is parallel to the external magnetic field

direction, which should be perpendicular to the incoming axion as shows equation 3.1. Being A the amplitude of the parallel photon component, the axion state, characterized by its amplitude a, propagating along the z axis in the presence of a perpendicular magnetic field B is defined by the wave equation

$$i\partial_z \begin{pmatrix} A \\ a \end{pmatrix} = \begin{pmatrix} \frac{E_a - m_\gamma^2}{2E_a - i\Gamma/2} & \frac{g_{a\gamma}B}{2} \\ \frac{g_{a\gamma}B}{2} & \frac{E_a - m_\gamma^2}{E_a} \end{pmatrix} \begin{pmatrix} A \\ a \end{pmatrix} \tag{3.11}$$

where Γ is the inverse absorption length for the x-rays in the medium, and m_γ is the effective photon mass, defined in equation 3.5. Using the equation 3.4, the effective photon mass is expressed in terms of the gas density ρ in the magnetic region as

$$m_\gamma \simeq 28.77 \sqrt{\frac{Z}{W_A}\rho \left[\frac{\mathrm{g}}{\mathrm{cm}^3}\right]}\ \mathrm{eV} \tag{3.12}$$

The conversion probability of axions to photons going through a transversal and homogeneous magnetic field B with uniform buffer gas density along its length L is [136]

$$P_{a\to\gamma} = \left(g_{a\gamma}BL/2\right)^2 \mathcal{M}(q, L) \tag{3.13}$$

where the momentum transfer q is given in equation 3.6, and $\mathcal{M}(q, L)$ is a term that represents the coherence of the interaction

$$\mathcal{M}(q, L) = \frac{1}{L^2\left(q^2 + \Gamma^2/4\right)} \left[1 + e^{-\Gamma L} - 2e^{-\Gamma L/2}\cos\left(qL\right)\right]. \tag{3.14}$$

Conversion coherence

An helioscope can operate in two modes: in vacuum and with a buffer gas filling the magnet bores. In the vacuum case $\rho = 0$, and thus $m_\gamma = 0$ and $\Gamma = 0$. In this case, the term that leads the coherence of the interaction is reduced to

$$\mathcal{M}(q, L) = \frac{2}{\left(qL\right)^2}\left[1 - \cos\left(qL\right)\right]. \tag{3.15}$$

where $q = m_a^2/2E_a$. As shown in figure 3.4 (left), an helioscope operating in vacuum mode is sensitive only to axions with $m_a \lesssim 0.02$ eV for L$\sim$10 m.s

The coherence conversion is restored for higher masses in a narrow range of axion masses by means of filling the magnet bores with a refractive buffer gas. The buffer gas density sets the photon effective mass m_γ, maximizing the conversion probability for $m_\gamma \simeq m_a$. For $m_\gamma \neq m_a$, the conversion probability rapidly drops due to the axion-photon momentum transfer mismatch. As an example of the conversion probability restoration, figure 3.4 (right) shows the conversion probability for axions of different energies with ^{3}He at 10 mbar as the buffer medium. Note that for low axion energies, the probability drops as a result of the increase of the x-ray attenuation in the buffer medium.

The buffer gas technique for extending the axion search to higher axion masses is illustrated in figure 3.5 (left) for 3 keV axions. Note that the maximum of the probability of axion-photon conversion $P_{a\gamma}$ drops for increasing buffer gas pressures. This fact is due to the increase in the attenuation coefficient in the medium Γ with the pressure, as it is shown in figure 3.5 (right). Increasing the buffer gas density in small steps allows to overlap coherent conversion masses, as illustrated in figure 3.6, giving rise to a smooth axion mass range scanning. The price to pay is long data taking campaigns as the width of the coherence function is in the $\sim$meV range.

Finally, the search for higher axion masses with this technique is limited by the pressure at which it is produced the condensation of the buffer gas for the given temperature at which the superconducting magnet operates. The CAST experiment has successfully used this technique as it will be explained in the next Chapter.

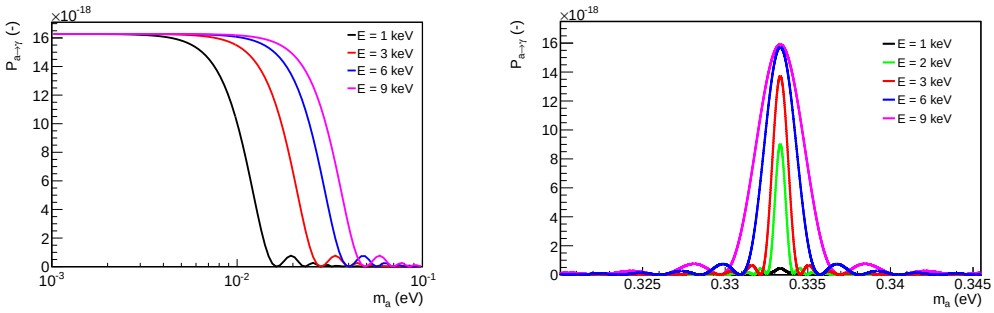

Figure 3.4: Axion to photon conversion probability as a function of the axion mass for some axion energies. On the left, with no buffer gas in the magnet bores, and on the right with ^{3}He as buffer gas at 10 mbar and 1.8 K. The chosen magnet parameters are L = 9.26 m, B = 8.8 T, the nominal values of the CAST magnet; while $g_{a\gamma} = 10^{-10}$ GeV^{-1}.

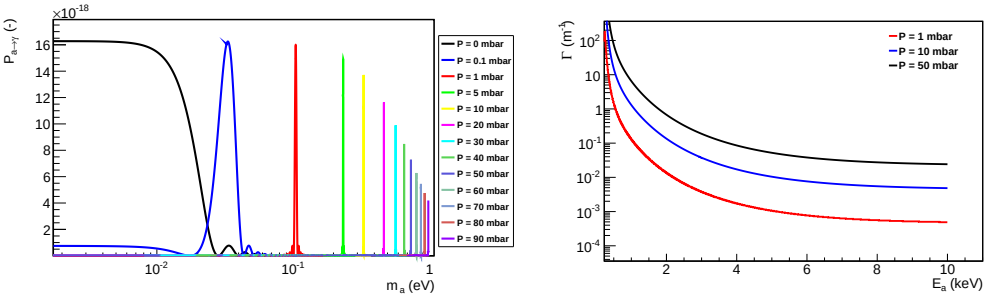

Figure 3.5: Left: axion-photon conversion probability for 3 keV axions as a function of the axion mass for ^{3}He as buffer gas at several pressures (see legend). The magnet parameters are L = 9.26 m, B = 8.8 T; and $g_{a\gamma} = 10^{-10}$ GeV^{-1}. Right: absorption coefficient as a function of the axion energy in ^{3}He.

3.4 Expected number of photons

The expected number of photons N_γ to be detected by the x-ray detectors situated at the ends of the magnet bores in the $[E_i, E_f]$ energy range is

$$N_\gamma = \int_{E_i}^{E_f} P_{a\to\gamma}\ \Phi_a\ A\ \varepsilon\ t\ dE. \tag{3.16}$$

where $P_{a\to\gamma}$ and Φ_a are the axion-photon conversion probability and the solar axion flux explained in previous sections. Here, A is the magnet cross sectional area, and t is the total time of the data taking campaign. The detection efficiency ε can be conveniently factored as $\varepsilon = \varepsilon_d \varepsilon_o \varepsilon_t$, where ε_d is the detectors' efficiency, ε_o is the x-ray optics' focusing efficiency, and ε_t is the Sun tracking efficiency of the apparatus. The Sun-tracking time is $\varepsilon_t t$. The number of expected x-rays produced from solar axions in a magnet like the one used by CAST between 2 and 7 keV is shown in figure 3.6 (right). As it is apparent in the figure, the buffer gas technique allows to extend the axion mass coverage for a broad range of axion masses. Note also that the number of expected photons from axion conversion in a single solar tracking for $g_{a\gamma} < 10^{-10}$ GeV^{-1} is less than one, pointing to the necessity of low background x-ray detectors.

Note from equations 3.10 and 3.13 that both Φ_a and $P_{a\to\gamma}$ are $g_{a\gamma}^2$ dependent, so the total number of expected photons for coherent axion-photon conversion is

$$N_\gamma \propto N^* \cdot g_{a\gamma}^4 \equiv B^2\ L^2\ A\ \varepsilon\ t\ g_{a\gamma}^4 \tag{3.17}$$

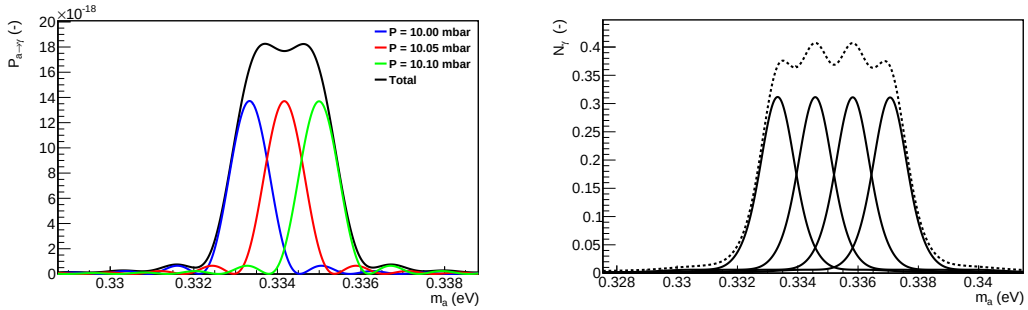

Figure 3.6: Left: conversion probability for 3 keV axions with three different ^{3}He pressures at $g_{a\gamma} = 10^{-10}$ GeV^{-1}. Right: total number of expected x-rays from solar axion conversion in a CAST-like magnet ($L = 9.26$ m, $B = 8.8$ T) in the energy region of [2-7] keV. The calculation uses a single detector covering the 14.55 cm^2 of the CAST magnet bore area at $g_{a\gamma} = 10^{-10}$ GeV^{-1}. The detection efficiency has been set to $\varepsilon = 1$; and the exposure time is set to 1.5 hours, the nominal duration of a tracking period in CAST.

3.5 Conclusions for a solar axion helioscope: figure of merit

In order to evaluate the contribution of each component of an helioscope to the overall sensitivity on $g_{a\gamma}$, it is useful to define a *figure of merit* f [163], which is directly related with the achievable bound on the $a\gamma\gamma$ coupling. The discovery potential is dependent on the axion signal events N_γ, and the background counts in the energy range of interest. The expected background events during Sun-tracking time is given by

$$N_b = b\ a\ \varepsilon_t\ t. \tag{3.18}$$

where b is the background level per unit area and time, and a is the area of the signal region on the detector plane.

In helioscope searches, it is easy to *turn off* the signal by just not pointing to the axion source, the Sun [1]. This feature allows to measure the background level of the x-ray detectors and thus calculate the background counts N_b expected during Sun tracking periods. Therefore, one can perform background suppression over the Sun-tracking data. Assuming background dominated measurements where $N_b \gtrsim 10$ (i.e. non-zero background regime, where gaussian statistics are applicable, and the standard deviation on the expected background counts is simply $\sqrt{N_b}$), the sensitivity of the experiment can be expressed as $N_\gamma/\sqrt{N_b}$.

For the definition of the figure of merit f, it is convenient to rewrite this expression in terms of the inverse of the minimal attainable coupling constant, which can be factored in the contributions from the different experimental parameters f_M (magnet), f_{DO} (detectors and optics), and f_T (time exposure of the experiment)

$$g_{a\gamma}^{-4} \propto f \equiv \frac{N^*}{\sqrt{N_b}} = f_M\ f_{DO}\ f_T$$

$$\begin{aligned} f_M &= B^2 L^2 A \\ f_{DO} &= \frac{\varepsilon_d \varepsilon_o}{\sqrt{ba}} \\ f_T &= \sqrt{\varepsilon_t t} \end{aligned} \tag{3.19}$$

[1] Alternatively, in detectors with larger active area than the signal spot, the background level can be estimated by using the detector surface not exposed to the signal

From these equations it is clear the relative importance of each subsystem of a helioscope. The magnet parameters are, of course, of great importance. In the next Chapter, the CAST experimental parameters are compiled. One of the main subjects of this Thesis regards the optimization of the detectors' contribution, i.e. the maximization of the term ε_d/b.

In [164], the most promising strategies to built a new enhanced axion helioscope are studied in the context of the proposed new generation axion helioscope, IAXO - The Interantional Axion Observatory. In short, the most important improvements on the figure of merit with respect to CAST would rely on:

- Building a new magnet with much larger cross sectional area ($\sim$ m^2) than the CAST one. This possibility seems feasible with the current technology while keeping high BL values. Prototypes of such a magnet have already been designed [165]. In figure 3.7, the expected number of photons of CAST-Phase I is compared with the different scenarios studied in [163] for the New Generation Axion Helioscope (NGAH), considering the same tracking time (1.5 hours) and energy range ([2-7] keV) in all cases. The particular assumptions about the magnet parameters of each scenario are described in the caption. It is evident that a dedicated magnet would significantly allow to improve the sensitivity.
- Equipping all the large cross section bores with x-ray optics of high ε_o and small focusing areas, increasing thus the signal-to-noise ratio. The technological challenge is the production of cost-effective x-ray optics of the appropriate size.
- Further development of x-ray detection systems, which may also extend the physics case. The two basic R&D lines in which these improvements rely are: further reduction on background level b, and lower energy thresholds. Other detection techniques are also being considered to enrich the potential of the experiment.

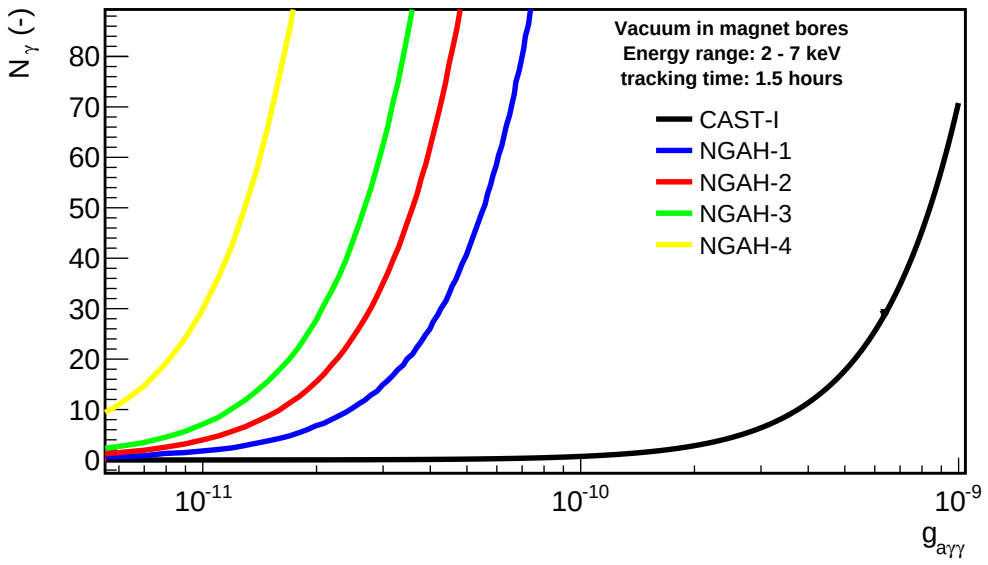

Figure 3.7: Number of expected photons as a function of the coupling constant for different parameters of the magnet: CAST-I (B = 8.8 T, L = 9.26 m, A = 14.55·10^{-4} m^2), NGAH-1 (B = 3 T, L = 12 m, A = 1.7 m^2), NGAH-2 (B = 3 T, L = 15 m, A = 2.6 m^2), NGAH-3 (B = 4 T, L = 15 m, A = 2.6 m^2), and NGAH-4 (B = 5 T, L = 20 m, A = 4 m^2).

Chapter 4

The CAST Experiment

Contents

4.1 CAST Experiment: a general description

The CERN Axion Solar Telescope (CAST) experiment [139] is the most sensitive axion helioscope built to date. The general layout of the experiment is shown in figure 4.1. CAST uses one of the 10 m long, prototype superconducting dipole magnets of the LHC, with twin and straight[1] aperture bores of about 15 cm^2. This magnet provides a magnetic field of about 9 T transversal to the expected direction of the solar axion propagation, triggering the axion-photon conversion. The magnet is equipped with a cooling system that allows to safely operate in the superconductive regime, at a nominal temperature of 1.8 K; and with a vacuum system, responsible to continuously pump the pipe manifolds in order to isolate the cold-bore and maximize x-ray transmission (see section 4.3). The system that allows to fill the magnet cold-bores with a buffer gas, and therefore, extend the axion search towards higher axion masses is described in section 4.4.

The rotating platform in which the magnet sits (see section 4.6), allows to move it from -8° to +8° in the vertical direction, and 80° in the azimuthal plane. This feature allows the magnet to point to the Sun for about 1.5 hours twice per day, during the sunrise and sunset ($\varepsilon_t \sim 0.12$). The CAST magnet length L and intensity of the magnetic field B are difficult to surpass with the current technology while keeping accurate tracking movement. The magnet movement is controlled by a tracking software that also monitors and stores the most relevant tracking data.

[1] In contrast to the current LHC magnets, which are slightly bended to account for the particle curvature therein.

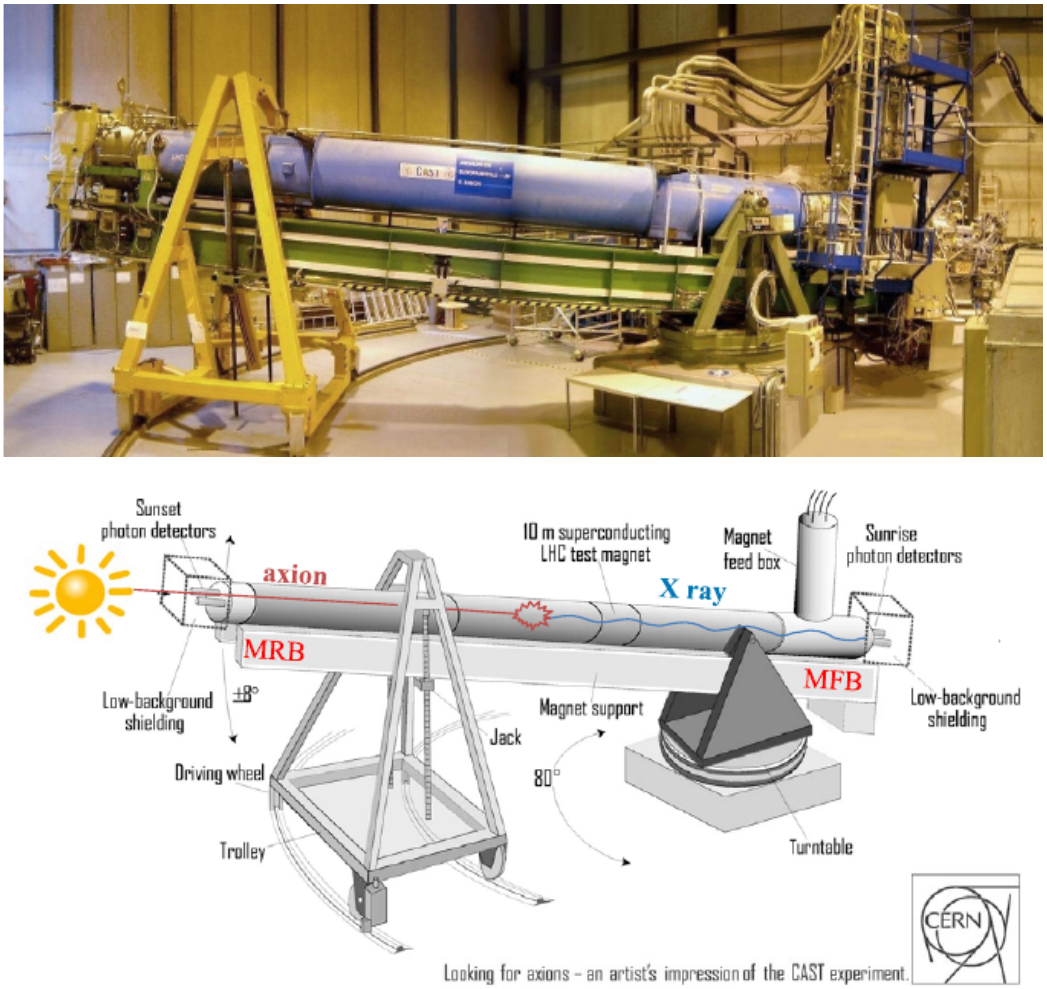

Figure 4.1: view of the CAST experiment (top) and artistic drawing of the main CAST systems (bottom).

The Slow Control System (SC) is a centralized acquisition system that continuously monitors and stores the main variables of the different experiment subsystems (see section 4.7). It is also responsible to activate automated responses and send alarms in case any parameter compromises the safety or the normal operation of any system.

Four low background x-ray detectors are installed at the end of each magnet bore tube (see 4.8), operating in axion-sensitive mode during Sun tracking periods. The rest of the time, when the magnet stays in horizontal parking position, the detectors are calibrated, and the reference background level is measured. One of the magnet bores is instrumented with x-ray optics (see section 4.8.1)that focus the expected signal in a few mm^2 area, enhancing the S/B ratio and increasing the identification potential [166]. A description of the x-ray detectors is given in section 4.8

After shortly reviewing the CAST history and main experimental results, this chapter describes the main subsystems of the CAST experiment, with special emphasis in the x-ray detectors (section 4.8).

4.2 CAST history and scientific program

CAST was first proposed in 1999 by K. Zioutas *et al.* [139]. It was commissioned between 2000-2003, and started its physics research program in 2003. The physics results obtained from the absence of an excess number of x-rays during the Sun tracking periods are summarized in table 4.1, while the exclusion plot in the $g_{a\gamma} - m_a$ parameter space is shown in figure 4.2.

During the first experimental phase (2003 and 2004, CAST Phase I), the magnet operated with vacuum in the magnet bores, setting the most stringent upper bound on the axion-photon coupling constant in a broad range of ALP masses, and exceeding the limits imposed by astrophysics.

In the second phase (CAST Phase II), the magnet bores were filled with a refractive buffer gas to enhance the conversion probability for narrow mass-ranges (see section 3.3). The strategy consists in increasing the gas density in small steps, chosen to partially overlap with the coherent conversion mass-range ($\sim$ 1 meV FWHM) of the previous setting. This technique has allowed to smoothly scan ALP masses up to 1.17 eV.

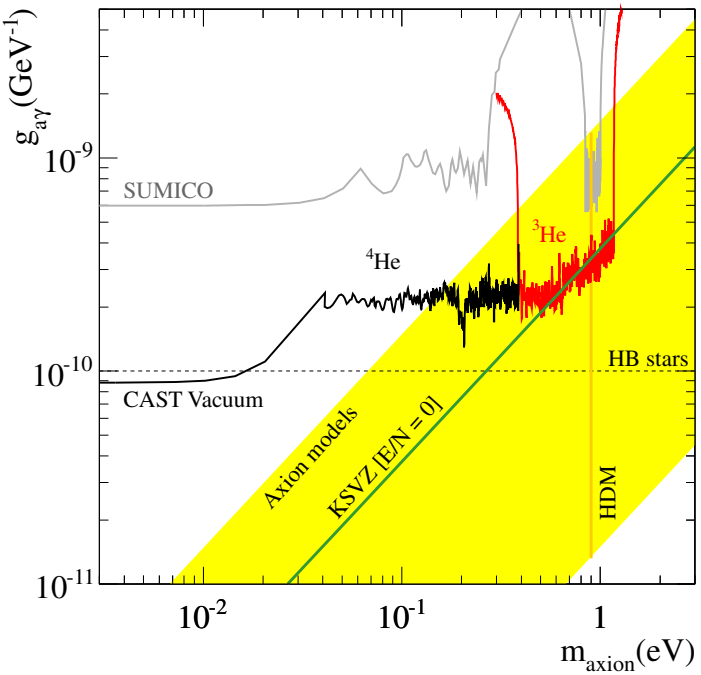

Figure 4.2: Exclusion regions in the $g_{a\gamma} - m_a$ plane achieved by CAST in the vacuum, ^{4}He and ^{3}He phases. Also shown the constrains set by Sumico [138, 167, 168], horizontal branch (HB) stars (without considering the new most restrictive bound coming from the suppression of blue loop stage of massive stars [110]), and Hot Dark Matter (HDM) overabundace limit. The yellow band represents the the most appealing theoretical axion models, and the green solid line corresponds to the KSVZ model with $E/N = 0$.

CAST Phase II was divided in two periods. In the first one, the magnet bore was filled with ^{4}He, extending the scan of ALPs to the mass range $0.02 \lesssim m_a \lesssim 0.39$ eV in 160 pressure steps. Again, the bound on the coupling constant is the most competitive in this mass range, exploring for the first time the band favored by the most compelling axion models (see figure 4.2) [142]. Since at 1.8 K ^{4}He condensates at 16.4 mbar, increasing the sensitivity to higher masses required filling the magnet with ^{3}He, which condensates at 135.6 mbar. The ^{3}He phase allowed to scan the axion mass range $0.39 \lesssim m_a \lesssim 0.64$ eV (in 252 density steps, up to 36 mbar) [143] and $0.64 \lesssim m_a \lesssim 1.17$ eV (452 density steps, from 36 to 105 mbar) [144], i.e., comfortably overlapping with the cosmological

hot dark matter bound, $m_a < 0.72$ eV (95% CL). Remarkably, the ^{3}He run allowed to exclude for the first time for a solar axion search KSVZ (E/N=0) axions in a small mass range.

In 2012, the ^{4}He run was revisited with increased sensitivity, mainly attributed to the lower backgrounds of the Micromegas detectors. An small mass range ($0.390 \lesssim m_a \lesssim 0.415$ eV) in the frontier between ^{4}He and ^{3}He coherence region was scanned in 17 pressure settings (in the pressure range 13.9-15.5 mbar at 1.8 K), corresponding roughly to 5 Sun-trackings per detector; in contrast to the 2006-2007, when only a tracking per detector was performed. The larger time exposure and enhanced x-ray detectors performance allowed set an upper bound to the axion-photon coupling constant reaching the KSVZ line. Additionally, some pressure settings with statistical excess in the former ^{4}He campaign were revisited.

Finally, between 2013 and 2015, CAST revisits the vacuum phase, searching for ALPs with masses below 0.02 eV with increased sensitivity with respect to the CAST Phase I in 2003-2004. The improvement in the sensitivity is due to lower backgrounds of the detectors, as well as the increase in the S/N ratio due to the installation of the new dedicated x-ray optics for the sunrise Micromegas. At the same time, these operations serve as a pathfinder project for future axion helioscopes.

Besides, lower energy threshold detection techniques were explored (see SDD or InGrid detectors below in this Chapter).

Year	**Phase**	**Mass range (eV)**	$\mathbf{g_{10}}$ **(GeV^{-1})**
2000-2003	Commissioning		
2003-2004	Phase I (vacuum)	$\lesssim 0.02$	0.88 (95% CL)
2006-2007	Phase II (^{4}He)	0.002 - 0.39	2.17 (95% CL)
2008-2011	Phase II (^{3}He)	0.39 - 0.64	2.33 (95% CL)
2008-2011	Phase II (^{3}He)	0.64 - 1.17	3.33 (95% CL)
2012	Phase II (^{4}He) Revisit	0.39 - 0.42	1.47 (95% CL)
2013-2015	Vacuum Revisit	$\lesssim 0.02$	–

Table 4.1: Typical upper limits on the axion-photon coupling constant achieved in each CAST Phase. Note that the exact value in the buffer gas phases depends on the pressure setting as can be seen in figure 4.2.

Parallel searches

As by-products of the main scientific program, CAST has also released or is preparing other physics results.

1. Using the Phase I (vacuum phase) data, CAST has provided limits on the axion-electron coupling constant g_{ae}. Based on the axion spectrum in non-hadronic axion models (which includes BCA processes), CAST set the constrain $g_{a\gamma} \cdot g_{ae} < 8.1 \cdot 10^{-23}$ GeV^{-1} at 95% CL for $m_a \lesssim 10$ meV (see figure 4.3, left) [169].

2. High-energy hadronic axions or ALPs could be produced in the ^{7}Li (0.478 MeV) and $D(p,\gamma)^3He$ (5.5 MeV) nuclear transitions occurring in the Sun. The absence of an excess of mono-energetic γ-rays in the data gathered by a γ-ray calorimeter (CWO cystal and readout by a photomultiplier) when the magnet is pointing to the Sun provides the modest constrains shown in figure 4.3 (right) [170]. This limit is provided by the CAST Phase I data.

3. The M1 nuclear transition of ^{57}Fe would produce 14.4 keV mono-energetic solar axions. CAST used the data collected during the Phase I to set a model-independent bound on the coupling constant of axions to two photons and to nucleons $g_{a\gamma} \cdot g_{aN}^{eff} < 1.36 \cdot 10^{-16}$ GeV^{-1} at 95% CL for axions with mass below 0.03 eV [171].

CAST has also looked for low energy solar ALPs with detector systems sensible to the eV energy range, and more recently, solar chameleons have been searched with a low-threshold and low-background Silicon Drift Detector (SDD).

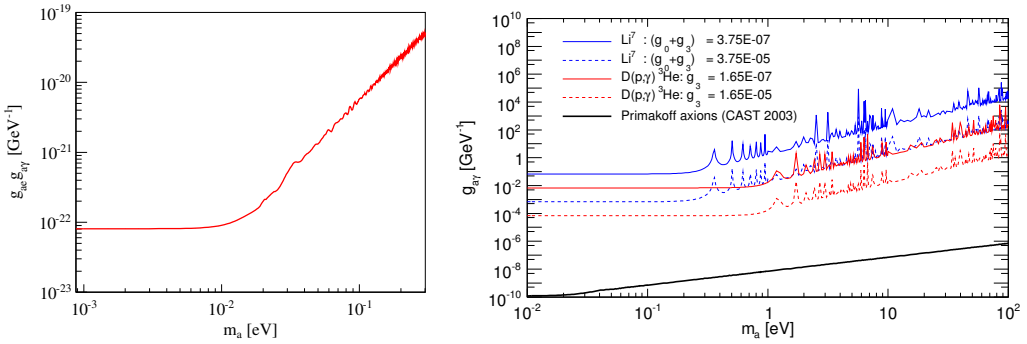

Figure 4.3: Upper bounds on the axion-electron coupling for non hadronic axions (left) [169], and on the axion-photon coupling from high energy axions produced in nuclear transitions in the Sun (right) [170].

4.3 The CAST magnet and cryogenics system

The CAST magnet is a LHC test magnet with two straight parallel beam pipes (cold-bores, CB) of 2.15 cm^2 radius, resulting in a cross sectional area of $A_{CB} = 14.53$ cm^2. The superconducting coils are made of Niobium-Titanium, material that becomes superconductive at temperatures below 9.2 K. The coils can be loaded up to 13 kA, providing a magnetic field of $B_{CB} = 8.8$ T over a length of $L_{CB} = 9.26$ m. A schematic cross-section of the magnet and the magnetic field configuration in the cold-bore is shown in figure 4.4 The subsystems that allow the proper operation of the CAST magnet are described in this section.

The magnet coils reach the superconducting regime by cooling down the magnet with a cryogenics system recovered from the LEP2 accelerator and the DELPHI experiment.

The electrical and cryogenic feed of the magnet are done through the Magnet Feed Box (MFB), shown in figure 4.1. The high current is applied to the coils via large cross-section water-flow refrigerated flexible cables, which allow the free movement of the magnet. The MFB is connected to the liquid ^{4}He supply and to the gaseous ^{4}He pumping unit. The cooling process consists in the periodical injection of liquid Helium and the continuous pumping of the boiled-off gas. At the final stage of the process, the magnet reaches its nominal operation temperature, T_{CB} =1.8 K. Below 2.17 K, ^{4}He becomes superfluid, ensuring its full circulation along the cold mass even when the magnet is tilted, and reaching the cryogenics circuit end at the Magnet Return Box (MRB).

The superconducting operation of the magnet can eventually terminate when a local part of the coil enters into resistive state. This small magnet region rapidly raises temperature due to Joule effect, heating the surrounding regions, which also become resistive. The heating process propagates in chain reaction and the whole magnet becomes resistive, converting the energy confined in the magnetic field into heat, which produces the evaporation of the liquid ^{4}He. This phenomenon is called *quench*, leading to a possible magnet damage due to the local mechanical stress. To avoid this, a *quench* protection system is activated when an increase in the resistivity of the coils is detected. It consists on the induction of a controlled *quench* by uniformly heating the coils, preventing that strong locals forces damage the magnet. The liquid helium boils off, producing an increase in the mean temperature of about a factor 20 in 120 seconds in the cold-bore tubes. In order to avoid a sudden high increase in pressure in the cold-bores (and thus, a possible damage in the cold windows, see section 4.4.1), when the magnet *quenches* the buffer gas helium is allowed to

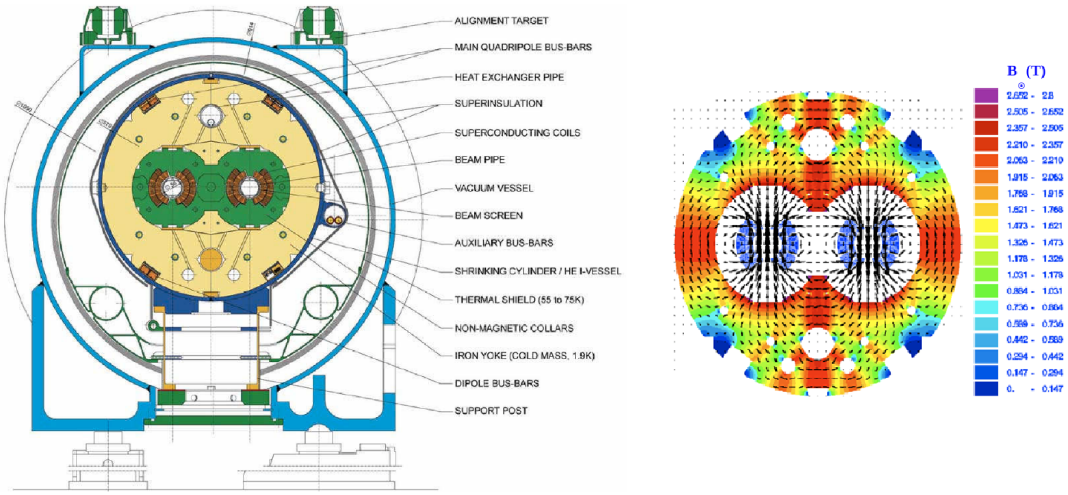

Figure 4.4: Left: schematic view of the CAST magnet cross-section. Right: configuration of the magnetic field lines.

expand to a 450 liters volume, while the cooling helium is purged out from the system via exhaust pipes.

4.4 The buffer gas system

After CAST vacuum phase, a new system was developed in order to insert precise and reproducible amounts of buffer gas into the magnet bores. This system allows to extend the search to higher axion masses. In 2008, the buffer gas was changed from ^{4}He to ^{3}He because of the difference on the saturation points at 1.8 K, 16.4 mbar versus 135.6 mbar respectively. This change required new upgrades and extra safety measurements, to avoid any leak of the very valuable ^{3}He gas. The main components and functionalities of the buffer gas filling system are described here.

4.4.1 The cryogenic x-ray windows

The introduction of the buffer gas in the cold-bores required the installation of new devices (the so-called *cold windows*) in order to confine the gas in the magnetic field region. The position of the cryogenic windows within the CAST magnet is represented in figure 4.9.

The windows have to fulfil a list of properties. They must be able to operate at low temperatures (down to 1.8 K), withstand the static and dynamic pressure differences between the buffer gas and vacuum regions (normally bellow 135 mbar, but could reach about 1 bar when the magnet *quenches*), be transparent to x-rays in the [1-10] keV range and to visible light (necessary to align the x-ray optics), and the leak rate of Helium to the vacuum side must be kept as low as possible. The adopted solution was developed by the CERN Central Cryogenics Laboratory (CryoLab), consisting in 15 μm thin polypropylene foil glued with epoxy into a UHV flange and supported by a squared grid structure machined by electro-erosion, the strongback (see figure 4.5). The strongback is a stainless steel element that provides the necessary mechanical robustness thanks to its 5 mm $\times$ 5 mm grid pointing to the vacuum side.

The leak rate of the x-ray cryogenic windows was tested, resulting in $7.4{\cdot}10^{-9}$ mbar·l/(s·cm^2) at room temperature. Also, they were subject to rapid pressurization up to 1.5 bar (simulating a magnet *quench*) with positive results, and it was found that they can withstand pressures above 3.5 bar [172].

Since the cold windows are in contact with the buffer gas at 1.8 K, they can reach temperatures

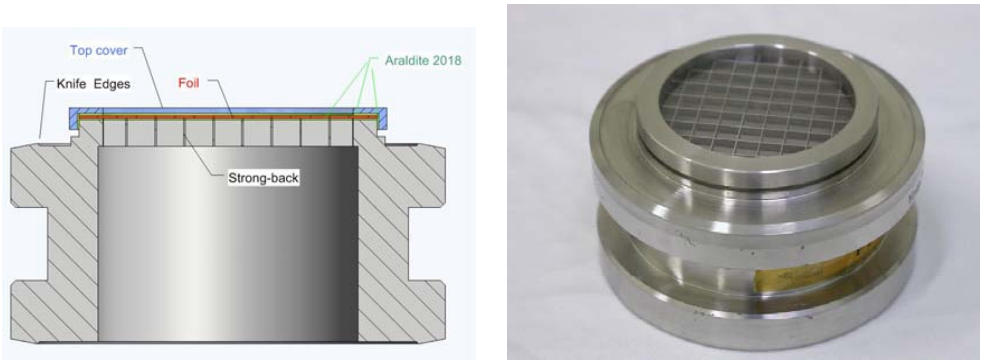

Figure 4.5: Cross-section scheme of the cold window layout (left), and picture of one of the four cold-windows installed in the magnet bores.

at which they perform effective cryo-pumping of the gases present in the vacuum side (see figure 4.6, left). The gas molecules trapped by the cold window would diminish its transparency to x-rays. To avoid this effect, they should be heated up to room temperature, but due to thermal restrictions they operated at 120 K during the ^{4}He phase (hot windows) and at 80 K during the ^{3}He phase (warm windows, see right of figure 4.6). Periodically, the cold-bore was emptied and the windows were baked-out by heating them to higher temperatures, inducing the degassing of the trapped gas molecules.

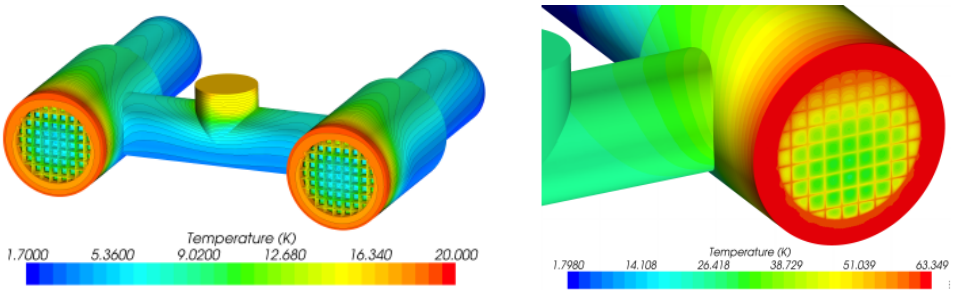

Figure 4.6: Temperature gradient in the cold (at 1.8 K) and warm (80 K) windows, on the left and right respectively.

4.4.2 The filling system

During the ^{4}He phase, the buffer gas system consisted in a helium filled metering volume at constant temperature (36°C), from which the gas was directly inserted into the magnet bores. The accuracy in the amount of gas metered into the magnet bores was guaranteed by the measurement of the pressure in the metering volume before and after the gas insertion.

The operation with ^{3}He required the upgrade of the whole system, which was also equipped with new functionalities. A general scheme of the gas system is shown in figure 4.7, where the main components of the system are shown: metering and purging systems, expansion and storage volumes. The green lines in the figure denote the normal path the helium gas follows from the storage volume to the cold-bores passing through the metering volumes, while the red lines denote the recovery path.

Helium purification. The ^{3}He gas is contained in the 963 litres capacity storage volume. From the storage to the metering volume, the gas is forced to pass through two charcoal traps that

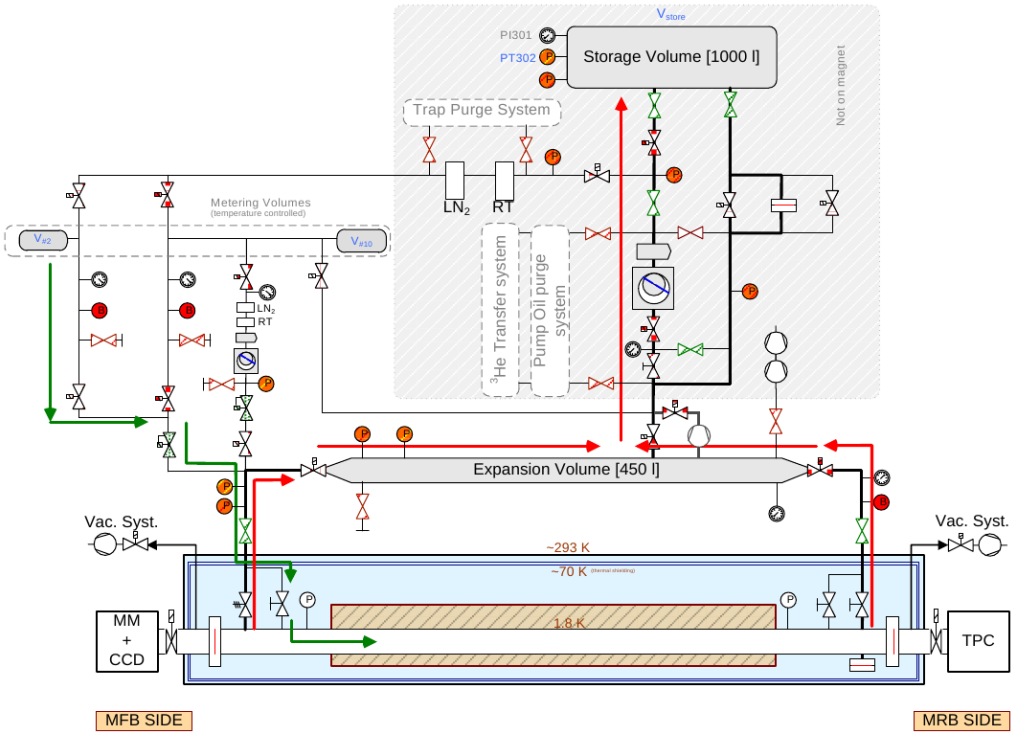

Figure 4.7: Schematics of the buffer gas filling system. In blue, the magnet cryostat; in brown, the magnetic field region at 1.8 K. The green lines show the path from the metering volume V_2 to the cold-bores, while the red lines show the recovery process. Also shown, the storage and expansion volume; the room temperature (RT) and liquid nitrogen (LN_2) purification system; and the recovery system.

aim to remove the impurities of the ^{3}He gas. The first trap operates at room temperature (RT), mainly capturing water vapor and oil; while the second is immersed in a liquid nitrogen bath (LN_2 at 77 K) and aims to further purify the gas.

The gas metering system. A precise measurement of the ^{3}He gas inserted into the cold-bores is necessary to accurately determine the axion mass coherence range. With this aim, the helium is inserted through one of the two metering volumes, MV2 and MV10 of 1.63 and 8.58 liters of capacity respectively. MV2 is used for normal gas injection of small ^{3}He gas amounts, while MV10 is conceived to inject large amounts of gas to achieve a certain pressure setting starting from vacuum. This is necessary to fasten the filling process and gain tracking time, as the cold-bore is periodically fully emptied for the bake-out of the cold windows, and eventually, due to magnet *quenches*.

The accuracy in the amount of gas injected is provided by the precise pressure measurement in the metering volumes before and after the gas injection. The reproducibility of the process is guaranteed by the immersion of the metering volumes in a thermal bath at constant temperature of 36°C. The gas injection from the metering volumes to the cold-bores is done via remotely operated pneumatic-valves, which are handled by the PLC system described below.

The flexibility of the system was enhanced by adding to the system the possibility of subtracting precise amounts of gas from the cold-bore.

^{3}He recovery. In the event of a magnet *quench*, the temperature in the cold-bore rapidly rises, ^{3}He boils-off and the pressure can reach up to 2.7 bar. Even though the cold windows have

been tested up to 3.5 bar, the integrity of the cold windows could still be compromised, which would produce the leak of a large amount of ^{3}He. To avoid this situation, an extra safety system was deployed. It consists in a 10 m long, 450 L expansion volume connected to the cold-bore through two electro-pneumatic valves, one in each side of the magnet (see figure 4.7), which are automatically opened when the alarm of the *quench* protection system is activated. The expansion volume guarantees that the pressure difference the windows must withstand is always below 1.2 bar.

After the *quench* protection system has been triggered and the gas has filled both the magnet bores and expansion volume, the ^{3}He is recovered through the transfer system, which uses an oil-leak-free pumping unit to prevent gas contamination.

In the unlikely event of window breakdown or large leak through the , there still exist additional safety measurements activated via interlocks of the general vacuum system (see section 4.5).

The PLC system. The control and monitoring of the gas system is done by means of a Programmable Logic Controller (PLC) system, which incorporates a graphical user interface (GUI). It allows to control the pneumatic valves and pumping units of the system, either by automated predefined routines or manually. Predefined procedures, such as filling the metering volumes, injecting a precise amount of gas into the cold-bores, or recovering the gas, can be done without deep knowledge of the gas system. In manual mode, experts on the system can perform more complex operations. The PLC also controls a set of interlocks that prevent any damage to the system or inappropriate operations, as well as it acquires and logs the status of the different valves, flow-meters, and pressure sensors.

4.4.3 The CAST scanning protocol

The flexibility of the gas system allows to define a scanning protocol to cover all the axion mass range available in the running period of the experiment. The signal triggering protocol is implemented in the following way: for a given pressure setting, if the statistical significance of the measured tracking events with respect to the mean background events of all the detectors combined is above a given threshold, the pressure setting is considered to be *candidate*, i.e., an axion signal of the associated mass could be responsible of the signal excess, and the pressure setting is worth revisiting.

The threshold, or *critical significance* $S_c = 1 - P_c$, below which a pressure setting is considered to be a potential candidate must be predefined taking into account the disposable fraction of the overall running time devoted to revisiting steps, α, defined as

$$\alpha = \frac{N_{rep}}{N_P + N_{rep}} \tag{4.1}$$

where N_P are the pressure steps to cover along the data taking period and N_{rep} are the total necessary tracking repetitions to reduce the overall significance below P_c.

P_c must be calculated for a fixed α value by means of MonteCarlo simulation. The simulation consists in iterating over P_c values until the goal α value is reached. This is done by running N_{exp} simulated experiments for each P_c value, each with the N_P pressure steps to cover along the data taking period.

The measured number of counts N_i per pressure setting of the detector i with background b_i is computed as the Poissonian probability function $P(b_i)$ summed over all the tracking repetitions m at that particular pressure setting.

$$N_i = \sum_m P(b_i) \tag{4.2}$$

The total statistical significance of the measured signal in each pressure setting S_{tot} is simply the product of the single significance of each individual detector S_i, calculated as the integral of the Poissonian probability function from the number of measured counts N_i to infinity

$$S_{tot} = \prod_i S_i = \prod_i \int_{N_i}^{\infty} P(b_i m) \tag{4.3}$$

where the expected background events is accordingly multiplied by the number of repetitions in each pressure setting. If the computed significance is below $S_c = 1 - P_c$, more trackings in that pressure setting are taken, accumulating the measured counts until the overall significance exceeds S_c. Averaging over all the simulated experiments performed, the number of extra trackings is followed, and the fraction of the overall operation time that they represent α is obtained. The critical significance is finally obtained as the one that produces the desired α. The right of figure 4.8 shows an example of the dependence of the extra time fraction needed to wash out the potential signals induced by statistical fluctuation of the background counts with the critical significance S_c, for a run of $N_P = 100$ pressure steps.

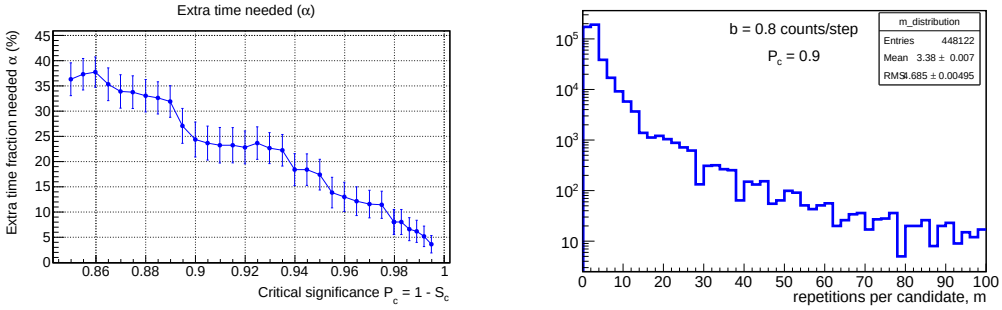

Figure 4.8: Left: distribution of the number of pressure setting repetitions necessary to wash out a candidate signal induced by statistical fluctuation of the background counts. Right: extra time needed (in % respect to total data taking time) as a function of the critical significance S_c above which a pressure setting is considered to be an axion candidate.

The statistical fluctuation of the background events during one tracking usually leads to have a potential axion candidate. On the left of figure 4.8, we show the distribution of the number of necessary repetitions m to wash out a potential positive signal, assuming a single detector with 0.8 counts/tracking (equivalent to about 10^{-6} keV^{-1}cm^{-2}s^{-1}, current Micromegas backgrounds in CAST), and a critical significance $S_c = 1 - P_c = 0.1$. Note that only about 0.5% of the 10^7 conducted experiments have triggered the potential signal protocol, and that the potential positive signal is usually washed up after 3-4 tracking repetitions.

4.5 The vacuum system

We can distinguish between four vacuum subsystems in CAST, each one using separate and independent vacuum pumping units: the cryostat vacuum, the general vacuum, and the detectors' vacuum. A general schematic layout of the CAST vacuum system is shown in figure 4.9, where the first two vacuum subsystems are apparent as well as the buffer gas tubes.

The aim of the cryostat vacuum is to provide a first thermal shield of the magnet cold mass against the environmental temperature. The second subsystem is the general CAST vacuum, placed between the cold windows (see section 4.4.1) containing the buffer gas and the gate valves (VT1-T4). The four gate valves are located at the end of each magnet bore, just outside the vacuum vessel. Finally, between the gate valves and the x-ray detectors there is the detectors' vacuum system. Each detector implements its own pumping system, whose operation is full responsibility of the detectors' groups. The vacuum systems of the Micromegas detectors is further described in chapter 5. The aim of the two last

The gate valves must be opened during tracking data taking and during x-ray calibrations of the optics from the other magnet side, due to their low x-ray transmission. They are automatically closed in case of magnet *quench* or important vacuum degradation, and they can also be closed manually in case of need. For example, if the vacuum system of one detector fails or the vacuum

line is opened for any reason, the corresponding gate valve can be independently closed, letting the rest of the detectors run normally.

The cryostat and general vacuum systems are equipped with Residual Gas Analyzer (RGA), consisting in mass spectrometers for monitoring any possible contamination of the systems. As the RGA identifies which is the polluting agent, it can help to identify the source or origin of the leak.

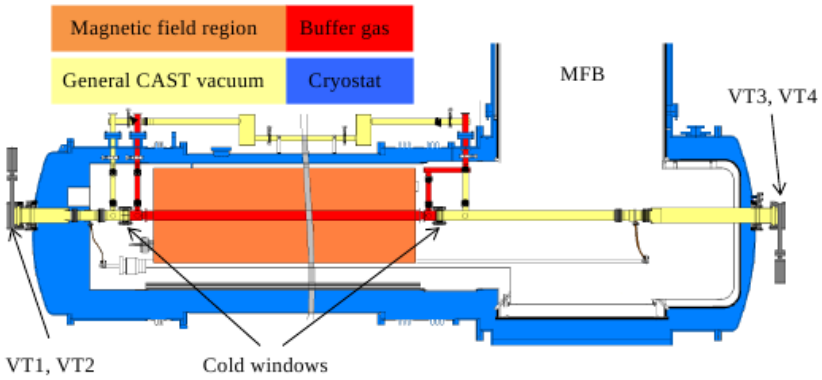

Figure 4.9: Scheme of the vacuum system of CAST, explicitly showing the different vacuum subsystems and components.

4.6 The movement and tracking system

The CAST magnet sits on a rotating structure that allows it to move from 46.7° to 133.3° in the azimuthal plane (with respect to geographic nord), and from -7.2° to 7.95° in the vertical direction. The center of rotation is located in a turntable platform close to the MFB side of the magnet (see figure 4.10, left), avoiding in this way too much tilting of the main component of the cryogenics system. The MRB side of the magnet is supported by a four wheel trolley that can move along the two rails installed in the CAST hall area (see figure 4.10, right).

The magnet movement is provided by two motors, responsible of the vertical and horizontal movement respectively. The *horizontal motor* is connected to one of the outer wheels of the trolley, driving the magnet along the horizontal plane (see figure 4.11, left). The vertical movement is provided by the *vertical motor*, which rotates two lifting jacks situated in the trolley.

The motors are controlled either manually or by a *tracking program*, which implements automatic solar tracking when the Sun is within the available movement range of the magnet. The driving mechanism works in a local reference system defined by two motor encoders (see figure 4.11), one coupled to the driving wheel and the other to the lifting jacks. The encoder units are integer values, with vertical range [0-53000] and horizontal range [0-33000], providing a precision of about 1 and 10 arcseconds respectively. In a solar tracking, the full vertical range is scanned, resulting in a horizontal movement of about 16°, whose starting and finishing points depends on the time of the year.

The conversion of global coordinates to motor encoder values (see figure 4.12) allows the tracking program to set the appropriate direction and frequency to the motors, enabling the precise tracking of the Sun. The process for accurate tracking precision follows these steps. Firstly, the tracking program calculates the position that the Sun will reach in the following minute using the Naval Observatory Vector Astrometry Software (NOVAS) code provided by the U.S. Naval Observatory [173]. Then, it performs the conversion from global to local coordinates associating to any pair of global angles their corresponding encoder values. This operation is done by interpolating a set of reference coordinates, for which the conversion is precisely determined (see GRID measurements below in section 4.6.1). If the Sun is within the magnet movement range, the tracking program sets the appropriate frequency to the motors so that the magnet can reach the target

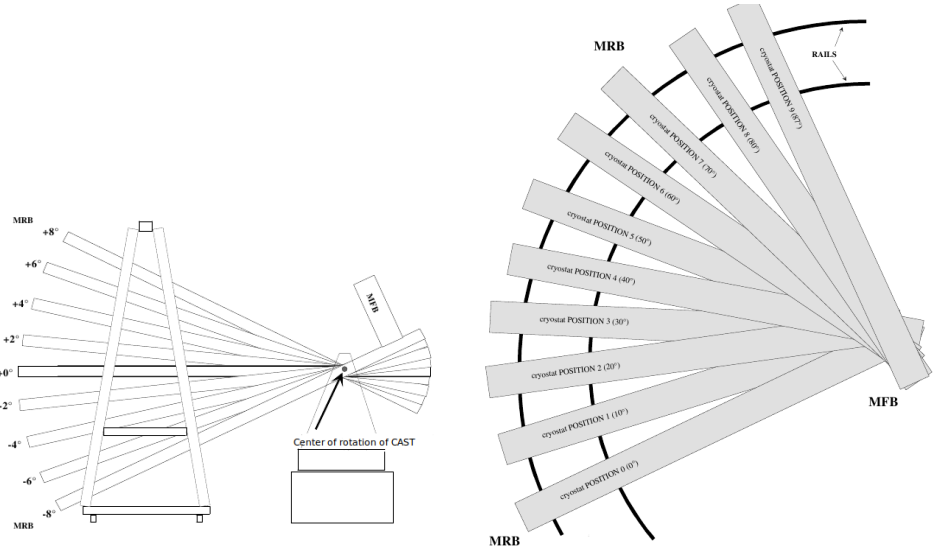

Figure 4.10: Schematic representation of the vertical (top) and horizontal positions within the CAST hall. The origin of the horizontal angle is the geographic north, while the vertical angle origin is the local horizontal plane.

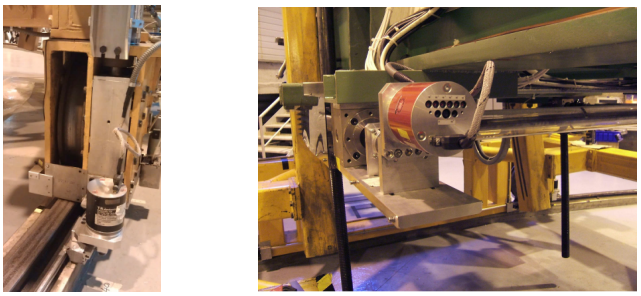

Figure 4.11: Left: driving wheel responsible of the azimuthal movement and horizontal motor encoder. Right: the two lifting jacks are visible, as well as the vertical motor encoder.

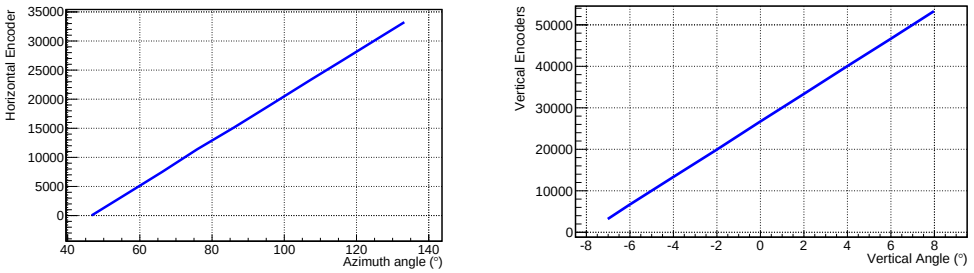

Figure 4.12: Conversion of the motor encoders of the local coordinate system to the angles in the global reference system.

position. The full operation cycle is repeated every minute. When the Sun is unreachable, the tracking program sends the magnet to a user-predefined *parking position*.

4.6.1 Solar tracking precision

Obviously, solar tracking precision is essential for CAST, since the expected solar axion flux rapidly decreases with the solar radius, as it is shown in figure 3.3. Taking into account all the uncertainties and sources of error (astronomical calculations, GRID measurements and their mathematical interpolation, motor encoders precision, hysteresis, etc.), the achieved tracking accuracy is better than the required 1 arcmin (0.01-0.02°) from the center of the Sun. The solar tracking precision is periodically verified by two independent methods, the GRID measurements and the Sun filming.

GRID measurements The first conversion calibration from global coordinates to motor encoder values was done by the surveyors group of CERN in 2002. The calibration consists in measuring the conversion for a defined set of magnet positions (GRID) intending to cover the whole magnet movement range. This calibration was incorporated into the tracking program for tracking the Sun with the required precision. Since then, periodical GRID or *mini-GRID*[2] measurements are performed in order to detect any possible drift with respect to the original calibration values.

In general, only small deviations with respect to the original values are observed in the periodical cross-checks. In 2011, full GRID measurements were carried out, showing a deviation of about 2 mm projected to a plane at 10 m with respect to the original calibration of 2002, as shown in figure 4.13 (left), where the required 1 arcmin precision and the 10% of the solar radius are also shown for comparison. Even though, the measured deviation was within the tolerable range of 1 arcmin, the new measurements were set as reference in the tracking program for better tracking accuracy.

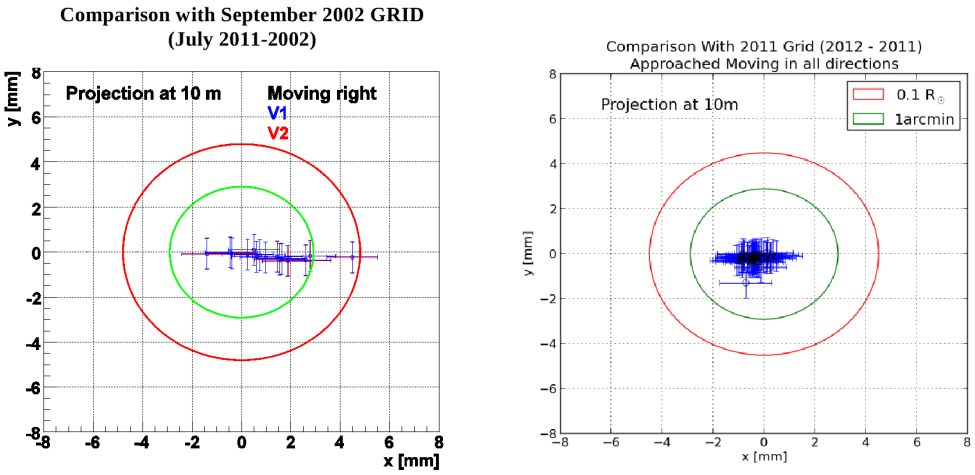

Figure 4.13: Deviation in the solar tracking projected to a plane at 10 meters of both magnet bore lines (V1 and V2 in blue and red crosses respectively). On the left, deviation between the original calibration in 2002 and the GRID measurements of 2011, which are considered the reference coordinates from 2012 onwards. On the right, the comparison between 2011 and 2012 GRIDs. Figures extracted from [174].

Sun filming The Sun becomes visible for the CAST magnet only twice per year, in March and September, through a specifically built window in one of the walls of the experimental hall (see figure 4.14, left). The aim of the Sun filming is to cross-check the accuracy of the solar tracking by an independent method, complementing the GRID measurements.

The Sun filming consists in directly photographing the Sun with an optical camera equipped with a CCD sensor. The camera must be aligned with the reference axis of the magnet bore

[2] A reduced set of the original reference points.

(V1). This is accomplished by setting a laser beam parallel to the magnet bore with the aid of surveyors, and aligning the camera with this beam line. The tracking program steering the magnet movement must be set to a special mode in which it is taken into account the light refraction due to the atmosphere. The results of the 2012 and 2013 Sun filmings are shown in figure 4.14.

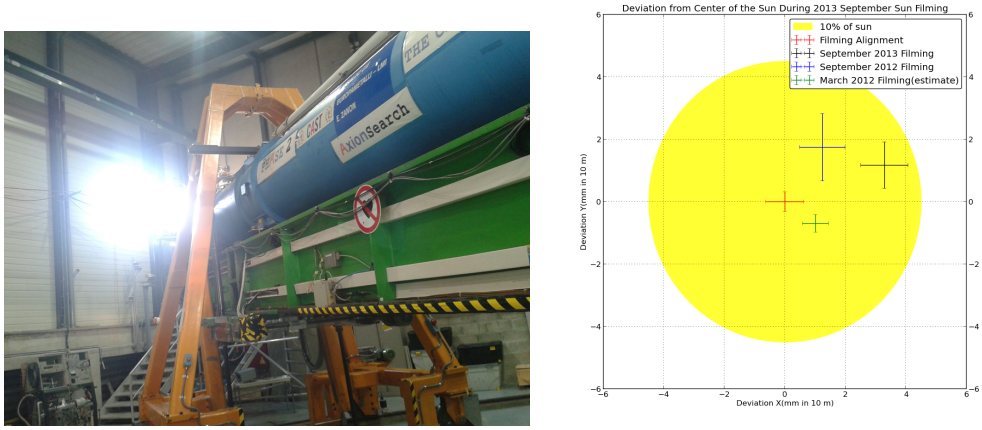

Figure 4.14: Left: Sun filming window in the building that hosts the CAST experiment. Right: Measured deviation from the center of the Sun in three different filmings. In yellow, the 10% of the solar radius. Figure extracted from [175].

4.7 The slow control system

All the key parameters of the different subsystems of the experiment are continuously measured in real time. The CAST slow control system is a a centralized acquisition system able to read and write analog and digital signals of the sensors connected to the system. A dedicated LabVIEW program displays a graphical user interface (see figure 4.15) that monitors and logs the key parameters of the different subsystems of the experiment.

The nominal updating time of the log files is 1 minute, which is shorten in case of rapid change of any variable. The main functionalities of the slow control are:

1. Online monitor and plot of the key variables of all subsystems, as well as periodic logging of the gathered data to AFS file system. Regarding the magnet system, temperatures, intensity and magnetic field are displayed; regarding the vacuum and buffer gas systems, many pressures, temperatures and valves' status are monitored; regarding the tracking system, the motor encoder values or the load on the lifting jacks are shown; regarding the x-ray detectors, the intensity, chamber pressure, and other parameters.
2. A system of alarms can also be activated to give a fast response to arising problems or prevent the damage of any device: in case any of the parameters drops below or exceeds a user predefined value, it sends a SMS alarm or email to the experts of the system.

4.8 The x-ray detectors

Four x-ray detectors placed at both ends of the two cold-bores must detect the photons converted from axions. During evening solar tracking, *sunset axions* would enter the magnet from the MFB side and the converted x-rays would be detected in the so-called *suset detectors*. During sunrise solar tracking the opposite process is expected: axions entering the magnet through the MRB side, producing x-rays to be detected by the *sunrise detectors*. The main detector types operating in CAST throughout its history are:

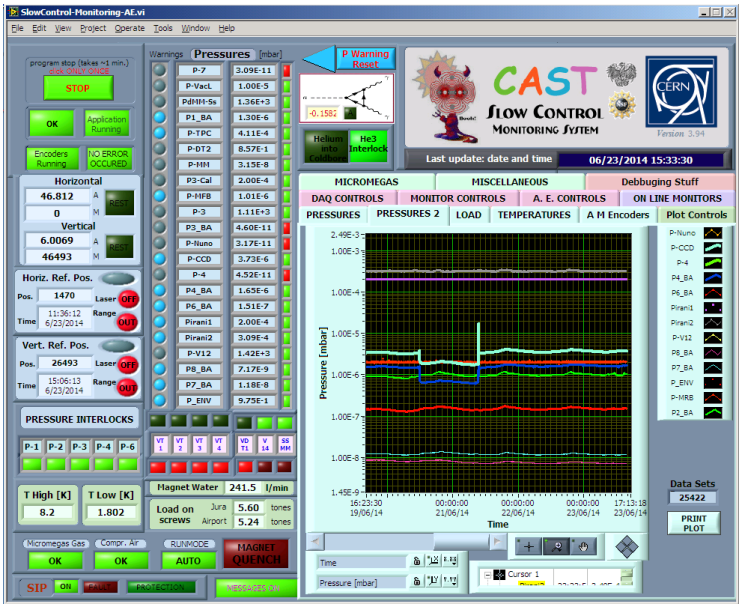

Figure 4.15: Display of the user interface of the CAST slow control system.

1. The pn-Junction Charge Coupled Device (pn-CCD): operated from the beginning of the experiment in the V2 line of the sunrise side of the magnet, until 2013. A x-ray optic device covering all the area of the magnet bore focused the expected converted photons to a smaller area, remarkably enhancing the S/N ratio. In 2014, it was replaced by an InGrid gaseous detector (see bellow).
2. The TPC: it was read by a multiwire proportional counter (MWPC) plane, and covered both magnet bores of the sunset side of the magnet during the vacuum and ^{4}He runs of the experiment. In 2008, it was replaced by two Micromegas detectors.
3. The Micromegas detectors: this detector technology proved higher background rejection power than the TPC, so since 2008 they cover the two magnet apertures of the sunset side of the magnet. The remaining magnet aperture in the V1 line of the sunrise side has been always covered by a Micromegas detector, whose readout fabrication has evolved in parallel to the development of the technology. In 2014, a dedicated x-ray focusing device was installed in front of it in order to increase the S/N ratio. It also serves as a test of the most compelling detector candidate technology for covering the magnet bores of the IAXO project.
4. Integrated GEM/Micromegas and silicon sensor (InGrid): it is a novel readout fabrication technology for gaseous detectors belonging to the same general technological category that the Micromegas, the Micro Pattern Gaseous Detectors (MPGD) technology. It replaced the former CCD.

The are two main requirements to all these detectors. In first place, they must have high quantum efficiency to x-rays in the [1-10] keV energy range, and secondly, they should have as low background as possible. The background suppression techniques used for the Micromegas detectors is described in chapter 5.

Other detection techniques used to look for other than solar axions, such as paraphotons or chameleons, have been used in CAST. Such detectors are described in section 4.8.5.

4.8.1 The x-ray optics and the pn-CCD detector

The x-ray flux coming from the conversion of axions in the magnet can either be observed directly by a detector covering the full area of the cold-bore, or it can be focused and observed with a

detector placed in the focal plane of the x-ray optics. The main advantage of the latter approach is that the focusing of the signal from 1450 mm^2 to around 9.4 mm^2 produce an enhancement of the signal-to-background ratio of a factor of about 150, compensating the efficiency loss it introduces.

The first CAST x-ray focusing device (figure 4.16) is a spare module of the ABRIXAS satellite mission [176], based in well proven technology in many x-ray astronomy missions. It is installed in one port of the sunrise side of the magnet. In 2014, the remaining port of the sunrise side was equipped by another x-ray focusing device, specifically designed for axion physics, with a Micromegas detector in its focal point. The latter system is described in section 4.8.1. Here, we describe the first x-ray telescope of CAST.

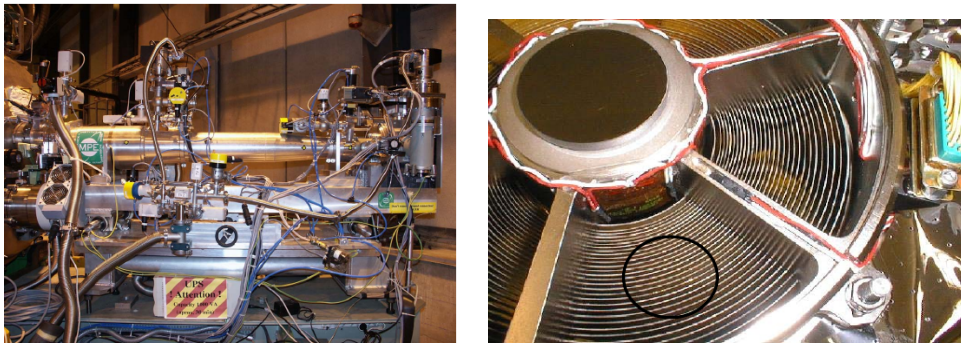

Figure 4.16: Left: x-ray telescope installed in the CAST line. Right: front view of the x-ray focusing device. The device is situated off-axis, covering the cold-bore area (black circle) with one of the sectors of the telescope.

Conventional mirror telescopes for visible light do not work well for x-rays because it does not exist the material that refracts the x-rays when they incise in nearly normal direction. Instead, x-ray mirrors must have very low angle from the plane of reflection (typically up to 2°). The x-ray telescope of CAST [166] is a 1600 mm focal-length, Wolter I type mirror system (figure 4.16), consisting in six sector of 27 nested, gold-coated parabolic and hyperbolic nickel shells. Since the cold-bore area is smaller than the size of each sector, only the one that showed better performance in the calibrations performed in PANTER is used.

The detector in the focal plane of the optics until 2013 was a fully depleted 280 μm silicon pn-CCD detector (figure 4.17, left), like the ones successfully used in the XMM-Newton satellite mission [177]. The rectangular sensitive area (30×9.6 mm) is subdivided in 200×64 squared pixels of 150 μm side. The focusing spot generated by the solar axion flux would only have a diameter of 19 pixels, which allows to simultaneously measure the expected signal and background. The detector has integrated front-end readout electronics, which is continuously taking data, without external trigger, in loops of about 6 ms. The charge collected during these periods is integrated in parallel in about 66 ms. The detector operates in vacuum conditions (below 10^{-5} mbar) at 153 K, and it is installed inside a shielding made of copper and lead layers of 1 and 2 cm respectively.

The overall x-ray detection efficiency of the system given by the mirrors reflectivity and the quantum efficiency of the pn-CCD detector is shown in figure 4.17 [166]. The integrated efficiency of the system for x-rays over the CAST energy region of interest is of about 30%. The efficiency lost is mostly due to the x-ray optics, since the quantum efficiency of the pn-CCD detector in the 1−7 keV energy range exceeds 95% [177]. The efficiency of the mirrors reflectivity depends on the alignment of the magnet and optics axes. An adjustment done in the alignment to better focusing the signal in the CCD sensitive area produced a small reduction in the overall efficiency from 2003 to 2004, as it is apparent in the figure. The reduction of the efficiency in the 2−3 keV range is due to the M-edge x-ray absorption in the gold coating of the mirror shells.

The x-ray focusing device is operated in vacuum, with levels below 10^{-6} mbar to avoid further efficiency loss due to the absorption of impurities in the mirrors' surface. The x-ray telescope system incorporates a gate valve in each side of the telescope as an extra safety measure.

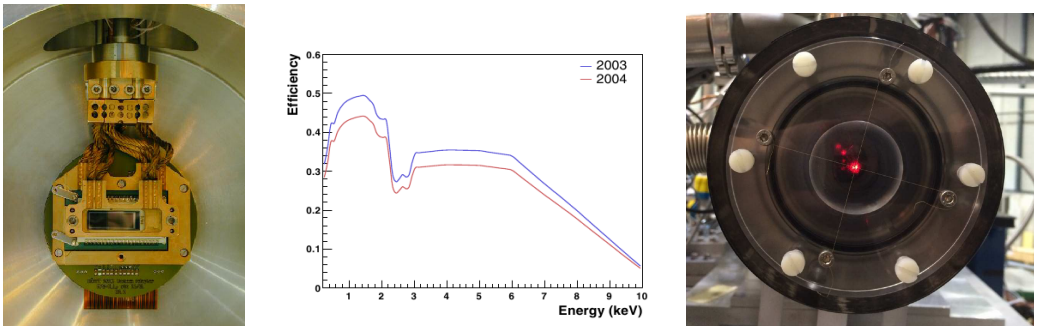

Figure 4.17: Left: a picture of the pn-CCD detector. Centre: overall x-ray detection efficiency of the x-ray mirror system and the pn-CCD detector in the energy range of interest for CAST. Extracted from [166]. Right: a picture illustrating the the x-ray telescope alignment with the laser beam and cross-wires.

A key operation in the x-ray telescope installation is the parallel alignment of the system with the magnet axis. A parallel and centered laser beam is defined by the Survey group of CERN and the use of crosshairs in both sides of the magnet. The laser is installed in the sunset side of the magnet[3], shinning through the whole magnet and traversing the x-ray optics. The pn-CCD detector can be replaced by a focusing screen, which allows to observe the image and fine tune the telescope position. A picture of this process is shown on the right panel of figure 4.17, while the left panel of figure 4.18 shows the intensity distribution of the laser beam in the CCD detector plane, showing also for comparison the expected axion signal area.

An additional and independent way of evaluating the alignment when the sunset detectors are installed is based on a x-ray generator placed in front of the sunset detectors. The device produces and accelerates electrons towards a Cu target, leading to a flux of mainly 8 keV x-rays. The device, usually in parking position off-axis, is only turned on to do the measurements, when it is remotely moved to the center of the bore area. In the center of figure 4.18, the intensity distribution of the 8 keV photons in the CCD is represented. Note that the focusing spot produced by the parallel laser beam is within the larger spot produced by the x-ray generator, which would confirm that the system is well aligned.

The stability and uniformity of the CCD chip is daily checked by ^{55}Fe calibrations. The high granularity of the readout allows to apply discrimination algorithms to the background data. For example, as the expected x-ray signal usually does not activate more than four adjacent pixels, cosmic muons or high energy electrons can be rejected. The background level of the CCD integrated from 1 to 7 keV and the whole detector area is $(8.00 \pm 0.07)\cdot 10^{-5}$ counts keV^{-1}cm^{-2}s^{-1}, i.e 0.16 counts/hour in the 9.4 mm^2 of the solar spot. The pn-CCD background studies point to backgrounds dominated by external gammas [178]. A uniform intensity distribution on the CCD chip during a background run is shown on the right of figure 4.18. The absence of an excess in the number of counts in the solar axion spot area with respect to the rest of the detector is the concept used to set upper bounds on the $a\gamma\gamma$ coupling.

4.8.2 The CAST TPC

The history and evolution of gaseous detectors, as well as the phenomenology of a Time Projection Chamber (TPC) are described extensively reviewed in chapter 1 and 5. Here, the TPC used in CAST [179] is described in some detail (see figure 4.19). The TPC was operative since the beginning of the experiment until 2008 in the sunset side of the magnet, when it was replaced by Micromegas amplification structures. The main requirements to the TPC are: high gas gain in order to achieve low energy thresholds, low background and high efficiency in the energy region of

[3]this operation requires uninstalling the sunset detectors and shielding.

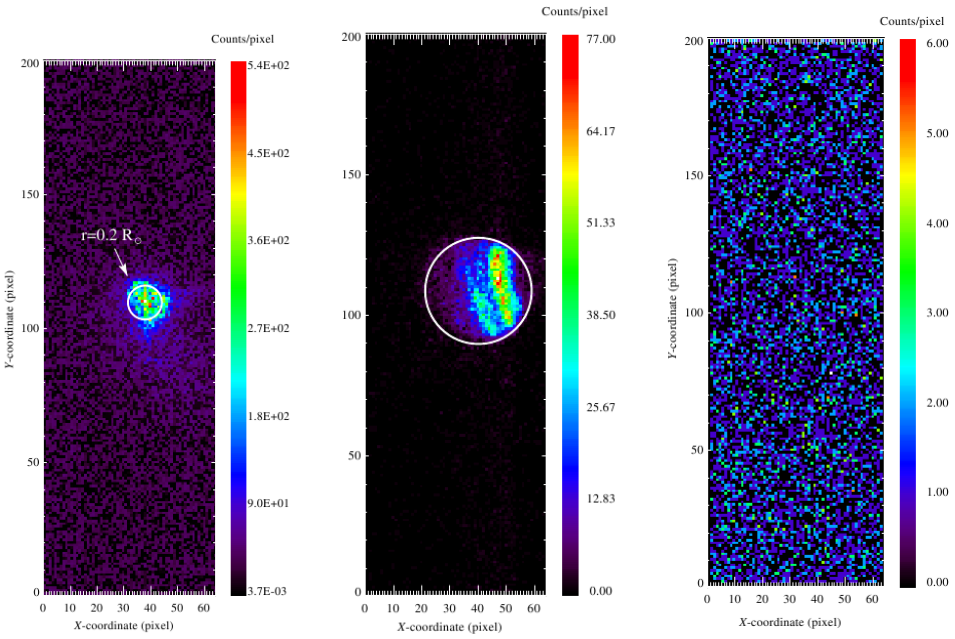

Figure 4.18: Intensity distribution registered by the pn-CCD detector illuminated by a parallel laser beam (left), the 8 keV photons produced by the x-ray generator (centre) and background particles (right). The white circles represent the expected image generated by axions coming from the $0.2R_{\odot}$ and the magnet bore projection in the left and central images respectively. Figures extracted from [166].

interest (RoI), position sensitivity and stable operations.

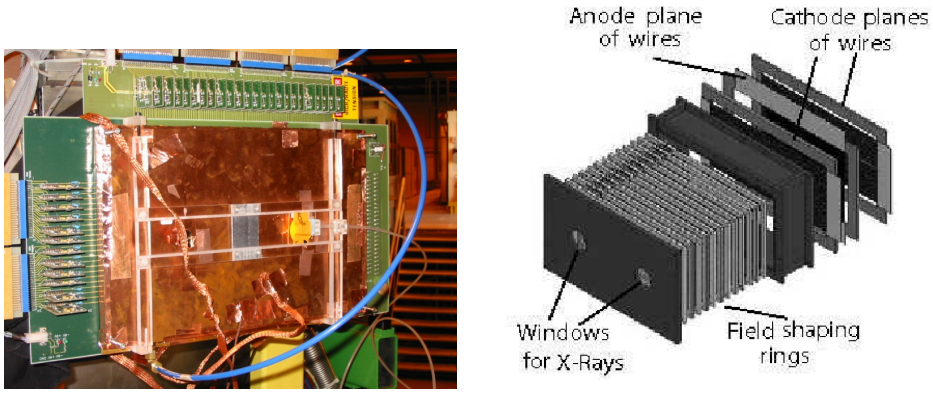

Figure 4.19: Left: back view of the TPC installed in the CAST line. Right: schematic view of the CAST TPC, where the x-ray windows and the anode wires are labelled.

A detector that fulfilled all these requirements was a Time Projection Chamber with a Multiwire Proportional Chamber (MWPC) as electron collection structure. The principle of operation of the TPC is simple: ionizing radiation generates primary electrons in the gas-filled conversion volume of $10\times15\times30$ cm^3. The 10 cm side of the chamber is the drift direction, parallel to the magnet pipes, while the 15×30 cm^2 section covers both magnet apertures. The conversion volume is filled with Ar(95%)/CH_4(5%) mixture at 1 bar providing almost 100% quantum efficiency for x-rays transversal to the detection plane in the energy RoI. Primary electrons drift towards the plane of

wires in the back side of the chamber by means of a 700 Vcm^{-1} drift field. There, the avalanche multiplication of the primary ionization cloud takes place triggered by the high electric fields present between the anode (+1.8 kV) and cathode (grounded) wires. The anode plane contains 48 wires, displayed in orthogonal direction to the 96 cathode wires. The spacing between wires of the same plane and between the anode and upper cathode is 3 mm, while the lower cathode is at 6 mm from the anode.

The low background is achieved by a shielding made of (from inside to outside): 5 mm thick copper box and 25 mm thick lead layer block the environmental gamma radiation; a 1 mm thick cadmium layer to absorb the neutrons thermalized by a 225 mm thick polyethylene layer; an overpressurized plastic bag flushed with N_2 gas to avoid the presence of radon in the detector surroundings; a scintillator detector on top of the shielding in anti-coincidence with the detector to reject events induced by muons. Besides, all the detector materials are chosen to be radiopure.

The chamber connects to the magnet pipes by means of two circular apertures, covered with 5 μm aluminized mylar foils glued to a metallic grid structure. These windows withstand the pressure difference between the detection volume and the vacuum pipes, while being highly transparent to x-rays. Two other apertures in the back side of the chamber allow to perform ^{55}Fe calibrations, which are used to monitor the stability of the detector, as well as defining the characteristics of x-ray events. These calibrations allow to apply a set of background rejection algorithms mainly based on the difference between the expected spread of an x-ray signal (essentially point-like energy deposition) and the more wide typical background tracks. The background level achieved by the TPC between 1 and 10 keV was about $4{\cdot}10^{-5}$ $keV^{-1}cm^{-2}s^{-1}$ [179].

4.8.3 The Micromegas detectors

The Micromegas technology is one of the most successful amplification structures of the new type of micropattern gaseous architectures (MPGDs). These novel amplification structures came to replace the wire-type detectors, providing higher rate capabilities and improved energy and position resolution. These type of detectors are described in detail in chapter 5.

Since 2008, when the TPC was replaced, three of the four detectors coupled to the magnet bores are of the Micromegas type: two looking for sunset axions and the other for sunrise axions. The evolution of the technology, the improvement in the analysis routines, and the continuous upgrades on the system (shielding, electronics, etc.) allowed to improve the background level of the former TPC by more than one order of magnitude. It was precisely the enhancement of the Micromegas detectors what motivated the revisit of the CAST vacuum phase from 2013 to 2015. The Micromegas detectors used in CAST are extensively discussed in chapter 5, where other detector subsystems such as the vacuum line and the gas system are described.

4.8.4 The InGrid detector

InGrid is a novel detector concept based on the integration of a Micromegas gas amplification structure and a silicon readout chip by means of wafer post-processing technology [180]. The avalanche multiplication of the primary ionization is produced in the gap (typically of 50 μm) between the Micromegas mesh and the wafer anode, which are kept at a uniform distance by means of insulating pillars (see figure 4.20, left).

The InGrid detectors are manufactured with very recent CMOS chip production technology, resulting in very uniform gap homogeneity. This fact implies higher gain uniformity than conventional Micromegas and superior energy resolution. A remarkable feature of InGrid structures is that each mesh hole is aligned with high precision to each readout pixel providing an unprecedented granularity for a gaseous detector. This makes that the signal induced by each electron avalanche is collected by only one pixel, enabling the detection of individual electrons [181], and resulting in very low energy thresholds.

The CAST InGrid detector [182], installed in the experiment line for the first time in 2014, is shown in figure 4.20 (right). The design is based in the Micromegas chambers previously used in CAST. It consists in a chamber body made of acrylic glass filled with Ar/iC_4H_{10} (97.7/2.3 %) at

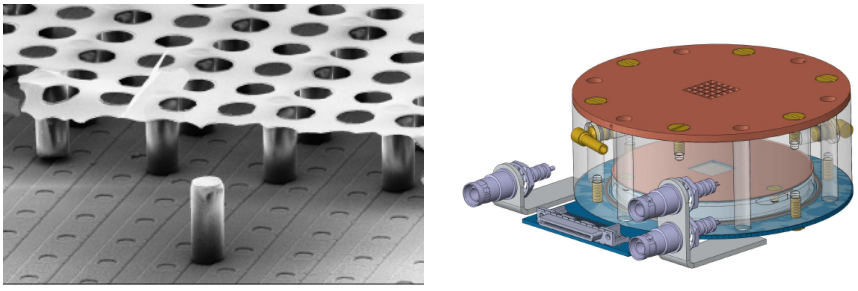

Figure 4.20: Left: picture of the InGrid detector, where mesh, pillars and silicon wafer are apparent. Right: the CAST InGrid TPC. The ports for gas input/output are visible in yellow, the HV and signal connectors are in grey, and the cathode with the strongback is represented in orange.

1 bar. A copper cathode at 3 cm from the amplification structure defines the conversion region, to which x-rays coming from the magnet would arrive through a 2 μm aluminized mylar window glued on a strongback. Such a window provides higher than 50% x-ray transmission above 1 keV, and more than 90% above 2 keV (see figure 4.21). A 0.9 μm thick mylar window serves for the differential pumping of the vacuum pipes, preventing the contamination of the x-ray mirrors, the cryogenic windows or the magnet with the detector gas. The connection of the InGrid detector to the CAST line is shown in figure 4.21.

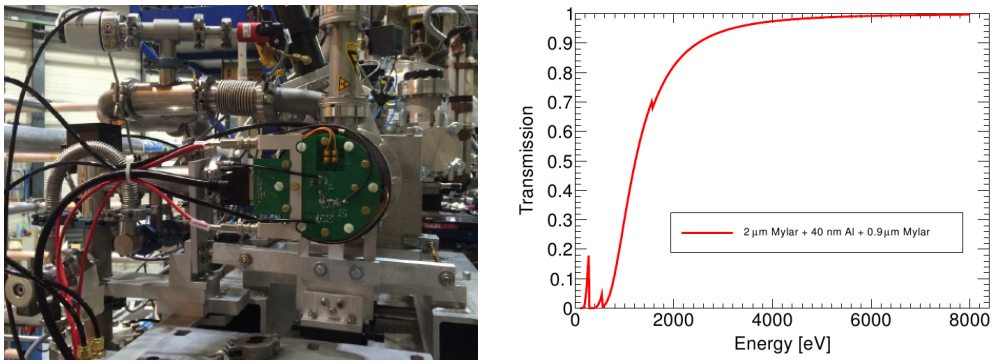

Figure 4.21: Left: InGriD detector installed in the sunrise V1 line of the CAST magnet. Right: x-ray transmission in the CAST energy RoI through 2 μm mylar window with 40 nm of Al deposition and 0.9 μm of the differential window.

The readout chip of the InGrid detector in CAST is a Timepix ASIC [183] of 1.4×1.4 cm^2 with 256×256 pixels (55 μm side). The data acquisition system is continuously taking data with no need of external trigger. The measurement of the deposited energy of each event can be calculated either as the sum of the charge in all pixels, or by pixel counting. The detector shows very good energy resolution (down to 9% FWHM at 5.9 keV in Ar/iC$_4$H$_{10}$ (90/10% Ar/iC$_4$H$_{10}$). The topological information provided by the readout allows to do event-shape analysis and reduce backgrounds. An example of the shape difference between x-ray and cosmic events is shown in figure 4.22.

Scalability and stability over long data taking periods must still be demonstrated, as well as it competitiveness as low background detector. Its operation in CAST could confirm the InGrid technology as a good candidate for rare event searches.

4.8.5 Other detectors

Apart from the detectors described above, other detection systems have been used to look for low energy solar axions, hidden-photons [184] or chamaleons [171], as by-products of the main CAST

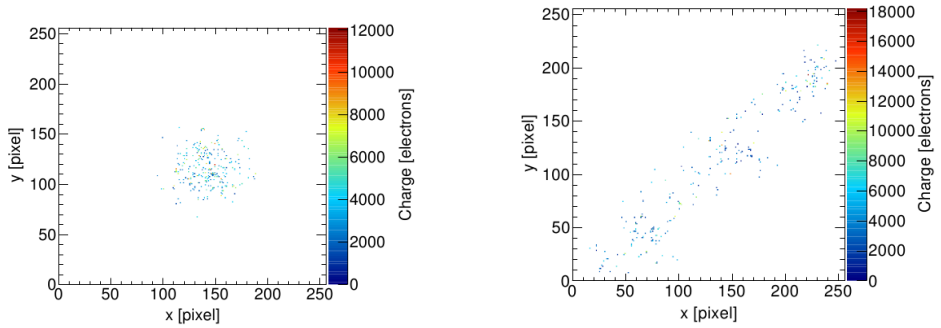

Figure 4.22: Comparison of x-ray (left) and cosmic (right) events in a intensity distribution map. Clearly, x-ray events produce a cloud-like distribution, while cosmics typically produce much more spread signals. Figures extracted from [182].

research line. These detectors are briefly described here.

The BaRBE detector The BaRBE detector is a single-photon counting system in the very low energy interval range of [1-100] eV. It was commissioned during 2009-2010, and took data during 2011 and 2012. The setup is coupled off-axis to the V2 line of the sunrise side of the CAST magnet. This is achieved by means of a semitransparent 5 μm thick polypropylene mirror assembly with 10 nm of aluminum metalization. The signal is read-out by means of a optical fibre and a photomultiplier, resulting in an overall 10% detection efficiency. An upcoming paper will report on the physical results achieved by the detector.

The SDD detector In 2013, the x-ray telescope was dismounted for recalibration in PANTER. Taking advantage of the free port, a 100 mm^2 sensitive area Silicon Drift Detector (SDD) was installed. The SDD is a system assembled from commercial parts, whose most important characteristic is its high quantum efficiency above very low energies (400 eV), as there is no window between the vacuum pipes and the sensitive area.

Chapter 5

The Micromegas detectors of CAST

Contents

5.1 Microbulk Micromegas in CAST

Three of the four x-ray detectors of the CAST Experiment are microbulk Micromegas (MM) detectors since 2008, two in the sunset side, one in the sunrise side. In this chapter, the use of MM detectors for axion searches is motivated, and the Micromegas detection systems of CAST are described from 2012 onwards.

The main requirement to the x-ray detectors in CAST is to bring their experimental background as low as possible, as shows equation 3.19. Microbulk Micromegas detectors offer unique features for this purpose. The techniques used to achieve low background x-ray detection are listed below, while their implementation and the impact on the CAST detectors background will be explained in the following sections.

1. **Background suppression:** the use of highly patterned readout offers topological information of the event, a powerful tool for signal/background discrimination. The power of this discrimination is related with the quality of the readout so that improvements in readout design or manufacturing yield improvements in discrimination power. The same stands for the front-end electronics and acquisition system.
2. **Shielding:** passive and active shielding techniques are used in order to block the gamma radiation and identify the muon-induced events respectively. The design of the passive shielding, made of high-Z materials such as copper or lead, must take into account the space and weight constraints of the magnet moving platform and the geometry imposed by the connection to the magnet.
3. **Radiopurity:** a careful selection of the detector components is required given that the intrinsic radioactivity of the detector materials could be a source of background. CAST-MM readout planes are made of kapton and copper, two materials of well known radiopurity. Indeed their intrinsic radioactivity have been strongly constrained by a series of dedicated measurements carried out with a high purity Ge detector in the Canfranc Underground Laboratory (LSC) [185]. The geometry of the chamber is relatively simple and its components

(chamber's body, x-ray window, screws, gas gaskets, connectors, etc.) have gone through screening campaings and are built up from radiopure materials.

The anode of the CAST-MM follows the pattern presented in figure 5.1 (left). It consists on an array of pixels of 400×400 μm interconnected in x and y directions. An implementation of this schema can be observed in the middle of figure 5.1, where half of the pixels are connected at the pixels level (thus reducing the material budget), and the other half are connected in an underlying copper plane. The micromesh holes are arranged in groups that correspond to the pixels underneath, as shown on the right of the figure 5.1.

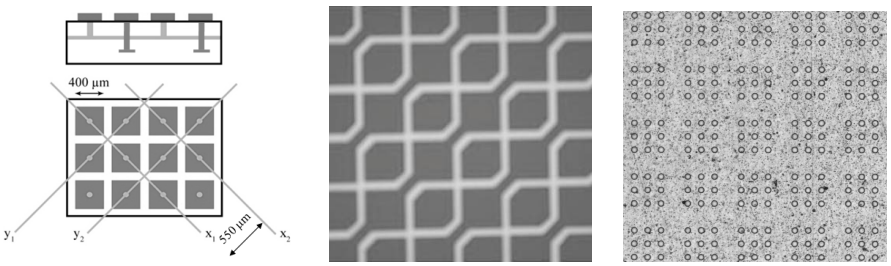

Figure 5.1: Schematics of the readout pattern of CAST-MM detectors (left). In modern readouts, the strips in one direction are formed by connecting the pixels at the anode level (center) and the strips in the other direction in a copper-kapton back-layer. The mesh is patterned in cells of 3×3 holes. Each cell is immediately above one pixel.

Besides, the simplicity, robustness and mechanical precision of the readouts is guaranteed by a mature and consolidated manufacturing process. CAST-MM show high stability over long running periods, a high ($\gtrsim 10^4$ in argon-based mixtures) and uniform gain and energy thresholds below the keV [186]. These facts will be shown in subsequent chapters.

5.2 Sunset and Sunrise Micromegas detectors

The CAST-MM detectors are shielded small gaseous TPCs made of radiopure components. Here, we first describe the Sunset Micromegas detectors (SSMM) and their shielding from 2012 onwards. Finally, we present the upgrades introduced to the Sunrise Micromegas detectors (SRMM) in 2013 and 2014. Three branches of *microbulk* detectors have been developed so far, denominated *M*, *C* and *R-branch* plus a number for identification. The improvements introduced in each new design are discussed.

5.2.1 Sunset Micromegas

The SSMM detectors are composed of a 15 mm thick plexiglas vessel, with an inner diameter of 80 mm, and a length that defines a drift/conversion region of 30 mm. This vessel is screwed to the plexiglass support where the Micromegas readout is glued. On the other side, the vessel is screwed to a metallic squared grid (strongback) to which a thin 4 μm aluminized mylar x-ray window is glued. The strongback and the window are the cathode of the TPC, being biased to a voltage that defines the drift field. The x-ray window allows the passage of the x-rays through it and withstands the pressure difference between the chamber and the vacuum line. The chamber has two gas ports that allow to operate the detector in gas circulation mode, normally at 1.4 bar of Ar+2% iC_4H_{10}. The overpressure guarantees a large quantum efficiency for x-rays in the energy range of interest (RoI), while the leak tightness of the detection chamber is achieved by viton o-rings.

The detector (*M-branch*) is all made in copper and kapton following the manufacturing process described in section 1.6. The copper mesh is 5 μm thick and defines and amplification gap of 50 μm. The active area of the detector is a square of 60×60 mm^2, divided in squared pads of 400 μm, with a pith of 500 μm. Pads are alternatively interconnected in x and y directions (106

strips per direction) through metallized holes, which are routed to the connector prints at the side of the plexiglass support (figure 5.2). The strips are connected to the detector ground via a $10M\Omega$ resistor that can be removed in case of mesh-strip shortcircuit. Meanwhile, the mesh and the cathode strongback are biased via metallic connections outside the detection chamber, which define the amplification and drift fields respectivelly. The readout electronics are directly coupled to the connector prints (Gassiplex electronics) or they are connected through adaptation cards and flat cables (AFTER-based electronics). See section 5.5 for details on the readout electronics.

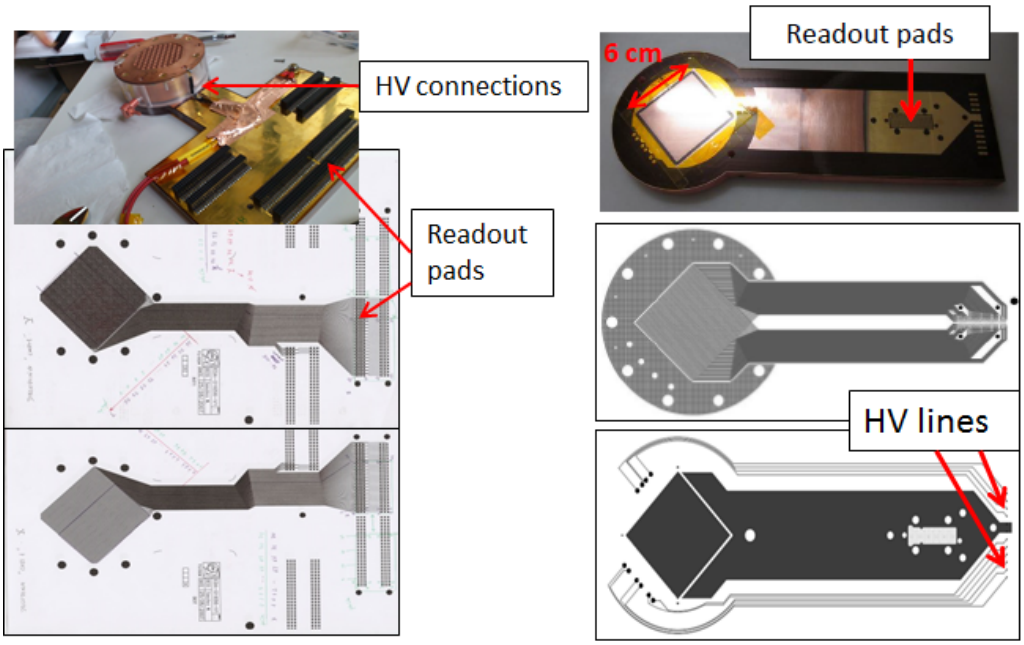

Figure 5.2: Left: Sunset Micromegas detector and routing of the strips to the readout electronics connectors. Right: Sunrise Micromegas detector without the vessel and routing of the strips and high-voltage lines.

The detector shielding of SSMM detectors was fully upgraded in 2012, following a symmetric design for both sunset detectors. The new shielding was envisaged to reduce the stainless steel fluorescences (Fe-K_α at 6.4 keV, Mn-K_α at 5.9 keV or Cr-K_α at 5.4 keV) in the CAST RoI. The new system incorporates extra 10 mm thick, 200 mm long high-purity copper pipes, coated with a polytetrafluoroethylene (PTFE) layer to absorb the 8 keV copper fluorescences. The MM detectors are coupled to the copper tube via PTFE screws. A PTFE gasket is used to preserve the vacuum tightness and to electrically isolate the vacuum tube and the cathode. All around the plexiglas chamber extend a 10 mm thick copper layer. The lead shielding extends approximately 200 mm all around the detectors, covering also the copper pipes. The shielding has openings for the connection of the readout electronics and for the connection with the magnet, being these the only weak points of the shielding.

5.2.2 Sunrise Micromegas

Before 2013, both SRMM and SSMM detectors were of the type *M-branch*. The SRMM shielding was composed from inner to outer layers: 5 mm copper, 25 mm lead, 1 mm cadmium and 100 mm polyethylene. This shielding was conceived following the classic scheme of underground dark matter experiments.

However, in 2013 the whole system was re-designed according to the strategies extracted from the present background model, discussed in chapter 10. The design of the new detector (figure 5.4)

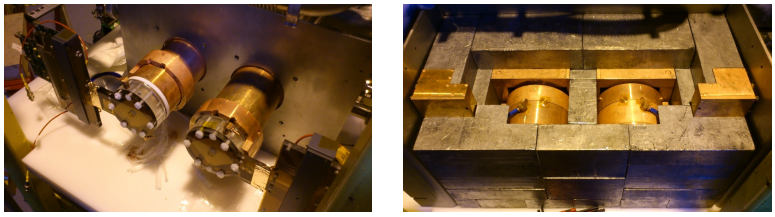

Figure 5.3: Two intermediate stages of the SSMM installation in the CAST vacuum line. The copper tube couples the magnet bore to the detectors (left), which are subsequently shielded with copper and lead layers (right).

is the prime example of the current state-of-the-art low background techniques developed for the Micromegas detectors.

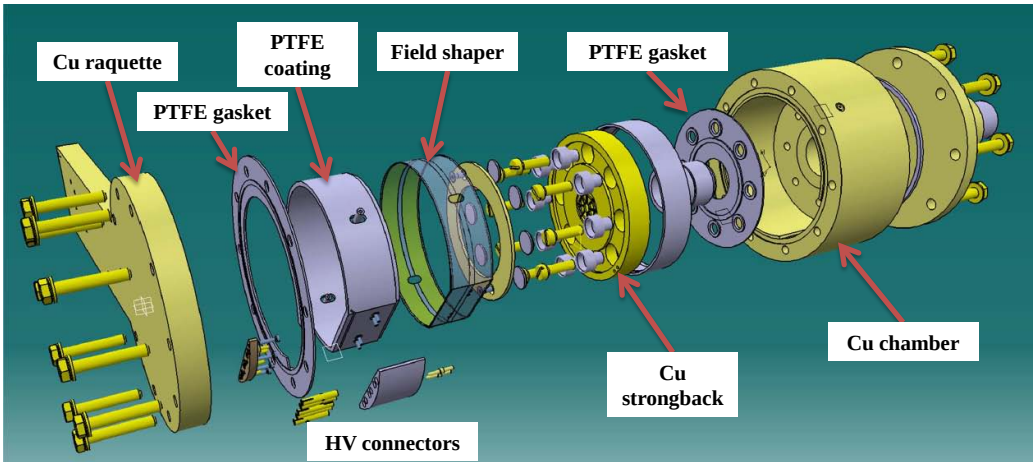

Figure 5.4: Sketch of the Sunrise Micromegas detector, where the different parts or the chamber are labeled. The components are described in detail in the text

The upgrade brought the *C-branch* of *microbulk* detectors, which was replaced by the *R-branch*, since the first were problematic, as explained bellow. The upgrades were done basically at two levels:

1. **Re-design of the readout PCB:** The active area of the readout is 60×60 mm^2, patterned in 120 strips per axis (500 μm pith), in contrast to 106 strips of the previous designs (550 μm pith). The strips are build from the diagonal connection of the pixels making the active area, one direction is connected at the pixels level, an the other in a back-layer. The strips' signals are routed through the copper support towards the fingerprint pads of a 300-pin SAMTEC connector. All the high voltage pads, mesh, cathode and field shaper rings, are implemented and routed in the detector printed circuit board, ending in regular connectors coupled to the so-called HV-box, which implements BNC and SHV feedthroughs and RC low-frequency filters to dim ripples from the high-voltage sources.

   In the first version of the readout design, there were problems at two levels: several short-circuits in the active area, and destructive discharges between the HV lines and the ground. The first problem was solved by increasing the pixels' spacing by reducing the size of the pixels and the pitch of the mesh holes, while keeping a similar distance between the outer mesh hole and the pixel border (a requirement to have a good detector performance). In the final design, the pixels are 313×313 μm^2, with 40 μm spacing between pixels. The mesh is patterned in groups of 3×3 holes lying over each pixel, with 95 μm pitch and about 41 μm hole-pixel border distance.

The second problem was solved by enlarging the width of the copper support. This fact allowed to avoid any overlap in the vertical direction between the ground layer, which covers the signal paths for electronic noise reduction issues, and the HV lines.

2. **Shielding, radiopurity, and TPC properties:** the gas chamber, Faraday cage and inner shielding are completely integrated in a *all-in-one* piece. In contrast to previous designs, the chamber of the detector is made of 18 mm thick radiopure copper. The plexiglas base (raquette) is replaced by a copper one, which is the base of the shielding and the support where the readout is glued. The copper support is long enough to allow bringing the strips' paths out of the shielding (figure 5.2). As all the high-voltage paths are routed to the outer edge of the copper raquette, the connections with the power supply and electronics, which are potential radioactivity sources, are moved away from the TPC without the need for exit points in the shielding.

   A new field shaper has been designed in order to homogenize the drift field and reduce border effects. It is printed on a flexible multilayer circuit with polymide as substrate. The circuit contains two tracks, 10 mm thick each one, to emulate the typical conductor rings. The outer side of the circuit is used to bring the high-voltage connections from the detector board to the field-shaper tracks and the drift cathode. An inner 3 mm thick PTFE foil prevents fluorescence from these tracks without disturbing the field lines.

   The dirtiest components from the radiopurity point of view have been replaced by PTFE and copper, which are proven to be clean. For example, all the gaskets are now made of PTFE instead of previous elastomeric ones. Besides, this copper has been carefully cleaned: firstly with ultrasonic baths of basic and acid soap, and secondly with acid (nitric acid) etching, and finally passivated with a solution of citric acid. The lead shielding is the thickest possible (from 5 to 10 cm) given the mechanical constraints of the setup.

   The installation of the x-ray focusing device in 2014 (see section 4.8.1) allowed to use a smaller x-ray window (with a spider-web design, which avoids the opacity of the strongback grid in the expected signal area) and extend the line with a copper pipe much narrower than the SSMM one (figure 5.5). This fact allows to use a more compact shielding, reducing the non-shielded solid angle. This fact and the absence of a plexiglas neck crossing the shielding are the main differences with respect to the present SSMM. In this way, the two main weak points of the shielding are minimized.

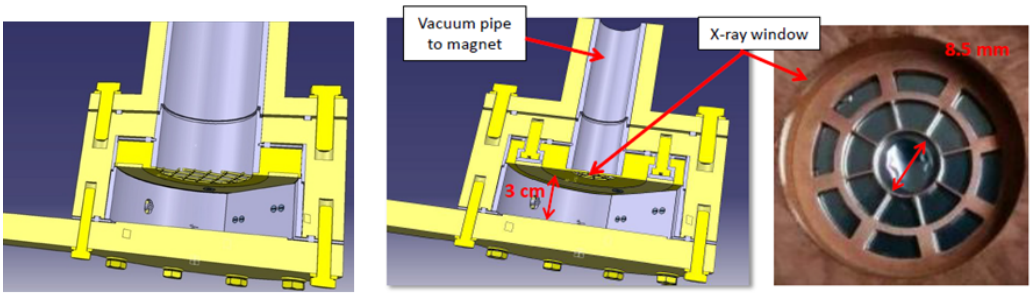

Figure 5.5: Comparison of the 2013 (left) and current (right) sunrise Micromegas strongback design. Photo of the new copper strongback with the spider web design

5.3 Gas, vacuum and calibration systems

The schematics of the vacuum, gas and calibration systems of SRMM and SSMM are shown in figures 5.6 and 5.7. The gas used in the Micromegas detectors is Ar + 2-2.3% iC_4H_{10} at 1.4 bar. The gas comes from a pre-mixed bottle, and the detectors are operated in circulation mode at a user-defined gas flow. The pipes of the gas system are made of copper, except in the proximity of

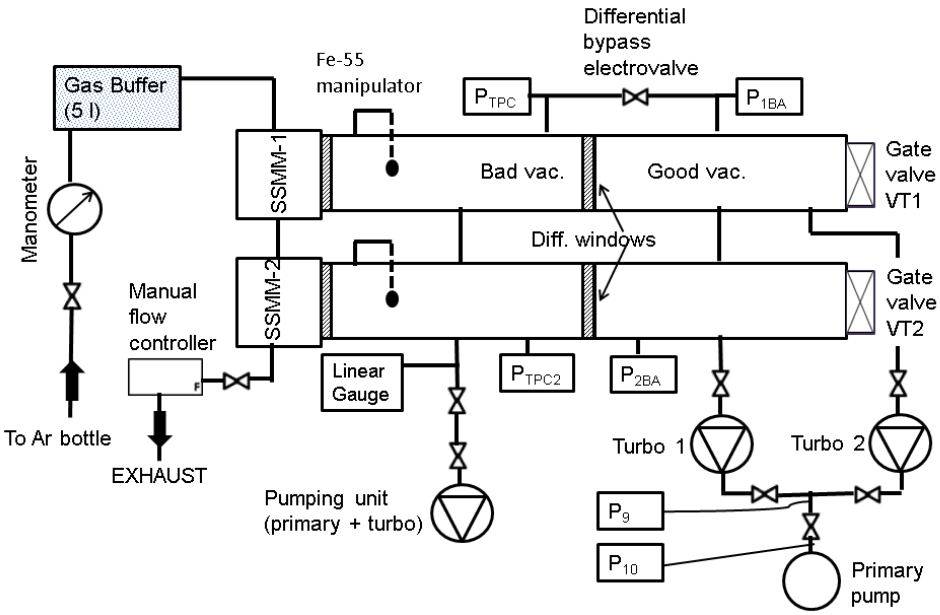

Figure 5.6: Sketch of the SSMM vacuum, gas and calibration systems.

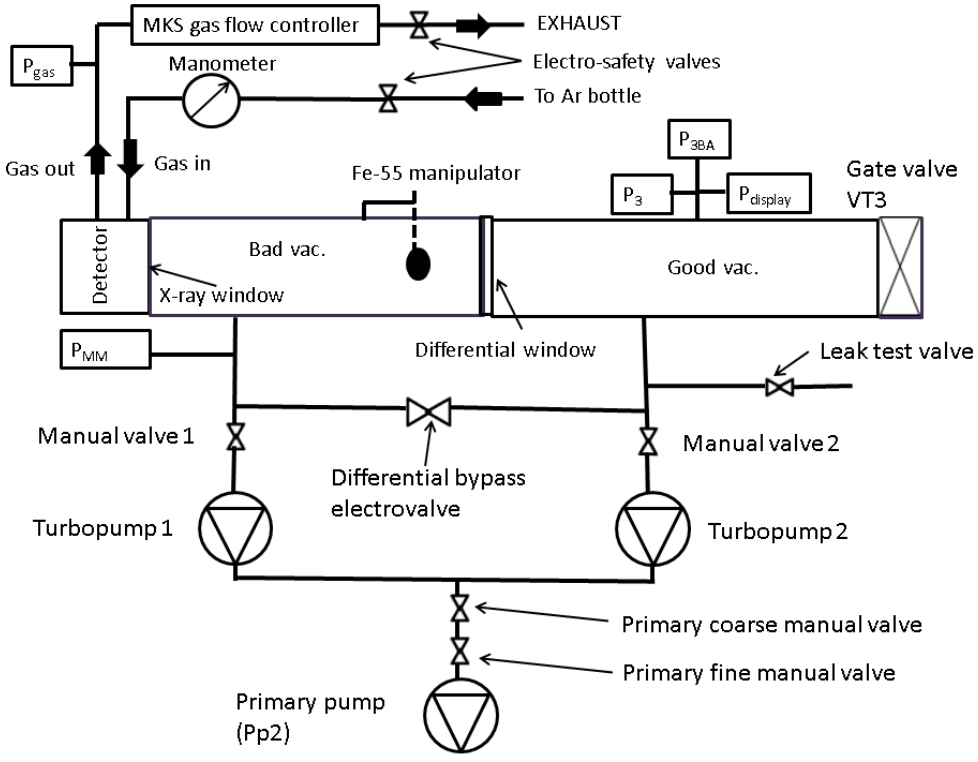

Figure 5.7: Sketch of the SRMM vacuum, gas and calibration systems.

the detectors, where plastic tubes are preferred for flexibility. Two consecutive pressure regulators set a maximum pressure in the line of 1.6 bara. The working gas pressure is finally adjusted by manometer installed before the detectors. In SSMM, a buffer volume of 5 liters is installed before

the two detectors, which are interconnected between them. In SRMM, a *gas panel* implements mass flow and high accuracy pressure regulator, devices controlled and monitored by a *control box*. The gas flux is normally set to 2-5 l/h. The pressure at the detector chamber is continuously monitored by a sensor placed just at the gas output of the detector. The detector chambers can be isolated by means of electro-valves, which are automatically closed in case of power cut for safety reasons. These valves are also manually closed to measure the leak rate of the detector chambers after they are installed or in any other intervention in the system.

The vacuum system of the sunrise and sunset lines is divided in two volumes by a 4 μm polypropylene differential window: the volume close to the detector (bad vacuum side) and the volume close to the magnet gate valves (good vacuum side). Argon and iC_4H_{10} molecules penetrate into the bad vacuum side by diffusion through the x-ray window of the Micromegas detectors, which are reinforced with a strongback in order to withstand the pressure difference between the detector chamber and the vacuum side. The differential window reduces the amount of these molecules going into the magnet bore (or, in the helium-filled runs, it prevents attachment and condensation of these molecules into the cold-windows, which would produce a lost in x-ray transmission), while keeping a high x-ray transmission. The two volumes divided by the differential window are physically connected through the differential bypass electrovalve, whose purpose is to protect the differential window in case of large pressure difference. The differential window, which is not reinforced by any strongback structure, cannot withstand more than few mbar pressure difference so it is kept opened until nominal vacuum conditions are reached (i.e., bellow 10^{-3} mbar). Then, the bypass valve is closed and the pressure at the good vacuum side drops normally bellow 10^{-6} mbar. Only when these vacuum levels are reached, the gate valves (VT1, VT2 and VT3) are opened and data taking can start. If for any reason, good vacuum pressure suddenly rises above a certain value ($\sim 10^{-6}$ mbar), gate valves are automatically closed and bypass valve is opened. In data taking conditions (bypass valve closed), both vacuum sides are pumped by independent turbo-molecular pumps. In the sunrise system, both turbo-molecular pumps are assisted by the same primary pump, while in the sunset system the primary pumps are also independent. Besides, sunset system counts with two turbo-molecular pumps for the good vacuum side, in case one fails.

A very critical part of the vacuum line are the 4 μm polypropylene differential and detector windows since any sharp edge in the metal where they are glued can damage them. The leak tightness, vacuum level and pressure resistance are usually verified as part of the commissioning of the system. In appendix B, some of these tests are presented.

The calibration system comprises a ^{55}Fe source situated in a holder with a very thin window facing the detectors. The holder is attached to a manipulator that can move up and down, from the *calibration position* to the *garage position* (outside the field of view of the detector). The source position is controlled and monitored by the data acquisition system, via the VME module and a *calibration box* that translates the electric logic signal from the DAQ to an air pressure pulse.

5.4 Active muon vetos

Muon-induced events can be an important part of the background level of the Micromegas detectors when operated at surface level. In order to suppress these events, an active detector can be installed over the Micromegas to act as a muon veto. The strategy is to use the time difference between the signal in the muon veto and the delayed Micromegas trigger. A comprehensive study of the time difference distribution an the effect on background is given in section 6.3.

A plastic scintillator acting as a muon veto was installed over the Sunset detectors for the data taking of 2012. It consisted on a plastic scintillator coupled to a low-noise photomultiplier. When a ionizing particle crosses the crystal, scintillation light is emitted and reflected in the scintillator walls. A light guide collects the scintillation light towards a photomultiplier. In the entrance of the photomultiplier there is a photocathode that generates photoelectrons from the incoming scintillating photons. The photoelectrons are amplified by the successive dynodes and a fast (few ns) electronic signal is generated. The plastic scintillator thickness is selected in such a way that the minimum ionizing particles release more energy than any natural gamma radiation. This fact

allows to set the detection threshold well above the natural radioactivity maximum energy, and cosmic muons are identified.

Figure 5.8: Schematic view of the muon vetos over the SSMM detectors (left) and photographs of the plastic scintillators on a test-bench (center) and installed in CAST (right).

Due to space constrains, the 2012 scintillator was not placed in a high efficient position. According to Geant4 simulations in which the theoretical angular distribution of the cosmic muon flux is implemented, only 44% of the muons that traverse the Micromegas detectors are identified by the muon veto. We will refer to this factor as veto coverage, which does not include the production of secondary particles or the quantum efficiency of the scintillators. The contribution of cosmic muons to background and its possible mitigation by means of higher efficient vetos was evaluated in dedicated experimental setups. It was found that further reductions in background level were possible. Therefore, a higher-efficiency system based on two plastic scintillators was designed, manufactured and installed (figure 5.8) in 2013, replacing the former one, which is used in the Sunrise side since the 2014 data taking campaign. The Sunset veto system consists on two plastic scintillators, one placed over the Micromegas shielding and the other on the back side of the shielding (figure 5.8), which required some changes in the allocation of the vacuum elements of the Sunset line. The base material of the plastic scintillator is polyvinyltoluene (ELJEN EJ-200 [187]) and the dimensions of the active area are respectively 1080×600×50 mm and 630×600×50 mm. This material combines long attenuation length, high light output, and an emission spectrum well matched to the common photomultipliers. The photomultiplier used is the H11285 assembly of Hamamatsu [188]. The veto coverage of this system was computed by Geant4 simulations resulting in ∼95% .

5.5 Readout electronics

Electric signals are induced both on the mesh and the strips of the Micromegas detector. The mesh pulse is amplified by a CANBERRA 2004 preamplifier and an ORTEC 474 Timing amplfier. This signal is duplicated by a linear Fan-in/Fan-out. One of these copies is sent to a discriminator that triggers the acquisition of the mesh and strips' signals if the mesh pulse amplitude is higher than a certain threshold. The mesh pulse is sampled at 1 GHz frequency in a 2.5 μs and recorded by a 12-bit dynamic range VME digitizing board, MATACQ (MATrix for ACQuisition) [189]. The strips signals are driven away from the active area by printed paths in the medium layer of the Micromegas detector.

In 2013, the Gassiplex-based [190] front-end electronics were replaced by the AFTER (ASIC For TPC Electronics Readout)-based cards [191, 192], developed for the readout of the large T2K time projection chambers. The fundamental difference between these two readout electronics is that while Gassiplex just records the integral value of each strip signal, AFTER electronics digitize the full pulse waveform of every strip (figure 5.9). Figure 5.10 shows the schematics of the Gassiplex

and AFTER electronic chain, while the reader is referred to appendix A for a detailed view of these chains as installed in CAST. Here, we will briefly describe the two systems:

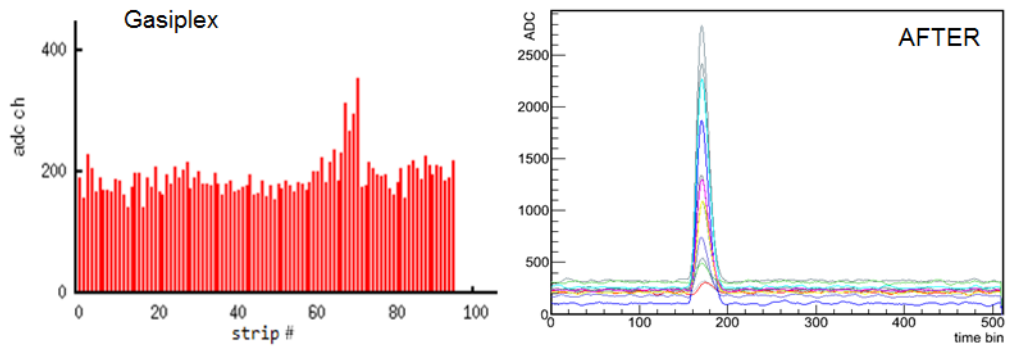

Figure 5.9: Comparison of an x-ray event as seen by the Gassiplex electronics (without pedestal subtraction) and AFTER-based electronics.

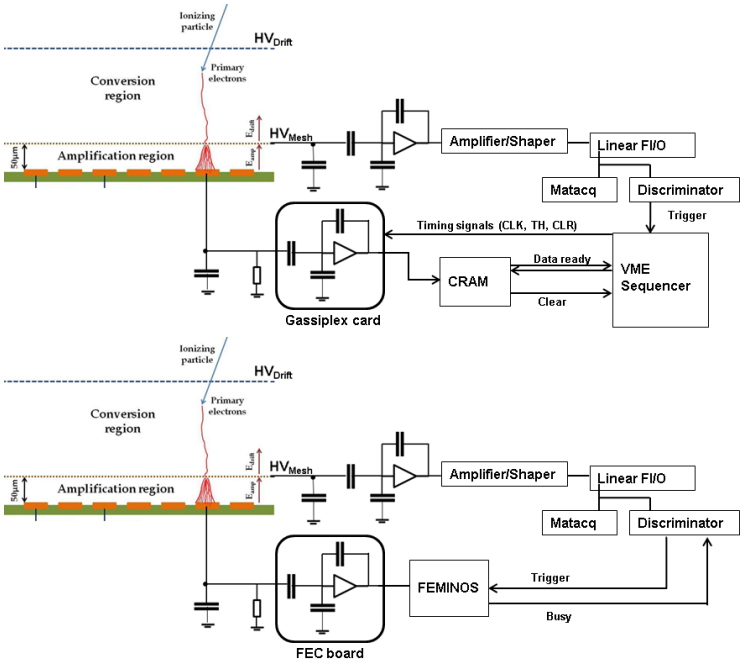

Figure 5.10: Schematics of the Gassiplex (top) and AFTER (bottom) electronic chains of the CAST-Micromegas detectors.

- **Gassiplex electronics:** the strips signals are integrated by the Gassiplex card and acquired by means of a VME CAEN Sequencer mod. V551B and CRAMS V550 (CAEN Readout for Analog Multiplexed Signals). The sequence of the digital signals that are produced during the acquisition is shown in figure 5.11. The paths of the strips printed on the CAST-MM detectors end at the fingerprint connector of 4 Gassiplex cards, each of which can handle up to 96 strips. When a mesh pulse is above the threshold a track-and-hold (TH) digital signal is sent to the Gassiplex cards, freezing the memory that stores the integrated strip signals. During TH duration (192 μs), the 96 clock (CLK) signals of 2 μs frequency are sent to the Gassiplex card, each for reading and multiplexing one of the 96 channels. At the end

of the TH, a clear (CLR) signal is send to the Gassiplex card to reset the memory. During the time the electronics is busy, new triggers are blocked, producing a dead time of around 1 ms per event. A VME CAEN controller mod. V2718 is used to communicate with the data acquisition program of the DAQ-PC via fiber optic, doing input/output operations and sending the detector data for storage.

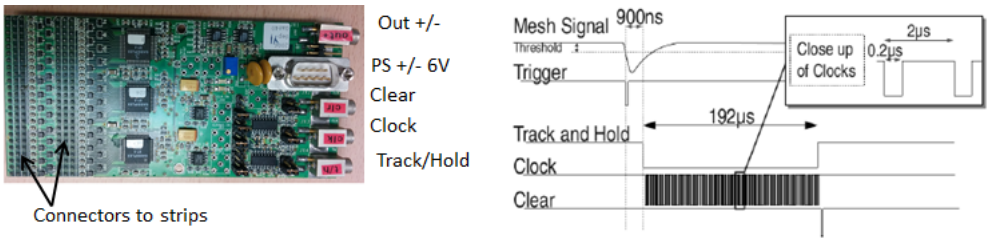

Figure 5.11: The Gassiplex card (left) and the relevant signals for the acquisition of Gassiplex data.

- **AFTER electronics:** the main component of this readout electronics is the 72-channel AFTER (ASIC For TPC Electronics Readout) chip. It is a modular and versatile electronics with several adjustable parameters, like the sampling frequency, shaping time, input capacity (gain) or test mode. In CAST-MM detectors, a transition card is used to distribute the strip signals from the physical channels printed on the detector (Gassiplex-like or SAMTEC connectors) to four ERNI-ERNI flexible cables, which are connected to the Front-End Card (FEC). The FEC comprises four of these chips, enabling to read 288 channels with a single board (figure 5.12). CAST-MM detectors have 106-120 strips per axis, so a single FEC is enough to read whole detector. Each channel of the AFTER chip collects, amplifies, shapes and samples the detector signal continuously at 100 MHz (minimum adjustable value) in 511 samples per channel, recording a window of $\sim$5 μs, which is longer than the maximum pulse duration, determined by the maximum drift time of charges created in the active volume of the detector. The sampling is stopped when the external trigger is received. Then, the analog data from all 72 channels is multiplexed into a single analog output and sent to an external ADC converter for digitization. The main components of a single channel of the AFTER chip are shown in figure 5.12: a Charge Sensitive Amplifier (CSA), a pole zero cancellation, a Sallen-Key low-pass filter and the sampling module, a Switched Capacitor Array (SCA). Finally, a pure digital electronics card, the FEMINOS [193], gathers ADC data, performs the pedestal subtraction and sends the active channels' data to the DAQ system by means of a standard ethernet connection.

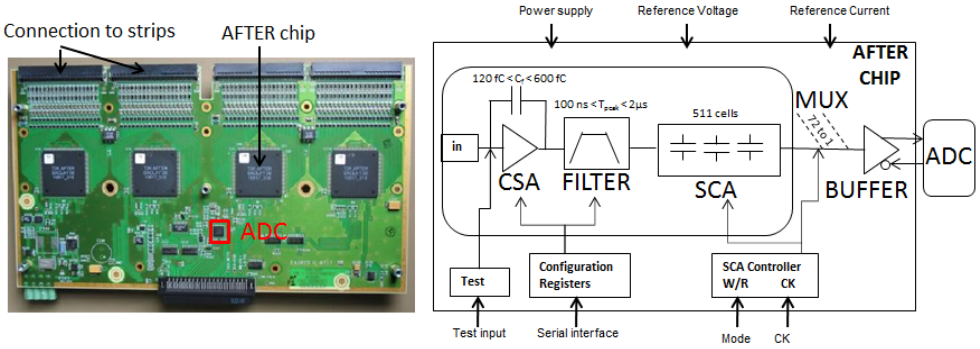

Figure 5.12: Front-End Card (FEC) with four AFTER chips (left) and schematics of its electronics' components (right).

Special attention has been paid to grounding in the electronics design: signal paths are sur-

rounded by a ground layer both at the detector, the interface card and the flat cables to avoid any coupling; the AFTER-based cards and the preamplifier are fixed to the inner part of a Faraday cage to minimize induced noises.

The data acquisition software of the Gassiplex electronics is based on a Labview program developed for the first SRMM of CAST. Input/output instructions are sent to the VME modules through the controller and the back-plane bus of the VME crate. Both mesh and strips data are gathered from the VME modules described before. However, the acquisition of the AFTER data (i.e., the strips data) is based on the software developed at CEA/Saclay, while the mesh pulse, other input/output operations and graphical user interface are developed in a C++ code.

5.6 The CAST x-ray beam facility

An x-ray beam facility was built in the Max-Planck-Institut für extraterrestrische Physik (MPE) and installed in the CAST detectors' laboratory at CERN (figure 5.13). The purpose of this line is to be able to calibrate x-ray detectors at several energies, aiming to: a) better characterize the dependence of the x-ray signals with the energy, which can translate in a better background suppression; b) determine more precisely the efficiency of the rejection algorithms for the whole CAST energy RoI; c) study the general performance of detectors, like the energy threshold with low energy x-rays or the linearity.

The x-ray generator is comprised by a electron gun (a heated filament in vacuum) that produces free electrons, which are accelerated with a high electric field towards a target, producing x-rays with the energy characteristic of the target material transition lines. These x-rays travel through the vacuum system towards the detector. X-ray filters can also be applied to absorb breemstrahlung radiation or x-rays with non-relevant energy.

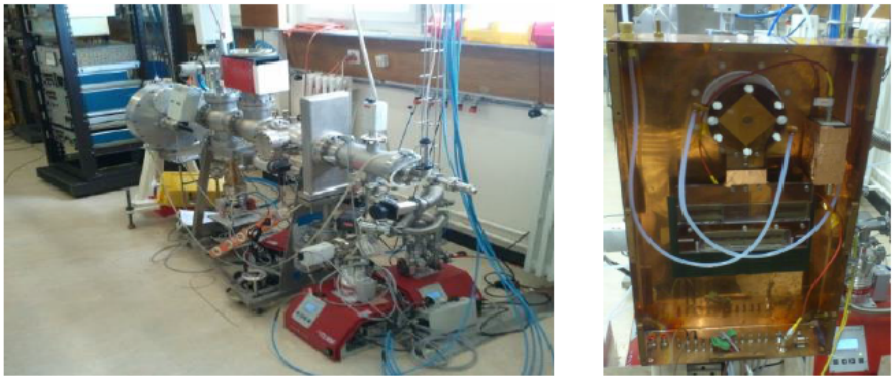

Figure 5.13: The x-ray beam line in the CAST Detectors' laboratory (left) and Micromegas detector coupled to the line (right).

Chapter 6

Data analysis and background discrimination

Contents

6.1 Introduction

Energy depositions in the Micromegas TPC are recorded by the data acquisition system. The recorded information includes the *mesh pulse* and the charge induced in every strip, the integrated charge in Gassiplex electronics and a set of pulses with AFTER electronics.

The *mesh pulse* provides information about the energy and temporal evolution of the event, i.e., the rate at which charges arrive to the amplification gap. On the other hand, the highly patterned Micromegas readout provides the topological information of the physical event along with energy measurement. In AFTER-based electronics the strips signals also provide the temporal information.

The final purpose of the data analysis is to discriminate between x-rays (axion signature) and any other type of event. In a first step, the data analysis extracts the physical information of the event from the raw data, each event being parameterized by a set of physical observables. ^{55}Fe calibrations are performed regularly in order to define the properties of x-ray events. The selection of the ^{55}Fe source is motivated by the fact that its main emission line is at 5.9 keV, i.e., within the energy range of interest (RoI) of the expected axion signal, defined as (2−7) keV. The rest of the time the detectors are measuring background data. The calibration runs are used in the second data analysis step, in which the x-ray parameters or their combination are used to elaborate discrimination criteria and suppress the backgrounds.

6.2 Raw data analysis

Here, we describe the *pulse shape analysis* and *cluster analysis* applied to the mesh and strips signals respectively.

6.2.1 Mesh pulse analysis

The mesh pulse is recorded by the Matacq board at 1 GHz frequency in 2500 samples, i.e., a total of 2.5 μs per event. Figures 6.1 shows the pulse shape parameterization of a random x-ray signal.

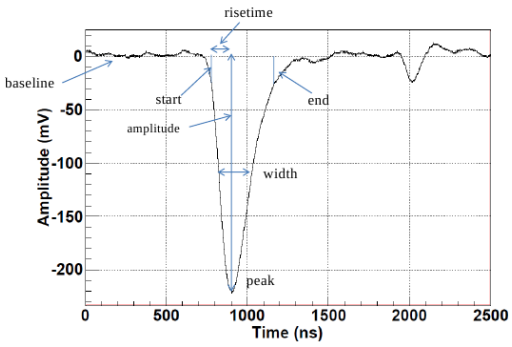

Figure 6.1: Parameters of a mesh pulse.

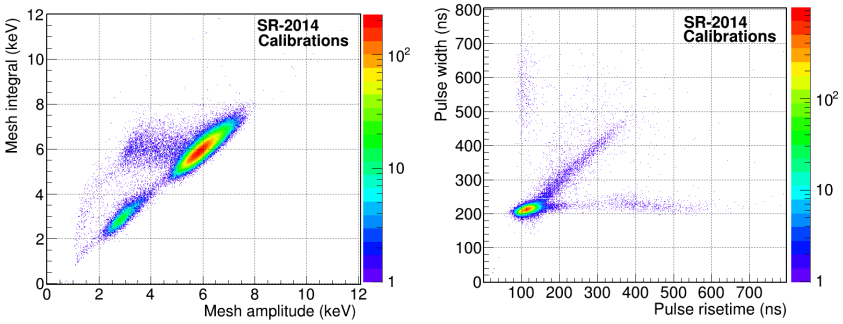

Figure 6.2: Energy determination with the amplitude and integral of the mesh pulse (left) and distribution of the pulse shape parameters (right) of SRMM-2014 x-ray calibrations.

Before finding the parameters of the event, the pulse is smoothed by means of a FFT (Fast Fourier Transformation) which allows to remove high frequency pulse shape fluctuations usually related with noise fluctuations. This pulse preprocessing leads to a more accurate definition of the pulse shape characteristics. The energy of the event is proportional to the *pulse amplitude* and *pulse integral*. The temporal information is mainly described by the *risetime* and *width* parameters. The definition of the main parameters is given here:

1. **Baseline:** mean value of the mesh voltage when no signal is induced in the electrode. It is determined from the first 200 samples of the recorded mesh pulse.
2. **Baseline fluctuation:** the standard deviation of the baseline level.
3. **Peaking time:** time at which the pulse reaches its maximum absolute value.
4. **Pulse amplitude:** the pulse height at the peaking time after subtracting the baseline level.

5. **Pulse integral:** the pulse area between the starting and ending pulse times, i.e., the times at which the pulse reaches the N% of the pulse amplitude at the both sides of the peaking time. The value of N can be set to 5-15% depending on noise fluctuations.
6. **Pulse time length:** the time between the starting and ending pulse times.
7. **Pulse risetime:** the time between the starting pulse time and the time at which the pulse reaches (100-N)% of its absolute amplitude.
8. **Pulse width:** the time between the points at 50% of the pulse amplitude.

Figure 6.2 shows the correlation between the energy determined by the *pulse amplitude* and the *pulse integral*, as well as the main pulse shape parameters of x-ray calibration events. In the figure, those events outside the linear range or beyond the high intensity region correspond to pile-up pulses or background events that also occur during calibration runs. The pulse shape parameters or their combination is used in the definition of the background discrimination criteria.

6.2.2 Cluster analysis

Since x-rays produce point-like electron clouds, the strips signals are used to find localized charge depositions or *charge clusters*. The goal of the cluster analysis is to reduce the information of the strips signals to a set of descriptive parameters. Figure 6.3 shows the strips signals for random calibration and background events in Gassiplex electronics (top) and AFTER electronics (bottom).

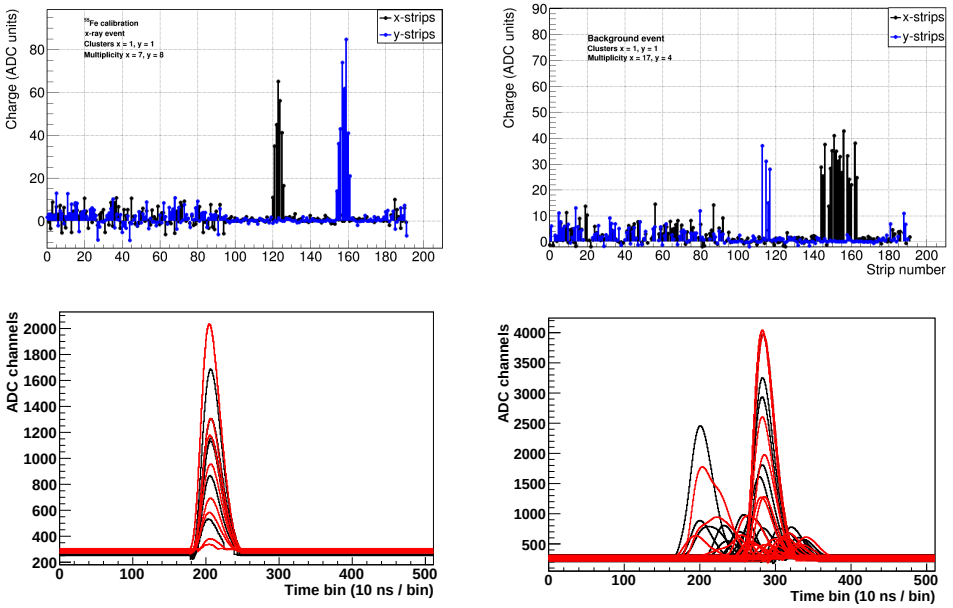

Figure 6.3: Calibration (left) and background (right) events as recorded by the Gassiplex electronics after pedestal subtraction. Note that the channels between roughly 0-90 and 180-192 are not instrumented, being larger the noise fluctuations.

The noise level or pedestal value p_i of each strip i is defined from background runs or specific pedestal runs, where the standard deviation of each pedestal value σ_{p_i} is also calculated. The pedestal values are subtracted to the integrated charge measured by each strip $\bar{c_i}$, defining the actual level of the strip $c_i = \bar{c_i} - p_i$. In Gassiplex electronics, the active strips are those which satisfy $c_i > N\sigma_{p_i}$, where N usually ranges from 2 to 5. In AFTER-based electronics the same applies with the singularity that it is not the user who must implement the criterion in the off-line analysis, but it is the front-end electronics who internally does it. This is an important feature of AFTER electronics as it implies a significant data reduction.

The active strips are used to perform the *cluster analysis* independently for x and y axes. A *charge cluster* is defined as a set of consecutive active strips larger than 2 and lower than 30. In order to handle with dead or non-electronically instrumented strips, there can be up to two consecutive non-active strips inside a cluster. If the AFTER electronics are used, the *cluster analysis* can be extended to the temporal axis since the strip pulses provide information about the relative z-position of the event. The *peaking times* t_i of consecutive strip pulses are used to define an equivalent *cluster condition* in the z-direction: the strip $i+1$ belongs to the same cluster than the strip i if $(t_{i+1} - t_i) \leq \Delta$ is satisfied, where Δ is a user-defined time constant.

The number of clusters and their properties (energy, position, shape) characterize each event. X-ray events typically produce single clusters in each direction since they are absorbed by photoelectric effect. In argon-based mixtures the absorption is followed in roughly 85% of the cases by Auger electrons, resulting in a single ionization cloud. In the rest of the cases the photoelectron emission is followed by a secondary photon which can escape from the active volume (forming the characteristic escape peak in the energy spectrum) or it can be re-absorbed inside the active volume. In the last case and in pile-up events, more than one cluster are produced.

Figure 6.4 shows the number of clusters in the xy plane in a CAST-MM detector during ^{55}Fe calibrations and background runs. Note that during calibration, background events also occur, resulting in higher cluster numbers. In the analysis, we define an x-ray as a mono-cluster event or alternatively, as an event in which the dominant cluster carries at least 85% of the total energy. This criterion reduces the signal efficiency very slighly but it is a very good discriminant, as the figure shows.

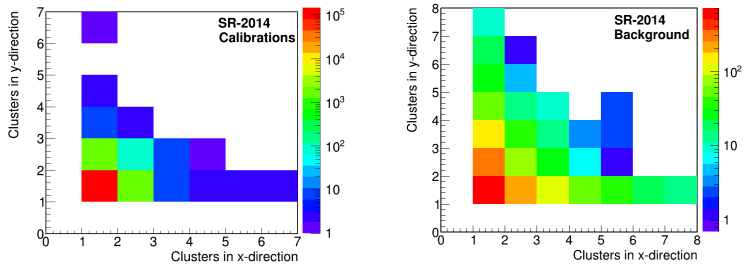

Figure 6.4: Number of clusters in the xy plane in a CAST-MM detector during ^{55}Fe calibrations (left) and during background runs (right).

The parameters that define the dominant cluster of each event in the x, y and z directions are described in the following list:

1. **Cluster amplitude,** $a = \sum_i a_i$: Addition of the pulse amplitude of each strip inside the cluster. Provides the energy of the event.
2. **Cluster integral,** $c = \sum_i c_i$: Addition of the pulse integral of each strip inside the cluster. Provides the energy of the event.
3. **Cluster position,** $\mu_{xy} = 1/a \cdot \sum_i i a_i$, and $\mu_z = 1/a \cdot \sum_i t_i a_i$: The mean position of the event calculated as the charge amplitude of each strip weighted by the strip number (xy-axes). or the peaking time (z-axis).
4. **Cluster multiplicity:** Number of active strips inside a cluster.
5. **Cluster size/sigma,** $\sigma^2_{xy} = 1/a \cdot \sum_i a_i (i-\mu)^2$, and $\sigma^2_z = 1/a \cdot \sum_i a_i (t_i - \mu_z)^2$: The variance of the charge distribution inside a charge cluster. It measures of the the cluster width.
6. **Cluster skew,** $\gamma_{xy} = 1/a \cdot \sum_i a_i \left(\frac{i-\mu}{\sigma}\right)^3$, and $\gamma_z = 1/a \cdot \sum_i a_i \left(\frac{t_i-\mu}{\sigma}\right)^3$: The third standardized moment of the charge distribution inside a cluster. It measures the asymmetry of the cluster.
7. **Time length:** number of active time bins n inside a cluster. Time bins containing overlapping pulses in the time domain are only considered once.

8. **Position** $z_{x,y}$, $z = 1/c \cdot \sum_i \sum_n c_{ni} n$: mean temporal position of the k pulses belonging to the x- or y-cluster. It is calculated as the charge integral of each time bin in the i-pulse weighted by the temporal bin number n.

Note that if Gassiplex electronics are used, some of the cluster parameters can only be calculated for the spatial coordinates (x and y directions) and, particularly, the last two parameters (*time length* and *position* $z_{x,y}$) cannot be calculated as there is no information of the temporal evolution of the strip signals.

The 3D reconstruction of an event is made combining the strip pulses, whose temporal position determines the z position, and the detector decoding, used for the spatial coordinates, x and y. The charge collection of each event is projected in both spatial and temporal direction. As an example, the resulting xz and yz projections of a background and a calibration event are shown in figure 6.5. Note that the x-ray event is a point-like, symmetric energy deposition, while the background event presents an extended track with a δ-ray around the center and a small blob at the end.

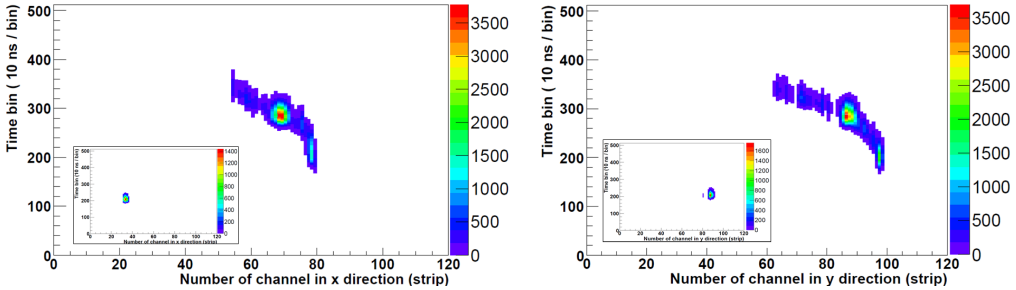

Figure 6.5: Projection of a background event in the xz *(left) and* yz*-plane (right). The insets show the same projections for a calibration event.*

Since x-ray events are symmetric roughly the same charge is expected to be collected in both spatial directions. Equivalently, the same energy is expected to be collected by the strips and mesh signals. An example of these dependencies is shown in figure 6.6. A quick cross-check of the detector performance, such as event correlation between strips and mesh pulse, can be derived from the above argument. The relation between the aforementioned observables can be used as well to define discrimination criteria.

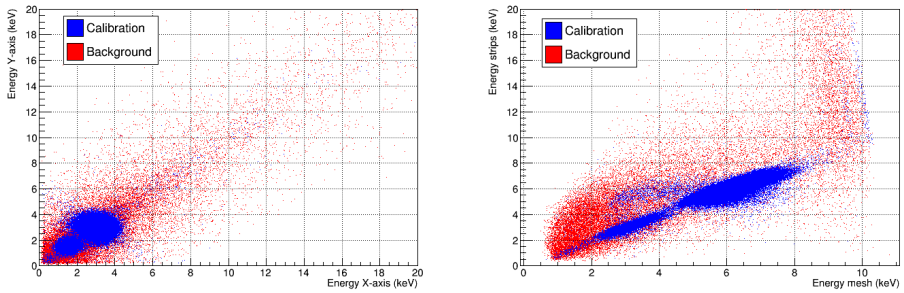

Figure 6.6: Comparison between calibration and background observables.

6.2.3 Energy determination and correction of gain fluctuations

Micromegas detectors are regularly calibrated with a ^{55}Fe source, emitting x-rays mainly at 5.9 keV. The knowledge of the peak energy allows to calculate the conversion factor (or *detector gain*) from

the digital units as readout from the electronics to energy in keV units. The *gain* determination is fundamental to get access to the energy of background events. Several factors can produce a change in the *detector gain*, such as fluctuations in the detector pressure or temperature, variations in the mesh voltage and others. This makes necessary the periodic calibration of the detectors and the monitoring of the *detector gain*.

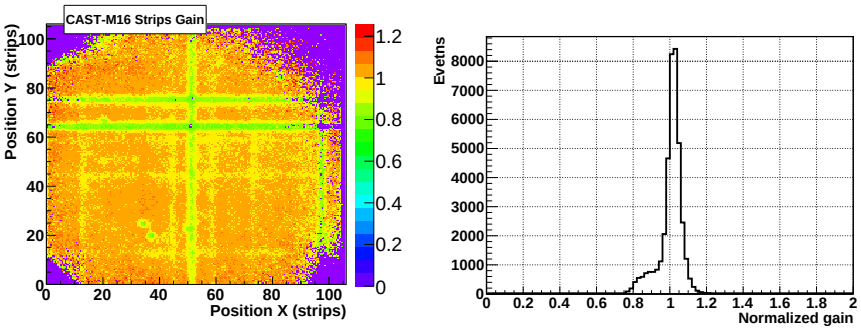

Figure 6.7: Gain distribution in the detector surface (left) and relative gain (right).

Besides the temporal gain variations, there are also fluctuations of the gain within the detector surface. Figure 6.7 (left) shows the gain distribution over the detector surface. The detector shows a uniform gain with fluctuations bellow 10%. However, there are three strips (one in x-direction, two in y-direction) not electronically instrumented. The clusters whose mean position lays in these strips show gains up to roughly 30% lower. The right of figure 6.7 shows the distribution of the normalized gains: a narrow distribution around 1 is accompanied by a bump at lower gains, corresponding to the dead regions of the detector. It must be noted, however, that the presence of dead strips does not entail a loss of efficiency since the multiplicity of even the smallest event is always larger than 2.

The gain maps are used to re-calibrate the detector energies. Figure 6.8 shows the application of this correction in the relation between the energy as calculated with the mesh pulse amplitude and the strips energy in ^{55}Fe calibration. In the corrected plot, the accumulation of events at non-linear energies has been reduced significantly. Similarly, figure 6.9 shows the energy spectra before and after the gain surface correction. The energy resolution is slightly improved, allowing better energy determination of the background events.

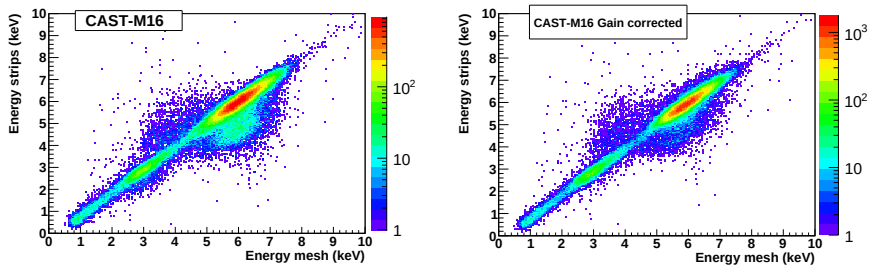

Figure 6.8: Relation between the energy as measured by the strips and the mesh before (left) and after (right) the correction of gain fluctuations in the detector surface.

6.2.4 Distribution of x-ray observables

In this section, we show the distribution of several of the cluster parameters described before. These parameters are used to characterize the x-ray events acquired during ^{55}Fe calibrations and

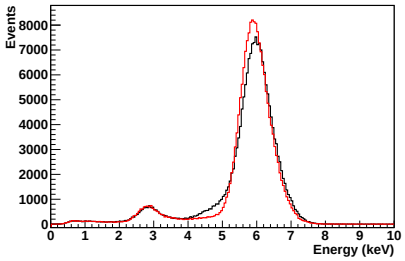

Figure 6.9: Energy spectra of the ^{55}Fe calibrations before (black) and after (red) the gain correction.

discriminate between x-ray events and any other source of signals. Figure 6.10 shows a comparison between x-ray and background parameters, from top to bottom: a) *time length* of the pulses generated in the strips of both spatial coordinates, b) multiplicity in both spatial coordinates, c) *position* $z_{x,y}$ and d) *cluster size* in the spatial coordinates.

The detector observables depend on the x-ray energy and in the absolute z position of the event. Both dependencies are correlated since the mean free path of x-rays in gas depends on its energy (see figure 1.3). In section 7.3 the energy dependence is analyzed in the light of detector characterization with different discrete x-ray energies. However, in next section we illustrate the z dependence with some examples.

6.2.5 Observables dependence on the z-position

The absolute z-coordinate of the event determines the amount of longitudinal and transversal diffusion of the primary electron cloud. For a given x-ray energy (and the associate primary electrons), events occurring close to the cathode present larger cluster size than those occurring close to the amplification gap, resulting in a dependence of the observable parameters with the interaction point along the z-axis.

In CAST-MM background events are discriminated from reference ^{55}Fe calibration data sets performed from the detector x-ray window side. The interaction position along the z-axis is not uniformly distributed (see figure 1.4) but its mean value is at around 1 cm from the detector window (the drift distance is 3 cm), slightly biasing the observables distribution. This dependence could introduce an undesired *fiducial cut* in the z-coordinate since x-rays close to the amplification gap have less weight in the construction of the discrimination criteria.

It is not possible to directly measure the absolute z position in a *ionization-only* TPC like the CAST-MM detector. However, we have indirectly measured the absolute z position using the time difference between the signal in the muon veto (see section 5.4) and the delayed Micromegas trigger. This time distribution is shown in figure 6.11, where the muon-induced events are clearly identified in a narrow window of approximately 40 clock cycles of 25 ns each (in the range 25−65 cycles). This time difference is related to the absolute z-position through the drift velocity of the primary electrons. Indeed, this window gives a measurement of the drift velocity of the electrons: the maximum time the electrons take in drifting the 3 cm of the TPC is 40×25 ns $= 1$ μs, which gives an estimation of 3 cm/μs, in good agreement with the theoretical estimations for this gas mixture at the nominal operation drift field of 100-200 V/cm (see figure 1.10).

In figure 6.11, the black line represents the raw background events and the red line represents those events that survived to the discrimination criteria, i.e., they are x-ray events or produce a very similar pattern in the detector. These x-ray like events are used to study the dependence of the cluster size observables with its absolute z-position. The dependence of the cluster size in both spatial coordinates and the mesh pulse risetime is shown in figure 6.12. The results clearly indicate that the cluster size increases with the drifted distance. The inversion of this argument would allow to estimate the absolute z position of x-ray events from the cluster size.

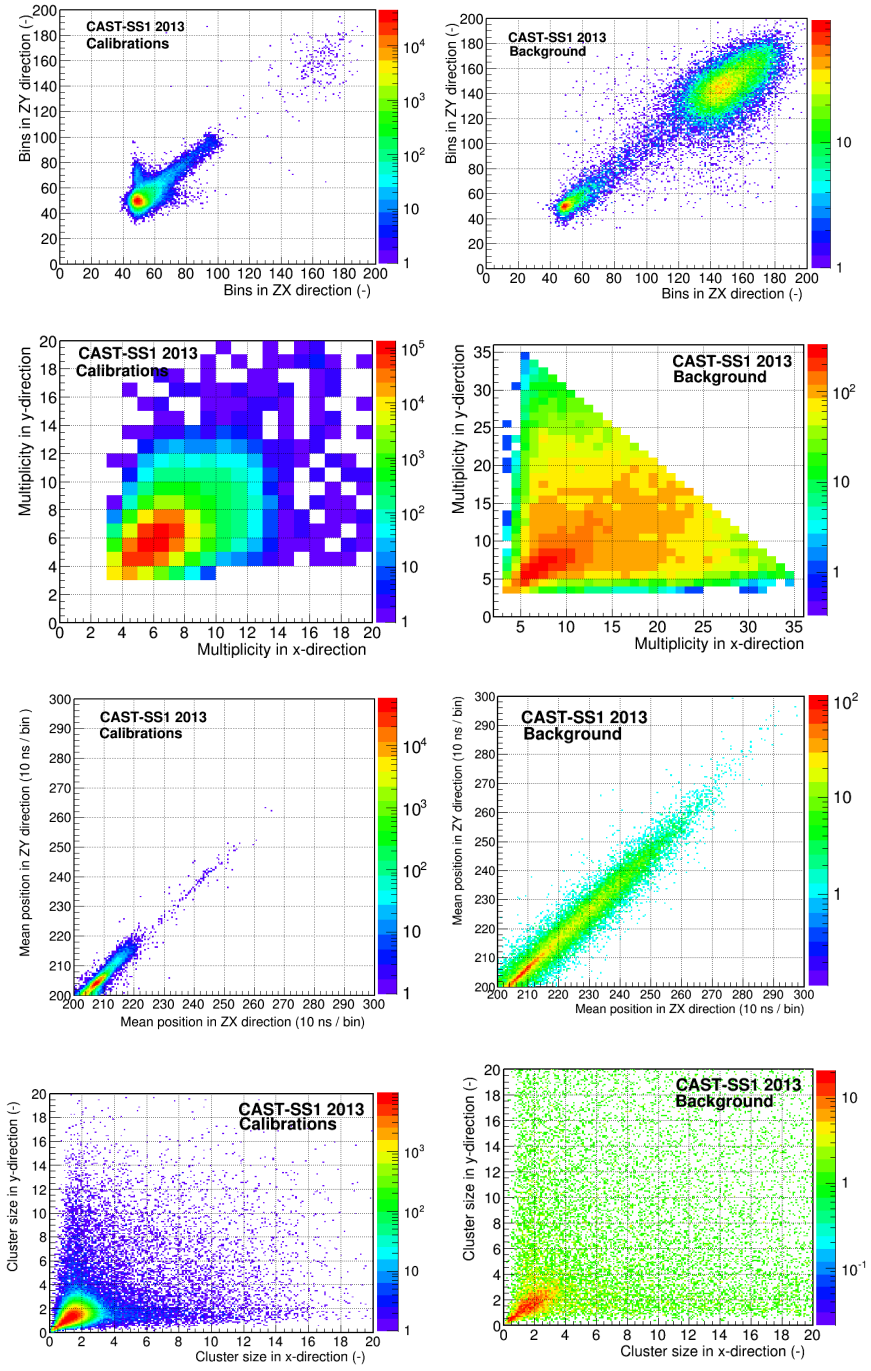

Figure 6.10: Comparison between calibration (left) and background (right) observables.

6.3 Background discrimination

The background discrimination process consists in a statistical treatment of the observables generated by the ^{55}Fe calibration x-rays with the aim of generating the selection criteria to accept or reject background events. The selection criteria must minimize the number of accepted background

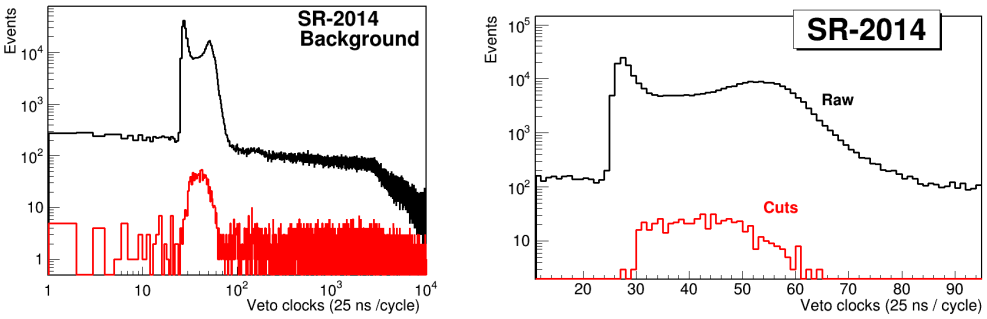

Figure 6.11: Time difference between the signal in the muon veto and the delayed Micromegas trigger. The black line is raw background events, while the red represents the events that survived the discrimination criteria.

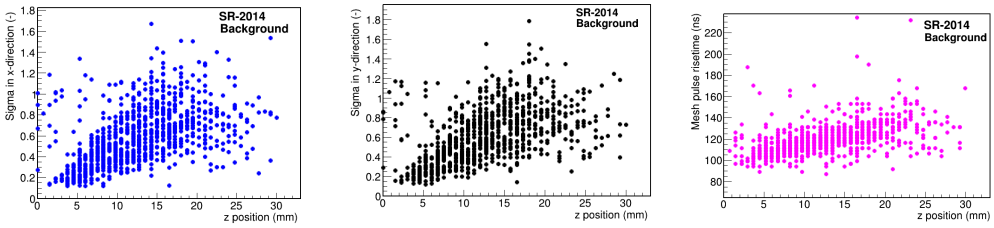

Figure 6.12: Dependence of the cluster size in the x and y directions with the absolute z position. The explanation of the z position calculation is given in the text.

events, while keeping the *signal efficiency* as high as possible, i.e., maximizing the number of accepted calibration events. In this section we describe the discrimination methods applied along with the studies to optimize the *figure of merit* of the detector.

6.3.1 Definition of discriminants

The raw data analysis described in the previous section allows to define a set of *discriminants* that are finally used in the construction of the selection criteria. These discriminants must reveal the differences between x-ray and background events. Since normally detectors are only calibrated at 5.9 keV (and 3.9 keV from the escape peak), it is desirable that the *discriminants* are as less energy dependent as possible. In some discrimination methods, Gaussian shaped *discriminants* are preferred since they involve fits to the observables distribution.

Prior to the application of the statistical discrimination method, some **quality cuts** or manual cuts are implemented to reject events that are certainly not x-rays, obtaining thus the first data reduction: events must have one and only one cluster per direction, and the *multiplicity* of each cluster must be larger than 2 and lower than 30. Besides, a **fiducial cut** rejects any event whose mean position is beyond the projection of the cold-bore area, where all the axion signal is expected. This cut defines an acceptance circumference of 2.15 cm radius (14.5 cm^2) around the center of the detector, reducing the detector border effects.

In the following list the most representative *discriminants* for the x-ray selection and background discrimination are shown:

1. **Mesh:** *discriminants* based on the mesh pulse characteristics.

   - **Risetime, t_r:** x-rays are point-like energy depositions that usually produce the lowest risetime values among all the sources of ionization processes. This fact is due to the

brief time difference between the arrival of the electron cloud charges. Its value depends on the absolute z-position and the shaping time of the electronics.

- **Width, t_w:** similarly to the risetime, x-rays produce the lowest width values, which also depend on the absolute z-position and the shaping time of the electronics.
- **Ratio t_r/t_w:** relation between the mesh pulse risetime and width (see figure 6.1). The values are concentrated in a very small region of the parameter space.
- **Pulse length, t_l:** total duration of the mesh pulse. X-rays show the lowest t_l values.
- **Amplitude-Integral energy balance, $\frac{E_a-E_i}{E_a+E_i}$:** correlation between the energy measured by the mesh pulse amplitude and integral. The expected x-ray distribution is Gaussian-shaped with mean value zero.

2. **Strips:** *discriminants* based on the *cluster* size and shape.

   - **Single cluster condition:** x-rays usually have one and only one cluster per axis (see figure 6.4).
   - **xy energy balance $\frac{c_x-c_y}{c_x+c_y}$:** deviation between the energy measured by the x and y strips. The expected x-ray distribution is Gaussian-shaped with mean value zero, since the electron cloud is symmetric and the readout pattern favors the equal distribution of charge in both directions.
   - **Amplitude-Integral energy balance, $\frac{C_a-C_i}{C_a+C_i}$:** correlation between the energy measured by the strips pulse amplitude and integral. The expected x-ray distribution is Gaussian-shaped with mean value zero.
   - **Time length in $zx-zy$ axes:** total duration of the pulses induced in the x and y-strips respectively. Equivalently to the mesh *pulse length*, x-rays usually present the lowest values (see figure 6.10).
   - **Mean position in $zx-zy$ axes:** mean position of the pulses induced in the x and y-strips respectively. (see figure 6.10). Although the distribution is linear in both for background and x-ray events, the last are condensed in a small region of the parameter space.
   - **Size, σ_x, σ_y, σ_z:** cluster size calculated as the variance of the charge distribution in each axis. X-rays are the smaller type of events (see figure 6.10).
   - **Size balance, $\frac{\sigma_x-\sigma_y}{\sigma_x+\sigma_y}$:** deviation between the size in the x and y-directions. The expected x-ray distribution is Gaussian-shaped with mean value zero, since the electron cloud is symmetric and the readout pattern favors the equal distribution of charge in both directions.
   - **Multiplicity, m_x, m_y, m_z:** number of active strips inside the cluster in each detector axis, including the *virtual strips* in the temporal direction, as described in section 6.2.2.
   - **Skewness, γ_x, γ_y, γ_z:** asymmetry of the cluster in each axis. The expected mean value of x-ray distribution is zero.

3. **Mesh & Strips:** *discriminant* based on the correlation between mesh and strips signals.

   - **Strips-Mesh energy balance, $\frac{E_i-C_i}{E_i+C_i}$:** correlation between the energy measured by the mesh *pulse integral* and the strips *pulses integral*. Expected x-ray distribution is Gaussian-shaped centered in zero.

4. **Veto:** *discriminant* based on muon tagging capability of the plastic scintillator.

   - **Mesh-scintillator difference, δ:** time elapsed between the signal in the plastic scintillator and the delayed Micromegas trigger. Events within the *muon windows* (see figure 6.11) are rejected.

The discrimination criteria are based in a subset of the *discriminants* listed above or in any combination of them (e. g. total cluster size $\sigma_x \cdot \sigma_y$), which are selected to maximize the rejection power at a given x-ray acceptance or *signal efficiency*.

6.3.2 Discrimination methods

The *discriminants* defined above are used to statistically select x-rays and reject the events caused by natural background sources. The distribution of the calibration *discriminants* defines a volume in the parameter space where x-rays are most likely to be found. This volume must procure the maximization of the energy dependent detector's *figure of merit*, $\mathcal{F}_D$

$$\mathcal{F}_D = \Phi_a \cdot \varepsilon / \sqrt{b} \tag{6.1}$$

where b is the detector background level, Φ_a is the axion flux and ε is the total efficiency, i.e., the convolution of the detector quantum efficiency ε_q, optics efficiency ε_o and the signal efficiency ε_s, which is the efficiency with which x-rays are accepted or recognized. Therefore, the selection volume must be large enough to accept as many x-rays as possible, enlarging ε_s, but not too large, so that the ratio is maximized.

Although the discriminants are selected to be as less energy dependent as possible, two selection volumes are usually defined: one with the main 6 keV peak, the other with the escape 3 keV peak. This division of the energy range requires large calibration statistics, as the escape peak is only composed by roughly 5% of the total number of events. The two selection volumes are used to discriminate background events with energies below and above 4.5 keV respectively. One can also build a single acceptance volume with both 6 and 3 keV events and weighting the last ones by a factor ∼20 so that they become statistically significant. Alternatively, if only the main population of events at 6 keV is used, a continuous energy dependent selection volume must be defined if one wants to avoid a drop in ε_s at low energies.

The discrimination methods used in this thesis work are described here:

Sequential cuts analysis: the sequential analysis consists in the consecutive application of several independent selection rules. These rules are defined from the fit to the one or two-dimensional Gaussian-shaped distributions of the *discriminants*. A background event is rejected if any of its *discriminant* values is beyond an adjustable multiple of standard deviations ($n_i\sigma_i$) from the mean of the distribution. The selected n_i-value determines the signal efficiency and the rejection power of the cut. The two-dimensional rules take into account the correlation between the different discriminants.

Contour cuts analysis: the contours cuts analysis is a variation of the secuential cuts analysis. It consists in the manual selection of the contours that define the acceptance areas in the two-dimensional *discriminants* space (like the ones shown in figure 6.10). If the *discriminants* distribution changes in time, the contours do not contain the most representative population of x-rays, so new contours must be defined. The signal efficiency can only be approximately imposed at a certain value, contrarily to the rest of the discrimination methods which can very accurately do it.

Likelihood analysis: in the likelihood analysis the fit to the Gaussian observables are combined to define a single probability distribution function instead of a multiple number of selection rules to be applied sequentially. Each calibration event is defined by a single quantity q that merges the information of the N *discriminants* as:

$$q = \sum_i^N \frac{x_i - \mu_i}{\sigma_i} \tag{6.2}$$

The q-values of all the calibration events define the probability distribution function or q-distribution. The signal efficiency is imposed at a certain value, unequivocally determining a single limit value q_L of the distribution function which sets the border between accepted and rejected events: bellow q_L events are accepted, above it events are rejected. The q-value of each background event is calculated equivalently and they are rejected when $q > q_L$. An example of the probability distribution functions is shown on the left of figure 8.21, while the application of the selection rule to the calibration data is shown on the right.

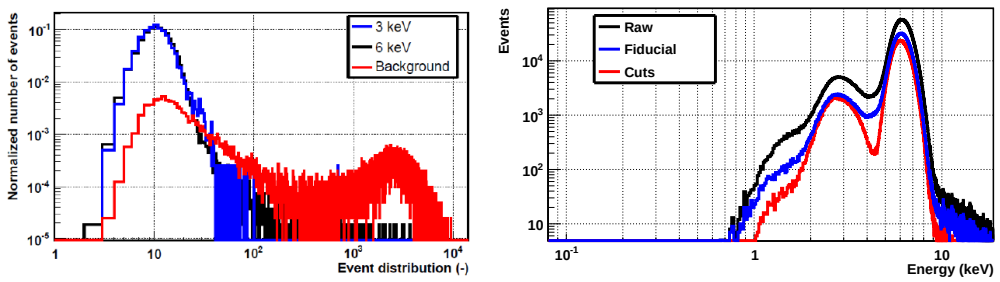

Figure 6.13: Probability distribution functions of the calibration and background events (left) and calibration energy spectrum before and after the application of the discrimination criteria with a signal efficiency imposed at a constant value of 0.80 (right).

Mutivariate analysis: the multivariate analysis method was introduced in CAST by K. Kousouris and was further developed by J. Galan [194], where a detailed description of the theory underlying the discrimination method is done. In a nutshell, the multivariate analysis calculates a quantity, denominated q, for each calibration event, which contains the weighted standard deviation of each discriminant and the correlations between them:

$$q = X^T \rho^{-1} X \tag{6.3}$$

where $X_i = (x_i - \mu_i)/\sigma_i$ is the distance of a Gaussian parameter to the mean of the distribution in standard deviation units, and ρ is the correlation matrix. The calibration data defines a volume around zero in the N-dimensional space. The quantity q plays the same role than in the previous method: it measures the distance from the event coordinates X_i to the origin in this N-dimensional space. Similarly, the required signal efficiency fixes the q_L value that sets the border between accepted and rejected events.

6.3.3 Optimization of the discriminants

The multivariate analysis method is used to systematically study the effect on background of all the possible $\binom{N}{m}$ combinations of the N *discriminants* taken in subsets of m. A CAST-MM detector instrumented with AFTER electronics is used and the signal efficiency ε_s is imposed at 0.75 in all cases.

The results are summarized in figure 6.14, where the background level for the best, worst and average combination of *discriminants* is shown as a function of m. It is observed that the worst background levels are achieved with a low number of discriminant parameters. In this case, the appropriate election of the discrimination parameters is critical, resulting in background level differences as high as a factor ~ 10. The difference in rejection power between the worst and best combination decreases at high m-values, and the background level differences above 16 *discriminants* is below a factor ~ 5. It is remarkable that above 14 *discriminants*, the background level achieved with the best combination starts a slight increase. This effect is due to the fact that the addition of new observables introduces redundant information, allowing larger deviations in non-redundant observables. This phenomenon is known as *statistical noise* or *redundancy*.

Generally speaking, the minimum set of *discriminants* that an efficient analysis must include are: a) a signature of the size and symmetry of the charge cluster, such as σ_x, σ_y or the *multiplicity* and the xy energy balance; b) a signature of the temporal evolution of the event inside the TPC, as the mesh pulse *risetime*, *width*, or the strips *time length*; c) a signature to identify complex structure in the temporal dimension, like the *risetime-width* ratio, σ_z or the *amplitude* versus *integral* energy determination.

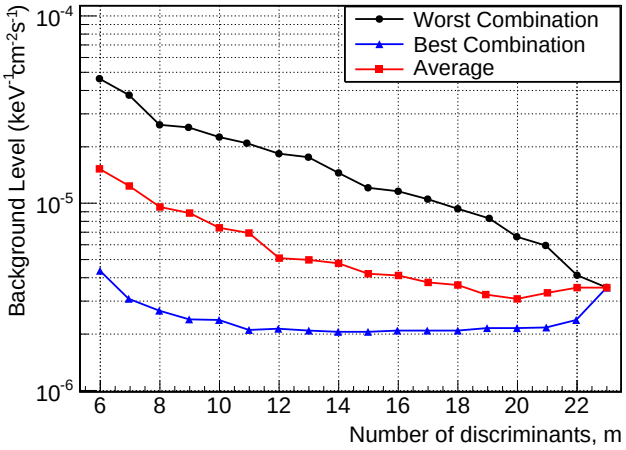

Figure 6.14: Background level as a function of the number of discriminants, m, for the best, worst and average combination.

6.3.4 Maximization of the figure of merit

The maximization of the detector discovery potential or *figure of merit*, $\mathcal{F}_\mathcal{D}$, defined in equation 6.1 is critical for the sensibility of an axion helioscope. Figure 6.15 shows the ratio $\varepsilon_s/\sqrt{b}$ in the CAST energy RoI for several CAST-MM detectors. In the last expression ε_s is the energy dependent signal efficiency and b is the background level. Both the background level and the signal efficiency are discretized in 1 keV bins. The signal efficiency is discretized from the calibration data at several x-ray energies performed in the CAST x-ray beam (see section 5.6). These calibrations allow to compute the acceptance of the discrimination method for x-rays of different energy.

The $\varepsilon_s/\sqrt{b}$ ratio contains information about the discrimination power of a detector. The two upper plots show the characteristic trend of good performing detectors: the ratio increases with the escape peak efficiency since the signal-to-noise ratio is large enough, allowing to increase the size of the selection volume without accepting too many background events. On the contrary, the lower plots show the trend characteristic of detectors with low signal-to-noise ratio: many background events are accepted when the efficiency to low-energy x-rays is increased. The appropriate election of ε_s results in increase of the $\varepsilon_s/\sqrt{b}$ ratio by a factor $1.2 - 2$, depending on the detector.

Increasing the signal efficiency at low energies has an effect on the background energy spectrum. Figure 6.16 shows this effect for two detectors with opposite trend. In the detector with low signal-to-noise ratio (SS2-2012), an increase in $\varepsilon_s(3\text{ keV})$ leads to a dramatic rise in the low-energy region of the spectrum.

A further step consists in the maximization of the $\mathcal{F}_\mathcal{D}$ factor. The axion flux, Φ_a, the quantum efficiency of the Micromegas detector, ε_q, and the efficiency of the optics, ε_o are fixed by nature and by the experimental setup. The quantum efficiency is the product of the x-ray transmission of the cold-window (CW), differential window (*Diff. W.*) and detector window (*Det. W.*) and the absorption of these x-rays in the Micromegas TPC. This term has been computed by the *Geant4* simulation of several monochromatic x-ray emission lines ($2 \cdot 10^4$ x-rays per line) in the CAST energy RoI with 0.5 keV spacing. The convolution of these factors determines the expected x-ray axion energy spectrum detected by the Micromegas detector before the application of the discrimination criteria, which is shown in figure 6.17.

The maximization of $\mathcal{F}_\mathcal{D}$ relies on the appropriate choice of the signal efficiency, ε_s, taking into account the energy dependencies of the previous parameters. An iterative method has been developed to study the value of $\mathcal{F}_\mathcal{D}$ for several combinations of the signal efficiency at 3 and 6 keV.

As an example, figure 6.18 shows the results for the two Micromegas detectors operated in the *sunset* side of CAST in 2013. The overall $\mathcal{F}_\mathcal{D}$ factor is color-coded in the two-dimensional signal

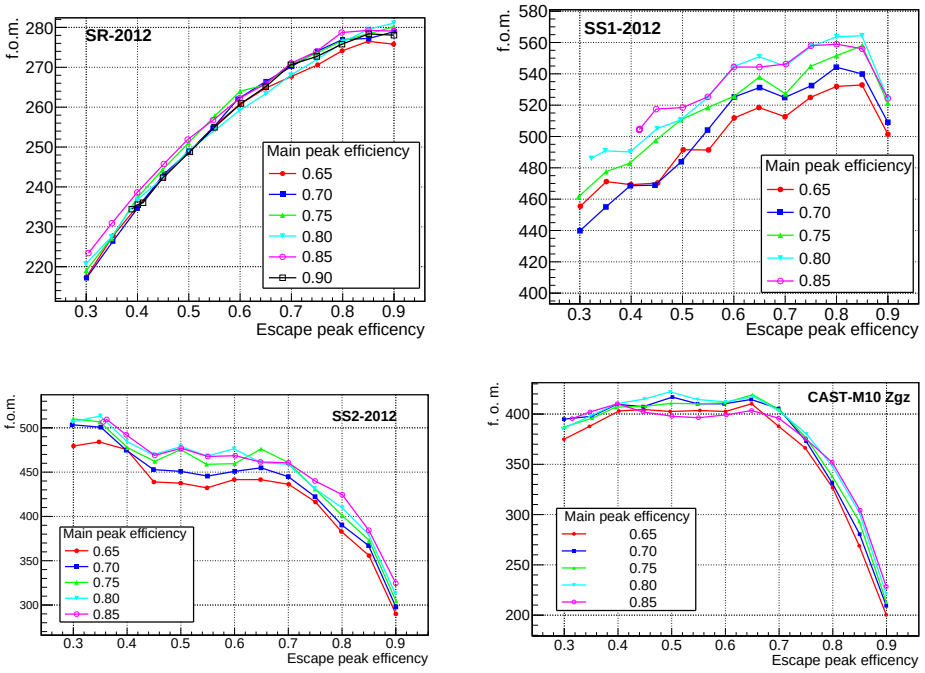

Figure 6.15: Dependence of the detector figure of merit on the signal efficiency at 3 and 6 keV for the three detectors used in CAST in 2012 (SRMM, SS1 and SS2) and for a replica (CAST-M10) operated at Zaragoza.

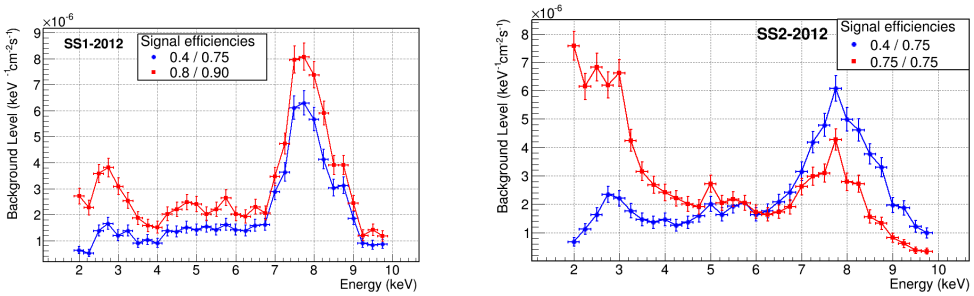

Figure 6.16: Background energy spectra for two different combinations of signal efficiencies of SS1 (left) and SS2 (right) Micromegas detectors in CAST-2012.

efficiency parameter space. In these detectors, the correct choice of the signal efficiencies enhances the detector figure of merit by a factor 5−10%.

6.4 Effects of the electronics upgrade on discrimination

In this section, the discrimination capabilities of the upgraded readout electronics (described in section 5.5) are compared. In CAST, AFTER-based electronics replaced the former Gassiplex cards for the 2013 data taking campaign. The discrimination tools and possibilities that AFTER electronics provide are discussed, and the rejection power of both electronics are compared.

Table 6.1 compares the background levels obtained with Gassiplex and AFTER electronics in two different setups. In the first one, AFTER electronics is used as readout system of a CAST spare detector (CAST-M10) in a setup at the University of Zaragoza. Meanwhile, the signals

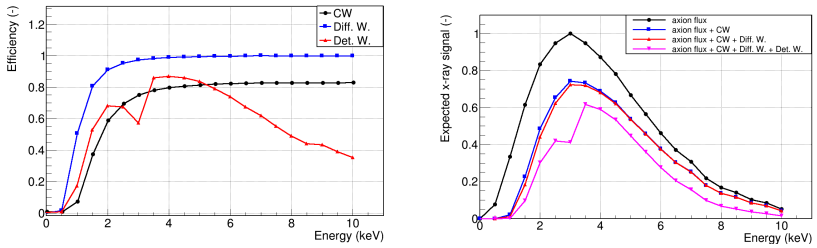

Figure 6.17: X-ray transmission of the cold-window (CW), differential window (Diff. W) and detector window (Det. W.) as a function of the photon energy (left). The absorption efficiency in the Micromegas detector is included in the last curve. Expected x-ray axion energy spectrum in a Micromegas detector prior to the application of the discrimination criteria (right).

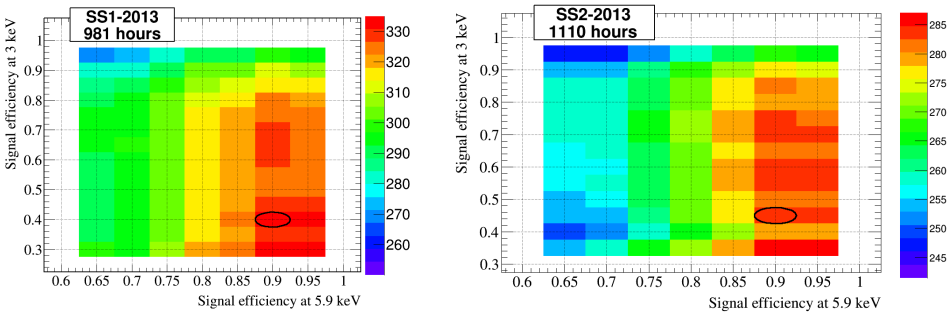

Figure 6.18: Dependence of the value (color coded) of the detector figure of merit, $\mathcal{F}_{\mathcal{D}}$, with the signal efficiency at 3 and 6 keV for CAST-SS1 and SS2 detectors of 2013.

of the Gassiplex electronics were *simulated* by reducing the temporal information of the pulses to the charge's integral. In the second setup, the comparison is established between CAST-M18 detector operated in CAST during the years 2012 and 2013, when Gassiplex and AFTER electronics were used as readout system respectively. Apart from the upgrade in the electronics, the system remains unchanged. It is worth noting that the background levels obtained with CAST-M10 are systematically higher than those obtained with CAST-M18 in equivalent shielding conditions. This is due to the better performance of CAST-M18 with respect to CAST-M10, which it is a much older detector with some strips not electronically instrumented for being short-circuited with the mesh.

Setup	**Year**	**Electronics**	**Run time** hours	**Level** ([2-7] keV) 10^{-6} keV^{-1}cm^{-2}s^{-1}
CAST-M10	2013	Gassiplex	303.1	2.07 ± 0.19
CAST-M10	2013	AFTER	303.1	1.60 ± 0.12
CAST-M18	2012	Gassiplex	2265.5	1.66 ± 0.05
CAST-M18	2013	AFTER	445.9	1.23 ± 0.10

Table 6.1: Comparison of the background levels obtained in the CAST RoI between Gassiplex and AFTER electronics for two different setups. The statistical errors expressed as 1σ.

The rejection power with AFTER-based readout electronics is higher than with former Gassiplex readout electronics: in both cases, the improvement in background level due to the electronics upgrade is quantified in a factor of about ∼25%. This fact is a consequence of the improvement in

the signal-to-noise ratio of the strips signals and the information about the primary charge distribution along the z-axis provided by the strip pulses. These improvements have major consequences. Firstly, the cluster identification can be extended to the temporal or z-direction by means of the pulse shape analysis of the strip pulses. The pulse shape analysis allows the instantaneous baseline determination, subtracting it to the strip pulse instead of the average pedestal level. This fact in fundamental for the recognition of the weak ionization tracks produced by minimum ionizing particles, such as muons.

The only source of temporal information with Gassiplex electronics is the mesh pulse, which due to the larger surface of the electrode has higher capacitance and is more sensitive to electronic noise. Figure 6.19 shows a comparison between the mesh pulse as digitized by the *Matacq* board and the envelope of all the pulses generated in the strips and processed by the AFTER electronics. Random calibration and background events are shown on the top and bottom respectively. The temporal pattern of the event is very similar in both cases, although there are two differences. The first one is that the mesh pulse is digitized at 1 GHz (1 ns per sample) with shaping times of 50 ns, while the strip pulses cannot be digitized faster than at 100 MHz (10 ns per sample) with shaping times higher than 100 ns. Consequently, the mesh pulse has more detailed information on the temporal evolution of the event. On the other hand, the mesh electrode has around 1000 pF capacitance while the individual readout strips have only around 70 pF. This fact makes the mesh pulse more sensitive to electronic noise, as the figure shows.

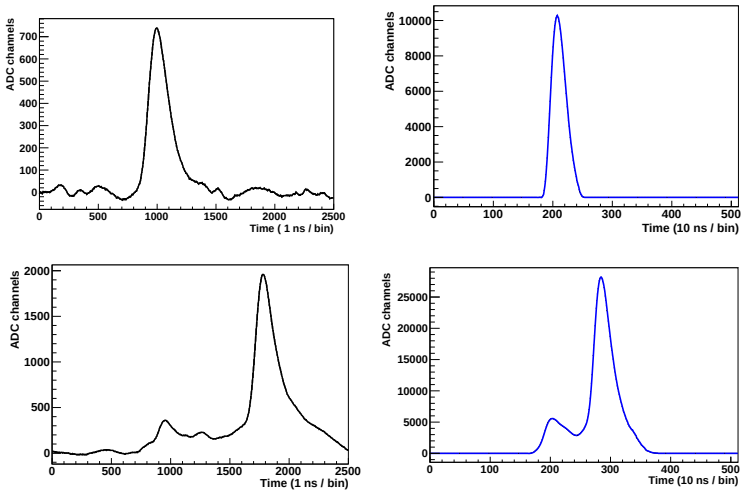

Figure 6.19: Top: mesh pulse of a calibration event as seen by the mesh with the Matacq *board (left) and as the evelope of the strips' pulses with AFTER electronics (right). Bottom: the same for a background event. The individual pulses of the strips for the same events are shown in figure 6.3*

The mesh pulse was very valuable in the discrimination process before the electronics upgrade precisely because it was the only information source of the charge distribution along the z-axis. Figure 6.20 (left) shows the background suppression of the raw background spectrum after surface fiducialization and applying the selection criteria related with the strips and mesh observables. However, the upgrade on the electronics raises the question of whether the mesh information is complementary or redundant. The mesh pulse was mainly used to discriminate vertical tracks and aligned multi-cluster events in the z-axis. These type of events can be identified and rejected with the temporal information of the strips signals. In fact, compatible background levels within 1σ have been obtained with and without the inclusion of mesh *discriminants* and the same signal efficiency (see figure 6.20, right).

Besides, the lower capacitance of the strips with respect to the mesh electrode allows to achieve better energy resolutions. Currently, the main purpose of the mesh pulse is producing the trigger signal, but if readout electronics with self-trigger capabilities are used (such as the AGET chip [273],

which have already been tested in CAST-MM detectors) the mesh pulse would become auxiliary. In this case, the pre-amplified signal could be directly recorded without passing it through the shaping-amplifier, conserving therefore more detailed time information of the event and, possibly, new tools for discrimination.

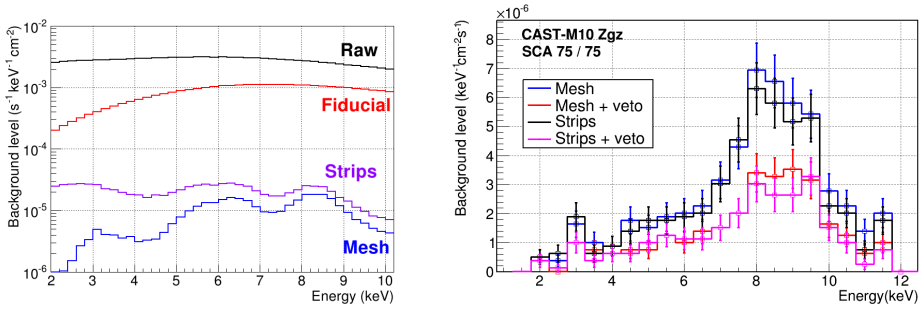

Figure 6.20: Left: background suppression of the raw background spectrum (black) after surface fiducialization (red) and applying the selection criteria related with the strips (purple) and mesh (blue) observables. Right: Background spectra after applying the selection criteria based on the observables related with the strips (black), strips + muon veto (magenta); mesh (blue) and mesh + muon veto (red).

6.5 Effect of discrimination on background data

In this section, we discuss the effect of the discrimination criteria on background data. For illustration, figure 6.21 shows the effect of the discrimination process on the background energy spectrum of a CAST-MM *sunset* detector during 1854 background hours. The signal efficiency of the discrimination criteria is 75% at both the 3 and 6 keV calibration peaks.

The black line (labeled as *raw*) represents the raw background data, the pink (*fiducial*) represents the application of a fiducial cut, selecting only events whose projection is within the magnet cold-bore. The blue line (*strips*)is the spectrum after applying the discrimination criteria based on the strip planes, while the red line includes the muon veto cut (*veto*). Finally, the difference between the *strips* and *veto* spectra represents the events identified as muon-induced (green line labeled *muons*).

The overall background suppression is around 3 orders of magnitude in the energy RoI, and reveals peaks at 3 and 8 keV, associated with the fluorescence emission of the K_α lines of copper and argon respectively. These events are caused by actual x-rays that cannot be rejected by analytical methods based on the Micromegas pattern recognition. However, the source of these background events can be identified, allowing the development of strategies to minimize its contribution. For example, muon-induced events can be tagged by higher efficient muon vetos, events induced by radon decay can be minimized by fluxing the detector surroundings with a N_2 vapor, or gamma-rays can be blocked with the enough thickness of lead. The identification of the background sources and the development of these strategies is one of the main tasks developed in this work.

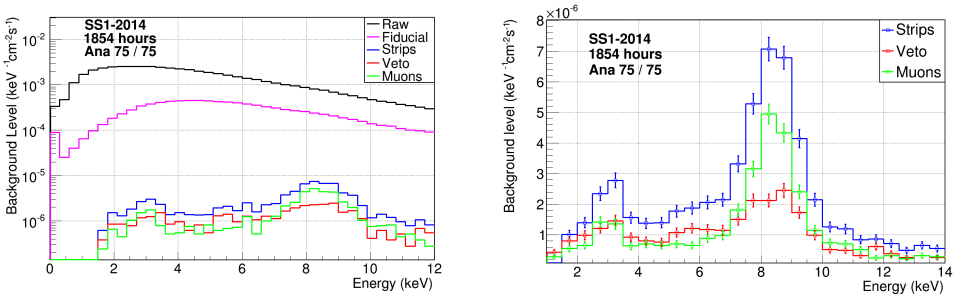

Figure 6.21: Background suppression of the raw background spectrum (black) after surface fiducialization (magenta) and applying the selection criteria based on the strips (blue) and muon veto (red) observables. The component of background identified as muons is in green. On the left, a zoom to the suppressed background spectra to show the fluorescence peaks.

Chapter 7

Micromegas detector characterization

Contents

7.1 Introduction

In this chapter, the characterization of CAST *microbulk* Micromegas (CAST-MM) detectors with x-rays is presented. Two difference approaches are discussed: the first type uses the x-rays from a ^{55}Fe source, which is the standard calibration method; the second type uses the x-rays from the x-ray beam generator described in section 5.6.

7.2 Characterization with ^{55}Fe

After producing the micropattern structure and assembling the whole the detector chamber, CAST-MM detectors are tested in argon-isobutane mixtures wit a ^{55}Fe source at the standard operating pressures of 1−1.4 bar. The results for the three latest types of CAST *microbulk* detectors (*M-brach*, before 2012; *C-branch*, in 2013; and *R-branch*, in 2014; described in section 5.2) are presented and discussed.

Firstly, the electrical connectivity of the mesh and drift electrodes is checked, and a high-voltage test in air is done to assure that there is no short-circuit between mesh and strips planes, evaluating whether the detector is operative or faulty. In a second step, the connectivity of the x and y strip lines is checked by measuring its capacitance to ground. This measurements allows to locate short-circuits between pairs of strips and other defects. As an example, figure 7.1 shows the capacitance values of the strips measured in the CAST-R3 detector. A pair of strips are noticeably short-circuited, while the rest present standard values around 60−70 pF.

If the high-voltage test and the capacitance measurements are satisfactory, the argon-isobutane mixture is circulated by the chamber. The leak tightness of the TPC at the operation pressure is

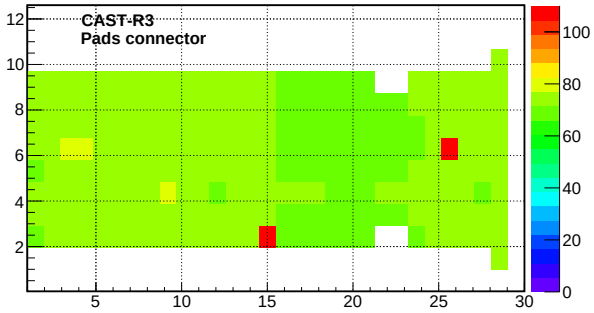

Figure 7.1: Array of capacitances of the CAST-R3 detector as measured in the fingerprint of the pads' connector. Two short-circuited strips are visible in red. Capacitance units in the color scale are in pF.

tested by isolating the detector with the gas inlet/outlet closed and monitoring the pressure. The chamber is considered to be correctly assembled if the pressure drop is below $\sim 10^{-3}$ mbar·l/s.

If the test is successful, the gas inside the chamber is renewed a few times before starting with the detector performance study. The detector performance is firstly characterized illuminating all its surface by a ^{55}Fe source and reading the mesh signal. Varying both the mesh and drift voltage allows to determine the optimum operational point, and the main detector properties, such as the electron transmission, gain or energy resolution (parameters described in section 1.6.2). Secondly, the strip planes are electronically instrumented and read out to evaluate the detector surface. The mesh voltage is typically varied from 280 to 400 V and the drift from 350 to 1000 V depending on the detector and gas mixture. Both voltages are powered independently by an CAEN N471A module, which allows leak current monitorization.

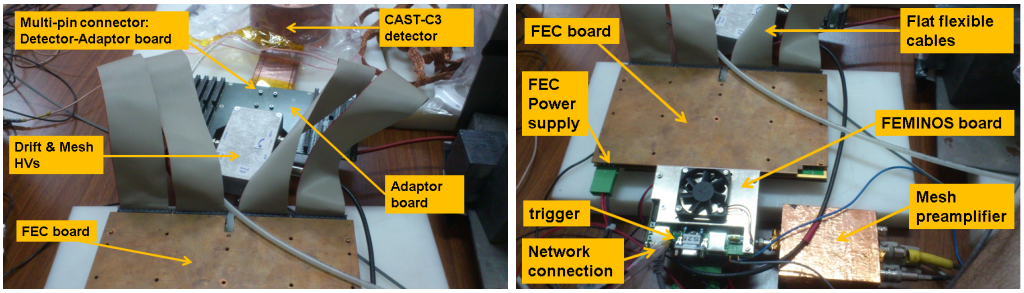

Figure 7.2: A Micromegas detector read out by AFTER-based electronics. The flat cables bring the strips' signals from the detector connector to the FEC (shielded in the picture with a copper plate) using a custom-made adaptation card. The HVs are supplied via the same printed circuit glued on the copper base. The signal induced on the mesh electrode after being preamplified is used for triggering the electronics. Data is recorded by the DAQ system via a standard network connection.

The mesh signal is usually read out by a CANBERRA-2004 or ORTEC 142C preamplifier, whose output is fed into a shaper/amplifier (such as ORTEC 474) and subsequently into a multi-channel analyzer AMPTEK MCA-8000A or an oscilloscope Tektronix TDS5034B, for digitalization and spectra building. In each voltage setting, a spectrum containing at least 10^5 events is generated to avoid statistical errors and then fitted to get the mean position and the width of the peak, as show in figure 7.3. Just after the characterization, the mesh voltage is fixed to a high amplification field, with large gain, but some tens of volts apart from the spark limit. The signals induced in the strips are read by the Gassipex or AFTER electronics, as show in figure 7.2. These front-end electronics, described in section 5.5, are triggered externally. The amplified mesh signal is fed into

a FAN IN/OUT Lecroy 428F and subsequently into a NIM-TTL converter, which is the trigger signal.

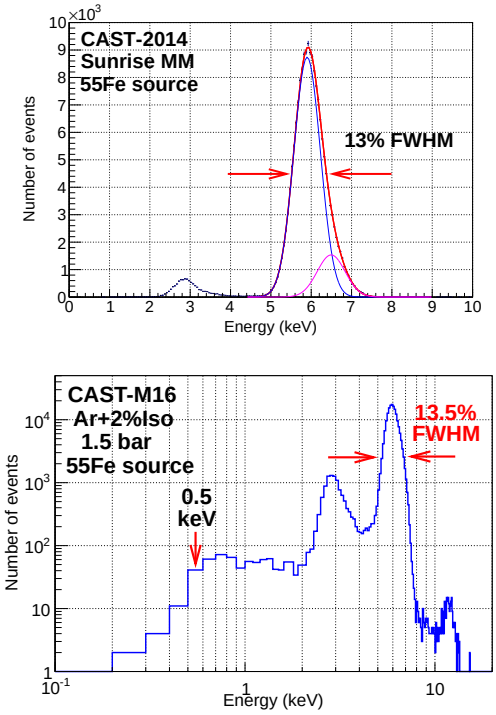

Figure 7.3: Left: ^{55}Fe calibration spectrum of a Micromegas detector. The main peak has been fitted to two gaussian functions (blue and magenta lines), corresponding to the K_α (5.9 keV) and K_β (6.4 keV) lines. Right: calibration spectrum showing the energy resolution and energy threshold of the CAST-M16 detector.

7.2.1 Electron transmission

The variation of the peak position with the drift voltage for a constant amplification field (i.e., constant mesh voltage) gives the electron transmission curve. Some of the curves obtained in the *microbulk* Micromegas of CAST are shown in figure 7.4. The detectors show a range of voltages for which the mesh is transparent to primary electrons. It is remarkable that the latest detectors, the $R-$branch, show a wider plateau of maximum electron transmission, which is reached at higher drift fields. This means that the detector works at optimal operation conditions in a wider range of drift-to-amplification fields, and thus voltage fluctuations have less impact in the detector performance.

The optimum $E_{\text{drift}}/E_{\text{amp}}$ ratio for the latest detectors is around 2×10^{-3}, while for the first type of *microbulk* detectors it is at 7.5×10^{-4}.

At very low drift fields, the electron transmission curve drops because many primary charges generated in the conversion volume do not reach the mesh as a consequence of high recombination and attachment with the gas impurities. At high drift fields, beyond the plateau of maximum electron transmission, the mesh stops being transparent to primary electrons and the gain and energy resolution degrade. This effect is due to the fact that at high fields many field lines end up at the mesh electrode.

Figure 7.4 (right) shows the electron transmission curves for the $C-$branch detectors, which operated with and without fields shaper rings along the drift distance (see chapter 5 for a description of the chamber details). The effect of the field shaper is a higher electron transmission at low

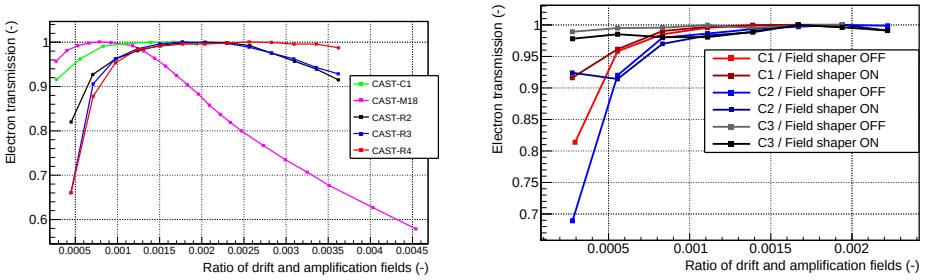

Figure 7.4: Left: dependence of the electron transmission with the ratio of fields for some detectors of the M−, C− and R−branches in Ar+2% iC_4H_{10} at 1.4 bar. Right: effect of the field shaper on the electron transmission for the C−branch detectors in Ar+2% iC_4H_{10} at 1.4 bar.

drift fields. The energy resolution depends on the fraction of primary electrons that are able to pass through the mesh holes. Figure 7.5 shows the dependence of the energy resolution at 5.9 keV with the ratio of drift-to-amplification fields. The energy resolution is correlated with the electron transmission curve: the best energy resolutions are achieved at the plateau of maximum transmission, i.e., at around $E_{\text{drift}}/E_{\text{amp}} = 2 \times 10^{-3}$. The energy resolution of achieved is limited by the electronic noise.

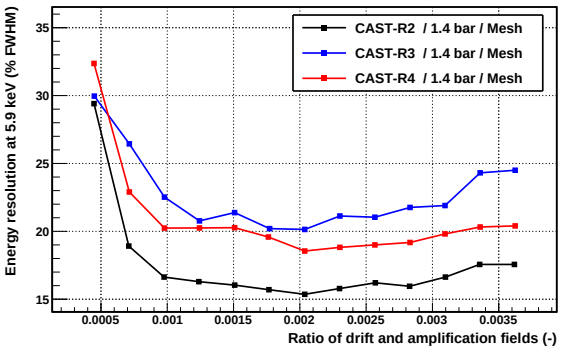

Figure 7.5: Dependence of the energy resolution at 5.9 keV with the ratio of fields for the R−branch detectors in Ar+2% iC_4H_{10} at 1.4 bar.

7.2.2 Gain curve

The dependence of the peak position with the amplification field generates the gain curve, i.e., the dependence of the amplification factor of the primary electrons with the applied mesh voltage. The absolute gain is calculated according to equation 1.26 $G = \frac{n}{n_0}$. The determination of G requires: a) calculate the mean number of primary electrons n_0 generated by the 5.9 keV x-rays in argon (W = 26.3 eV), i.e., 224.14 electrons; b) calibrate the electronic chain to obtain the conversion factor from ADC units (registered in the digitalization module) to the number of electrons after the avalanche. This calibration is done by means of a pulse generator fed to a capacitance to transform the input voltage into a charge, and subsequently to the charge-mode preamplifier, amplifier and digitalization board.

Figure 7.6 shows the gain curves obtained for several Micromegas detectors for argon-isobutane mixtures. In these measurements the ratio of drift-to-amplification fields is chosen in the range of maximum electron transmission and the drift voltage is changed to keep this ratio constant, as well as the bias of the field shaper which is varied accordingly. The maximum gain before the spark

limit for almost all detectors is in the range $1-2\times10^4$. The absolute gain rises exponentially with the amplification field, following the Rose and Korff gain model [25]. However, some detectors show a deviation from this model at high amplification fields. This over-exponential behaviour is due to the fact that the low quencher concentrations (2−5%) cannot absorb all the UV photons generated in the primary avalanches, producing secondary avalanches by photoelectric effect [195].

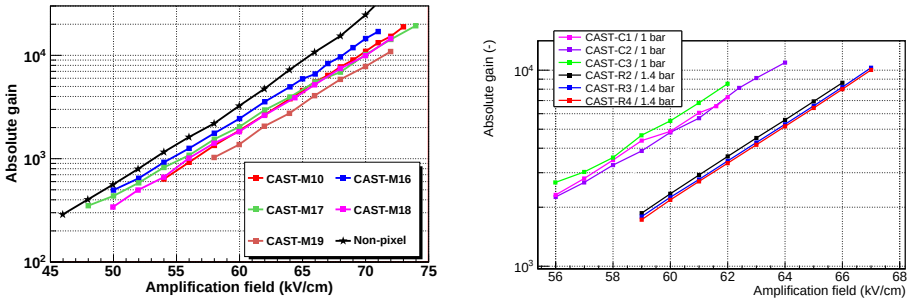

Figure 7.6: Left: dependence of the absolute gain with the amplification field for the M−branch detectors in Ar+5% iC_4H_{10} at atmospheric pressure. As a comparison, the curve generated by a non-pixelized microbulk detector in the same conditions has been included. Right: same dependence for the C− and R-branch detectors in Ar+2% iC_4H_{10} at the indicated pressure.

The energy resolution has also a dependence with the gain (or the amplification field), as it is shown in figure 7.7 for several CAST-Micromegas detectors. At low gains, the energy resolution degrades because the signal amplitude is comparable with the electronic noise. At high gains, the energy resolution degrades too due to the over-exponential behaviour of the amplification process, which produces larger gain fluctuations. There is a range of amplification fields for which the energy resolution is constant at its best value.

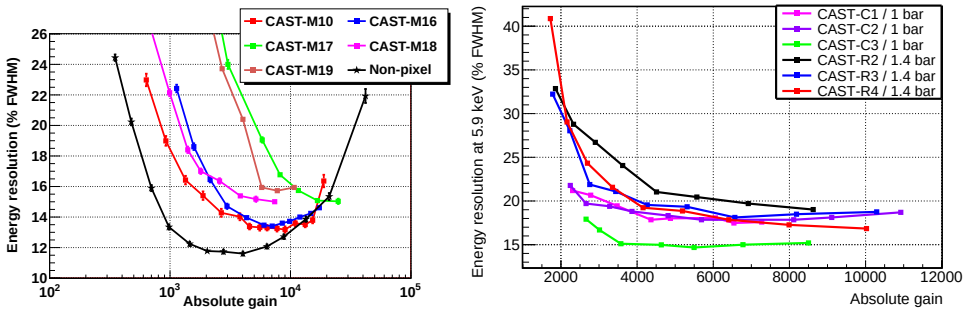

Figure 7.7: Left: dependence of the energy resolution at 5.9 keV with the absolute gain for the M−branch detectors in Ar+5% iC_4H_{10} at atmospheric pressure. As a comparison, the curve generated by a non-pixelized microbulk detector in the same conditions has been included. Right: same dependence for the C− and R-branch detectors in Ar+2% iC_4H_{10} at the indicated pressure.

The detector should be operated at the higher amplification field within this range, since the **energy threshold** depends on the absolute gain. In CAST-Micromegas detectors energy thresholds well below 1 keV are achieved, allowing to observe most of the classical axion flux (energy RoI defined from 2−7 keV). As an example, figure 7.3 (right) shows a calibration energy spectrum with a ^{55}Fe source in which the energy threshold is at sub-keV energies. Currently, there is significant interest in achieving lower energy thresholds and higher quantum efficiencies at low energies since in some axion production scenarios the axion signal is shifted towards lower energies. This issue is addressed in section 10.4.

The parameters reviewed here are also dependent on the quencher concentration and gas pressure. For a detailed study of the behaviour of *microbulk* Micromegas detectors as a function of these parameters the reader is referred to [196].

7.2.3 Overall stability

The typical physic runs of CAST are of several months. Hence, the stability of operation and robustness of the detectors is critical. If the detector performance degrades with time or the detector fails it must be replaced, which entails lost of tracking time and sensibility.

The Micromegas detectors have demonstrated to be quite stable and they are daily calibrated to evaluate any change in the detector performance. Some parameters, like the gain, energy resolution, energy threshold or cluster size can be affected by aging effect and changes in the environmental conditions. As an example, figure 7.8 (left) shows the detector pressure fluctuation in a Micromegas detector over a month of continuous operation. The variations in the pressure are less than 3%. Temperature and humidity changes can also affect the detector performance for example through the diffusion coefficients. In order to minimize these fluctuations, the detectors are kept inside a plastic tent with a continuous flow of N_2 vapour.

The evolution of the gain and the energy resolution at 5.9 keV of the Sunrise Micromegas detector along the 2014 data-taking are shown in figure 7.8. The fluctuations, measured both at the mesh and at the strips are less than 10% over roughly two months of continuous operation. Hence, it is possible to exclude gain shifts and variations in detector noise as a significant source of the fluctuation in the descriptive parameters of x-ray events.

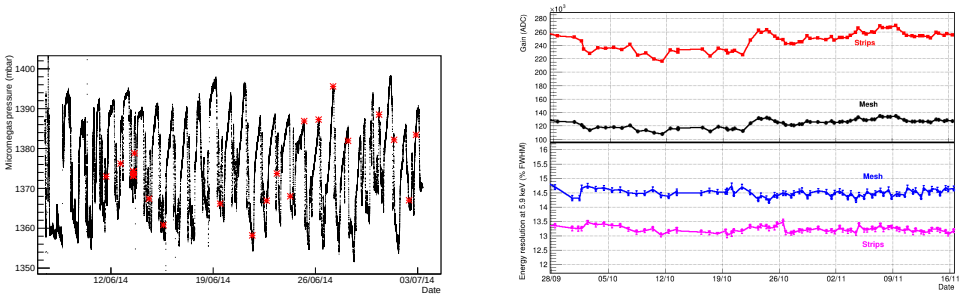

Figure 7.8: Left: evolution of the gas pressure inside the detector chamber and time at which calibrations are performed (red crosses). Right: evolution of the gain and the energy resolution of the Sunrise Micromegas detector along the 2014 data-taking. The fluctuations, measured both at the mesh and at the strips are less than 10%.

7.2.4 Surface characterization

Once the drift and amplification fields are fixed at its optimum values, the detector surface is studied with the signals induced in the strips. A long enough calibration with ^{55}Fe allows to acquire the statistics (more than 10^6 events are usually acquired) necessary to build an intensity map (*hitmap*) of the detector surface, defined from the mean position of the cluster.

Figure 7.9 shows the calibration *hitmaps* for the *sunset* detectors of 2013. The uniform shadowed regions correspond to the pattern of the strongback. Micromegas detectors usually present inactive areas at the corners, like the ones shown in the figure, but they present an active area large enough to cover the cold-bore area. Besides, the short-circuited or not electronically instrumented strips become evident as a vertical/horizontal region with less number of events. This characterization also reveals problems in the manufacturing process such as regions were the kapton has not been properly etched (see position (20,40) in the left plot of the figure). The sunset 2 detector shows a clear distortion of the strongback projection due to non-uniform drift fields towards the edges of the detector.

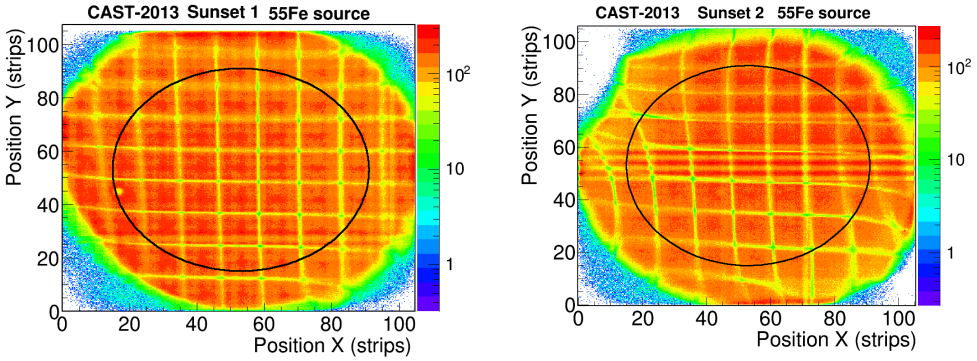

Figure 7.9: Calibration intensity maps of both Sunset Micromegas detectors during the 2013 data taking. The black circumference represents the projection of the cold-bore area (21.5 mm radius). The color scale represents the number of events per bin.

Finally, a relative *gain map* is obtained in order to study the inhomogeneities in the detector gain over the active area. The active are is binned in two-dimension and each bin is filled with the amplitude weighted by the mean peak position of those events belonging to the 5.9 keV x-rays whose mean position is within the bin range. An example for the same detectors is shown in figure 7.10.

From the figures, it is clear that the detector on the left (Sunset 1) has a larger and more uniform active than the detector on the right (Sunset 2). While the first detector only has one dead strip partially entering the cold-bore area, the second detector has five strips in the y-axis and another oner in the x-axis.

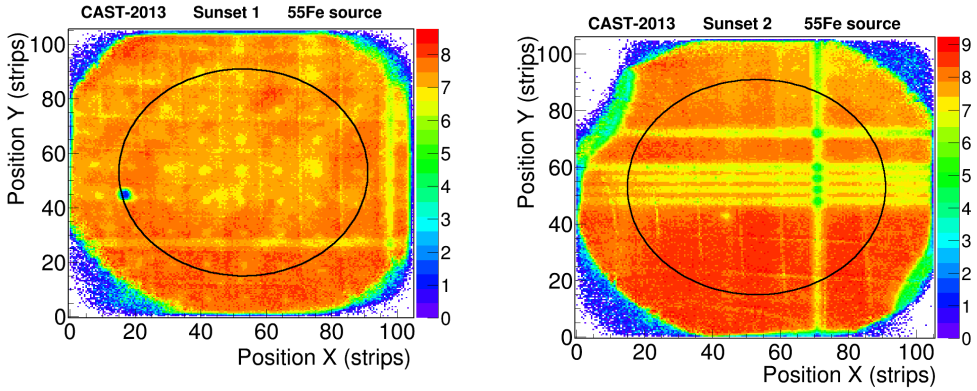

Figure 7.10: Surface gain maps of both Sunset Micromegas detectors during the 2013 data taking. The color scale represents the relative gain, in arbitrary units.

7.3 Characterization in the x-ray beam

The CAST x-ray beam facility, described in some detail in section 5.6, is used to generate x-rays of different energies by means of the PIXE (Particle Induced X-ray Emission) technique. Part of the setup is shown in figure 7.11. The Micromegas detector is bolted to the vacuum line in front of the x-ray generator, which is designed equivalently to the CAST vacuum lines, i.e., there is a thin mylar window that allows for differential pumping and a gate valve that can split the detector and the x-ray generator sides. Table 7.1 lists the target materials used to produce the fluorescence emission

(along with its characteristic energy) and the filters to absorb the breemstrahlung radiation. It also shows the energy range for which the x-ray calibration is used as the reference dataset in the definition of the discrimination criteria of a new background rejection method based on these x-ray generator runs (see section 7.3.4.)

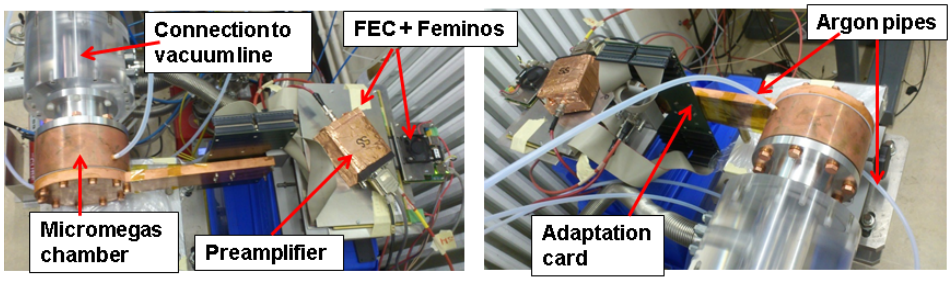

Figure 7.11: A Micromegas detector coupled to the x-ray generator vacuum line. The main elements of the Micromegas readout system are labeled.

Target	Energy (keV)	Filter	Range (keV)
Al	1.5	Al	-
Au	2.1	PEEK	2.0-3.5
Ag	3.0	Ag	-
Ti	4.5	Ti	3.5-5.5
Mn	5.9	Cr	5.5-6.5
Co	6.9	Fe	6.5-7.5
Cu	8.0	–	7.5-10

Table 7.1: Set of target materials used in the x-ray beam generator with the characteristic K_α emission energies and the filter used to absorb part of the breemstrahlung radiation.

Three Micromegas detectors (M18, M19 and C3) were characterized in the x-ray beam generator. At least 10^6 events are recorded for each target material in order to reduce statistical fluctuations in the descriptive parameters of the analysis. The x-ray runs have been used to: a) verify the performance of the detectors before its installation in CAST experiment, b) calculate the efficiency as a function of the energy, c) make an *energy independent* analysis for the *Sunset* 1 Micromegas ($M18$) used in the CAST data taking in the year 2013.

7.3.1 Energy resolution

The fluorescence lines produced by the electron beam in the different target materials irradiated the Micromegas detectors, producing the spectra shown in figure 7.12. The calibration peaks of the x-ray runs encompass the whole energy RoI.

The generated spectra are fitted to gaussian functions and the mean position and width of the peaks are obtained. The relative energy resolution for each peak σ/E is represented as a function of the x-ray energy in figure 7.13. As expected, the energy resolution improves with energy, with a dependence dominated by a term proportional to $1/\sqrt{E}$, a consequence of the statistics of the generated electrons, that is to say a lower relative fluctuation in the number of electrons (see chapter 1). Two fitting functions have been used to parameterize the dependence

$$\frac{\sigma}{E} = \frac{a}{\sqrt{E}} + b \tag{7.1}$$

$$\frac{\sigma}{E} = \frac{a}{\sqrt{E}} + \frac{b}{E} \tag{7.2}$$

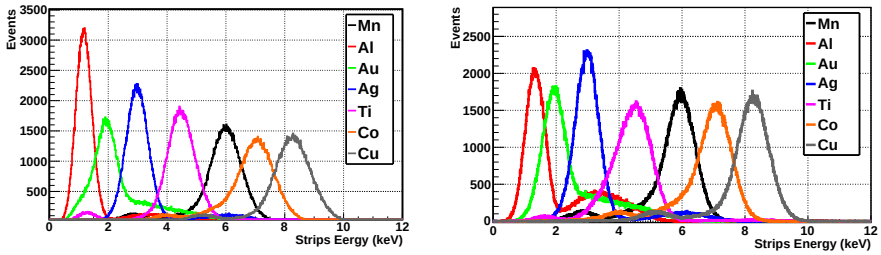

Figure 7.12: Calibration energy spectra of the M18 (left) and C3 (right) detectors installed in the x-ray beam of the CAST Detector Laboratory. Several materials were used as targets of the PIXE system to scan the whole CAST energy RoI.

where a and b are free parameters. The second parameterization includes a calibration term proportional to $1/E$ arising from the error in the energy determination of the measurement produced, for example, by electronic noise or non-linearity of the amplification electronics.

The data points and the fitting functions are shown in figure 7.13 for the three characterized detectors. The second function better fits the data at low energies (where the $1/E$ term dominates) since the energy determination is more affected by detector or electronics shifts. Table 7.2 shows the value of the fitting parameters.

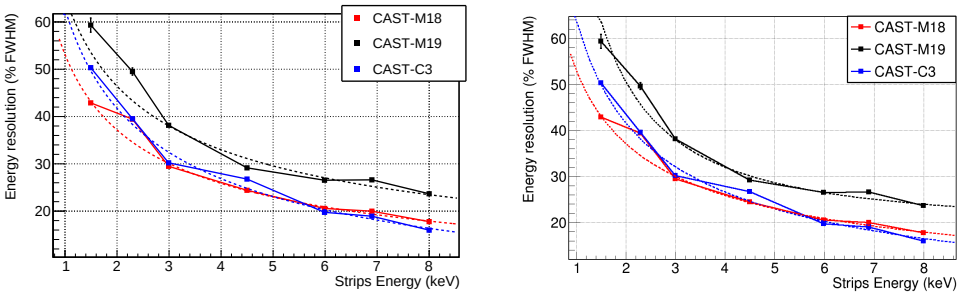

Figure 7.13: Dependence of the energy resolution registered by the strips with the energy of the incident x-ray for three CAST-Micromegas detectors. The points of the left and right plot have been fitted respectively to equations 7.1 and 7.2.

Detector	Fit	a	b
CAST-M18	Eq. 7.1	54.4 ± 0.52	-1.37 ± 0.25
CAST-M19	Eq. 7.1	64.8 ± 1.14	0.54 ± 0.47
CAST-C3	Eq. 7.1	71.7 ± 0.52	-9.02 ± 0.24
CAST-M18	Eq. 7.2	49.3 ± 0.45	4.46 ± 0.82
CAST-M19	Eq. 7.2	65.2 ± 0.94	2.13 ± 2.11
CAST-C3	Eq. 7.2	37.4 ± 0.46	29.7 ± 0.81

Table 7.2: Fit parameters for the measurements of the energy resolution as a function of the energy of the incident x-ray in the three detectors used.

7.3.2 Signal efficiency: data versus simulation

The mean signal efficiency over the energy RoI, a parameter directly related with the sensibility of the axion search, can be evaluated on basis of experimental data using the x-ray runs. The ^{55}Fe calibration runs are used to define selection criteria to be applied to the x-ray runs. The fraction of accepted events is the signal efficiency at the energy of the incoming x-rays. Formerly, this parameter was calculated using *Geant4* Montecarlo simulations of the x-rays at different energies, and subsequently simulating the electronic response and signal induction in the detector readout planes. Finally, the analysis and discrimination routines developed for real data are also used in the analysis of the simulated data. This issue is extensively discussed in chapter 10.3.3.

A comparison between the simulated and experimentally determined signal efficiency is shown in figure 7.14. The analysis is done for two sets of imposed efficiencies at the available energies during ^{55}Fe calibrations, i.e., at 3 and 6 keV. The results, although slightly dependent on the discrimination method applied and on the detector, show that experimental and simulated data reasonably agree below 6 keV, but they start to differ above that energy. While the signal efficiency for the simulated data decrease very slightly above 6 keV, the experimental efficiency drops much faster. The divergence is attributed to an idealistic signal generation in the simulated data.

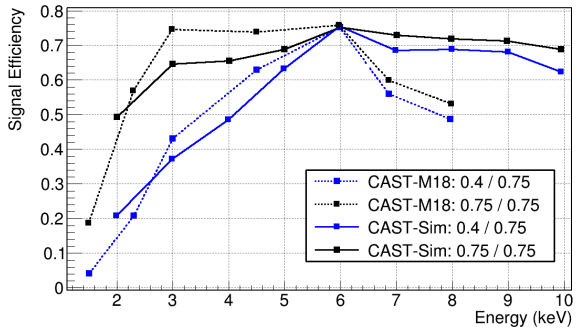

Figure 7.14: Comparison between the simulated and experimentally measured signal efficiency for two different sets of imposed efficiencies (values shown in the legend) at 3 and 6 keV, the main and escape peak of the ^{55}Fe source respectively, used for the definition of the discrimination criteria.

7.3.3 Energy dependence of the discriminants

During the periodical ^{55}Fe calibrations, only 3 and 6 keV events are available, and these peaks are used to define the selection criteria for the whole energy RoI. The x-ray runs provide information about the energy dependence of the *discriminants* used in the rejection algorithms.

Figure 7.15 shows the dependence of some observables with the energy of the incident x-rays. The figures shows how the width of the distributions increases at low energies. For example, the balance between the charge collected by x and y strips planes widens at lower energies since there are less charge to be shared between detector planes, increasing the fluctuations. Note that the aluminum fluorescence at 1.5 keV only produces around 57 electrons! The same argument applies for the rest of observables shown in the figure. Besides, x-rays with energies below 3 keV have shorter mean free paths, their mean drift distances is larger and consequently they experience larger diffusion effects. If the signal-to-noise ratio of the detector signals is poor the effect is even larger.

For all of these reasons, the signal efficiency at low energies usually cannot be increased to very high values without producing a large increase in background events. As an example, figure 7.16 shows, in the parameter space of the cluster size, the contour lines encompassing 95% of the calibration x-rays. As it is shown, x-rays from aluminum fluorescence (1.5 keV) occupy a much wider region in this space, and hence, the probability of accepting background events at this

efficiency increases. In the next section, we present a discrimination analysis based on the x-ray runs that take into account the energy dependencies of the *discriminants*.

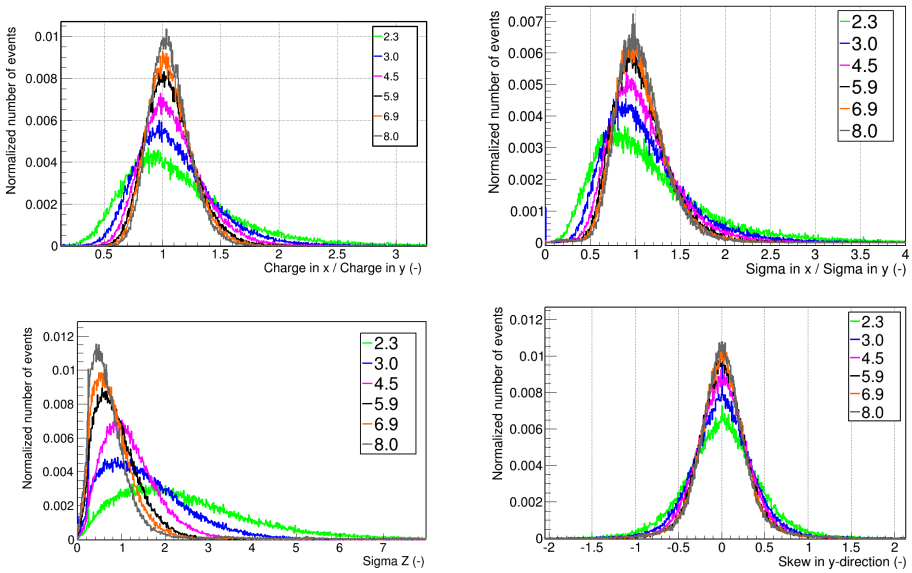

Figure 7.15: Dependence of some observables with the energy of the incident energy.

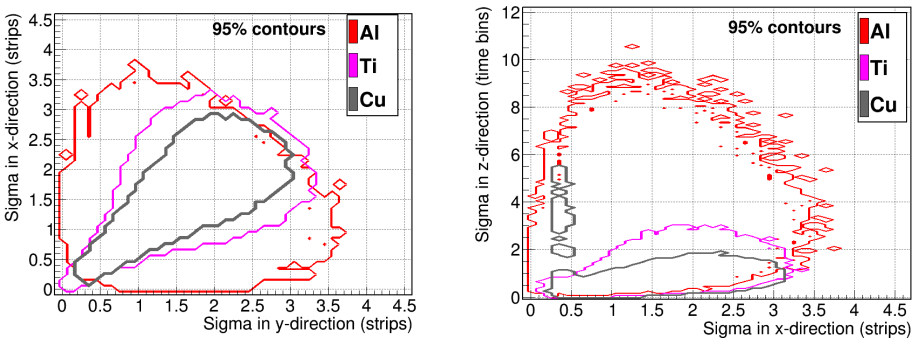

Figure 7.16: Projection of the cluster size observables in a two-dimensional map, the contour lines containing 95% of the x-ray events coming from three different target materials (Al, Ti and Cu) of the x-ray beam generator.

7.3.4 A discrimination based in the x-ray runs

An analysis based on the x-ray runs described in the previous section has been implemented. It consists in the definition of the selection criteria in independent discrete energy ranges based on the x-ray calibrations. The energy RoI is divided in four smaller ranges ($2.0 - 3.5$ keV, $3.5 - 5.5$ keV, $5.5 - 6.5$ keV and $6.5 - 7.0$ keV) each of which is referenced to a calibration with the x-ray beam, respectively Au (2.1 keV), Ti (4.5 keV), Mn (5.9 keV) and Co (6.9 keV), as table 7.1 shows. Two different selection criteria, denominated *X-rays(1)* and *X-rays(2)*, are built with slightly difference efficiencies.

The background data (1749 hours) of the Micromegas detector used in CAST in 2013 has been analyzed with this technique. Before its installation in the CAST experiment, this detector

(CAST-M18) was tested in the x-ray beam generator, which allows to directly apply the selection criteria derived from these runs to the subsequent background data taking. However, some of the *discriminants* typically used in discrimination cannot be used since their distribution depends on the voltage settings of the detector, which were slightly different during the x-ray runs and CAST data taking. Note that other fluctuations or shifts in the detector settings produce less efficient cuts.

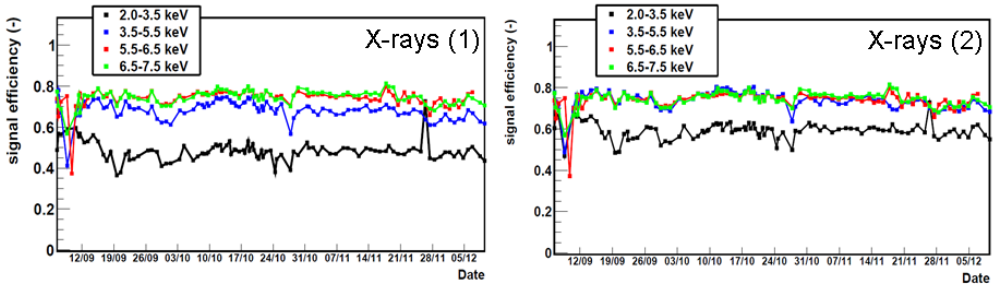

Figure 7.17: Signal efficiency evolution of the Sunset 1 *Micromegas detector in CAST during 2013. The cuts are defined in the x-ray runs and applied to the periodical ^{55}Fe calibration data. Two definitions of the cuts are used, one with lower efficiency −left, X-rays(1)− than the other −right, X-rays(2).*

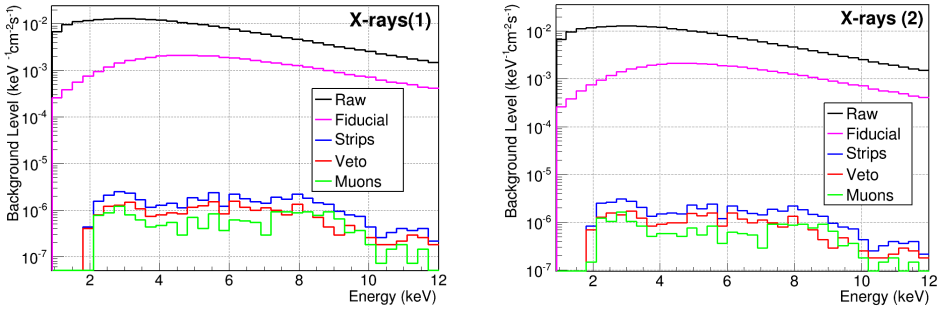

Figure 7.18: Background energy spectra of the Sunset 1 *Micromegas detector in CAST during 2013 analyzed with the selection criteria derived from the x-ray runs. Two analysis with different efficiency (left and right) are applied (see the text for details).*

The discrimination criteria are also applied to the regular ^{55}Fe calibration data in order to study the evolution of the efficiency to x-rays. As the figure 7.17) shows, the efficiency is reasonably stable for the discrimination parameters used. Note that the efficiency is probably underestimated outside the ^{55}Fe peaks since the events therein are not usually real x-rays of that energy.

The effect of applying this discrimination method to the background data is shown in figure 7.18, and a zoom to the final background level is shown in figure 7.19. The spectrum rises significantly in the lowest energy range (2.0-3.5 keV), where the Au K_α peak at 2.1 keV is used to define the cuts. This peak is probably no the best choice to define the selection criteria as it is very close to the left energy edge, and consequently is not very representative. For the same reason, the efficiency in this energy range is somewhat underestimated given the wider distributions of the *discriminants* shown in section 7.3.3.

Table 7.3 shows the mean efficiencies, background level and *factor of merit* obtained with this analysis, and they are compared to the results obtained using a classic *run-to-run* analysis, i.e., using the ^{55}Fe calibrations for discrimination (labeled in the table as *Ana (1)* and *Ana(2)*, depending on the efficiency).

Although the analysis based on the x-ray runs underestimates the efficiency for the reasons given above, the *factor of merits* are compatible.

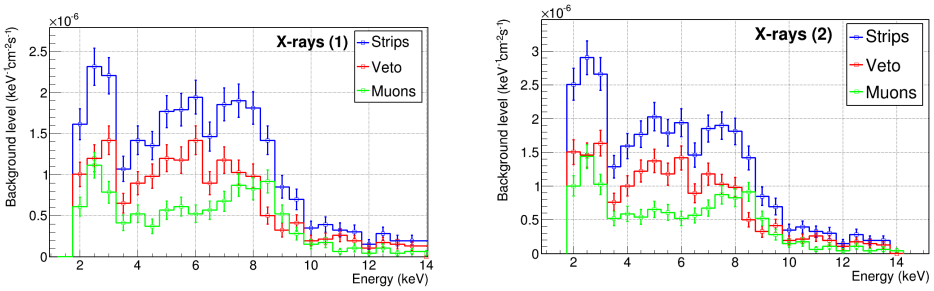

Figure 7.19: A zoom to the background energy spectra of the Sunset 1 *Micromegas detector in CAST during 2013 analyzed with the selection criteria derived from the x-ray runs. Two analysis with different efficiency (left and right) are applied (see the text for details).*

Analysis	**Mean eff.**	**Level (10^{-6}keV^{-1}cm^{-2}s^{-1})**		**FOM (2-7 keV)**	
		Strips	Veto	Strips	Veto
Ana (1)	0.57	1.25 ± 0.07	0.76 ± 0.06	0.51 ± 0.03	0.65 ± 0.06
Ana (2)	0.69	1.81 ± 0.09	1.02 ± 0.07	0.53 ± 0.02	0.68 ± 0.05
X-rays (1)	0.64	1.69 ± 0.06	1.08 ± 0.08	0.49 ± 0.01	0.62 ± 0.04
X-rays (2)	0.71	1.99 ± 0.07	1.25 ± 0.08	0.50 ±0.01	0.64 ± 0.03

Table 7.3: Summary of background and factor of merit results obtained with the run-to-run *analysis and with the x-ray runs. The background data analyzed correspond to 1749 hours of the* Sunset 1 *Micromegas detector in CAST during 2013.*

Chapter 8

Limit to the axion-photon coupling with the Micromegas detectors the 2012 ^{4}He phase.

Contents

8.1 Motivation and physics case

As discussed in section 3.3, for a fixed coupling strength $g_{a\gamma}$, the probability of axion-photon conversion decreases when the $a-\gamma$ oscillation length becomes smaller than the magnet length, which limits CAST's sensitivity to an axion mass range $m_a \lesssim 0.02$ eV. For larger m_a values, the conversion probability is restored by providing photons with a refractive mass using a low-Z gas filling (see figures 3.4 and 3.5). The gas density inside the magnet bores (i.e., the cold bore pressure at 1.8 K) defines the search mass and one needs to step through many pressure settings to search a broad m_a range.

CAST carried out its phase I with vacuum in the magnet bores, in 2003 and 2004. The limit obtained to the axion-photon coupling $g_{a\gamma} < 8.8 \times 10^{-11}$ GeV^{-1} for $m_a \lesssim 0.02$ eV, surpassing the astrophysical bound $g_{a\gamma} < 10^{-10}$ GeV^{-1}. With ^{4}He filling (2005 – 2007), the maximum search mass was extended to ∼0.4 eV, corresponding to the ^{4}He vapor pressure at cryogenic temperatures. The limit obtained excluded for the first time theoretically motivated QCD axion models. With ^{3}He filling (2009 – 2011), the search was finally extended up to 1.17 eV, which exceeds the cosmological hot dark matter limit for axions (see chapter 2). For $m_a > 0.6$ eV the ^{3}He search has reached the "axion line" of the typical KSVZ model($E/N = 0$).

After completing the ^{3}He phase, the gas was removed from the system. In 2012, after improving the Micromegas detectors and shielding, the magnet bores were filled again with ^{4}He gas, taking

advantage of the sophisticated gas metering system capable of filling the cold bore in small steps with a reproducibility of better than 100 ppm. The search masses were selected to cover a previous *candidate setting* with mass $m_a \sim 0.2$ eV, where unusually many events above background were detected, and the range $0.39 - 0.42$ eV, the upper axion mass range reachable with ^{4}He, to cross the axion line for the KSVZ model.

In this chapter, the results from the three Micromegas working in the 2012 data taking campaign with ^{4}He as buffer gas are presented. First, we do a general overview and we report on the performance of the Micromegas detectors along the data taking campaign. Then, we obtain the limit on the axion-photon coupling constant for the mass ranges explored. This result has already been published by the CAST collaboration in reference [197].

8.2 Micromegas data taking overview

The total exposure time in axion-sensitive conditions (solar tracking) was about 147 h per detector with a background time of around 2277 h per detector. In the first part of the 2012 data taking campaign, the axion mass range $0.39 < m_a < 0.42$ eV was scanned, which corresponds to the pressure range $13.9 - 15.5$ mbar at 1.8 K. During this period, 18 pressures settings were covered with a step size of 0.1 mbar and an average exposure time of ~ 24 h per setting. At each pressure setting, we integrated about 7.5 h per detector (5×1.5 h solar trackings), in contrast to 1.5 h (one solar tracking) in our earlier ^{4}He campaign. This phase started on 22nd of June and finished on 7th of October. In the second part of the data taking campaign, a single setting at $m_a \simeq 0.20$ eV, corresponding to a pressure of around 3.8 mbar, was covered during ~ 30 h. This phase started on 7th October and finished on 21^{st} October. The 31st of August there was a magnet quench, i.e., part of the magnet coil lost superconductivity entering into resistive regime, which produces a rapid boil-off the the cryogenic ^{4}He fluid. After this incident, data taking resumed on 11th of September. The evolution of the pressure in the cold bore is shown in figure 8.1. A summary of the Micromegas data taking efficiency is shown in table 8.1. The tracking efficiency of sunset detectors is 100%, i.e., no tracking time was lost due to sunset Micromegas detectors failure or malfunctioning. However, sunrise Micromegas suffered a severe shortcircuit on 7th of October, being impossible to recover the detector. This fact lead to the lost of the latest 12 trackings of the data taking campaign at the pressure of 3.8 mbar.

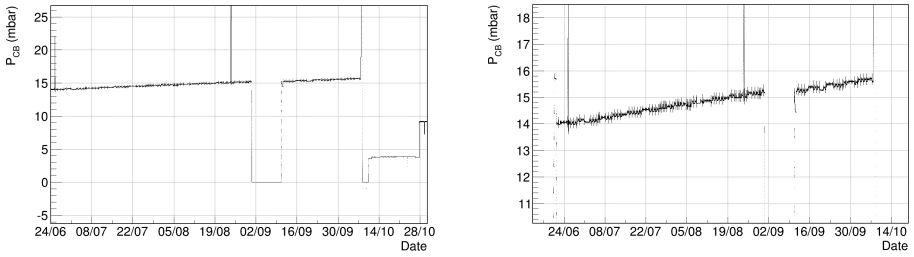

Figure 8.1: Left: evolution of the ^{4}He pressure in the cold bore during the 2012 data taking campaign. Right: a zoom to the $13.9 - 15.5$ mbar region.

Detector	**N$_{\text{tracks}}$**	**Tracking** (hours)	**Background** (hours)	**Trackings lost**	**Efficiency** (%)
Sunrise	88	138.2	2376.0	12	88
Sunset 1	100	153.0	2226.5	0	100
Sunset 2	100	153.0	2252.1	0	100

Table 8.1: Statistics of the Micromegas data taking campaign in 2012 with ^{4}He buffer gas.

The Micromegas detectors were of the microbulk type, one in the sunrise and two in the sunset side. While the detector in the sunrise side remained unchanged since the previous data taking campaign, the Micromegas detectors and shielding on the sunset side were upgraded, improving the background level of the detectors. The upgrades are described in detail in chapter 5, including the techniques that lead to the background reduction. In brief, the upgrade focuses on reducing the contribution of the environmental gamma flux and cosmic muons. The inner copper shielding was increased from 5 to 10 mm. The detector connect to the magnet bores by a 100 mm thick copper pipe, which has an inner polytetrafluoroethylene coating of 2.5 mm thickness conceived to attenuate the 8 keV copper fluorescence. The lead shielding thickness was also increased from 25 to 100 mm in a more compact design, extending the shielding around the pipes that connect to the magnet. In addition, the aluminum strongback was replaced by a more radiopure one, and all the components around the detector have been selected according to radiopurity criteria. A plastic scintillator was installed on top of the shielding, allowing the discrimination of background events induced by cosmic muons.

8.3 Sunrise Micromegas performance

The sunrise Micromegas detector is filled with Ar+2.3%iC_4H_10 at 1.4 bar. It is daily calibrated from the front side with a ^{55}Fe source that is moved out of the field of view of the detectors during background and tracking runs. These calibrations are used to check the detector performance evolution, identify any failure and define the discrimination criteria. The 7th of October the sunrise Micromegas suffered a severe shortcircuit between the mesh and strips and we were unable to recover its functionality. This fact produce a lost of 12 trackings at a pressure of around 3.8 mbar at 1.8 K.

The sunrise Micromegas detector shows a large active area that covers the whole cold bore area. The intensity distribution and gain maps of figure 8.2 have been done using the full calibration data set acquired during the 2012 data taking campaign. The grid pattern of the hitmap distribution represents the shadow of the drift window strongback illuminated by frontal calibrations. It is noticed that the detector has two consecutive non-instrumented channels around the strip number 80 in the y-direction. The intensity map indicates that those events that would naturally lay in that region, accumulate around it. The gain map shows a very uniform pattern in most of the active area, with fluctuations below 10% except in the region mentioned before, where the gain is reduced up to a factor 40%. There is also a vertical band with lower gain but this almost outside the cold bore projection area.

The linearity between the energy determined with the strips and mesh signals is shown in figure 8.3. On the left, the raw calibration data is represented, while on the right, we fiducialize and remove the band with lower gain. The raw data shows clear accumulation of events out of the linear trend. In particular, there are many events whose strips' energy is underestimated, while the mesh' energy is fully reconstructed. These regions are clearly suppressed once the fiducialization is applied. Besides, there are another set of events out of the linear trend that does not disappear after fiducialization. The energy reconstructed from the strips signals is larger than the one reconstructed from the mesh. This is certainly due to pile-up events and events in which the excited argon atom decays to the fundamental state via fluorescence, which is in turn reabsorbed within the active volume.

Figure 8.5 (left) shows the energy spectrum of the full calibration data set of the 2012 data taking campaign. The black line represents the energy of the raw data, while the red one represents the energy reconstructed correcting the fluctuations of the gain over the detector surface. The improvement in the energy resolution is apparent.

The evolution along the data taking of the gain and energy resolution is represented in figure 8.4. The gain is remarkably stable, with fluctuations below 10%. The steps in the mesh gain are due to controlled setting changes in the amplification stage. The energy resolution after cuts also shows stable values of around 16% FWHM at 5.9 keV.

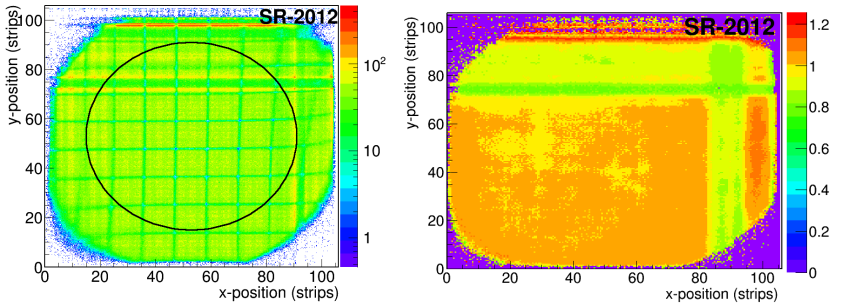

Figure 8.2: Sunrise calibration intensity (left) and gain (right) maps in the 2012 data taking campaign. The black circumference represents the cold bore area. The strips pitch is 0.56 mm.

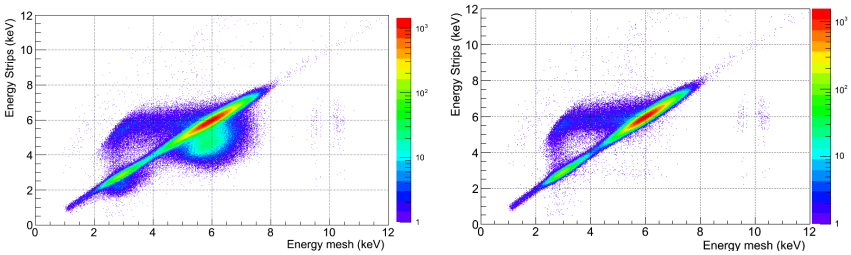

Figure 8.3: Energy balance between the energy measured by the strips and by the mesh before (left) and after (right) the application of fiducial cuts in the sunrise Micromegas of 2012.

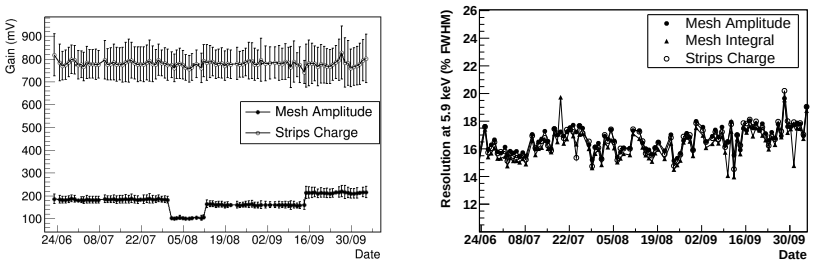

Figure 8.4: Evolution of the gain (left) and energy resolution after cuts at 5.9 keV (right) of the sunrise Micromegas in 2012.

8.3.1 Optimization of detectors' sensitivity

The detector factor of merit, defined in section 6.3.4, is studied for the 2012 data set using the multivariate and sequential cuts analysis. The sunrise results for multivariate analysis are shown on the right panel of figure 6.15. This factor is maximized for large values of the signal acceptance at 3 keV (escape peak of the main ^{55}Fe peak in argon). Therefore, the signal efficiencies have been fixed at 90% both at 3 and 6 keV, which determines the q_L value that separates accepted and rejected events.

The evolution of the signal efficiency along the data taking campaign is shown on the right of figure 8.5. The fluctuations are negligible (below 0.3%) and, for all purposes, it is assumed to be constant.

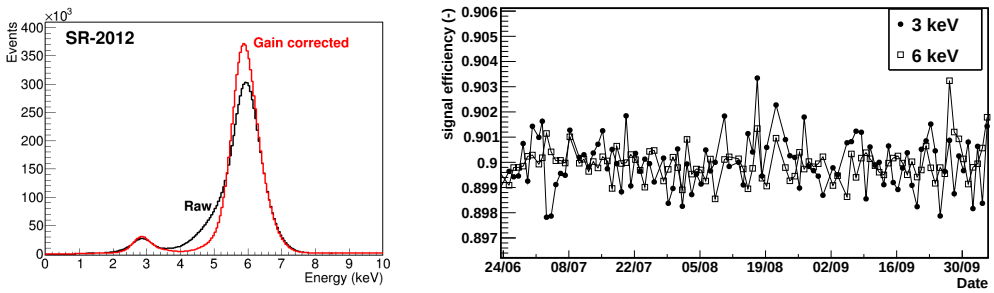

Figure 8.5: Left: calibration energy spectrum of sunrise Micromegas in 2012 before (black) and after (red) the gain correction over the detector surface. Right: evolution of the x-ray signal efficiency chosen for the calculation of the limit to the axion-photon coupling strength in the 2012 data taking.

8.3.2 Background and tracking levels

Micromegas are daily calibrated, the rest of the time being devoted to measure the background level of the detector. The axion-sensitive periods, or tracking periods, are defined as those in which the magnet is pointing to the sun (tracking program set to solar tracking mode and the Sun is reachable), the magnetic field is turned on and higher than 8 T, the difference in the magnet vertical and horizontal position between predicted and measured value is below 10^{-2} and the corresponding gate valve is opened.

The background spectra of the cold bore area before and after cuts are shown if figure 8.6, while the background levels achieved at different signals efficiencies are shown in table 8.2. The cuts reduce the background level more than a factor 10^2. The background spectrum after cuts is dominated by the fluorescence peaks of the different elements surrounding the detector. The 8 keV peak corresponds to the copper K_α emission, while the peaks in the CAST RoI around 5 and 6 keV correspond to the fluoresnce emission of the stainless steel (iron and chromium K_α at 6.4 and 5.4 keV, respectively) vacuum pipe that connects the detector to the magnet.

The background and tracking spectra at 90% signal acceptance are shown in figure 8.17. The levels in the CAST RoI are compatible within 2σ, as it is noticed by comparing the values of table 8.2. The distribution of background and tracking events over the detector surface is shown on the right of figure 8.17. Since the region non-electronically instrumented shows neither background nor tracking, the effective area is reduced a factor 8%.

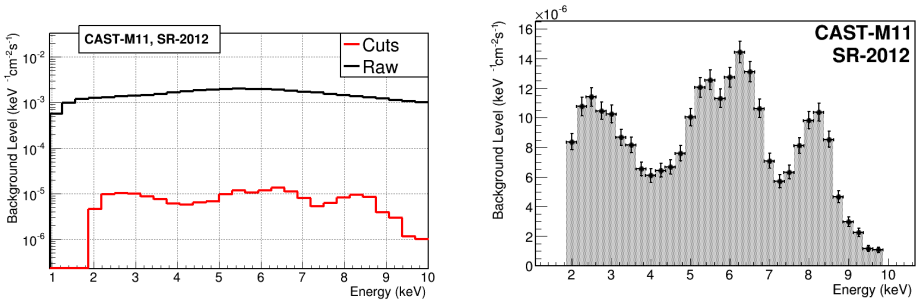

Figure 8.6: Sunrise Micromegas background spectra accumulated over the 2012 data taking campaign. On the left, the raw spectrum (black line) and the effect of the cuts (red line). On the right, a zoom to the final background spectrum obtained with 90% of signal acceptance both at 3 and 6 keV.

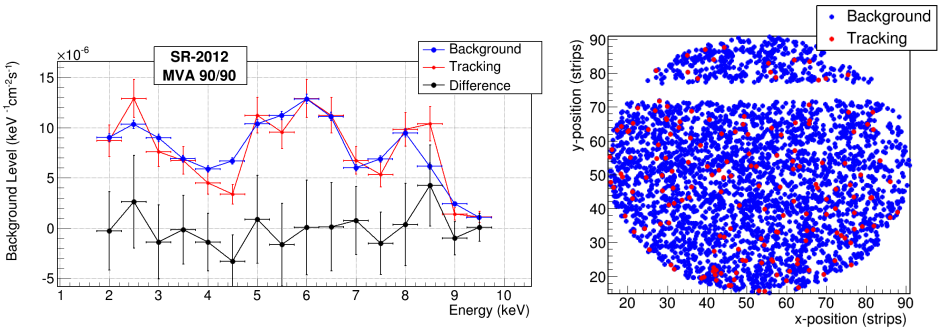

Figure 8.7: Background (blue) and tracking (red) spectra accumulated over the 2012 data taking campaign. The difference between both spectra is shown in black.

8.4 Sunset Micromegas performance

The sunset Micromegas detectors are filled with Ar+2%iC$_4$H$_{10}$ at 1.4 bar. As in sunrise, they are daily calibrated from the front side with two ^{55}Fe sources, for sunset 1 and 2, respectively. Remarkably, sunset detectors did not lose any solar tracking due to fault or malfunctioning.

Both detectors present a large active area, wide enough to cover the whole cold bore projection. The hitmap distribution and gain maps of figures 8.8 and 8.9 have been done using the full calibration data set acquired during the 2012 data taking campaign. The grid pattern of the hitmap distributions represent the shadow of the drift window strongback illuminated by frontal calibrations. The patterns show deformations towards the borders of the detectors, which are due to non-uniform electric drift fields. This effect is especially evident in sunset 2, which also shows larger dead regions in the corners of the active area.

Sunset 1 presents a shortcircuited strip around the strip number 20 in the y-direction, which is mostly out of the cold bore projection region. It shows very uniform gain over the active area, with fluctuations below 10%. On the other hand, sunset 2 presents two shortcircuited strips, one in the y-direction (strip number 15) and the other in the x-direction (strip number 35). While the first one is completely out of the cold bore projection, the second is inside it. Gain fluctuations are somewhat larger than in sunset 1, but the higher shifts tend to be towards the detector edges.

Figure 8.10 shows the calibration energy spectrum of sunset Micromegas detectors for the full calibration data set of the 2012 data taking campaign. The black line represents the energy of the raw data, while the red one represents the energy reconstructed correcting the fluctuations of the gain over the detector surface. The improvement in the energy resolution is not so relevant as in the sunrise Micromegas detector, given the more homogeneous response of sunset detectors. However, the energy resolution at 5.9 keV is poorer for the sunset detectors, even after the gain surface correction. In the inset of the figure, a logarithmic view of the spectra are shown, where the aluminum K_α emission peak at 1.5 keV can be noticed. This peak is due to the thin aluminum films making the windows of the ^{55}Fe source holder. This peak demonstrated energy thresholds well below the nominal CAST energy RoI.

The evolution of the gain, energy resolution at 5.9 keV and background level along the data taking campaign is presented in figure 8.11, both for sunset 1 and 2. The gain is stable in both detectors both in the mesh and strips signals. The fluctuations are typically below 10% along the roughly four months of data taking.

Sunset 1 shows a large step in the strips gain around 7th july, which is due to a programmed change in the amplification field. This detector had previously suffered sparks which limited its operation voltage but they disappeared after an intervention. Afterwards, increasing the mesh voltage was considered to be save enough, and it was consequently increased to have both detectors operating at the same operation point. The mesh gain of sunset 1 does not follow this gain step because the amplifier settings of the mesh signal are changed at the same time. Both detectors present a slight trend to slowly decrease starting from around 22nd July, which can be attributed

to a gas or pressure drift. From around 25th July, this trend disappears. The sunset 1 shows a ∼15% higher gain than sunset 2.

The energy resolution of sunset 1 and 2 at 5.9 keV are respectively around 20% and 22% FWHM for both strips and mesh charge. These values are quite far from the best results obtained with *microbulk* Micromegas. The reason for this, beyond the inhomogeneities and dead regions, is that although the detectors are operated at the plateau of maximum electron transmission, the mesh voltage is kept below the optimum for energy resolution. This decision is a conservative measure with the aim of preventing from sparks and detector damage. Sunset 2 suffered a progressive electronic noise increase peaking at around 15th of july (see mesh energy resolution on figure 8.11), when it was fixed by the replacement of a noisy Gassiplex front-end electronic card.

The background level obtained by both detectors are also very stable, compatible along the full campaign within poissonian errors.

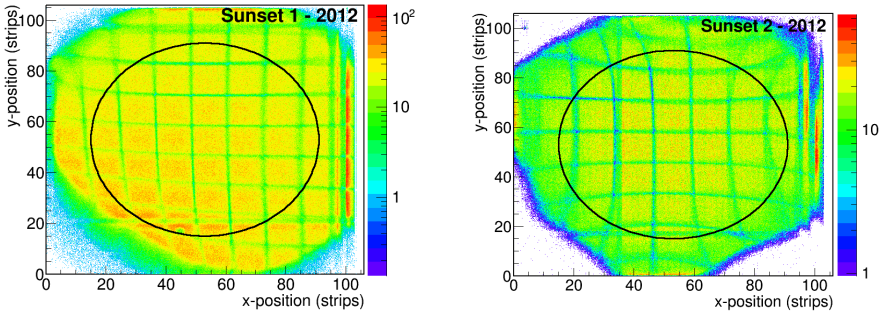

Figure 8.8: Calibration intensity maps of sunset Micromegas 1 (left) and 2 (right) along the 2012 data taking campaign. The strips pitch is 0.56 mm.

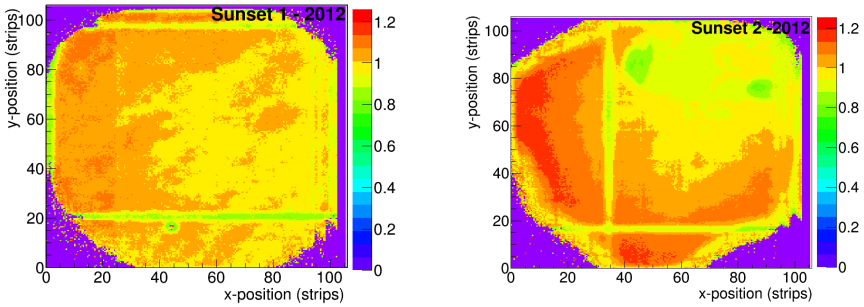

Figure 8.9: Gain maps of sunset 1 (left) and 2 (right) Micromegas along the 2012 data taking campaign.

8.4.1 Optimization of detectors' sensitivity

The detectors factor of merit of sunset 1 and 2 are studied for the 2012 data set using the multivariate and sequential cuts analysis. As noticed in figure 6.15, the behaviour is completely different for both detectors. In sunset 1 the factor of merit increases with the efficiency at 3 keV up to high values (∼85%), while in sunset 2 it decreases monotonically. In figure 6.16 it was shown how the increase in the efficiency at low energies in sunset 2 produces a critical rise in the background energy spectrum.

In basis of these results, the signal efficiencies finally chosen for the analysis of sunset 1 are 80 and 90% at 3 and 6 keV, respectively. Meanwhile, the chosen efficiencies for sunset 2 are 40 and

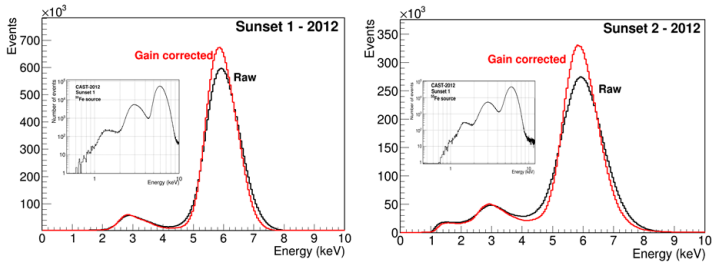

Figure 8.10: Calibration energy spectrum of sunset 1 (left) and 2 (right) in 2012 before (black) and after (red) the gain correction over the detector surface.

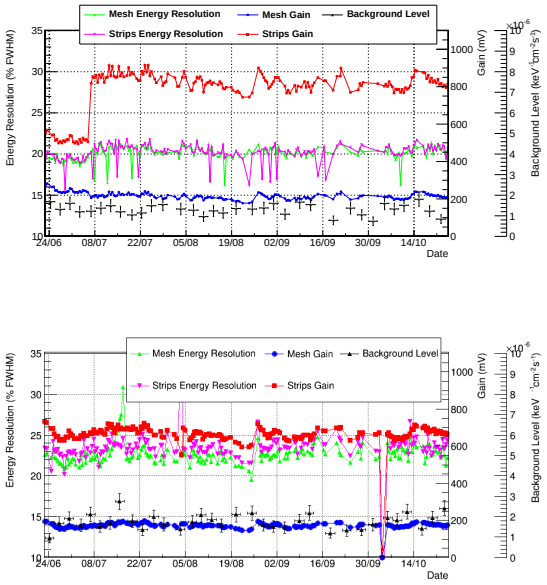

Figure 8.11: Evolution of the gain and energy resolution at 5.9 keV for the sunset 1 (top) and 2 (bottom) along 2012 data taking campgaign. The evolution of the background level for a signal acceptance of 40% and 75% at 3 and 6 keV is also shown.

75%. The evolution of the signal efficiency along the data taking campaign is shown on figure 8.12. The fluctuations are negligible and, for all purposes, they are assumed to be constant.

8.4.2 Background and tracking levels

The background spectra in the cold bore area of sunset detectors are shown in figures 8.13 and 8.14, while the background levels at different efficiencies are shown in table 8.2. The application of the cuts reduce the background level almost a factor 10^3.

The fundamental difference with respect to the sunrise spectral shape is that the iron peak is absent of both spectra. This is a result of the shielding upgrade reported in chapter 5. The spectra are now dominated by the copper K_α peak at 8 keV, its escape peak at 5 keV and the argon emission at 3 keV. As a result of its worse performance, the sunset 2 detector shows a background level significantly larger than the sunset 1 detector. The application of the muon veto cut described in section 6.3 produces a background reduction in sunset 1 and 2 of 23.2 $\pm$ 0.6% and 24.8 $\pm$ 0.6%, respectively. This is an important reduction considering that the scintillator veto coverage was not

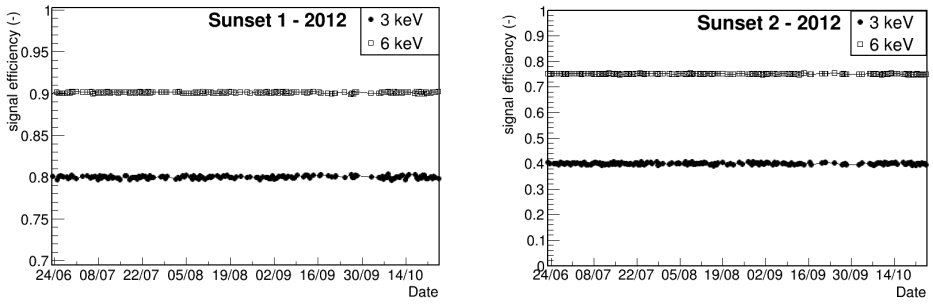

Figure 8.12: Evolution of the x-ray signal efficiency chosen for the calculation of the limit to the axion-photon coupling strength in the 2012 data taking.

optimal, as described in section 5.4. The good results motivated the upgrade of the system for following data taking periods.

The background levels here reported were the lowest ever achieved by a Micromegas detector operated at sea level, although they would be quickly surpassed in the following years by the new upgraded Micromegas detectors, as we will see in next chapter.

The background and tracking spectra of both detectors are shown in figure 8.15. The levels in the CAST RoI are compatible within 1σ, as it is noticed by comparing the values of table 8.2.

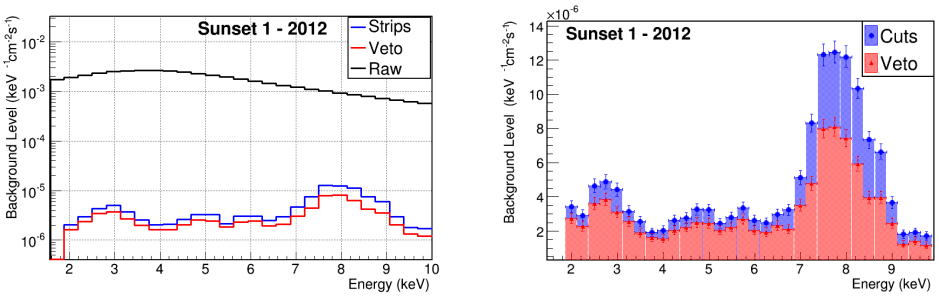

Figure 8.13: Sunset 1 Micromegas background spectra accumulated over the 2012 data taking campaign. On the left, the raw spectrum (black line), the effect of the cuts based on the mesh and strips observables (blue line) and the veto cut (red line). On the right, a zoom to the final background spectrum obtained with 80% & 90% signal acceptance at 3 and 6 keV, respectively.

Detector	Efficiency 3 & 6 keV	Time Background (hours)	Time Tracking (hours)	Level $[2-7]$ keV Background (10^{-6} keV^{-1}cm^{-2}s^{-1})	Level $[2-7]$ keV Tracking (10^{-6} keV^{-1}cm^{-2}s^{-1})
Sunrise	40 & 75	2376.3	136.0	5.2 ± 0.1	4.7 ± 0.4
Sunrise	90 & 90	2352.9	136.0	9.8 ± 0.1	9.0 ± 0.5
Sunset 1	40 & 75	2216.0	153.1	1.3 ± 0.1	1.1 ± 0.2
Sunset 1	80 & 90	2226.5	153.1	2.4 ± 0.6	2.1 ± 0.2
Sunset 2	40 & 75	2251.9	153.1	1.7 ± 0.1	1.9 ± 0.2
Sunset 2	75 & 75	2251.9	153.1	3.7 ± 0.4	3.8 ± 0.2

Table 8.2: Summary of background and tracking levels of Micromegas detectors in CAST 2012 data taking campaign.

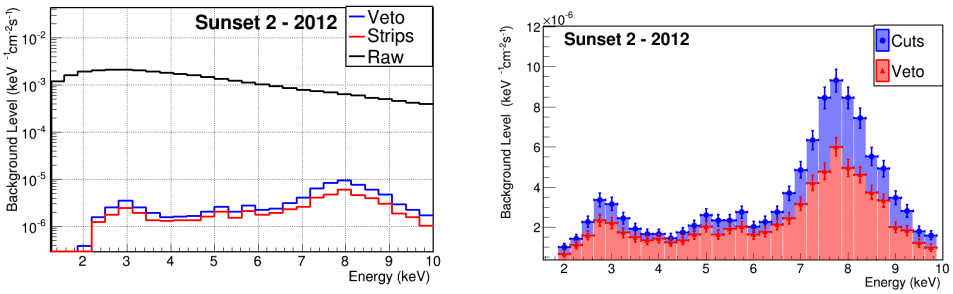

Figure 8.14: Sunset 2 Micromegas background spectra accumulated over the 2012 data taking campaign. On the left, the raw spectrum (black line), the effect of the cuts based on the mesh and strips observables (blue line) and the veto cut (red line). On the right, a zoom to the final background spectrum obtained with 40% & 75% signal acceptance at 3 and 6 keV, respectively.

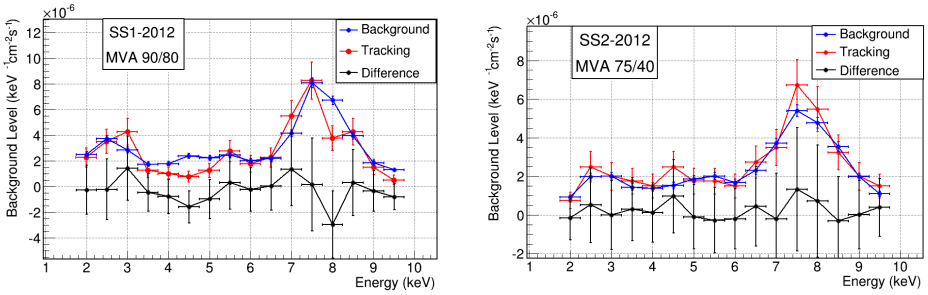

Figure 8.15: Background (blue) and tracking (red) spectra accumulated over the 2012 data taking campaign in the sunset Micromegas 1 (left) and 2 (right). The differece between both spectra is shown in black.

8.4.3 Comparison between 2011 and 2012 levels

The upgrade in the sunset system lead to an important improvement in the background level of the detectors and, consequently, in the sensitivity of the experiment. Figure 8.16 compares the background spectra of sunset detectors during 2011 and 2012 data taking campaigns at roughly the same signal efficiency. The overall reduction in 2−7 keV is a factor 4−5, while the detectors' figure of merit increases about a factor 2.

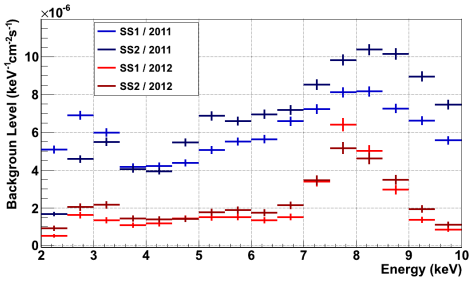

Figure 8.16: Comparison between sunset Micromegas background spectra in 2011 and 2012, both years with approximately equivalent signal acceptance.

8.5 Statistical tests to background data

The poissonian nature of the background events is checked by splitting the background time of each detector in several time length units. The distribution of the number of events in each time unit produces the results of figure 8.17. The experimental data are well fitted to a poissonian distribution as the curve in the figures shows.

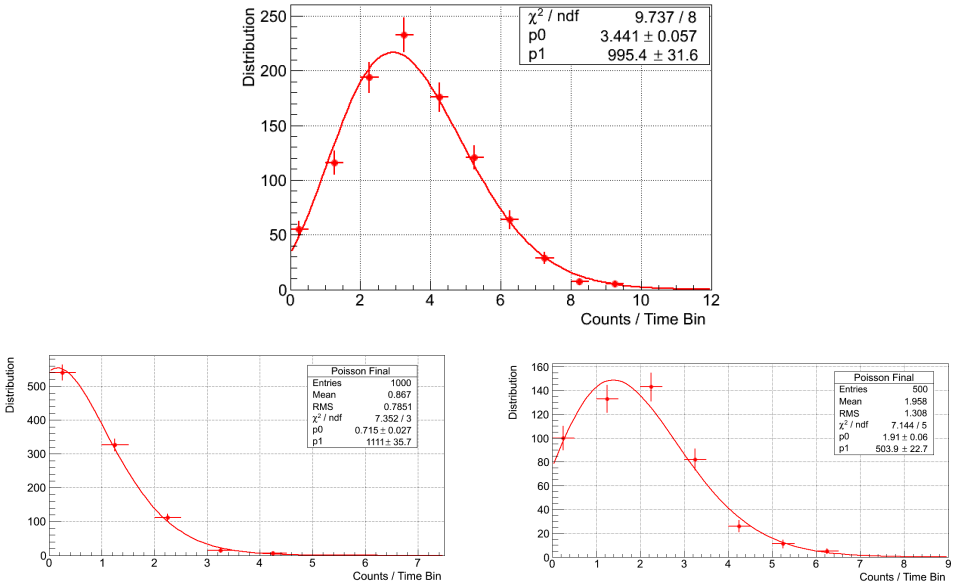

Figure 8.17: Distribution of the number of background events after cuts in a fixed time length .

8.6 Coupling constant limit with the 2012 ^{4}He filling

In this section we present the data analysis and the results of the 2012 data acquired with the three Micromegas detectors, whose performance along the season is reported above. From the absence of a positive signal, the unbinned likelihood method is used to derive an upper limit on the axion to photon coupling strength as a function of the axion mass, $g_{a\gamma}(m_a)$.

8.6.1 The maximum likelihood method

The analysis of the data is performed using the maximum likelihood method with an unbinned likelihood function. The low statistics of each density step motivated the use of likelihood methods for the CAST phase II data analysis. During the first ^{4}He phase a binned likelihood function in the density steps was used, arguing that each density step was sensitive to a well defined axion mass resonance given by a constant buffer density during a full tracking run. However, an unbinned likelihood function better accounts for the pressure variations in the cold bore during a pressure setting, which are not negligible as figure 8.1 shows, so the unbinned method was preferred thereafter. The mathematical derivation of the unbinned likelihood function from the original binned function is shown in appendix C. The likelihood function used in this work for the 2012 ^{4}He Micromegas data is

$$\log \mathcal{L} \propto -R_T + \sum_i^n \log R(t_i, E_i, d_i) \tag{8.1}$$

where R_T is the expected number of counts from the axion to photon conversion over all the exposure time, energy and detectors. The sum is over each of the n detected counts during the tracking time, for an expected rate $R(t_i, E_i, d_i)$ as a function of the event time t_i, energy E_i and detector d_i, given by the expresion

$$R(t, E, d) = B_d + S(t, E, d) \tag{8.2}$$

where B_d is the background level of the detector d and $S(t, E, d)$ is the expected rate from axion conversion in the detector d given by

$$S(t, E, d) = \frac{d\Phi_a}{dE} P_{a\to\gamma} A \varepsilon_d \tag{8.3}$$

Here, ε_d is the detector efficiency, A is the magnet bore area, $\frac{d\Phi_a}{dE}$ is the differential solar axion flux of equation 3.10, and $P_{a\to\gamma}$ is the axion to photon conversion probability inside a strong magnetic field given in equation 3.13. The detection time of each tracking counts t_i determines the conditions of axion detection given by the cold bore density at that particular time. The expected axion flux $S(t, E, d)$ is evaluated at the time the tracking count was detected.

The axion mass m_a participates of the likelihood function through the conversion probability, which is enhanced for axion masses that match the refractive photon mass m_γ as determined by the buffer gas density. Therefore, for a given axion mass m_a, only the counts for which the coherence condition is fulfilled will contribute significantly to the likelihood function $\log \mathcal{L}$.

By minimizing $\log \mathcal{L}$ we get the best fit value for the coupling constant $(g^4_{a\gamma})_{\min}$. This value is compatible with the absence of a signal in the entire axion mass range and thus an upper limit on $g_{a\gamma}(m_a)$ can be estimated by integrating the Bayesian probability on g^4 over the phyiscs region (positive values) till getting the 95% of it:

$$\frac{\int_0^{g^4_{95}} P(g^4) dg^4}{\int_0^{\infty} P(g^4) dg^4} = 0.95 \tag{8.4}$$

Here, the Bayesian probability is indentified as the likelihood function, which implies that a prior probability flat on g^4 has been assumed. The full contour line $g_{a\gamma}(m_a)$ is thus obtained at 95% confidence level. The results of the 2012 data taking with the three Micromegas detectors are shown below.

8.6.2 Limit on the coupling constant versus axion mass

The results presented in this work correspond to the data aquired by the three Micromegas detectors during 2012, using ^{4}He as buffer gas. The total exposure of each detector in axion-sensitive conditions is shown in table 8.2, while in figure 8.18 we show the exposure as a function of the measured gas pressure inside the magnet bores. The first part of the data taking was devoted to re-scan the axion mass region 0.39–0.42 eV (13.9–15.5 mbar at 1.8 K), which was done in 17 pressure steps, as can be noticed on the right of figure 8.2. In the second part, a single setting at around $m_a \simeq 0.2$ eV (3.8 mbar at 1.8 K) was scanned.

For this run, the gas density was calculated from the equation of state of the ^{4}He gas using the measured cold bore temperature, gas pressure and magnet vertical angle. In the ^{3}He filling case, the gas dynamics affects the density distribution along the cold bore, shortening the region with uniform density. In the ^{4}He case the densities involved are relatively low and these effects are negligible. Therefore, the coherence length was taken as the full magnet length of 9.26 m. Computational fluid dynamic simulations showed that for ^{3}He gas at pressures around 14 mbar, the coherence length was above 8 m. Extrapolating these results to the ^{4}He case, the final effect on the limit on $g_{a\gamma}$ of using a magnet length of 8 m instead of 9.26 m is below 7%.

The stability of the background level over the entire campaign allow us to define the background used in the likelihood function as the total number of counts in the full background measuring periods. Other background definitions (background level measured from 5 days before to 15 after each tracking) were checked for consistency, but the low background counting (i.e., low statistics)

produced larger statistical fluctuations. The energy binning has been taken as 0.5 keV, limited by the detectors' energy resolution.

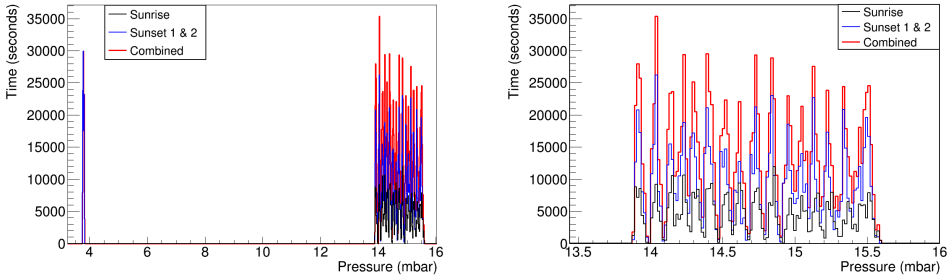

Figure 8.18: Left: exposure time as a function of the pressure in the cold-bore at 1.8 K. A single setting at $m_a \simeq 0.20$ eV, corresponding to ∼3.8 mbar was covered, and 17 pressure settings in the range 13.9–15.5 mbar with step size 0.1 mbar (right) were scanned, corresponding to the axion mass range 0.39–0.42 eV.

The overall efficiency as a function of the energy of the Micromegas detectors (quantum and signal efficiencies) used for the analysis of this data set is shown in figure 8.19 (left). Whilst sunrise and sunset 1 present similar efficiencies, sunset 2 shows lower values due to the reduced signal efficiency used in the discrimination cuts. The total exposure and the overall detector efficiencies are used to calculate the number of expected x-rays N_γ from axion-to-photon conversion in the magnet bores as a function of the axion mass (see figure 8.19, right).

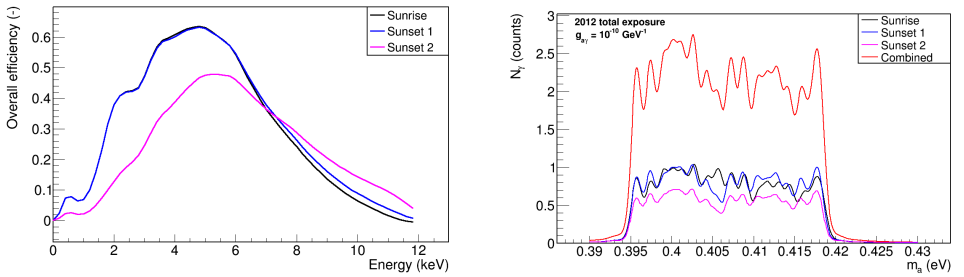

Figure 8.19: Left: overall efficiency of the three Micromegas detectors. Right: number of expected photons from axion-to-photon conversion, assuming $g_{a\gamma} = 10^{-10}$ GeV^{-1}, as a function of the axion mass, after integrating over all the 2012 exposure for the three Micromegas detectors.

The likelihood function described in the previous section (equation 8.1) is built for each axion mass and its maximization gives the best-fit value $(g^4_{a\gamma})_{\min}$. Figure 8.20 shows the likelihood function for a given axion mass ($m_a = 0.4$ eV) as a function of $g^4_{a\gamma}$.We observed before (see table 8.2) that tracking levels are compatible with our background definition, but this is not enough to exclude an axion signature. The standard deviation σ_g of $(g^4_{a\gamma})_{\min}$ is calculated according to equation C.4, which allow us to calculate the number of standard deviations from $(g^4_{a\gamma})_{\min}$ to $g_{a\gamma} = 0$ (i.e., the null-hypothesis) for each axion mass (see figure 8.21). Note that the likelihood distribution is asymmetrical, so the standard deviation to the right $\sigma_{g,r}$ and left $\sigma_{g,l}$ of the minimum will differ. In the case, $(g^4_{a\gamma})_{\min} < 0$ (un-physical value), $\sigma_{g,r}$ is used; while $\sigma_{g,l}$ is used for positive values of $g_{a\gamma}$. In our data set, we find no axion signature and thus an upper limit on $g_{a\gamma}$ is extracted using equation 8.4.

The computed upper limits on $g_{a\gamma}$ for the axion mass region $0.39 < m_a < 0.42$ is shown in figure 8.21, where the contribution from each individual detector is shown. The combined limits for this mass range and for the "candidate setting" around 0.2 eV is shown in figure 8.22, where

previous CAST limits and other constrains (horizontal branch (HB) stars, and the hot dark matter (HDM) bound) are displayed. In contrast to previous results, the structure of the $g_{a\gamma}(m_a)$ curve has a smooth shape, because of considerably larger exposure time per step, resulting in smaller statistical fluctuations. Note that the limit obtained crosses the KSVZ axion line near the highest possible ^{4}He pressure. The average values of the limits on $g_{a\gamma}$ are shown in table 8.3.

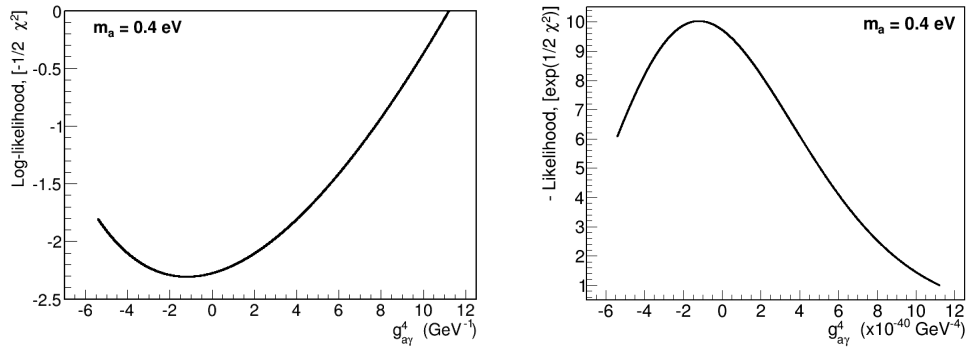

Figure 8.20: Left: log-likelihood function versus $g^4_{a\gamma}$ for $m_a = 0.4$ eV. In this case, $(g^4_{a\gamma})_{min}$ has a negative (un-physical) value. Right: $P(g^4)$ versus $g^4_{a\gamma}$ for $m_a = 0.4$ eV. Integration of equation 8.4 is done over this distribution, starting from $g_{a\gamma} = 0$.

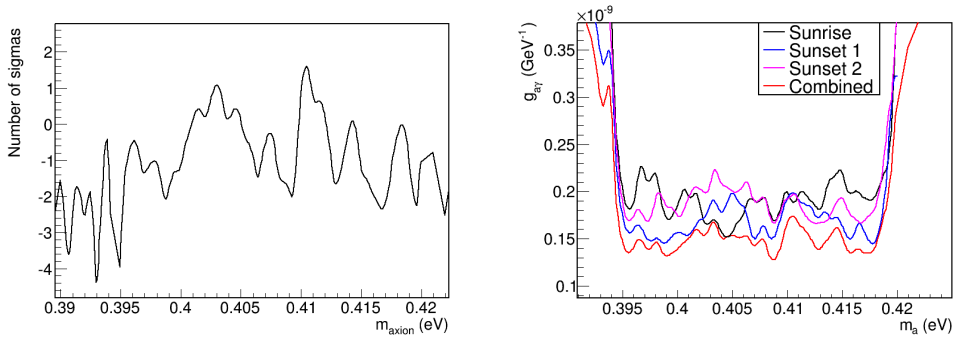

Figure 8.21: Left: number of standard deviations from $(g^4_{a\gamma})_{min}$ to the null hypothesis ($g_{a\gamma} = 0$). A negative (un-physical) number of standard deviations from $g_{a\gamma} = 0$ correspond to negative values of $(g^4_{a\gamma})_{min}$, as is the case for $m_a = 0.4$ eV (see previous figure). Right: exclusion curve (95% C.L.) in the m_a–$g_{a\gamma}$ plane achieved with the Micromegas detectors during the 2012 CAST data taking campaign, using ^{4}He as buffer gas. Here, we focus on the contribution of the different detectors in the axion mass region 0.39–0.42, while the next figure shows the combined result in all the axio mass range, including the "candidate setting" at 0.2 eV.

Year	Mass range [eV]	Detector	$(g_{a\gamma})_{\text{limit}}$ at 95% C.L. [$\times 10^{-10}$ GeV^{-1}]
2012	0.39–0.42	Sunrise	< 1.89
		Sunset 1	< 1.67
		Sunset 2	< 1.86
		Combined	< 1.47
2012	$\sim$0.2	Combined	< 1.40

Table 8.3: Summary of limits on the axion-to-photon coupling constant from the ^{4}He filling phase of 2012 with the Micromegas detectors.

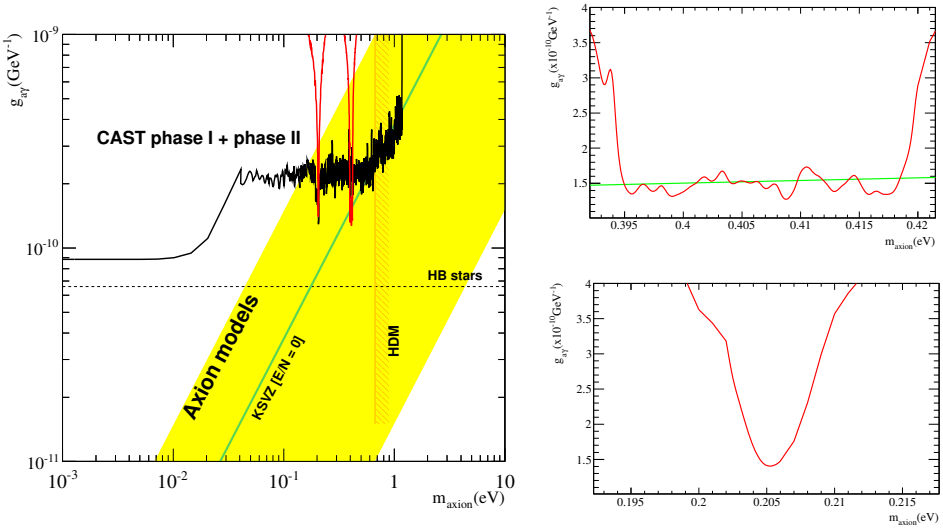

Figure 8.22: Left: exclusion regions in the m_a–$g_{a\gamma}$ plane achieved by CAST in the vacuum phase and with ^{4}He and ^{3}He filling. We also show constraints from horizontal branch (HB) stars, and the hot dark matter (HDM) bound. The yellow band represents typical theoretical models with $|E/N - 1.95| = 0.07$–7. The green solid line corresponds to $E/N = 0$ as in the KSVZ model [198, 199], a typical hadronic axion model. In red we show the limits near $m_a = 0.2$ and 0.4 eV from the Micromegas detectors in the 2012 data taking campaign with ^{4}He gas. Right: expanded view of the limit achieved during the 2012 CAST data taking campaign, using ^{4}He as buffer gas. The plot on the bottom corresponds to the "candidate setting" at 0.2 eV, while the plot on the top is the excluded region above 0.39 eV. The green line represents the KSVZ benchmark model with $E/N = 0$.

Chapter 9

The new vacuum data taking phase and its MM detectors

Contents

9.1 Introduction

Since 2013, CAST has returned to vacuum measurements (i.e., low-mass regime, $m_a \lesssim 0.2$ eV) with increased sensitivity and various improvements. Notably, for the 2014 season an additional x-ray telescope was installed in front of the sunrise Micromegas detector. In this chapter, we first review the motivation of measuring in this low-mass regime. Then, we report on the Micromegas detectors performance over the 2013 season and we extract new limits on $g_{a\gamma}$. Subsequently, we describe the installation and commissioning of the new x-ray telescope in 2014, and we report on the results obtained with the combined system of optics plus detector. We extract limits on $g_{a\gamma}$ with the Micromegas data acquired in the 2014 season, and finally, we combine 2013 and 2014 results.

9.2 Motivation and physics potential of the vacuum phase

CAST carried out its phase I, with vacuum in the magnet bores, in 2003 and 2004. The limit obtained to the axion-photon coupling $g_{a\gamma} < 8.8 \times 10^{-11}$ GeV^{-1} for $m_a < 0.02$ eV, the main result of CAST phase I, is now widely known and referenced by the community.

Technologically, CAST had the possibility to operate in vacuum with increased sensitivity compared with the 2003/04 runs, based on the ideas and developments that we are putting forward

in the context of IAXO (the International Axion Observatory), the future axion helioscope. The tests of these ideas in CAST are *per se* motivated in view of the large scale effort represented by IAXO. Two of the innovations in which CAST success has relied on are the use of x-ray focalization to increase the signal-to-noise ratio, and the use of low background techniques to reduce the detector backgrounds. The first strategy is exemplified by the CCD+ABRIXAS telescope detection line (see section 4.8.1), while the second one by the other 3 detection lines based on low background Micromegas detectors. Both options leading to similar final sensitivity. The new sunrise system, installed in 2014, combines both strategies in the same system: a new x-ray optics coupled to a low background Micromegas detector. The installation and commissioning of this sytem is presented in section 9.4. The implementation of this concept in CAST not only increases the signal-to-noise ratio of the sunrise Micromegas, and the sensitivity of the experiment, but also serves as a pathfinder project to test the technological options being proposed to build large scale, cost effective, x-ray optics with customized parameters for the future IAXO.

Although vacuum operation in CAST does not provide sensitivity to QCD axion models, the possibility of pushing CAST vacuum limit to lower $g_{a\gamma}$ values is also highly motivated, both theoretically and observationally. A sensitivity as low as $g_{a\gamma} \simeq 0.6 \times 10^{-10}$ GeV^{-1} is aimed for the low axion mass range, being able even to suprass a recently improved stellar-evolution bound from the helium-burning lifetime of globular-cluster stars [105]. A list of the motivations for the vacuum run are listed here:

- Although the axion is the best motivated and most studied prototype, a whole category of particles called axion-like particles (ALPs) or, more generically, weakly interacting slim particles (WISPs), are often invoked in several scenarios. Although not necessarily related with the axion, they share part of its phenomenology, and therefore they would be searchable by similar experiments. ALPs often appear in extensions of the SM as pseudo Nambu-Goldstone bosons of new symmetries broken at high energy. But most interestingly, string theory also predicts not just one ALP, but in most cases a rich spectrum of them (including the axion itself). Remarkably, the region of the ALP parameter space corresponding to the first orders of magnitude just beyond the current CAST bound in $g_{a\gamma}$ correspond to intermediate string scales and are specially motivated as they would contribute to the natural explanation of several hierarchy problems in the SM.

- Another point worth noting is the possible connection between ALPs and dark matter. Recently it has been noted that the non-thermal production mechanisms attributed to axions are indeed generic to ALPs. The range of ALP parameters including ALP models possibly solving the DM problem gets substantially enlarged both in $g_{a\gamma}$ and m_a and in particular includes part of the region that an improved CAST vacuum run can probe.

- Last but not least, a number of unexplained astrophysical observations may indicate the effects of an ALP. They must be treated with caution because usually an alternative explanation using standard physics or an uncontrolled systematic effect cannot be ruled out. One of them is the observation of VHE photons with directions correlated with very distant sources, apparently incompatible with the expected opacity of the intergalactic medium at such energies. Although not without controversy, this evidence might be supported by several independent observations. Different scenarios invoking photon-ALP oscillations triggered by intervening cosmic magnetic fields have been invoked by several authors to account for the unexplained observations. Interestingly, most of the required ALP parameters coincide roughly in requiring very small ALP mass $m_a < 10^{-10} - 10^{-7)}$ eV (to maintain coherence over sufficiently large magnetic lengths) and a $g_{a\gamma} \sim 10^{-12} - 10^{-10}$ GeV^{-1}(see figure 2.5). These parameters are far from the standard QCD axions, however, as more generic ALP models, they lie just beyond the best current experimental limits on $g_{a\gamma}$ from CAST and are therefore feasible. They also roughly correspond to the parameters favored by string theory commented before. Any improvement beyond the current CAST vacuum limit will imply that part of this parameter space region would be probed.

9.3 The 2013 data taking campaign

The major upgrades on the Micromegas detectors with respect to the previous year have been extensively discussed in chapter 5. In brief, a new dedicated muon veto system based on plastic scintillators was installed in the *sunset* side, around the shielding of the Micromegas detectors; and new readout electronics were used. Besides, the *sunrise* detector, shielding and vacuum line were redesigned. During the commissioning of this detector, many problems arose, as described in section 5.2.2. Finally, the detector worked installed in the CAST vacuum line, but only for around a week, at the very end of the CAST 2013 data taking campaign. The solution of all these problems paved the way for the 2014 season and for the installation of the new telescope (see section 4.8.1), but the exposure of the sunrise Micromegas during the 2013 data taking is very limited and the contribution to the sensitivity of the experiment is neglibible. Consequently, only the data acquired by the sunset Micromegas detectors are considered on the analysis presented in this work.

The data taking started on 22nd of september and finished on 7th december, for a total season of 76 days. The different technical problems, interventions and magnet quenches produced a solar tracking efficiency of around 83% (63 days). The sunset 1 Micromegas completed all the solar trackings for a total exposure of 93.7 hours. On the other hand, sunset 2 missed three solar trackings (95% efficiency) because it presented a persisten leak current that compeled us to replace it by a spare one. The total exposure of this line is 88.0 hours.

9.3.1 Micromegas performance

Both detectors present a large active area, wide enough to cover the whole cold bore projection. Sunset 1 detector is the same that the one used in the previous campaign, so its active are does not change much: the entire detector surface is active, except regions very close to the corners (see figure 9.1) and a small spot at the border of the cold bore area due to glue or kapton residuals. Sunset 2, instead, presents some missing strips at the central part and more relevant border effects.

As in the previous season, sunset 1 presents a shortcircuited strip, which is mostly out of the cold bore projection region, and it shows very uniform gain over the whole surface, with fluctuations below 10% . On the other hand, sunset 2 presents five bands in the y-direction and one in the x-direction with lower gain, corresponding to disconnected strips (see figure 9.2).

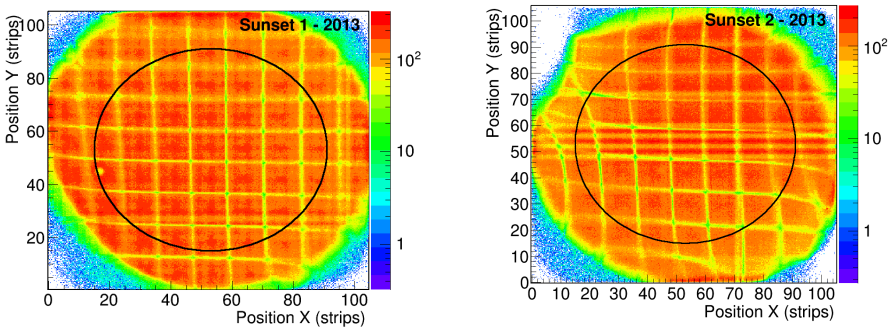

Figure 9.1: Calibration intensity maps of sunset Micromegas 1 (left) and 2 (right) along the 2013 season. The strips pitch is 0.56 mm.

Figure 9.3 shows the calibration energy spectra of sunset Micromegas detectors for the full calibration data set of the 2013 data taking campaign. The black line represents the energy of the raw data, while the blue and red ones represent the spectra after fiducial and discrimination cuts. The energy threshold is situated well below 2 keV.

The detector gain shifts during the data taking are at the level of 15-20% in both sunset detectors (see figure 9.4). The energy resolution in sunset 1 is around 22-23% FWHM at 5.9 keV for both mesh and strips signals, while in sunset 2 it is worse, aroud 25% FWHM. This fact is

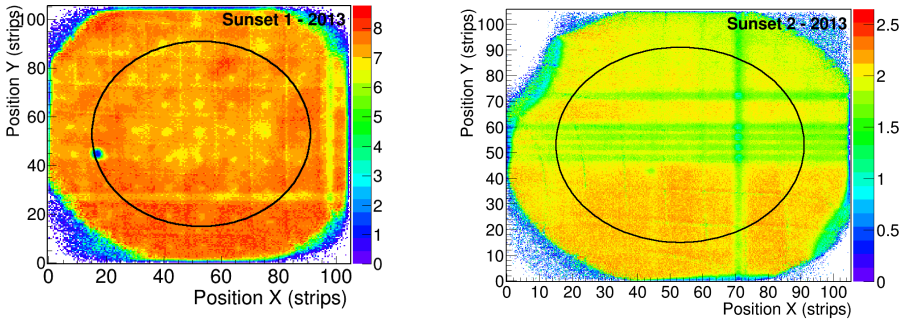

Figure 9.2: Gain maps of sunset 1 (left) and 2 (right) Micromegas along the 2013 season.

attributed to the non-instrumented strips present in the central part of sunset 2 surface. Both values for the energy resolution are slightly higher than those achieved during the 2012 season. It was decided that, after the 2013 run, the spare detector with best performance would replace the one in sunset 2.

From the Micromegas detectors side, the 2013 run went quite smoothly, except for the fact that an electronic noise above threshold came out sporadically, almost saturating the acquisition rate. This noise was related with the magnet movement and it only occurred at certain magnet positions and motor frequencies. The exposure lost because of this reason is below 5%.

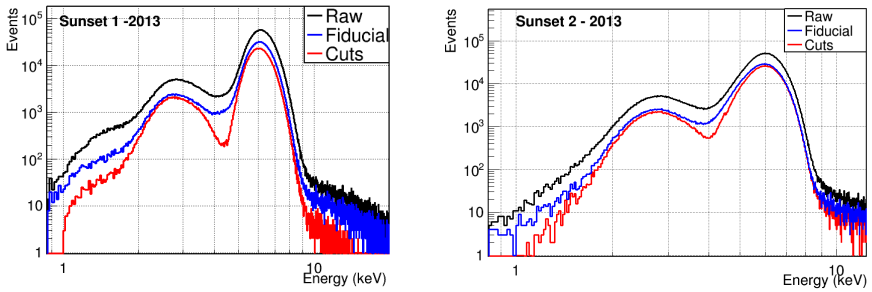

Figure 9.3: Calibration energy spectra of sunset Micromegas 1 (left) and 2 (right). We also the spectra after fiducialization and after cuts. As can be noticed, the energy threshold is well below 2 keV.

9.3.2 Optimization of detectors' sensitivity

The detectors factor of merit of sunset 1 and 2 are studied for the 2013 data set using the multivariate, sequential and likelihood cuts analysis. The figure of merit map for all the possible combinations of efficiencies is shown in figure 9.5. The optimal sensitivity to $g_{a\gamma}$ is achieved at around 90% and 40% signal efficiencies at 6 and 3 keV, respectively.

These results determine the signal efficiencies chosen for the statistical search of an axion signature, or the derivation of an upper limit on $g_{a\gamma}$ in the absence of such a signature. The overall efficiency (quantum efficiency convoluted with the efficiency to -ray events) is shown in figure 9.6 for sunset 1 and 2.

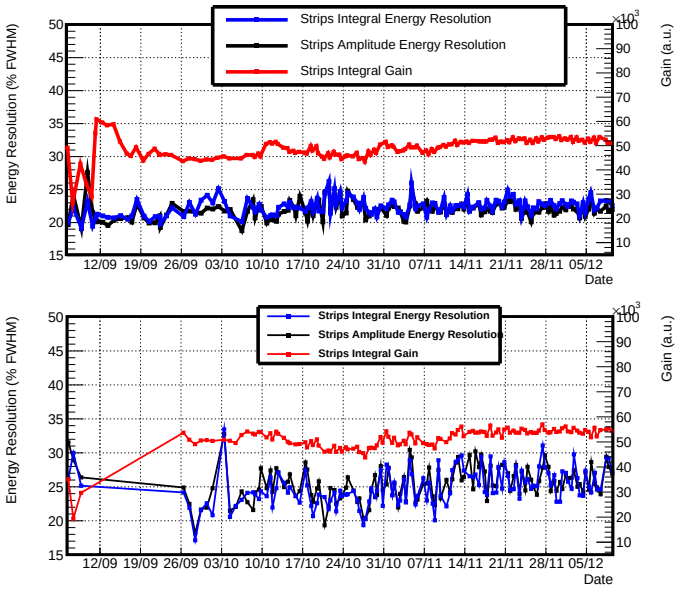

Figure 9.4: Evolution of the gain and energy resolution at 5.9 keV for the sunset 1 (top) and 2 (bottom) along 2013 data taking campgaign.

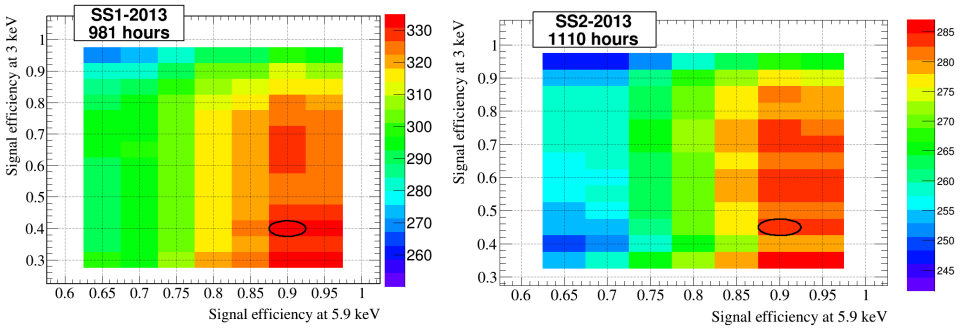

Figure 9.5: Sunset 1 (left) and 2 (right) factor of merit for several combinations of efficiencies at 3 and 6 keV in the 2013 season.

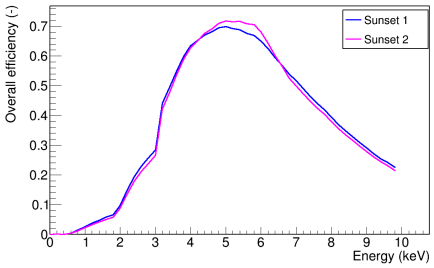

Figure 9.6: Overall detector efficiency as a function of the the x-ray energy for the sunset 1 and 2 on the 2013 CAST data taking campaign.

9.3.3 Background and tracking levels

The background level of the detectors is measured during the periods in which the magnet is not tracking the sun. The background is defined from a total time of 1680.9 hours (9.4 hours of death time) in sunset 1 and 1383 hours (9.0 hours of death time) in sunset 2. The background energy spectra in the cold bore area are shown in figures 9.7 and 9.8. The spectral characteristics are similar to those described before for the sunset detectors of 2012.

The background levels achieved at different signal efficiencies are shown in table 9.1. Particularly, at the efficiencies chosen for the $g_{a\gamma}$ upper limit calculation the levels are 1.0 and 1.3×10^{-6} keV^{-1}cm^{-2}s^{-1}for sunset 1 and 2, respectively. The levels achieved are lower than ever before because of the two main upgrades carried out for this season: the new discrimination tools provided by the upgraded readout electronics (see chapter 6), and the higher efficient muon veto, that reduces the background an extra factor ∼40%, instead of the 25% reduction achieved in the 2012 CAST data taking campaign.

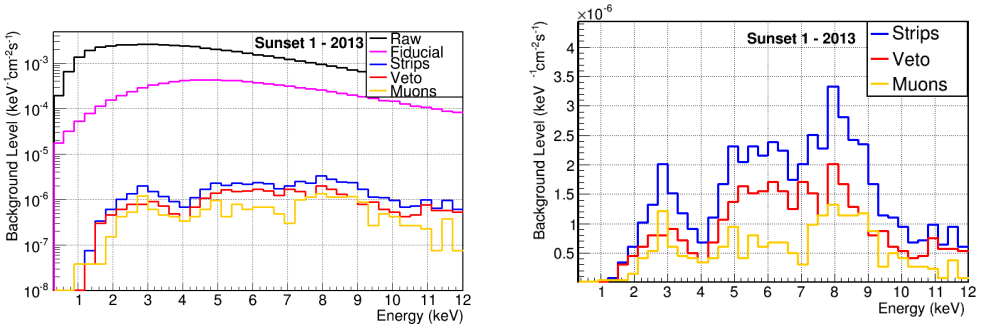

Figure 9.7: Sunset 1 Micromegas background spectra accumulated over the 2013 season. On the left, the raw spectrum (black line), the effect of the cuts based on the strips observables (blue line) and the veto cut (red line). On the right, an expanded view of the final background spectrum obtained with 40% & 90% signal acceptance at 3 and 6 keV, respectively.

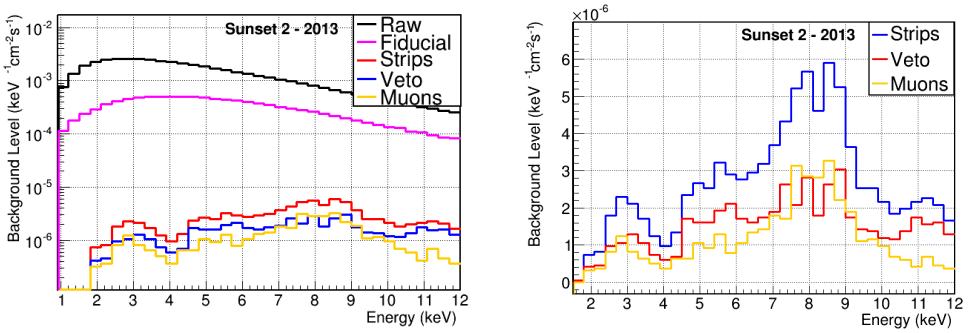

Figure 9.8: Sunset 2 Micromegas background spectra accumulated over the 2013 season. On the left, the raw spectrum (black line), the effect of the cuts based on the strips observables (blue line) and the veto cut (red line). On the right, an expanded view of the final background spectrum obtained with 40% & 95% signal acceptance at 3 and 6 keV, respectively.

The background and tracking spectra for both detectors are shown in figure 9.9. The levels in the CAST RoI are compatible within 1σ, as it is noticed by comparing the values in table 9.2, so no axion signature is evident.

Detector	Efficiency 3 & 6 keV	Background time (hours)	Level $[2-7]$ keV Strips (10^{-6} keV^{-1}cm^{-2}s^{-1})	Level $[2-7]$ keV Veto (10^{-6} keV^{-1}cm^{-2}s^{-1})	Veto reduction (%)
Sunset 1	40 & 75	1680.9	1.2 ± 0.1	0.8 ± 0.1	36
	75 & 75		1.8 ± 0.1	1.1 ± 0.1	39
	40 & 90		1.6 ± 0.1	1.0 ± 0.1	37
Sunset 2	40 & 75	1383.2	1.8 ± 0.1	1.0 ± 0.1	41
	75 & 75		2.4 ± 0.1	1.4 ± 0.1	41
	40 & 95		2.2 ± 0.1	1.3 ± 0.1	42

Table 9.1: Summary of background and tracking levels of Micromegas detectors in CAST 2013 data taking campaign.

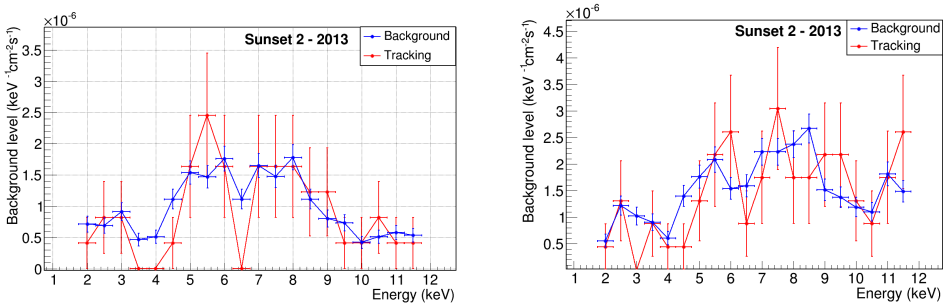

Figure 9.9: Background (blue) and tracking (red) spectra accumulated over the 2013 data taking campaign in the sunset Micromegas 1 (left) and 2 (right).

Detector	Efficiency 3 & 6 keV	Tracking time (hours)	Level $[2-7]$ keV Background (10^{-6} keV^{-1}cm^{-2}s^{-1})	Level $[2-7]$ keV Tracking (10^{-6} keV^{-1}cm^{-2}s^{-1})
Sunset 1	40 & 90	93.7	1.0 ± 0.1	0.8 ± 0.2
Sunset 2	40 & 95	88.0	1.3 ± 0.1	1.0 ± 0.2

Table 9.2: Comparison of the background and tracking levels in the energy RoI obtained with the sunset 1 and 2 during the CAST 2013 season, with vacuum in the magnet bores. The efficiencies are chosen to maximize the sensitivity.

9.3.4 Coupling constant limit with the 2013 vacuum data

The maximum likelihood method, described in section 8.6, is used to analyse the CAST 2013 data taking campaign, operating with vacuum in the magnet bores. The coherence length is taken as the full magnet length, 9.26 m, as there are no effects from gas dynamics that could shorten it. The remaining experimental parameters determining the sensitivity are fixed by the experiment, except for those reported in the previous sections: exposure, background and tracking counting rates, and efficiency curves.

From the absence of an axion signature, an upper limit on the axion to photon coupling strength as a function of the axion mass, $g_{a\gamma}(m_a)$, is extracted (figure 9.10). The contributions of the two detectors and the combined result are presented in the figure and the values are shown in table 9.3. The combined upper limit of the CAST 2013 vacuum run using only the sunset Micromegas detectors is $g_{a\gamma} < 0.80 \times 10^{-10}$ GeV^{-1} at 95% confidence level for axion masses $m_a < 0.02$ eV. This preliminary limit is slightly more stringent than the one achieved in CAST

phase I during the 2003 and 2004 runs.

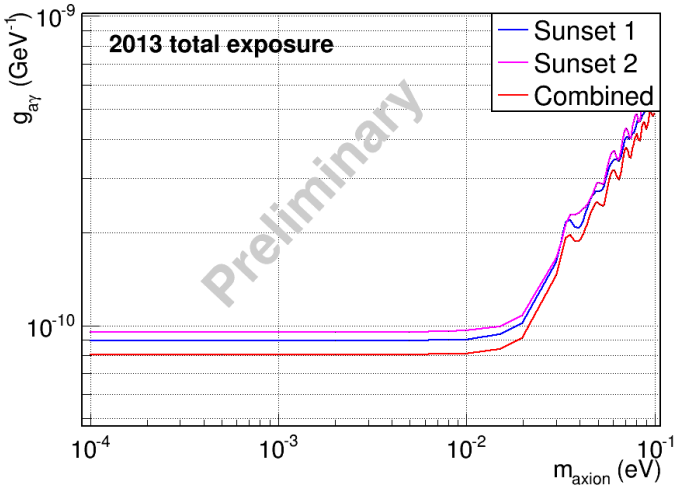

Figure 9.10: Exclusion curve (95% C.L.) in the m_a–$g_{a\gamma}$ plane achieved with the Micromegas detectors during the 2013 CAST data taking campaign, with vacuum in the magnet bores. The contributions of sunset 1 and sunset 2 are shown, as well as the combined result.

Year	Mass range [eV]	Detector	$(g_{a\gamma})_{\text{limit}}$ at 95% C.L. [$\times 10^{-10}$ GeV^{-1}]
2013	$\lesssim 0.02$	Sunset 1	< 0.89
		Sunset 2	< 0.95
		Combined	< 0.80

Table 9.3: Summary of limits on the axion-to-photon coupling constant from the vacuum phase of 2013 with the Micromegas detectors.

9.4 The 2014 data taking campaign

The vacuum run continued during 2014 with the aim of reaching a sensitivity for $g_{a\gamma} \simeq 0.6 \times 10^{-10}$ GeV^{-1} in the low-mass regime. From the Micromegas side, the main novelties were the installation of a telescope in the sunrise line, with an improved low-background detector (that solved the problems experimented the previous season) situated at its focal plane (see figure 9.11).

Here, describe the line in detail and review the installation and alignment processes, as well as the commissioning and the performance of the sunrise Micromegas along the CAST 2014 data taking campaign. Finally, we look for an axion signature in the data acquired with the three Micromegas detectors. No such a signal is observed, and a limit to $g_{a\gamma}$ is extracted.

9.4.1 A Micromegas detector coupled to a slumped-glass telescope

In 2014, a new SRMM line was installed and commissioned in CAST. The system was developed as a technological pathfinder for IAXO, combining two of the techniques (optics and detector) proposed in the technical design of the project. The x-ray detector system is a shielded Micromegas-based TPC made from radiopure materials and using the microbulk technique(described in detail in section 5.2.2), an evolution of the detectors already used in the past in the CAST experiment.

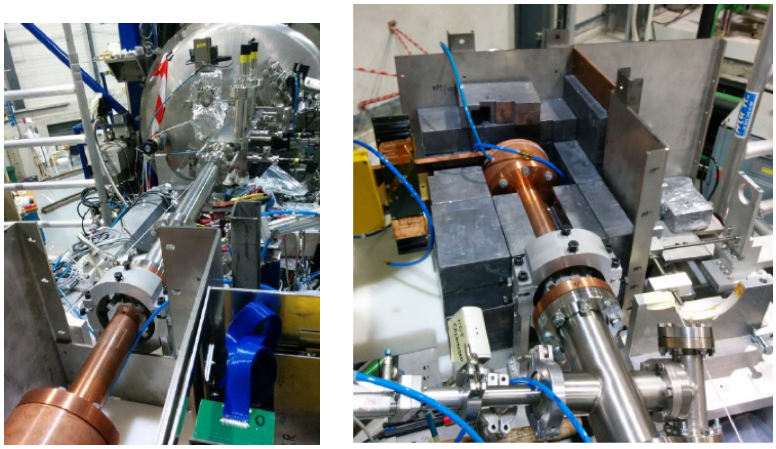

Figure 9.11: Pictures of the sunrise line installed on the CAST platform.

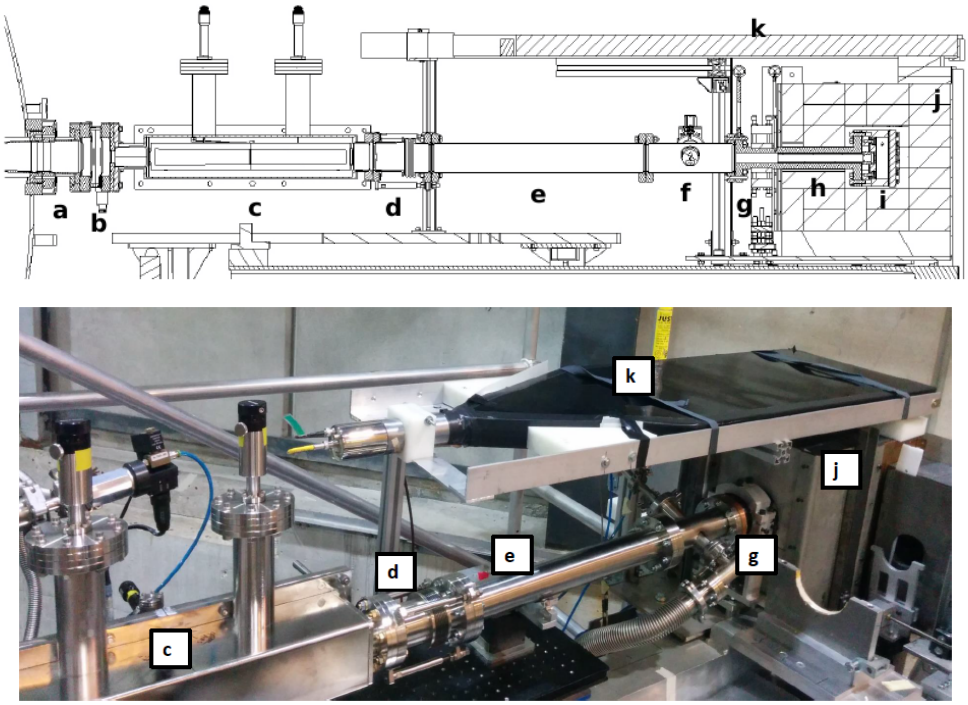

Figure 9.12: Sketch and photo of the new CAST Sunrise detection line composed of a low background Micromegas detector placed at the focal point of an x-ray optic. The different parts of the line are described in detail in the text: gate valve (a), differential window (b), Wolter I x-ray optic (c), bellow (d), stainless steel interface tube (e), calibration system (f), precision stage (g), copper interface tube (h), Micromegas detector (i), lead shielding (j) and muon veto (k).

However in the present configuration the detector is placed at the focal point of a ∼5 cm diameter, 1.3 m focal-length, cone-approximation Wolter I x-ray telescope comprised of thermally-formed (or "slumped") glass substrates deposited with multilayer coatings. This technology for x-ray optics is the one used in the hard x-ray mission NuSTAR and was identified in [163] to have the potential to cost-effectively cover the areas needed for IAXO with sufficient performance. Although CAST already used x-ray focusing optics for one of its four detector lines (one of the

spare optics from the ABRIXAS x-ray mission, see section 4.8.1), this is the first time an x-ray optic is designed and built for an axion application. It is also the first time a Micromegas detector is operated with an x-ray optic. The system was installed in 2014 in one of the sunrise ports of the CAST magnet. The combination of the telescope and Micromegas detector provides the best signal-to-background ratio obtained so far by any detection system of the CAST experiment.

The system is designed to fit the dedicated x-ray optics and the low background Micromegas detector, and to align these elements with the axis of the magnet bore. Both the optics and the detector have imposed some constraints in the line. On one side, the detector must be placed at the focal point of the optics, which has fixed the length of vacuum elements. On the other side, the lead shielding must be close enough to effectively reduce the external gamma flux, which limits the range of the alignment elements. A schematic view of the line is shown in figure 9.12.

Axion-converted x-rays coming from the cold-bore cross a gate valve (**a** at the sketch), which isolates the line from the magnet during commissioning periods, and a differential window (**b**), which protects the magnet cold-bore vacuum in case of a degradation of vacuum at the detector side. The optic (**c**) is directly bolted to this element. Between the Micromegas detector and the optic, there are four elements: a bellow (**d**), which precisely aligns the detector with the focusing device in combination with a precision stage (**g**); a stainless steel tube (**e**), whose length roughly fixes the detector position at the optic focal length; a calibration system (**f**), composed of an actuator with an ^{55}Fe source and a copper interface tube (**h**), which is screwed to the detector chamber (**i**) and forms also part of the shielding. An octagonal PTFE cassette covers the inner tube's walls to block the fluorescence coming from the copper, which might be activated by external radiation. As shielding, there is a lead layer of 10 cm thickness (**j**), which reduces the gamma flux, and a plastic scintillator coupled to a photomultiplier (**k**), which works as an active muon veto (see section 5.4).

This system was installed at CAST in august 2014. As a first step, the optical axis of the x-ray focusing device is aligned to be parallel with the axis of the corresponding magnet bore (V2 line). The procedure was carried out with a laser shinning through the bore from the opposite end, where one of the sunset Micromegas sits. Once the telescope is installed and calibrated with respect to the magnet axis, the vacuum components for the differential pumping were installed on either side (elements b, d, e, h of figure 9.12).

Subsequently, the alignment of the Micromegas detector followed, in such a way that the spot be focused at the centre of the sensitive area of the detector. In order to accurately fix the position of the detector, an xy–positioning stage was designed as a tailor-made solution. The alignment was performed with a fake Micromegas detector with a polycarbonate window at the focal plane of the x-ray telescope. The polycarbonate window had a design of the detector's cathode hole-pattern, on which the parallel laser beam was focused (figure 9.13, left). The xy stage allows to determine the Micromegas position in such a way that the laser beam is focused on the central point of the hole-pattern to avoid the cathode structure from being on the way of x-rays. When the chamber position is defined, the bolted unions of the xy stage are locked, fixing thus the position of line components. This step allows finishing up the entire vacuum piping between the Micromegas and the telescope. Finally, the actual Micromegas detector replaces the fake detector and the whole vacuum line can be finished up and leak tested.

The link between the vacuum line and the detector is made by a 20 mm-thick copper-pipe interface with a PFTE coating. The aperture of the pipe has a diameter of 25 mm and allows the design of a more compact shielding. The inner shielding is the detector chamber itself, made of 18 mm thick radiopure copper. A shielding of 10 cm of lead was then built around the detector, leaving only the side shared with the fourth CAST detector, an InGrid Micromegas at 7 cm because of space constraints. Following the results of extended studies performed as well as the experience acquired by the operation of the sunset Micromegas, a plastic scintillator for the detection of cosmic muons is installed on the top of the shielding. The scintillator covers a part of the pipe that connects the Micromegas with the optic, as external radiation interacting with it is thought to be the source of a signficant amount of the background. The induced x-ray-like events can be discriminated by the off-line analysis.

Detector calibrations are taking place at least twice a day, once after the tracking of the sun and

once during background data-taking, excluding the time when the sunset detectors are tracking the Sun. For this purpose, an actuator situated between detector and telescope places an ^{55}Fe source in front of the Micromegas detector and retracts it into a shielded position after the calibration. An intensity map of such a calibration can be seen in figure 9.13, left.

Because the expected region for the axion signal is minimized after being focused by the optic, the cathode pattern has been modified to a spider-web design with a central hole of 8.5 mm of diameter, large enough to contain the expected axion signal image. The x-rays focused by the optic go through the 4 μm aluminized polypropylene window, avoiding the grid structure, whose opacity was responsible of a $\sim$10% of efficiency loss in previous setups. A photo of the new strongback and a hitmap recorded by the detector during detector calibrations are shown in figure 9.13. An imprint of the cathode window strongback can be clearly discerned, over the homogeneous response of the detector. As already mentioned, the size of the inner circle of the cathode strongback (the position of which is indicated with a solid black line at the center of the plot) is calculated to cover an area larger than the expected spot.

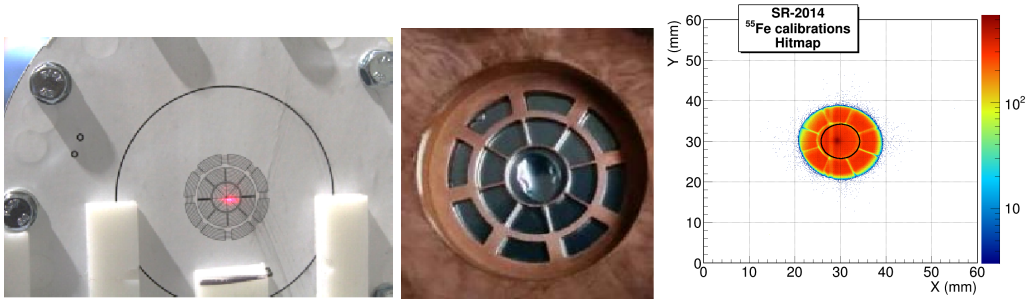

Figure 9.13: Left: view of the spot produced from the collimated laser beam through V2 magnet line on the polycarbonate target situated 15 mm behind the focal plane. The laser is focused at the center of the designed pattern, as expected. Centre: view of the cathode strongback used in the sunrise detector. Right: intensity map over the surface of the sunrise Micromegas detector produced by the ^{55}Fe calibrations during the CAST 2014 season. Only the inner part of the spider-web is visible because the PTFE cassette is blocking the rest from the field of view of the source. The black contour represents the theoretical position of the inner circumference of the spider-web.

The exact knowledge of the position of the spot is crucial for the data analysis of the experiment, as it defines the area where the expected signal from the axions is to be focused. It can be periodically monitored performing spot-calibrations with the help of an Amptek Cool-X pyroelecric x-ray generator emitting mainly 8 keV photons and breehmstrahlung x-rays ("x-ray finger") from the other side of the magnet. The finger can move the source in, placing it on the optical axis of the system, or out, placing it beyond the field of view of the optics. The calibration position of the finger is set to the horizontal centre of V2 line, while its vertical position cannot be set in our setup, but it is close to the centre of the beam line (error in the mm range). The generator does not produce a constant flux of x-rays but is thermally cycled between 2 to 5 minutes; the flux can vary throughout the cycle and from cycle to cycle. To perform the x-ray finger runs we profit from the information of the sunset Micromegas, sitting at the back of the x-ray generator, that monitors the actual cycling activity of the x-ray emission. Figure 9.14 shows the rate recorded by the sunrise Micromegas compared to the rate of the sunset Micromegas detector. The cycles of the generator are evident as well as the 3 orders-magnitude of difference in the recorded rates. The source being located at a finite distance to the optics, the spot to be formed on the detector plane has a larger diameter that the one expected when focusing a parallel beam or the expected signal.

The intensity map recorded during the spot-calibrations with the x-ray finger runs is shown in figure 9.15, where the centroids of the distribution of each run are marked and labeled. The low counting rate from the source at such distance enforces runs of approximately 8 hours in order to collect significant statistics. For this reason, spot-calibration runs cannot be taken very often so

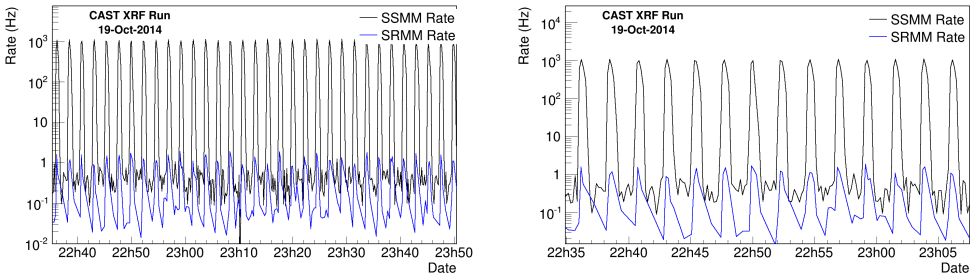

Figure 9.14: Trigger rate registered by the sunrise Micromegas (blue line) and the sunset Micromegas (black line) facing it, during an x-ray finger run. On the right, an expanded view of the same figure.

as not to disturb the normal data-taking program of the experiment.

At the commissioning phase two x-ray finger runs were performed, before and after the installation of the shielding, in order to ratify that the spot has not displaced due to structural deformations. The third run was performed after the installation of the sunset Micromegas detectors and shielding, while the last run was done at the end of the 2014 CAST data-taking campaign for consistency. Figure 9.15 (right) shows the spot centroid evolution from the four available measurements. A displacement of 1 mm is observed between the first and last spot calibration at the x direction, but only of the order of 0.5 mm between the first calibration with the complete shielding on and the end of the data-taking. The evolution of the centroid in the y axis projection shows a change of the order of 0.5 mm overall.

The x-ray finger is driven manually with a sub-mm precision wheel. The translation of the x-ray finger in one direction will result in a displacement of the spot centroid in the opposite direction. The factor will depend on the exact geometry, but to first order, the translation d of the centroid will be equal to

$$d \sim F \cdot \arctan(x/A) \tag{9.1}$$

where x is the displacement of the x-ray finger, A is the distance from the x-ray finger to the center of the optic ($\sim$13.5 m) and F is the focal length of the optic, which is 1.5 m. So, a 1 mm displacement of the x-ray finger from the nominal x-ray axis will shift the spot centroid 0.11 mm.

Despite the lack of a complete calibration of the x-ray telescope efficiency, the resulting spot follows the shape and imaging performance expected. The generated image is a roughly 7×5 mm^2 area made out of two quasi-symmetric blobs as suggested by x-ray tracing simulation. Figure 9.16 shows a comparison of real data and the simulated ray-tracing of the optics taking into account its reflectivity. The blobs are formed due to the position of the spacers in the center of the optic. The spacers are forming an angle of 5.35 degree relative to the horizontal plane at the actual alignment position.

The energy spectrum acquired in such a spot-calibrations by sunset and sunrise Micromegas are plotted in figure 9.17. The spectrum registered by the sunset detector presents the characteristic emission of the source at 8 keV plus an accumulation around 4–5 keV from its escape peak and the fluorescence emission of the steel components surrounding the source. On the other hand, the spectrum registered by the sunrise detector peaks at $\sim$5 keV, the higher end of the spectrum being suppressed due to the efficiency loss of the x-ray optic.

9.4.2 Focusing spot dependence on magnet position

During the solar trackings, the magnet moves in the horizontal ($\pm 80^\circ$) and vertical ($\pm 8^\circ$) directions. Structural deformations during the magnet movement could lead to an incorrect focusing of the x-rays, loosing sensitivity for the axion detection. With the aim of verifying that the spot position

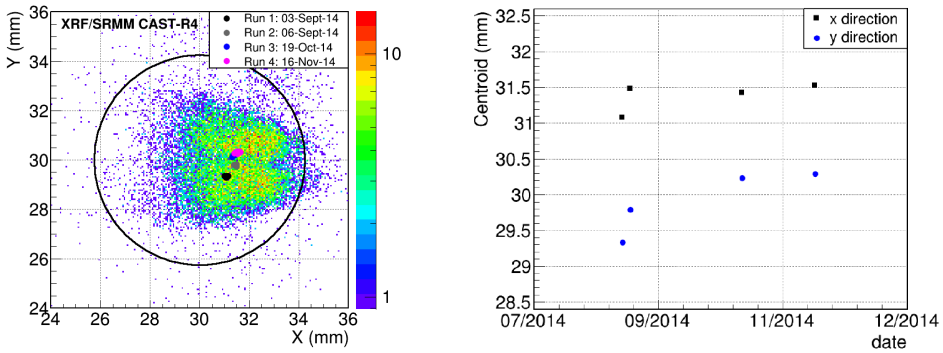

Figure 9.15: Left: Intensity map of the calibration with the x-ray finger source through the magnet line and the x-ray telescope. The outer contour represents the theoretical position of the inner circumference of the spider-web.

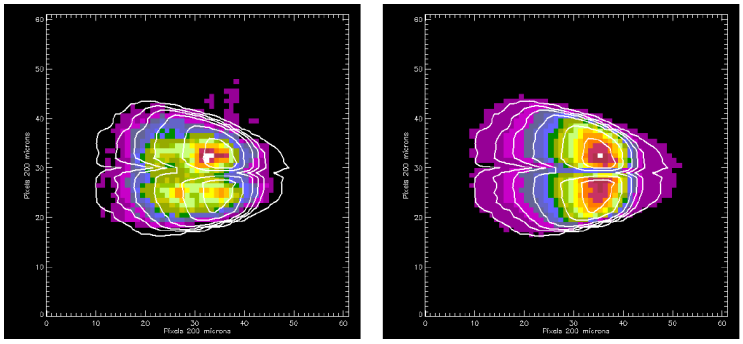

Figure 9.16: Left: white contours from the simulation of the x-ray finger source calibration over-plotted to the smoothed experimental data. Right: data and contours from simulation of the x-ray finger source.

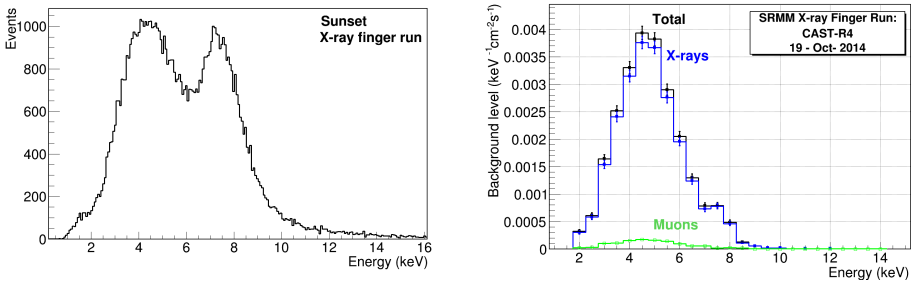

Figure 9.17: Left: energy spectrum registered by the sunset Micromegas in an x-ray finger run. The spectrum is dominated by the 8 keV emission of the source plus the fluoresce of the steel of the vacuum components. Right: energy spectrum registered by the sunrise Micromegas in an x-ray finger run.

is always within the Micromegas window, we have performed a set of measurements at different azimuthal and declination angles, covering the full range of movement of the CAST magnet.

The method used relies on the spot-calibrations described above: the sunrise Micromegas detector is irradiated from the sunset side of the magnet by means of a pyroelectric x-ray generator

(COOL-X) driven by a mechanical *finger*. The emitted photons have to traverse the magnet bore and the telescope, being detected by the Micromegas. Table 9.4 summarizes these measurements.

As explained before, the counting rate in the sunset Micromegas is used to monitor the cyclical activity of the source. Periods of high activity of the source should coincide with an increase in the trigger rate of sunrise Micromegas. An overview of the counting rate of sunrise and sunset Micromegas during the x-ray finger runs of 2015 is shown in figure 9.18 (left), where we have labeled the different run numbers. On the right of this figure, we show a closer view of run # 6, where the correlation between both trigger rates is apparent. Comparing figures 9.14 and 9.18, we conclude that the intensity of the source has decreased from the observation of the sunset trigger rate ($\sim 10^3$ Hz during 2014 runs and $\sim$500 Hz in 2015). Besides, the use of the source produce an activity decrease during the 2015 runs, being below 100 Hz in the x-ray finger # 10. In the last x-ray finger run of the set (# 11) the sunset Micromegas data was not recorded, but presumably it will be even lower. Indeed, sunrise trigger rate during the last run is barely higher than during background runs, as figure 9.18 shows, and no clear periodic pattern is observed in the rate (figure 9.19, right).

The SRMM trigger rate during the x-ray finger runs after background correction is shown in figure 9.20. The decrease observed in the trigger rate from the first to the last spot-calibration at SSMM and SRMM is similar in relative terms, and around a factor 10. This decrease is expected, since the estimated lifetime of the COOL-X is between 200 and 1000 hours, depending on the operation mode.

Figure 9.21 shows the accumulated hitmap during the spot-calibrations, as well as the centroid of the spot during the different runs. We observe that the spot position is within the inner circle (8 mm-diameter) of the Micromegas strongback in all configurations. Small shifts in spot position have been registered with the change in the magnet load, and with the declination angle, though, given the smaller expected axion-spot with respect to the one generated with the x-ray source, we confirm that $\sim$100% of x-rays coming out the telescope are focused on the Micromegas window during full solar trackings. The shift of the spot in the x-direction from 2014 to 2015 is attributed to a displacement of some mm of the x-ray finger source in this direction due to a mechanical problem in the movement of the driving wheel of the finger.

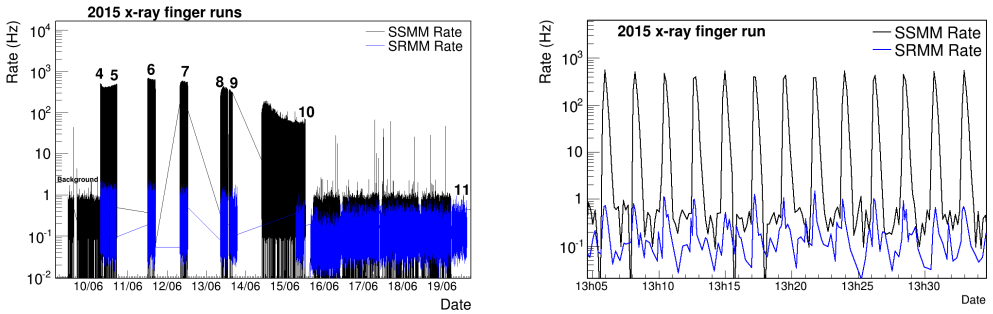

Figure 9.18: Left: overview of the trigger rate during the x-ray finger runs of 2015 in sunset (black) and sunrise (blue) Micromegas. Right: expanded view of run # 6, where the correlation between SSMM and SRMM is apparent.

9.4.3 Sunrise Micromegas performance

Three detectors of the new brand type were produced and the best (the so-called *CAST-R4* detector), in terms of gain level (figure 7.6), gain uniformity, electron transmission (figure 7.4) and energy resolution (figure 7.5), was selected to be installed in CAST.

So far, it is the Micromegas with the best performance at CAST with a 13% of FWHM at the 5.9 keV peak (see figure 9.22 left). The detector shows an excellent spatial resolution and a good homogeneity of the gain in the active area (see figure 9.22 right). Indeed, the energy

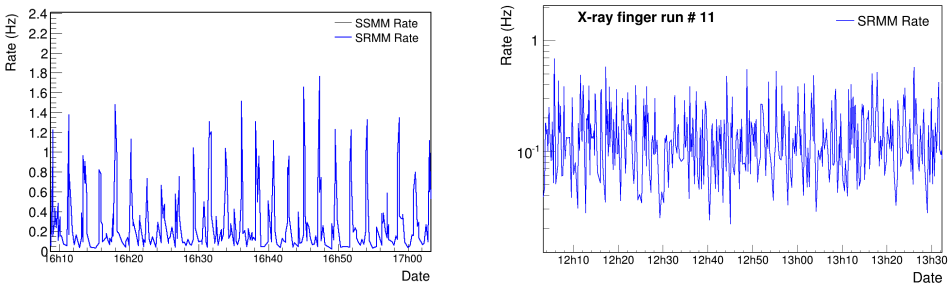

Figure 9.19: Close view of the SRMM trigger rate during the x-ray finger run # 6 (left) and run # 11 (right). Whilst in the first the periodicity of the source activity is visible, one cannot distinguish periodic peaks in the second. This is attributed to the activity loss of the x-ray finger source.

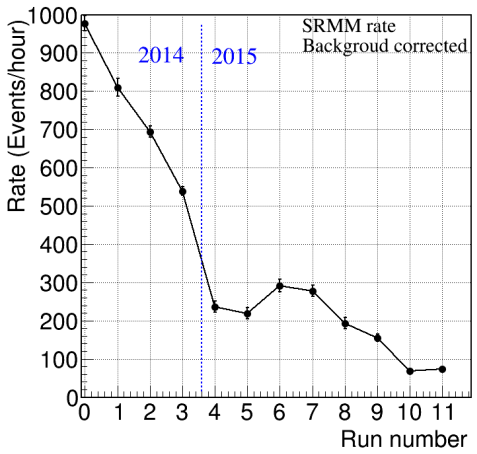

Figure 9.20: Sunrise Micromegas trigger rate during the different spot-calibrations. We have attributed the decrease in the rate to the intensity loss of the source.

resolution is closer to the 11% FWHM reached by small non-pixelated microbulk prototypes (3.5 cm diameter). This improvement in performance is due both to a better manufacturing technique and to a special care of grounding. The range of drift fields at which the detector can work (figure 7.4) has been enlarged due to the increased uniformity provided by the field shaper, while the gain curve (figure 7.6), mainly defined by the amplification gap and the gas conditions, is similar to previous designs.

The detector performance along the data-taking period has been stable, as it can be seen by the evolution of the monitored parameters like the gain and the energy resolution, plotted in figure 9.23 left. As described in previous chapters, the data analysis relies on the study of the patterns of the calibration events on the observation parameters, corresponding to x-ray photons of the energy range, which are then compared to the event population collected during the background data-taking. Events are registered quite uniformly in all the detector surface (see figure 9.23, right); a good part of them have a temporal stamp that coincides with the signal of the muon-veto, labelled "veto", which are then rejected by the analysis. The background level in the energy RoI achieved at a surface covering the calibration area is $(1.6 \pm 0.2) \times 10^{-6}$ keV^{-1}cm^{-2}s^{-1}, which when the veto condition is applied is reduced to $(1.0 \pm 0.2) \times 10^{-6}$ keV^{-1}cm^{-2}s^{-1}. The background spectra at 75% signal efficiency during the data taking are shown in figure 9.24.

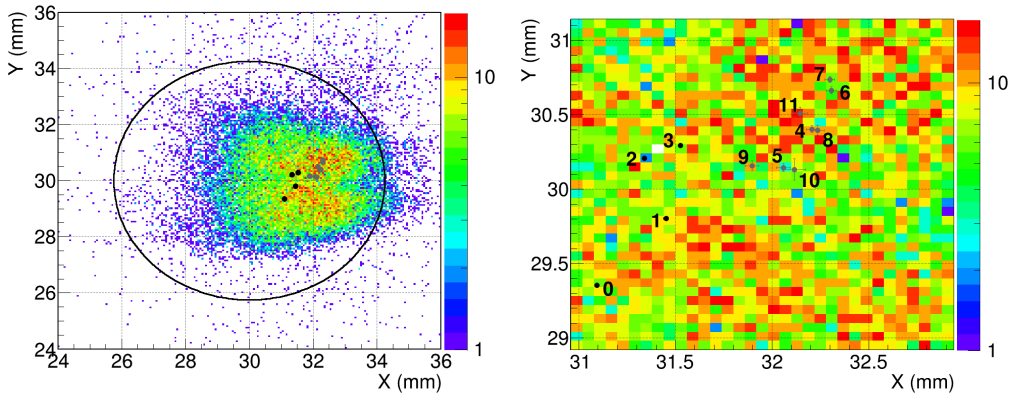

Figure 9.21: Left: spot position (centroid) of the x-ray finger runs of 2014 (gray dots) and 2015 (black dots). Right: an expanded view of the spot positions with labels described in the text.

Year	Run	Time (hours)	Events	Conditions	x-centroid (mm)	y-centroid (mm)
2014	0	9.13	8910	Before SR shielding	31.09 ± 0.01	29.35 ± 0.01
	1	5.29	4287	After SR shielding	31.46 ± 0.01	29.80 ± 0.01
	2	12.43	8617	After SS shielding	31.34 ± 0.01	30.21 ± 0.01
	3	13.94	7505	End of 2014 data-taking	31.53 ± 0.01	30.30 ± 0.01
2015	4	5.23	1238	h=18995, v=26464 (0°)	32.21 ± 0.03	30.40 ± 0.02
	5	4.05	886	h=18995, v=52000 (-8°)	32.06 ± 0.04	30.14 ± 0.03
	6	4.92	1432	h=18995, v=3600 (+8°)	32.31 ± 0.03	30.66 ± 0.02
	7	5.09	1416	h=11000, v=3600 (+8°)	32.30 ± 0.02	30.74 ± 0.02
	8	4.53	869	h=11000, v=26464 (0°)	32.24 ± 0.04	30.40 ± 0.03
	9	5.20	806	h=11000, v=52000 (-8°)	31.90 ± 0.04	30.16 ± 0.03
	10	5.11	353	h=27000, v=26464 (0°)	32.12 ± 0.06	30.13 ± 0.07
	11	9.31	690	h=27000, v=3600 (+8°)	32.15 ± 0.04	30.51 ± 0.04

Table 9.4: X-ray finger runs and spot positions. h and v represent the horizontal and vertical encoder-values of the magnet driving motors.

9.4.4 Coupling constant limit with the 2014 vacuum data

As stated before, in 2014 the CAST operated with vacuum in the magnet bores. The data taking was accomplished in two phases. In the first one, from 3rd of July to 25th of August, only the sunset detectors were operative; being the sunrise line in preparation for the telescope plus new Micromegas upgrade reported before. The data taking stopped on 25th August for carrying out this upgrade in one of the sunrise ports of the CAST magnet. This operation required uninstalling the sunset detectors for calibrating the optics with the laser beam from the other side of the magnet. The physics data taking resumed on 11th of September, this time only with the sunrise Micromegas detector. The sunset ones remained uninstalled waiting for the installation in the remaining port of the sunrise side of the second telescope (ABRIXAS) and the InGrid detector. These works were finalized on mid-October, and subsequently, the sunset Micromegas were installed, resuming the data taking on 20th of October, now with all the four x-ray detectors acquiring data, until the end of the season, on 17th of November.

The sunset Micromegas performed a total of 78 evening solar trackings, for a total exposure of

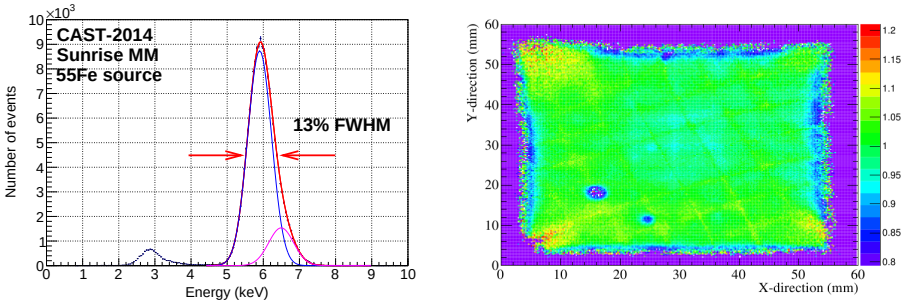

Figure 9.22: Left: ^{55}Fe calibration spectrum of the sunrise Micromegas detector. The main peak has been fitted to two gaussian functions (blue and magenta lines), corresponding to the K_α (5.9 keV) and K_β lines (6.4 keV). Right: gain uniformity of the sunrise Micromegas detector. The dead areas (in purple) show lower values than the unity (in green) and lie outside the axion-sensitive area.

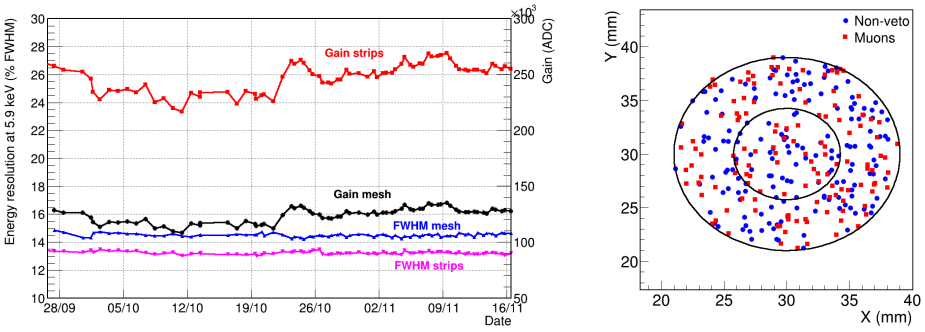

Figure 9.23: Left: evolution of the gain and the energy resolution of the detector along the data-taking. The fluctuations, measured both at the mesh and at the strips, are less than 10%. Right: A 2D hitmap of background events in the calibration area (outer circle) with energies between 2 and 14 keV, where the two populations of muon-induced events (muons) and the rest (non-muons) are indicated in red and blue respectively. The inner circle marks the inner circumference of the spider-web.

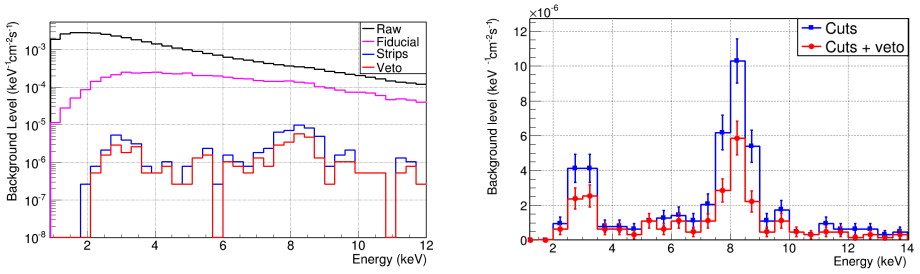

Figure 9.24: Left: Background energy spectra in the calibration area. The level achieved after the strips cuts (in blue) is $(1.6 \pm 0.2) \times 10^{-6}$ $keV^{-1}cm^{-2}s^{-1}$, and after the veto cut (in red) it is reduced to $(1.0 \pm 0.2) \times 10^{-6}$ $keV^{-1}cm^{-2}s^{-1}$. The total background time is 1449.2 hours. Right: a zoom on the spectra after the analysis; the peak at 8 keV is due to fluorescence in the copper materials of the entrance pipe and the detector and the one at 3.2 keV corresponds to the escape peak of argon.

118.0 hours per detector, with a loss of 5.1 hours due to detector death time produced by electronic noise, while the sunrise Micromegas performed 51 solar trackings, for a total of 69.8 hours.

In table 9.5, the results in terms of background level of the three Micromegas detectors during the 2014 CAST data taking campaign are shown. While sunset 1 level is compatible with the one measured in 2013, sunset 2 level is reduced significantly (∼30%) due to the detector replacement, as can be noticed by comparing with table 9.1.

Detector	Efficiency 3 & 6 keV	Time Background (hours)	Time Tracking (hours)	Level [2 − 7] keV Background (10^{-6} keV^{-1}cm^{-2}s^{-1})	Level [2 − 7] keV Tracking (10^{-6} keV^{-1}cm^{-2}s^{-1})
Sunrise	75 & 75	1449.2	69.8	1.0† (0.8) ± 0.2 (0.1)	—‡
Sunset 1	75 & 75	1854.0	118.0	1.03 ± 0.05	0.94 ± 0.17
Sunset 2	75 & 75	1819.6	118.1	1.05 ± 0.05	0.87 ± 0.17

Table 9.5: Summary of background and tracking levels of Micromegas detectors in CAST 2012 data taking campaign. † *background level defined in the detector area illuminated by the* ^{55}*Fe source. In parenthesis, the level in the projection of the whole cold bore area.* ‡ *zero tracking counts in the focusing spot.*

The levels measured during axion-sensitive periods are also shown in table 9.5 It is found that background and tracking levels are compatible within one standard deviation in both sunset detectors. On the other hand, zero counts are found in the spot and in the energy RoI in the sunrise Micromegas detector, while 0.38 counts were expected.

It must be noted at this point that our definition of the focusing spot relies on the spot-calibrations performed during the x-ray finger runs, and the efficiency (throughput) of the optics is defined from simulations (see figure 9.25, left). Both telescope parameters will be accurately measured at the end of its operation in CAST. Ideally, the optics should have been calibrated before its installation in CAST, but the lack of free time spots in the schedule of the PANTER x-ray test facility forced its prior installation.

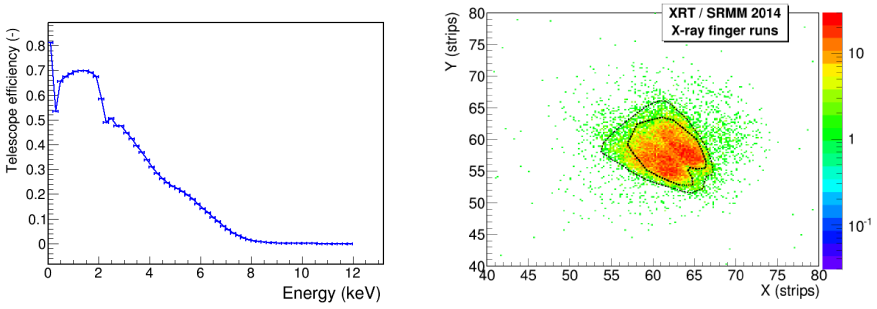

Figure 9.25: Left: efficiency of the x-ray telescope as a function of the energy. Right: spot-calibration hitmap in the xy-strips plane. The contours represent two possible definitions of the spot, the inner one with around 80% signal acceptance and the second with around 92% acceptance.

In this work, wee have conservatively taken the outer contour of figure 9.23 right, which encompasses approximately the 92% of the x-ray events from the source (91.9 (1.3)% of the x-ray finger run number 1, 92.8 (1.7)% of run number 2, 92.2 (1.2)% of run number 3 and 91.7 (1.2)% of run number 4). The actual axion signal region is smaller than in our definition, since the x-ray finger is placed at a finite distance from the optics and the emission is not a perfectly parallel beam.

No axion signature is found in the 2014 data, so an upper limit on the axion to photon coupling strength as a function of the axion mass, $g_{a\gamma}(m_a)$, is extracted (figure 9.26). The contributions of the three detectors and the combined result are plotted in the figure and the exact values

for $m_a \lesssim 0.02$ eV are shown in table 9.6. Sunset Micromegas detectors produce a similar limit because they approximately the same background level and exposure. On the other hand, the limit produced by sunrise Micromegas is given by the zero counts statistics, and the limit is worse than the others because of it had less exposure. The combined upper limit of the CAST 2014 vacuum run using only the sunset Micromegas detectors is $g_{a\gamma} < 0.73 \times 10^{-10}$ GeV^{-1} at 95% confidence level for axion masses $m_a < 0.02$ eV. This preliminary limit surpasses the one achieved in 2013 and it is *per se* the most stringent limit on $g_{a\gamma}$ on a wide axion mass range.

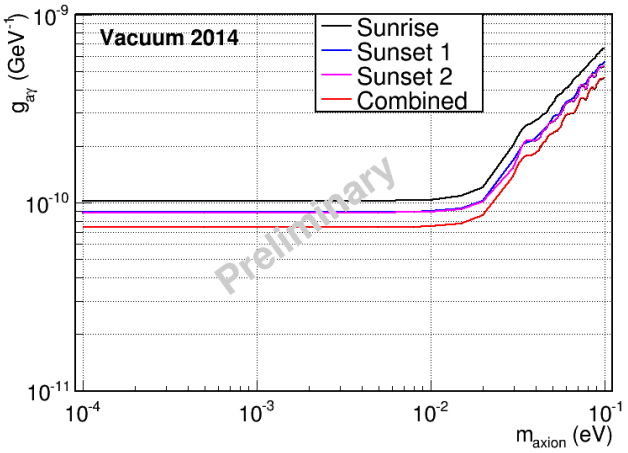

Figure 9.26: Exclusion curve (95% C.L.) in the m_a–$g_{a\gamma}$ plane achieved with the Micromegas detectors during the 2014 CAST data taking campaign, with vacuum in the magnet bores. The contributions of sunrise, sunset 1 and 2 are shown, as well as the combined result.

Year	Mass range [eV]	Detector	$(g_{a\gamma})_{\text{limit}}$ at 95% C.L. [$\times 10^{-10}$ GeV^{-1}]
2014	$\lesssim 0.02$	Sunrise	< 1.02
		Sunset 1	< 0.89
		Sunset 2	< 0.88
		Combined	< 0.73

Table 9.6: Summary of limits on the axion-to-photon coupling constant from the vacuum phase of 2014 with the Micromegas detectors.

9.5 Combined limit on $g_{a\gamma}$ from the 2013 and 2014 data taking campaigns

In this section, we present the combined results of the 2013 and 2014 seasons with vacuum in the magnet bores. The result is preliminary because it assumes the theoretical telescope efficiency, and cross-check of the data should be done for consistency. The limit obtained for the axion-to-photon coupling constant is

$$g_{a\gamma}(95\%\ \text{C.L.}) < 0.66 \times 10^{-10}\ \ \text{GeV}^{-1}\ \ \text{for}\ \ m_a \lesssim 0.02\ \ \text{eV} \tag{9.2}$$

This limit is in competition with the most stringent limit so far given by the stellar evolution from helium-burning lifetime of globular clusters, and it will be surely surpassed if the 2015 vacuum

data are combined, as well as the CCD (2013) and InGrid (2014–15) data. It can be thus said that the goal posed by the collaboration has been satisfied.

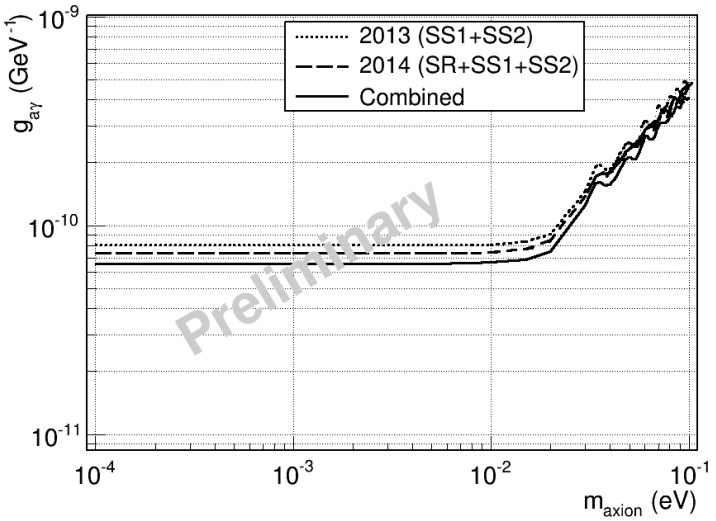

Figure 9.27: Exclusion curve (95% C.L.) in the m_a–$g_{a\gamma}$ plane achieved by the Micromegas detectors with the combined exposure of the 2013 and 2014 CAST data taking campaigns.

Chapter 10

Background model of CAST-MM detectors

Contents

10.1 Introduction

The thorough comprehension of the Micromegas background is essential for the attempt to reduce it. In this chapter we review the potential background sources of the Micromegas detectors of CAST. Some of these sources are common to any other rare event search, and therefore, the strategies to mitigate them are equivalent. The current understanding is based on compared studies of *in-situ* measurements in CAST, experimental tests carried out at installations located both at underground and surface level, as well as in detailed Monte Carlo simulations.

10.2 Overview of CAST-MM background

The main sources of natural background for the Micromegas detectors are: γ-rays, cosmic rays (mainly muons), presence of radon around the detector, intrinsic radioactivity of the detector components or shielding, neutrons and cosmogenic activation of the detector materials. All these radiations can produce secondary or fluorescence emissions that can reach the detector active volume. The strategies to reduce these backgrounds are: the use of high-Z material (lead, copper) passive shielding to block the pass of γ-rays; active shielding to tag muons, such as plastic scintillators; the continuous flux of vaporized LN_2 into the detector environment to avoid the presence of air-borne radon; a low-Z material to moderate neutrons plus a layer of a neutron absorber; and the use of radiopure components.

The application of these techniques along with the reliability of the microbulk technology, the upgrade of the readout electronics, the high granularity of the readout – which offers topological information of the event, a powerful tool for signal/background discrimination– and the tuning of the rejection algorithms led to a background level reduction of a factor 10^2 in CAST-MM detectors over the last ten years. Figure 10.1 shows a compilation of background levels achieved in CAST in the [2–7] energy range, at surface and underground test benches. The best level achieved at surface is already below 10^{-6} keV^{-1}cm^{-2}s^{-1} [201]. As we saw in previous chapters, the energy

spectrum is characterized by a fluorescence peak at 8 keV (from copper K_α emission), its escape peak at 5 keV and by the argon K_α line at 3 keV. The operation of a replica of the detector in the LSC sets a level as low as $\sim 10^{-7}$ keV^{-1}cm^{-2}s^{-1}, almost at the required IAXO levels.

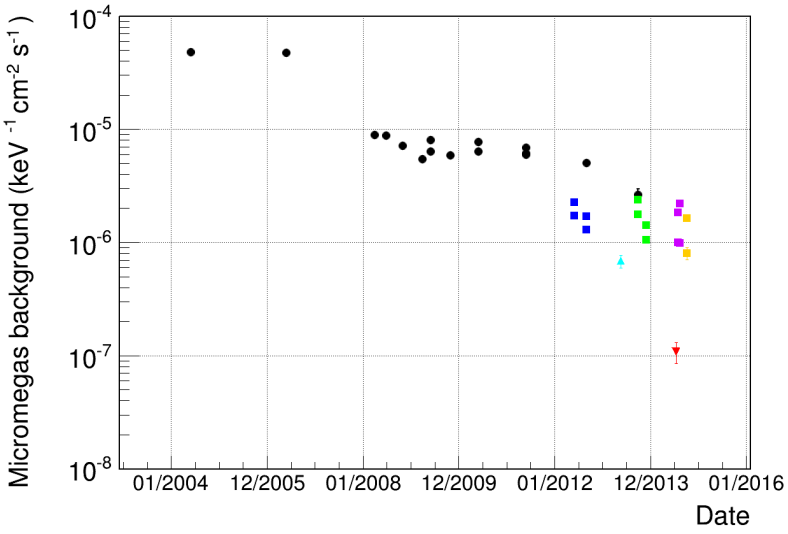

Figure 10.1: Evolution of the background level in the Micromegas of CAST since the first detectors were installed in 2003. Black circles represent the values obtained in in-situ *measurements at CAST. Blue, green and purple squares represent the levels of the sunset detectors during the 2012, 2013 and 2014 data-taking campaigns, each pair of points representing the level before and after the application of the veto cut. Yellow squares are the levels obtained after the sunrise upgrade in 2014 before and after the application of the veto cut. The cyan triangle is the level obtained in a test bench at Zaragoza laboratory, and the red triangle is the level obtained in the ultimate setup at Canfranc.*

The current understanding of the background sources is summarized in table 10.1. This model is based on in-situ measurements at CAST, tests underground (at the LSC) and at surface, as well as in Geant4 simulations. While the contributions from gamma rays, radon and internal radioactivity have been reduced to negligible levels, the dominant component is caused by cosmic muons and their secondary products, generated after their interaction in the setup components. The origin of the events limiting the LSC performance is uncertain. Some hypotheses are the β-decay of ^{39}Ar present in the detection medium, neutrons or cosmic activation of the materials.

The strategy to reduce background at surface level are based on the installation of thicker and more compact shielding and in a 4π enlarged muon veto system. Pushing the lowest underground limit requires a change in the active gas to xenon or neon, or the installation of a neutron shielding. These activities are being developed in the context of the R&D phase for the IAXO technical design report.

10.3 Background studies

Here, the R&D studies to understand the origins and reduce the background level of Micromegas are described. They include the operation of replica detectors at surface in the laboratories of the University of Zaragoza and underground at the Canfranc Underground Laboratory (LSC), and detailed Geant4 simulation of the detector setup and response.

Contribution	Level ($keV^{-1}cm^{-2}s^{-1}$) Before	After	Reduction technique applied
Gamma flux	7×10^{-5}	Negligible?	Full coverage by 10 cm lead shielding
Radon	8×10^{-7}	Negligible	Nitrogen flux inside the shielding
Cosmic muons	2×10^{-6}	7×10^{-7}	95% coverage by an active muon veto
Al cathode	5×10^{-7}	Negligible	Replacement by an ultrapure copper cathode
LSC limit	1.1×10^{-7}		^{39}Ar?, Neutrons?, cosmic activation?

Table 10.1: Summary of the different contributions to the background level in the RoI of the CAST-MM detectors and the techniques applied to reduce them. A detailed explanation of each measurement is done in the next sections along with the associated errors, which were intentionally omitted here for clarity.

10.3.1 Underground tests

The setup at LSC enjoys very stable environmental conditions and a cosmic muon flux a factor of 10^4[202] lower than at surface. With this setup (see figure 10.2), an intense program of tests with different shielding configurations has been carried out to evaluate the relative importance of different contributions to the background. Data taken with different amounts of lead or nitrogen flux give insight on the external gamma or radon contributions respectively. Finally, the background attributed to the intrinsic radioactivity of this setup is deduced, once all external components are brought to negligible levels. The contribution of muons can be estimated from the comparison between surface and underground data.

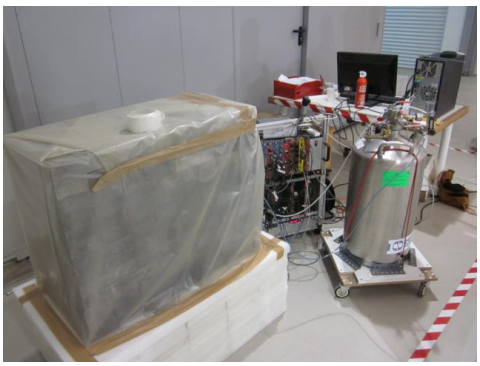

Figure 10.2: Micromegas setup installed at the LSC.

γ-rays, effect of shielding:

Several shielding configurations have been tested to evaluate the effect of γ-rays in the detector background, and to determine the amount of lead necessary to bring the γ contribution to the background to negligible levels. All the configurations share an inner copper shielding of 2–3 cm. The lead shielding around the detector has been varied from 0 cm to 20 cm [186]. The raw trigger rate varies from around 0.2 Hz to 0.01 Hz, while the background after cuts is reduced from $\sim 7\times10^{-6}$ to $\sim 0.2\times10^{-6}$ $keV^{-1}cm^{-2}s^{-1}$ in the 2–7 keV range.

A shielding made of 10 cm-thick lead was then tested, observing a background level and an energy spectrum compatible with that obtained for a 20 cm-thick. We can thus conclude that 10 cm of lead is enough to block γ-rays up to negligible levels.

Radon:

The concentration of 222Rn in air at the LSC is usually a few hundreds of Bq/m^3. The presence of air-borne radon in the detector environment is highly reduced by the continuous flux

of vapourized N_2 into a overpressurized plastic tent. However, the eventual interruption of N_2 allowed to estimate the contribution of air-borne radon to the background.

The 222Rn progeny are charged ions that can be trapped by the cathode, where they would decay, producing either sparks or background events. During a controlled interruption of the N_2 flux, the radon concentration in the detector environment was monitored with an alphaGUARD sensor [203]. The influence of the air-borne radon concentration on the Micromegas background (see figure 10.3) is estimated in $(3.0 \pm 0.8) \times 10^{-7}$ keV^{-1}cm^{-2}s^{-1} per Bq/m^3 in the 2–7 keV range [186].

In underground operation, radon could be the limiting contribution to the background since the large concentrations present at underground sites. However, at surface, where radon concentration are typically much lower ($\lesssim$10 Bq/m^3), its contribution to the background is not significant as it is well below the current levels. In any case, the use of an over-pressurized N_2-filled tent is highly recommended, since it prevents humidity and the risk of suffering breakdown sparks.

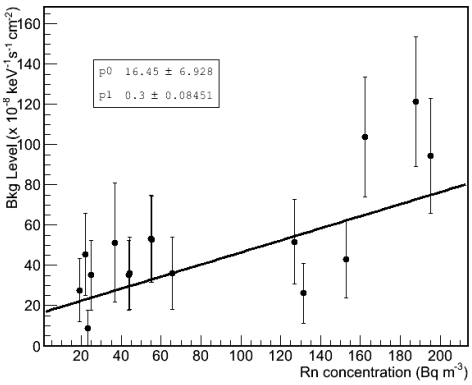

Figure 10.3: Dependence of the background level with the radon concentration at the LSC. Extracted from [27].

Intrinsic radioactivity:

All the detector components have been carefully chosen to be radiopure. However, Micromegas detectors operated during many years with aluminum cathodes instead of copper ones. The very low background levels achieved underground allowed to investigate its contribution to the Micromegas background.

The cathode is one of the heavier pieces making the detector and was found to be quite radioactive if compared with copper cathodes. The aluminum radioactivity levels, measured with a germanium detector at the LSC, are 30 Bq/kg of ^{238}U, broken beyond ^{222}Rn; 0.42 Bq/kg of ^{232}Th; and 0.49 Bq/kg of ^{235}U. On the other hand, copper cathode radioactivity is below 30 mBq/kg, i.e., more than a factor 10^3 less radioactive.

A measurement performed with the aluminum cathode during 35 days yields to a background level of $(6.7 \pm 0.6) \times 10^{-7}$ keV^{-1}cm^{-2}s^{-1}. Figure 10.4 shows the background spectrum obtained in such a measurement (blue points), while the level obtained with the same detector and the copper cathode is also shown for comparison (black points). The difference between both levels is $(4.4 \pm 0.9) \times 10^{-7}$ keV^{-1}cm^{-2}s^{-1} in the 2–7 keV range, with a similar spectral shape except at low energies, where the contribution of the aluminum cathode rises notably.

Lowest underground limit:

All the non-radiopure components of the setup, like the brass connectors or aluminum cathode, were replaced by copper ones. In this configuration, with a 10 cm-thick lead shielding, around 50 l/h of N_2 flux, a detector equipped with AFTER-based readout electronics operated at the LSC during nearly 8 months of 2014.

The detector showed a large active area (see figure 10.5, left) and stable energy resolution, which was around 18% FWHM at 5.9 keV both at the mesh and strips (see figure 10.5, right).

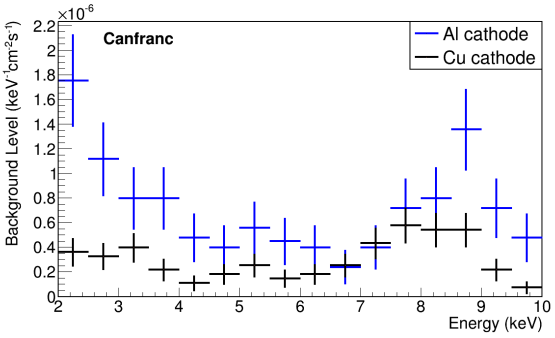

Figure 10.4: Background energy spectrum measured at the LSC with a cathode made on aluminum instead of the more radiopure copper.

The raw trigger rate is more than one order of magnitude lower than at a surface setup with a similar shielding due to the muon suppression by the rock overburden (see figure 10.6). The mean background level measured during 4448.1 hours after the application of the cuts is $(1.5 \pm 0.1) \times 10^{-7}$ keV^{-1}cm^{-2}s^{-1} in the 2–7 keV range. This value is 5–6 times lower than the lowest level obtained in CAST.

The shape of the energy spectrum is similar to those measured at surface, with characteristic peaks at 3 and 8 keV (see figure 10.6, right). The evolution of the background rate over the full data-taking period was reproducible and quite stable as figure 10.7 shows.

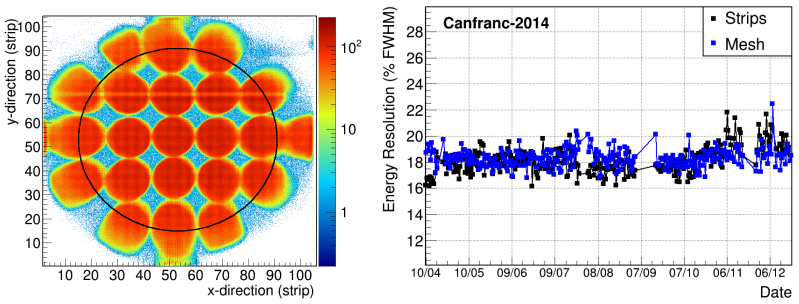

Figure 10.5: Left: hitmap distribution over the detector active area generated with the ^{55}Fe source at the LSC setup during the latest physics run. The shadowed regions correspond to cathode structure. Right: evolution of the energy resolution at 5.9 keV.

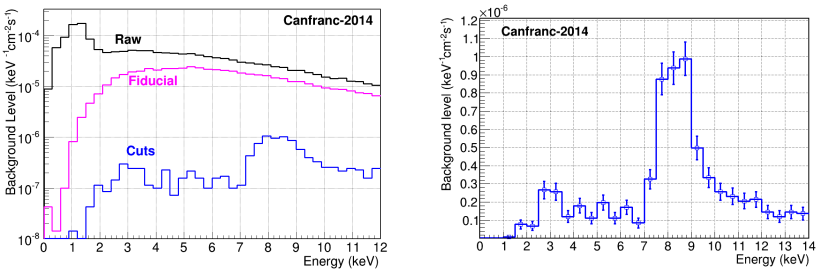

Figure 10.6: Background energy spectrum measured by the Micromegas detector during 4448.1 hours of the latest physics run at the LSC.

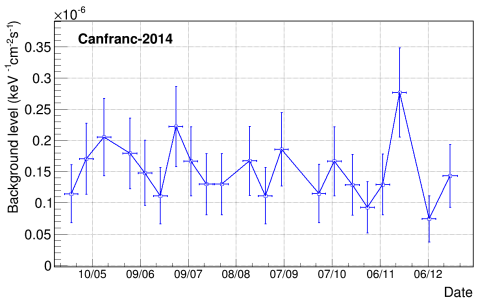

Figure 10.7: Background rate evolution over the ∼8 months of data-taking that lasted the data-taking.

Muons:

The direct comparison between the background levels measured underground and at surface (see CAST in-situ measurements, for example in chapter 9, or tests in next section) by detectors with an equivalent shielding configuration yields to a muon contribution of around 10^{-6} keV^{-1}cm^{-2}s^{-1} in the 2–7 keV range.

Provided a 4π 10 cm-thick lead shielding, radiopure detector components and anti-radon N_2 tent, muons are the dominant background component at surface. The use of muon vetoes allowed to mitigate their contribution, but they are currently still dominant due to imperfections of the active shielding system.

10.3.2 Surface tests

The headquarters of the research group is in Zaragoza, where we have an *on hand* general purpose laboratory for testing and commissioning. Among others, we have tested the mechanical assembly of detector and shielding, readout electronics, electronic chain, first characterization of detectors and plastic scintillators.

Furthermore, we installed a replica of the CAST sunset Micromegas, but with two plastic scintillators acting as muons vetoes extended along the perpendicular direction to the readout plane, i.e., along the pipe (see figure 10.8). The direct efficiency of the vetoes, i.e, the fraction of muons that cross both the Micromegas and the scintillators, was calculated by means of Geant4 simulations and it was found to be 75%.

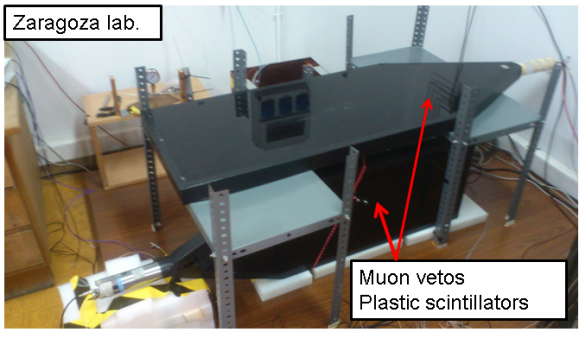

Figure 10.8: Micromegas setup installed at the Zaragoza laboratory.

The aim of the setup is: a) check what is the achievable background level in a setup with higher efficient configuration of the muon vetoes (without the space and mechanical constrains present in the CAST experiment), and b) check the influence of the pipe opening on the background, since it is the weak point of the shielding despite this is extend 20 cm along the pipe. For the last purpose,

Setup description	Level ($\times 10^{-6}$ keV^{-1}cm^{-2}s^{-1}) Cuts	Veto	Veto reduction (%)
Opened	1.9 ± 0.2	1.0 ± 0.1	50 ± 3
1.6 cm-thick steel	1.6 ± 0.1	0.8 ± 0.1	48 ± 5
10 cm-thick lead	1.5 ± 0.1	0.7 ± 0.1	55 ± 6

Table 10.2: Summary of results obtained with a CAST-MM replica at different configurations of the pipe aperture shielding. Background levels are defined in the 2–7 keV range and in the 14.5 cm^2 central circumference. Tests have been carried out in the Zaragoza laboratory.

three shielding configurations were used: in the first, the pipe was left completely opened to air; in the second, it was closed by a 1.6 cm-thick steel plate, simulating the CAST situation, where the steel pipe extends for several meters; and in the third, the pipe was closed by a 10 cm-thick lead wall.

Table 10.2 summarizes the measurements performed in this setup and the background levels obtained. The lowest background level is $(0.7 \pm 0.1) \times 10^{-6}$ keV^{-1}cm^{-2}s^{-1}, compatible with the lowest level achieved in CAST (sunrise-2014, see section 9.4). The background spectrum of this measurement is shown in figure 10.9. From the comparison between this level and the one obtained with the pipe walled with a 1.6 cm-thick steel plate it is found that the contribution of γ-rays entering through the pipe is $\lesssim 0.2 \times 10^{-6}$ keV^{-1}cm^{-2}s^{-1}. On the other hand, if the pipe is left completely opened, γ-ray contribution is somehow larger, as the table shows.

The shielding upgrade of the sunrise-2014 is conceived to reduce the γ-induced background through the pipe, since the pipe opening is much narrower due to the x-ray focalization of the telescope, which allows for a larger solid-angle shielding coverage.

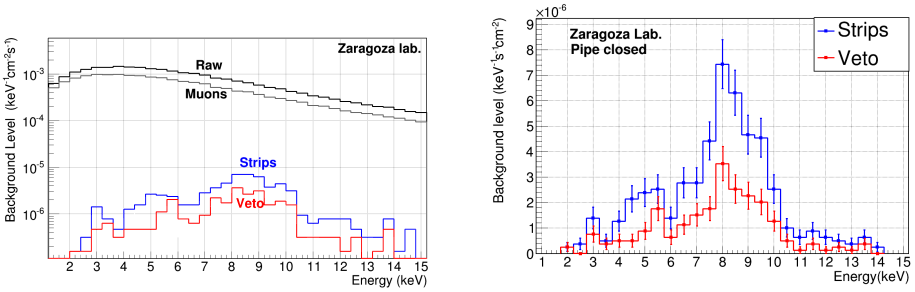

Figure 10.9: Background spectrum obtained with a CAST-MM detector in the Zaragoza laboratory with two plastic scintillators as muon veto and with the pipe opening closed with a 10 cm-thick lead wall.

10.3.3 Simulations

The goal of the Monte Carlo simulations is to provide a deep understanding of the physical processes that lead to background events in order to conceive strategies to reduce them. Here, we briefly describe the simulation codes, and then we show its application to two potential background sources: internal radioactivity of the detector components, and cosmic muons.

The simulation chain is composed of three steps: Geant4 [204, 205], a C++-based toolkit for the simulation of the interaction of particles with matter; RESTSoft (Software for Rare Event Searches with TPCs), a C++ library – initially conceived by I. G. Irastorza and further developed by many members of the group– that simulates the charge generation, electron drift and diffusion, charge amplification, pixelization and signal generation, as well as provides a common framework for data storage; data analysis and discrimination, using the same routines that for real data.

Geant4 is a modular software based on classes, each of one implements a different task in the generation, propagation and interaction of particles through the detector geometry. It tracks all the primary and secondary particles, offering several propagating models based on wide databases for each particle and physical process. All the relevant processes have been included, paying special attention to the low energy electromagnetic processes for photons, electrons and any other ionizing particle, extending the range of validity to lower energies than in the standard version of the program. The implementation of the low energy processes is valid down to 250 eV, and it includes the fluorescence and Auger emission of excited atoms.

The geometry implemented is a realistic approximation to the actual Micromegas setup installed at the sunset side of the CAST magnet. Some aspects of the detector and shielding have been simplified when they were considered to be physically irrelevant, but the main features are precisely described in order to have a reliable description of background events. The geometry consists in a classic 3 cm height plexiglas chamber filled with Ar+iCH$_4$ at 1.4 bar, with an internal diameter of 80.5 mm. Inside this volume, the *target*, i.e. the active volume, is defined as the 3D projection of the Micromegas readout, a square of 60×60 mm comprised and centered in the mesh plane. The conversion regions is closed by the amplification structure plus the plastic raquette on the one side and by the copper strongback in the other. A copper vacuum pipe (including the 1.5 mm thick teflon coat in its inner surface) and a complete shielding, made out of 1 cm of copper and 10 cm of lead, around the detector and along the vacuum pipe has been implemented. It has also been added the steel vacuum pipe that in real experiment is bolted to the copper one, and the two copper gas connectors used in practice for input/output of gas in the TPC chamber. Finally, the two scintillator vetoes installed in CAST sunset side during 2013 have been introduced. Different views of the simulated geometry are shown in figure 10.10.

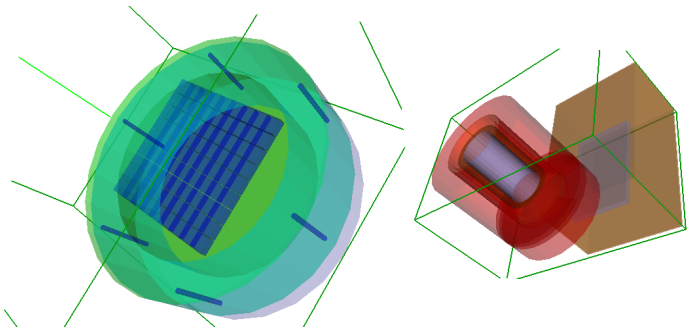

Figure 10.10: Schematic view of the simulated geometry: close view of the Micromegas TPC showing the strongback pattern (left) a complete view (right), including the copper Faraday cage (orange), lead shielding (red), vacuum pipe, and teflon coat.

Primary particles are generated from the *Generator* class, which includes methods for simulating different sources of ionizing radiation, like calibration sources, natural gamma background, etc. We have included methods for simulating the energy and angular distribution of cosmic ray muons and the decay of the main radioactive chains, ^{238}U and ^{2323}Th.

The simulation flow is managed by the *SteppingAction* class, in which the conditions for data storage are defined. This condition is set as any energy deposition in the active volume always the total energy release is below a user-defined value, above which the event is truncated. Energy depositions, or hits, are defined by the energy released to the gas molecules and its position. For each event, this information is stored in binary files along with the position and direction of the initial particle, type of physical interaction, and other auxiliary information for a better tracking of the events.

RESTSoft is a modular library written in C++ that provides all the functionalities needed to deal with the features and processes occurring on a gaseous ionization TPC, described in chapter 1. The software provides a set of classes to store complete generic event models and generic tools to manipulate the event's information. In the processing of simulated data, RESTSoft firstly

takes as input the result of the Geant4 simulations, i.e., collection of hits in the 3D sensitive volume (stored in an event holder class denominated *TRestPhysEvent*), and the different classes implement detector response effects such as primary charge generation, electron drift and diffusion, charge amplification, pixelization and signal induction in the readout planes. The processed data is stored in subsequent layers of event holder classes, which provides full traceability of the simulation chain. RESTSoft includes the ROOT [206] library, which provides all the functionalities needed for data processing, statistical analysis, visualization and storage. The data format output of the RESTSoft simulation chain is equivalent to the one of the real DAQ data, and it is stored in a branch of a ROOT *TTree*, as a class holder object defined in RESTSoft.

These files are ready to be analyzed using the same routines than the ones used for real data, which were described in chapter 6. On the other hand, the results of the intermediate simulation steps are also stored to get traceability of the final events.

A detailed description of RESTSoft and a complete validation of the simulation chain can be found in [27, 19]. Here, we apply the simulation framework to study the background contribution of the detector components and muons.

Muons Montecarlo simulations have been used to estimate the contribution of cosmic muons to the background level of CAST-Micromegas detectors. The use of active muon veto systems in surface tests and CAST data confirmed that the muon contribution to the background level is of $\sim 10^{-6}$ keV^{-1}cm^{-2}s^{-1}, being the main background component provided a relatively thick ($\sim$10 cm) 4π shielding covers the Micromegas detector.

Among all the primary and secondary cosmic ray particles, only the muonic component of the cosmics rays has been considered in this work, given that $p + n$ fluxes at sea level is around 2% of the muon flux, pion flux is 50 times smaller, and the e^+/e^- flux over $E > 1GeV$ averages about 0.0004 of the muon flux [209]. The expected contribution to the background of these remnant components of the cosmic rays is thus negligible. The results of the simulations are compared with experimental background levels of Micromegas detectors operated in surface. Additionally, some statistics regarding the phenomenology involved in the final background events are presented.

The initial muon vertexes and kinematics, the μ^+/μ^- fraction and the angular and energy distributions (see figure 10.11) are generated according to the current knowledge summarized in [209]. The angular and energy distributions of the initial muons are the following

$$\begin{aligned} \mu^+/\mu^- &= 1.25, \\ \Phi &= \int_{\theta<\pi/2} j(\theta,\varphi)\, d\Omega, \\ j(\theta) &= I\cos^2\theta, \\ d\Phi(\theta) &= \int_0^{2\pi} d\varphi\, I\, \cos^2\theta\, \cos\theta \sin\theta d\theta, \end{aligned}$$

where $I \sim 80$ m^{-2}s^{-1}sr^{-1}, and $0 < \theta < \pi/2$. The integrated flux has been assumed to be $\sim$ 130 $\mu^{-/+}$m^{-2}s^{-1} ($\sim$ 1 min^{-1}cm^{-2}), which has been used for background scaling.

Initial position of muons with respect to the TPC orientation is also reliably reproduced. Initial cosmic muons with the proper angular and energy distribution are randomly generated from a 4×4 m^2 flat surface situated at 1.5 m height from the center of the detector. In figure 10.12 it is shown the initial positions of the cosmics rays along this 4x4 m^2 surface that deposit, directly or by secondary interactions, an energy comprised in the defined energy RoI (0-15 keV) in the active volume of the MM. Note that $z = 0$ is the readout position, and $z>0$ is the direction towards the CAST magnet, i.e. the direction along which the pipe and shielding extend. Note that the distribution is almost symmetric, slightly polarized towards $z>0$. On the right of the figure 10.12 we find an example of these type of events, crossing also the top muon veto.

In figure 10.13 we show a comparison between a detector hitmap distribution of simulated and CAST-M10 background data (trigger rate largely dominated by cosmic muons). As the figure shows, a higher density of events is present close to the borders of the readout both in simulations

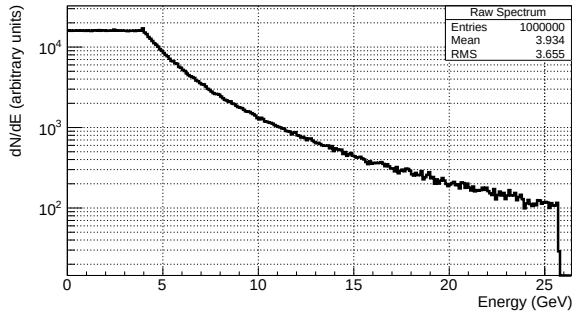

Figure 10.11: Cosmic ray muons energy spectrum.

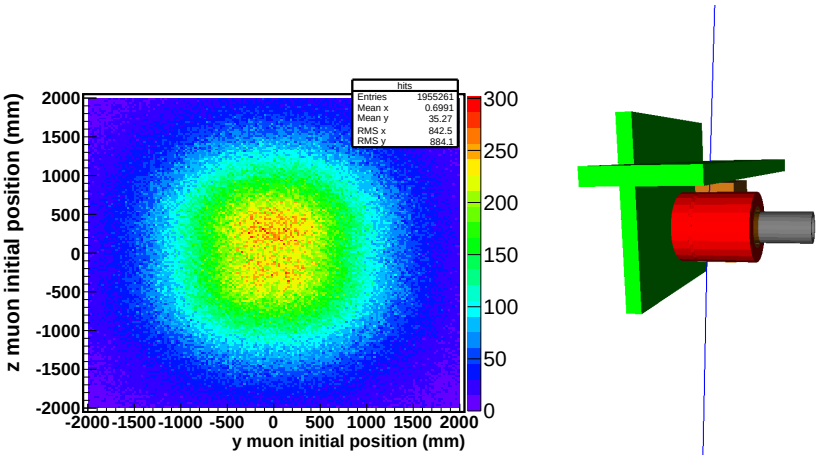

Figure 10.12: Left: Initial vertexes of the incident cosmic muons that deposited an energy lying in the CAST RoI (0-15 keV). z*-axis is the axis along the CAST vacuum line, while* y*-axis defines the horizontal plane over the Micromegas detectors. Right: example of a cosmic muon traversing the top scintillator (in green) and the detector.*

and real data. Readout and drift field imperfections and inhomogeneities are manifest in the hitmap distribution of CAST-M10 detector, contrarily to the simulated response, which it is more idealistic.

Raw simulated events are a set of energy depositions in the 3D detection volume. Additionally, some variables with physical information are also recorded for further investigation of the event history. Raw simulated events are then transformed into electronics signals according to the specific features of a CAST Micromegas TPC, as read out by Gassiplex electronics for the strips signals and a Matacq card for the mesh pulse. Primary charge fluctuations as well as avanlanche's fluctuations of the Micromegas detector have been considered. Electron cloud in the conversion region is gaussian spread in longitudinal and transversal directions. The processed simulated events are then analyzed following the same approach than for real data. The analysis is performed in two consecutive steps. In the first one, the program is able to find charge clusters from the physical signals and to generate the observable parameters of each event. The simulation of a ^{55}Fe source, whose spectrum is shown in figure 10.14, is also performed in order to define the selection criteria. As an example of the observable parameters, the distribution of the clusters size in x and y direction for simulated and real data are shown in figure 10.22 for ^{55}Fe calibration events.

In the second step, the discrimination parameters defined by calibration events are used to generate a selection criteria to reject or accept background events. The method consists in merging

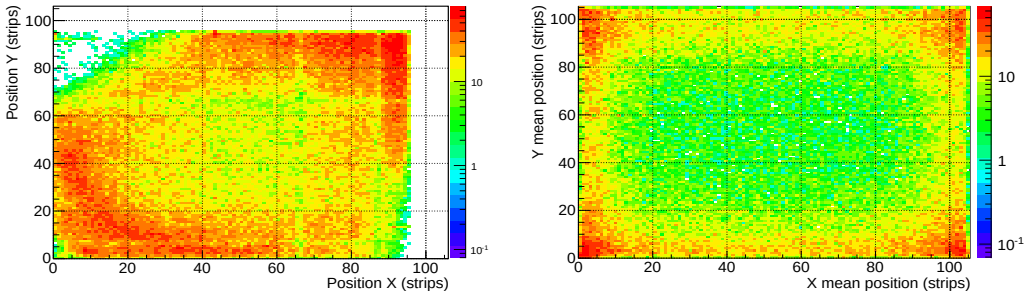

Figure 10.13: Hitmap distribution of background events generated in the RoI by the CAST-M10 detector in surface (left) and simulations (right). Note that in M10 detector the 10 outer strips in each axis are not read.

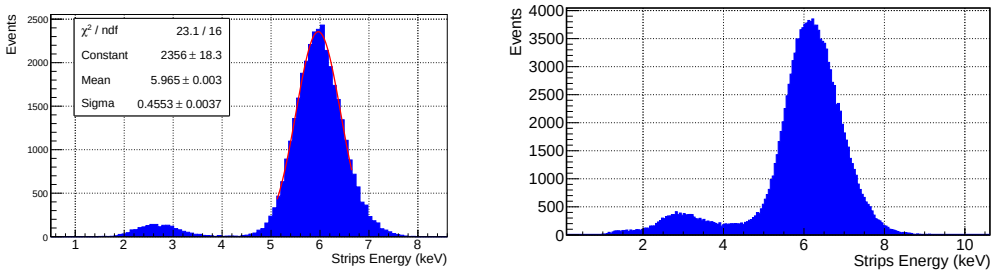

Figure 10.14: Energy spectrum of a simulated (left) and experimental CAST-M18 (right) run with a ^{55}Fe source.

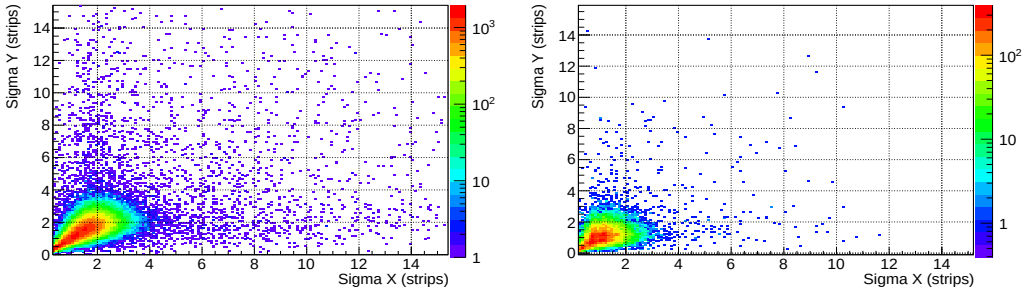

Figure 10.15: Strips width in each spatial direction ($x\Delta$ and y) for x-rays generated by a ^{55}Fe calibration run in in CAST-M18 (left) and in a simulated detector (right).

the set of observables used to discriminate into one single quantity, q. This value is set with the most representative fraction of the main peak (5.9 keV) events of the ^{55}Fe calibration. The set of observables used for the generation of the selection criteria include the mesh and strips signals:

- Pulse risetime: time length between 0.15 and 0.85 of the maximum pulse height or *amlitude*
- Charge Balance: difference between charge collected by X- and Y-strips.
- Energy balance 1: difference between energy given by mesh pulse amplitude and mesh pulse integral.

- Energy balance 2: difference between energy given by mesh pulse amplitude and strips integral.
- Energy balance 3: difference between energy given by mesh pulse integral and strips integral.
- Cluster size balance: deviation between X and Y cluster size.
- Multiplicity balance: deviation between X and Y multiplicity.
- Size: X and Y combined cluster size.

Additionally, a circular fiducial area with a radius of 21.5 mm centered in the middle of the readout is defined, as it is commonly done for Micromegas operated in CAST. Finally, we identify the muon-induced events in the real data: those events whose time difference between the triggers in the mesh and the scintillator veto are in a short time window (see figure 10.16, left). On the right of figure 10.16, the distribution of the simulated minimum drift distance of the primary electrons of each event along the z-axis is shown. Both experimental and simulated distributions show a large accumulation of events close to minimum drift distance, corresponding to events whose ionization track is crossing the Micromegas mesh; and an increase of events close to complete drift distance, presumably corresponding to short-track events originated in the cathode.

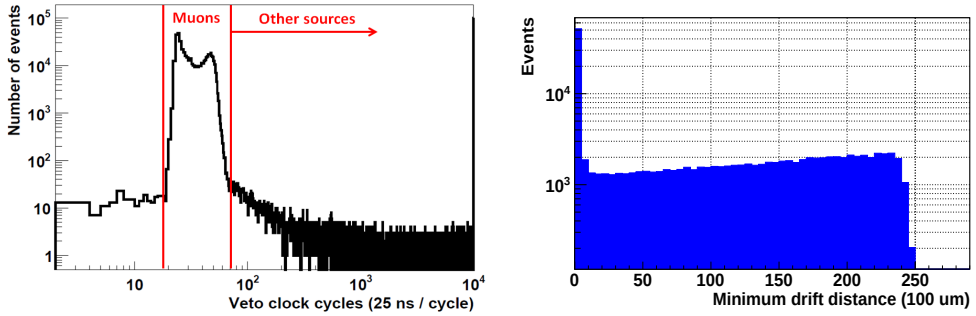

Figure 10.16: Distribution of the time elapsed between the scintillator veto and the mesh trigger in CAST-M18 data (left) and distribution of the minimum drift distance of the primary electrons generated by the muons simulation in a CAST-Sunset like setup (right).

CAST-M10 detector was operated in surface in a CAST-Sunset like setup with a muon veto system, whose position over the detector was very precisely known. The opening of the pipe that in CAST connects with the magnet was closed with 5 cm lead shielding. Simulations show that the veto efficiency (defined as the fraction of muons that ionize the active volume and are tagged by the veto respect the total number of ionizations in the energy RoI) is 75%.

In table 10.3, the simulation results of the CAST-M10 setup and CAST2013 Sunset setup (labeled as *Zgz-Sim* and *SS-Sim*) are summarized, and the experimental values are also shown for comparison.

The resulting background energy spectra are compared in figure 10.17 and 10.18. Both experimental and simulated energy spectra show a roughly flat shape in the RoI and a bump around 8 keV, corresponding to the Cu K_α line. The experimental and simulated reductions in background level due to the veto are in good agreement. As the values in the table indicate, this fact means that the contribution of other sources of background (external *gammas*, internal radioactivity, etc.) at sea level are modest with the current shieldings. This evidence is supported by Canfranc results, where levels as low as $\sim 10^{-7}$ keV^{-1}cm^{-2}s^{-1}have been obtained. Using all the statistics of the simulated datasets, the total muon contribution to the background is estimated in (1.37 $\pm$ 0.14) $\times 10^{-6}$ keV^{-1}cm^{-2}s^{-1}.

Simulations offer the possibility of reconstructing the phenomenology of each event. It is observed that the $\sim$ 42% reduction achieved in the CAST-Sunset (SS-Sim) due to the muon vetoes is the addition of 32% and 10% reduction of the top and back veto respectively. Remarkably, the background reduction obtained in the setup with only $\sim$75% geometrical veto efficiency (Zgz-Sim,

Detector	Time (hours)	Cover. (%)	Eff. (%)	Total bkg. (10^{-6} ×	μ cut keV^{-1}cm^{-2}s^{-1})	μ bkg.	Red. (%)
Zgz-M10^{+}	454	75	40/75	1.60 ± 0.12	0.83 ± 0.08	0.77 ± 0.08	48
Zgz-M10^{++}	303	75	40/75	1.50 ± 0.14	0.68 ± 0.09	0.82 ± 0.10	55
Zgz-Sim	564*	75	40/75	1.33 ± 0.20	0.66 ± 0.14	0.66 ± 0.14	50
SS1-M18	1061	94	40/75	1.24 ± 0.05	0.79 ± 0.04	0.45 ± 0.04	36
SS2-M15	713	94	40/75	1.75 ± 0.07	1.04 ± 0.05	0.71 ± 0.06	41
SS-Sim	765*	94	40/75	1.39 ± 0.17	0.82 ± 0.13	0.59 ± 0.12	42

Table 10.3: Summary of experimental and simulated results. Zgz-M10 detector corresponds to data taken with a CAST-Sunset like setup with the opening of the pipe closed with a 5 cm thick lead brick. SS1 and SS2 data correspond to CAST-2013 data taking campaign. Final background levels expressed in 10^{-6} $keV^{-1}cm^{-2}s^{-1}$ and statistical errors are given as 1σ. (*) simulation hours equivalent, i.e. number of initial vertexes normalized by the theoretical muon flux and surface. ($^{+}$) Pipe aperture closed with 1.6 cm steel plate, approximately reproducing CAST situation. ($^{++}$) Pipe aperture closed with 5m lead brick.

50% reduction) is slightly higher than for the setup with ∼94% efficiency (SS-Sim, 42% reduction). This fact points to the importance of covering the surface that extends in front of the detector, which cannot be done in CAST-Sunset due to the mechanical constraints of the setup. It is found that around 1/2 of the final events are coming through the x-ray window that closes the CAST Micromegas chamber. Regarding the type of interaction that triggers the ionization in the active volume it is observed that almost 3/4 of the final events are induced by electrons or a delta rays, while less than 10% are induced by gammas interacting via Compton process or photoelectric effect. From the background events that survive to the muon veto cut, 51% of them come through the window in the SS-Sim setup, while only 29% of them do it in the Zgz-Sim setup. Finally, it is found that around 85% of the final events triggered directly by a $\mu^{+/-}$ are rejected by the veto in both setups.

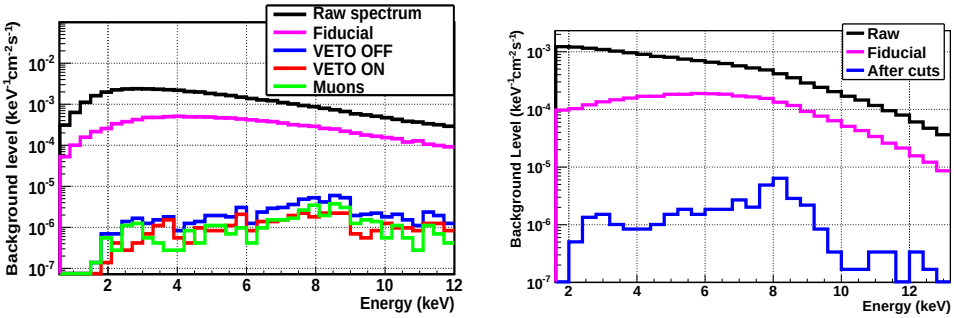

Figure 10.17: Left: background energy spectra of CAST-M15 detector in CAST-SS2 20013 data taking campaign. Right: simulated background energy spectra of a CAST-Sunset like setup. Blue line represents the total contribution of muons to the background after applying the rejection algorithms.

Montecarlo simulations have been used to estimate the contribution of cosmic muons to the background level of MM detectors on the sunset side of the CAST magnet. The total muon contribution to the background is around 1.4 keV^{-1}cm^{-2}s^{-1}, i.e., the dominant component of CAST-MM detectors at sea level. The reduction obtained in CAST with active veto systems is well reproduced in simulations. We find that even with $\gtrsim 90\%$ geometric efficient vetoes, backgrounds are still dominated by muon-initiated events. Consequently, paving larger areas with muon veto systems is a requirement for further reducing the backgrounds values at sea level.

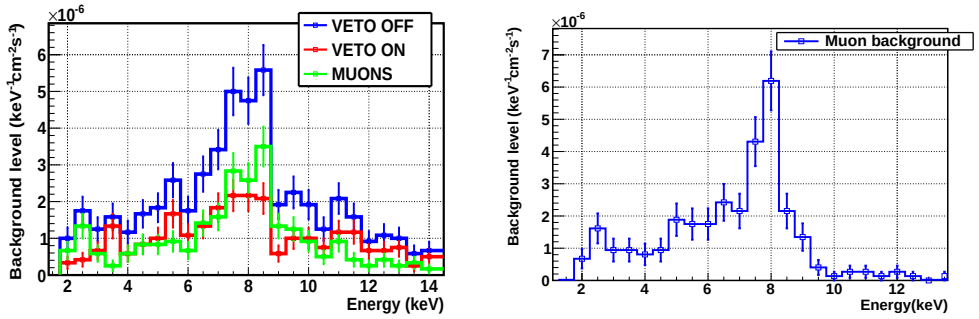

Figure 10.18: A zoom to the final background energy spectra after the application of the selection criteria for the CAST-SS2 (M15) detector during the 2013 data taking campaign at CAST (left) and the simulated sunset setup (right) with signal acceptance of 40% and 75% at 3 and 6 keV respectively.

Internal radioactivity The same approach has been used to estimate the contribution to the background of the detector components' radioactivity. The full decay chains of the ^{238}U (except when the secular equilibrium is found to be broken at the ^{222}Rn isotope), ^{232}Th and ^{40}K have been simulated as one single *Geant4* event by means of the Geant4 Radioactive Decay module. Each energy track has associated a global time in order to distinguish events which produce a track in a time lapse larger than the maximum drift time ($\sim$3 μs). Specific methods have been developed to confine the primary vertexes to the relevant volumes. As an example, we show in figure 10.19 the primary vertexes of those events depositing an energy in the CAST RoI from the simulation of the cathode and gas connectors radioactivity.

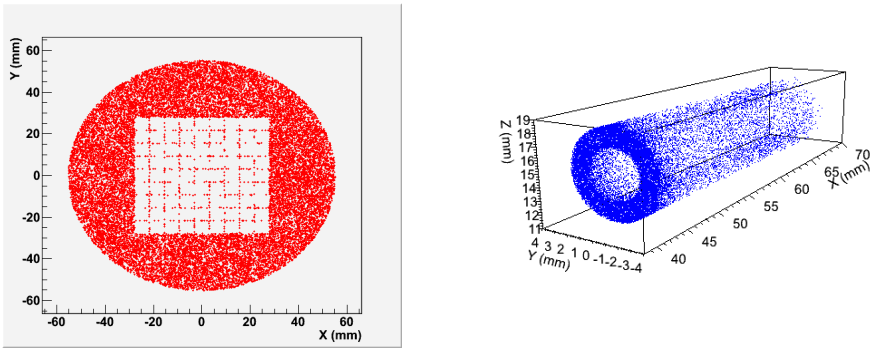

Figure 10.19: The primary vertexes of those events depositing an energy in the CAST RoI from the simulation of the cathode (left) and gas connectors (right) radioactivity.

The results of the simulation have been weighted by the activities of the components measured in a high-purity germanium detector in the LSC or taken from the database [208]. The first MM detectors were equipped with a cathode made on aluminum. These cathodes were found to be very radioactive, ^{238}U = 30 Bq/kg, ^{232}Th = 0.42 Bq/kg, ^{235}U = 0.49 Bq/kg. The contribution to the background of this contamination was evaluated, being at the level of $(6.9 \pm 0.6) \times 10^{-7}$ keV^{-1}cm^{-2}s^{-1} at 75% signal acceptance. The contribution of the aluminum cathode was also assessed at the LSC replacing it by a copper one. The difference in background between the runs performed with the aluminum and copper is attributed entirely to the radioactivity of the first cathode, being

$(5.2 \pm 0.9) \times 10^{-7}$ keV^{-1}cm^{-2}s^{-1} at 75% signal acceptance. We find thus simulations and experimental measurements to be in good agreement, both quantitatively and in the shape of the spectrum, as figure 10.20 shows. The most important contribution of this contamination is at low energies, below ∼3 keV.

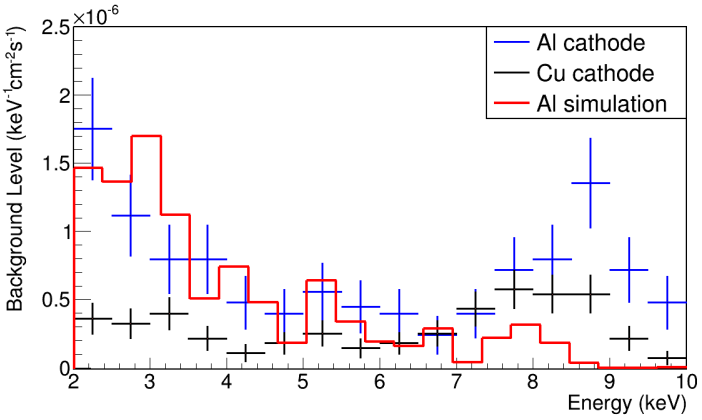

Figure 10.20: Comparison of the background spectrum produced by the simulation of the aluminum cathode and experimentally measured at the LSC. This cathode was replaced by a copper one, and the obtained spectrum is also shown.

The contribution of the remaining components was also studied. The activity of the relevant materials is summarized in table 10.4, along with the background levels computed with the simulations. Most of the values are upper limits, since some of the measured activities for some decay chains are just given from the minimum detectable activity. The total background induced by the contamination of the detector components is lower than 4×10^{-8} keV^{-1}cm^{-2}s^{-1}, a factor ∼3 below the best level measured at the LSC. The spectra obtained with the dominant contributions are shown in figure 10.21, where 3 and 8 keV fluorescence peaks are observed.

It was lately found that the isotope ^{39}Ar, present in natural argon with an abundance of $8{\times}10^{-16}$, has a beta decay with $T_{1/2} = 269$ years and $Q_\beta = 565$ keV. This is a potential background source since the decay takes place in the active volume itself. A back-of-the-envelope calculation (done by S. Cebrian) shows that the total activity of ^{39}Ar in the CAST chamber at 1.4 bar would be $3.3{\times}10^{-4}$ s^{-1}. Although only a small fraction (∼2%) of those decays would release energies below 7 keV, they may produce a background level as high as $\sim 5 \times 10^{-8}$ keV^{-1}cm^{-2}s^{-1} in the RoI. The current limits at the LSC are only 2 times larger. It is enough that only 3% of the decays above 7 keV produce secondaries in the RoI to completely explain the current limit. This is the reason why new gas mixtures based on xenon or depleted argon are being considered for the future. A detailed simulation of the ^{39}Ar in the CAST-MM is pending, while the simulation results of TREX-DM (see table 12.1) confirm that ^{39}Ar is critical to achieve ultra-low background levels.

10.3.4 Background dependence on detector size

A larger detector readout could possibly be more efficient in rejecting backgrounds because second clusters or longer tracks could be identified. The goal of this section is to study the dependence of the background level on the detector size and analyze the background distribution over the detector readout plane.

We only have CAST-MM detectors of $6{\times}6$ cm^2, but we can instead "build" virtual detectors by simply neglecting a certain number of outer strips in both detector plane directions. This is done by ignoring the signals induced in the excluded strips during the data analysis. This study is done

Component	^{238}U (mBq/kg)	^{232}Th (mBq/kg)	^{40}K (mBq/kg)	Background ($\times10^{-8}$ keV^{-1}cm^{-2}s^{-1})
vessel	100*	10*	30*	< 2.1
readout	2.63×10^{-2}	9.3×10^{-3}	5.73×10^{-2}*	< 1.2
o-rings	858	130	2.17×10^{3}	0.6
strongback (Cu)	1*	1*	1*	$<1.5\times10^{-2}$
gas ports	5*	10*	3*	$<2\times10^{-3}$
screws	14.8	10.4	16.6	6×10^{-4}
Total	–	–	–	< 4.0

Table 10.4: Measured activity and induced background in [2–7] keV region from each of the relevant components of the CAST-MM detector. Statistical errors below ∼10%. (*)Activity levels obtained from minimum detectable activity.

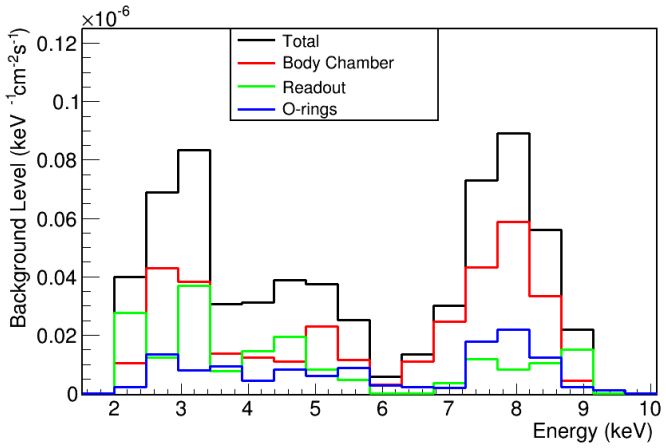

Figure 10.21: Simulated background spectrum of the dominant contamination sources. Argon and copper fluorescences are clearly activated, as the 3 and 8 keV lines are clearly visible.

with a dataset corresponding to 1416 and 1915 hours of background took by the *sunrise* and *sunset 1* detectors in the 2014 CAST data-taking campaign. The background rejection is done using the ^{55}Fe calibrations as reference for the production of the cuts in the energy ranges 2–4.5 keV and 4.5–12 keV at a 75% signal acceptance. Note that in the *sunrise* detector only the central 25 mm diameter circumference is illuminated during calibrations. We have thus extended the cuts to non-calibrated regions, assuming a good uniformity of the detector response, as observed in tests done previously to its installation in CAST.

The background level as a function of the detector size is summarized in figure 10.22 for the *sunrise* and *sunset 1* detectors. The different lines correspond to the different acceptance areas where the background is defined. Although statistical errors are large due to the low counting rate, we observe a clear trend in both detectors showing that lower backgrounds are achieved in larger detectors. For example, in the *sunrise* detector an increase of $(0.6 \pm 0.3) \times 10^{-6}$ keV^{-1}cm^{-2}s^{-1} is observed when passing from a 6×6 cm^2 to 2×2 cm^2 detector readout.

A systematic effect has been considered as the possible source of the result: *smaller* detectors cotain less calibration events (instead of $\sim10^5$, less than 10^4) and calibration observables could be then poorly defined, producing a higher background level. This hyptohesis has been verified by changing the analysis procedure. Instead of applying the usual "run-to-run" analysis, in which each calibration run is used as the reference for the closest background run, we have used several

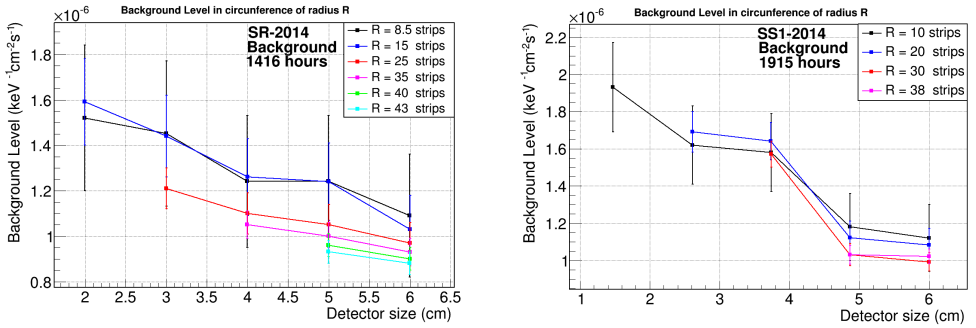

Figure 10.22: Background level versus detector size at different acceptance regions for sunrise and sunset Micromegas of the 2014 data-taking campaign. The "run-to-run" analysis is used.

calibrations runs to define the cuts, dramatically increasing the statistics.

The results obtained with this method are shown in figure 10.23, again for *sunrise* and *sunset 1* detectors. From the figure, it can be noted that the same trend persists. The background spectra registered in the inner and outer rings are compared in figure 10.25 (left), and the difference among them is plotted on the right of this figure after the application of the strips cuts (black line) and veto cut (red line). The spectral shape registered in both rings present the same characteristic features, with the difference increasing at the characteristic peaks.

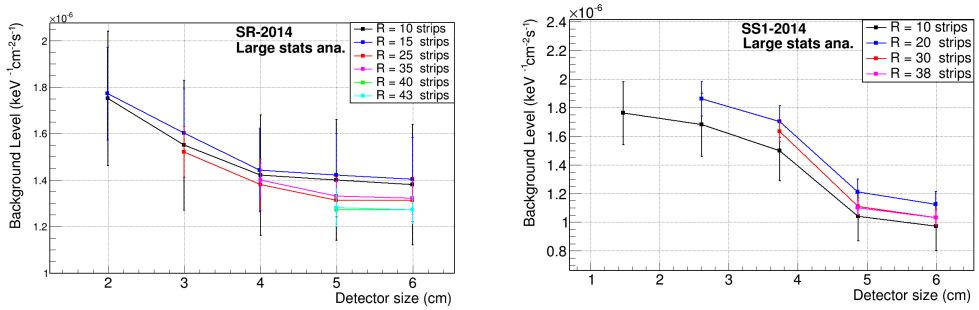

Figure 10.23: Background level versus detector size at different acceptance regions for sunrise and sunset Micromegas of the 2014 data-taking campaign. The analysis that gathers several calibration runs to define the cuts is used.

Background uniformity: It has also been studied the distribution of the background over the detector surface for a fixed detector size. With this purpose, the detector area has been divided in concentric rings of approximately the same area. The ring is defined by an external $R_{\max}$ and internal $R_{\min}$ radius. Figure 10.24 represents the dependence of the background level on the mean distance from the detector centre r, defined as $r = (R_{\max} - R_{\min})/2$, for five CAST-MM detectors. It is observed that the background level is slightly higher towards the center in all the detectors, although with different intensity. A tentative physical explanation for this effect is that the mean free path of photons in our range of interest is below 2 cm, so the x-rays produced in the surroundings of the fiducial area (for example in the mesh) are more likely to interact towards the edges of this area.

10.4 Conclusions and prospects for IAXO

The understanding of the background exceeds by far its measurement only: beyond the detailed recording we need to determine the origin and the physical mechanisms producing the detected

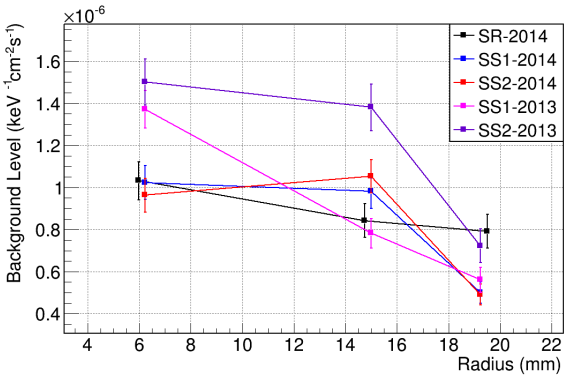

Figure 10.24: Backgroud level as a function of the distance r from the detector center. The distance r is defined as $r = (R_{max} - R_{min})/2$, defining concentric rings of similar area.

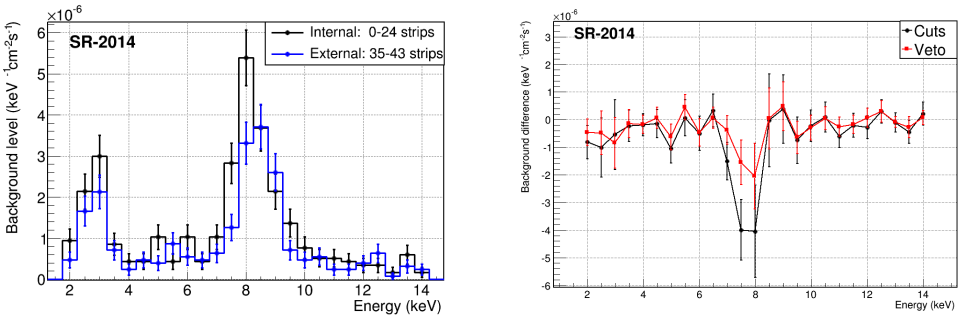

Figure 10.25: Background spectra of the inner and outer rings defined in the sunrise 2014 detector.

x-ray like events. The current understanding is based on comparison studies of *in-situ* measurements in CAST, experimental tests carried out at installations located both at underground and aboveground level, as well as in detailed Monte Carlo simulations.

Although the research in low background techniques in Micromegas detectors has led to an impressive reduction of the background at CAST, an ultra-low background detector is required for IAXO, a new generation axion helioscope that would improve the sensitivity to $g_{a\gamma}$ in more than one order of magnitude. The final goal in terms of background level is 10^{-7} down to 10^{-8} keV^{-1}cm^{-2}s^{-1} if possible.

Currently, the main target of our background reduction activities are: cosmic muons at surface and ^{39}Ar underground, which are limiting the background level at 7 and 1×10^{-7} keV^{-1}cm^{-2}s^{-1}, respectively. The first limit could be pushed down with a higher efficient veto system, while the second requires a change of gas (for example, xenon) or the use of depleted argon from underground sources. These strategies are currently being actively developed.

Thanks to IAXO, a large part of the parameter space could be explored in the next decade, entering in the most favored regions for axions and ALPs. Furthermore, IAXO could be sensitive to non-hadronic solar axions, and other more exotic particles, like chameleons or hidden photons. In both cases the key would be the reduction of the low energy threshold and the increase of the transparency of the detectors to soft x-rays.

With this purpose, new research and design lines are being investigated:

- New thin windows: The efficiency of the Micromegas at low energies is limited by the x-ray transparency of the cathode window. Different materials are being investigated.
- AGET front-end electronics: The novel AGET [273] electronics keep the main features of

the AFTER but with auto-trigger functionality. So the energy threshold could be reduced.

- Resistive Micromegas: The use of this type of detectors will allow to work at higher gain without the risk of damaging sparks, possibly allowing to achieve lower thresholds.

Part III

A Micromegas-based TPC for low mass WIMP detection: the TREX-DM project

Chapter 11

Dark Matter: evidence, candidates and searches

Contents

11.1 Introduction

The evidence for the existence of cold dark matter (DM) in our universe relies on an increasing body of observations at very different astrophysical scales and from very different fields of particle physics, astrophysics and cosmology. The interplay between these fields of knowledge and experimental physics is of great importance and it is in continuous evolution since DM was proposed in the 30s of the last century. Theoretical particle physics formulates new theories to fill the Standard Model (SM) caveats, and they usually come along with new particles that sometimes are excellent candidates for composing the DM of the universe. The most compelling particles proposed so far are axions (discussed in part II of this *Thesis*) and weakly interacting massive particles (WIMPs). In this chapter we will focus our attention in the latest.

A generic WIMP is the canonical and most widely studied DM candidate for several reasons: it would be produced thermally in the correct amount, accounting for the observed DM density; it arises naturally in very well motivated extensions of the SM, such as supersymmetry; a large well motivated parameter space has been within the reach of the experimental technology, which has dramatically improved in the last decades. WIMPs can be searched in particle accelerators (through missing energy events), indirectly (through the observation of its decay or annihilation products) or directly (through its elastic scattering with the nuclei of a target material).

In this chapter, we first review the dark matter evidences and main candidates, based on references [209] and [210]. For further details, the reader is referred to these publications and references therein. Subsequently, the experimental techniques and the challenges for the WIMP direct detection are discussed, and finally the status and prospects for these searches are reviewed.

11.2 Evidence for Dark Matter

The observational evidences of DM usually lead to setting a lower bound on its mass density, Ω_{DM}, where $\Omega_i \equiv \rho_i/\rho_c$, being ρ_c the mass density required for a flat universe ($k = 0$). The total energy density of the universe is thus expressed as $\Omega \equiv \sum_i \Omega_i = \sum_i \rho_i/\rho_c$.

The earliest and most convincing evidence for dark matter is the observation that some luminous objects move faster than expected from the gravitation attraction of visible objects. At **galactic scale**, the measurement of the velocity of stars and gas as a function of the distance from the galactic center (the so-called galactic *rotational curves*) is the most prominent observation. In Newtonian dynamics, the rotational velocity of an object is expected to scale as $v(r) \propto \sqrt{M(r)/r}$, where $M(r)$ is the mass inside the orbit, $M(r) = 4\pi \int \rho(r) r^2 dr$, being $\rho(r)$ the mass density profile. Beyond the optical disc of the galaxy one would expect $v(r) \propto 1/\sqrt{r}$. However, it is found that in most galaxies the velocity profile becomes approximately constant. This fact implies the existence of a *dark halo* with $M(r) \propto r$ and therefore $\rho(r) \propto 1/r^2$, which at some radius should drop faster to keep finite the galaxy size. These observations set a lower limit on the DM mass density, $\Omega_{DM} \gtrsim 0.1$.

The same type of observation were done at the **scale of galaxy clusters**. Indeed, the first hint of the existence of dark matter was inferred by F. Zwicky in 1933 [211], from the measurement of the velocity of galaxies (induced from the Doppler shift of their spectra) in the Coma cluster. Galaxy clusters are interesting objects because there are independent methods to calculate its total mass, which can be compared with its baryonic mass. The cluster mass is estimated in these ways:

- From the measurement the dispersion in the radial velocity of galaxies within the cluster, as in Zwicky's observation but with more accurate measurements and larger samples.
- From the x-ray emission spectra of the hot gas within the cluster, its temperature and density can be derived. The mass profile of the cluster is calculated assuming balance between the gas pressure and gravity forces.
- From the gravitational lensing of background objects, such as galaxies.

A very compelling observational evidence of the DM is the dynamics of a system known as *Bullet Cluster*, namely, a galaxy clusters passing through another. The x-ray observations show that most of its baryonic mass is decelerated as a result of the electromagnetic interaction of the gas particles. However, gravitational lensing observations show that most of the total mass of the clusters is not slowed down, passing through one another without any significant change. This is interpreted in terms of DM since it does not feel electromagnetic interactions and DM self-interactions are also weak.

The observations at the galaxy cluster scale set a lower limit on the DM mass density, $\Omega_{DM} \simeq 0.2 - 0.3$, somewhat larger values than observations at galactic scale.

Finally, observations at **cosmological scale** provide the most accurate measurement of Ω_{DM}. In particular, the latest measurements of the anisotropies in the cosmic microwave background (CMB) by the *Planck* mission [98] find a density of cold, non-baryonic matter

$$\Omega_{\rm nbm} h^2 = 0.1186 \pm 0.0020 \tag{11.1}$$

where h is the Hubble parameter in units of 100 km/s/Mpc. On the other hand, the density of baryonic matter is found to be $\Omega_{\rm b} h^2 = 0.02226 \pm 0.00023$, part of which may contribute to the (baryonic) DM. These observations report a total mass density $\Omega_{\rm m} = 0.308 \pm 0.012$, being the *dark energy* component $\Omega_\Lambda = 0.692 \pm 0.012$.

11.3 Candidates for Dark Matter

The non-baryonic DM of the universe must satisfy some conditions: a) structure formation in the universe requires that DM particles are *cold*, i.e., non-relativistic at the time of galaxy formation; b) they must be stable on cosmological time scales, otherwise it would have decayed by now; c) they must be very weakly interacting with SM particles; d) they must provide the correct amount

of relic density; e) neutral; f) it must not be in conflict with Big-Bang nucleosynthesis, stellar evolution and current null experimental results.

It must be stressed that dark matter is not necessarily made of a single particle type. In fact, SM neutrinos are known to contribute to equation 11.1 in an amount given by $\Omega_\nu \leq 0.00062$ at 95% confidence level, i.e., they contribute to DM but cannot account for all of it. Some candidates that could account for a part or the total amount of DM are: primordial black holes (formed before the Big-Bang nucleosynthesis to contribute to equation 11.1), sterile neutrinos with keV masses, Kaluza-Klein states which appear in models of universal extra dimensions, among others. For a full review of non-baryonic DM candidates see [210] and references therein. However, the most appealing candidates are WIMPs and axions.

The most widely studied WIMP candidate is the lightest supersymmetric particle (LSP) with exact R-parity, which prevents its decay to SM particles, being therefore stable in cosmological time scales. Among other LSP candidates the lightest neutralino χ is the most promising. The mass of χ usually ranges from few GeV to some TeV, and with cross-sections to SM particles roughly of the size of weak interactions. Their current contribution to the energy density of the universe is computed within the framework of standard cosmology. Assuming that χ is in thermal equilibrium with SM particles just after the inflation, their density drops exponentially when the temperature of the universe goes below m_χ. In this case, the expansion rate of the universe becomes larger than the rate of reactions of the type $\chi\chi \longleftrightarrow$ SM particles, breaking the thermal equilibrium. Consequently, the WIMP density *freezes-out* and stays roughly constant. The *freeze-out* occurs roughly at $T_F \simeq m_\chi/20$ in most models, so they are already non-relativistic (*cold*) at the moment of decoupling.

On the other hand, axions ,and more generic axion-like particles (ALPs), turn out to be excellent cold DM candidates because, although very light, they can be produced non-thermally. ALPs can saturate equation 11.1 if the Peccei-Quinn symmetry is broken at scale $f_a \sim 10^{11}$ GeV. For further details on axions see chapter 2 of this *Thesis*.

All the DM candidates must fulfil the set of conditions stated before, but their nature and properties are very different as shows figure 11.1.

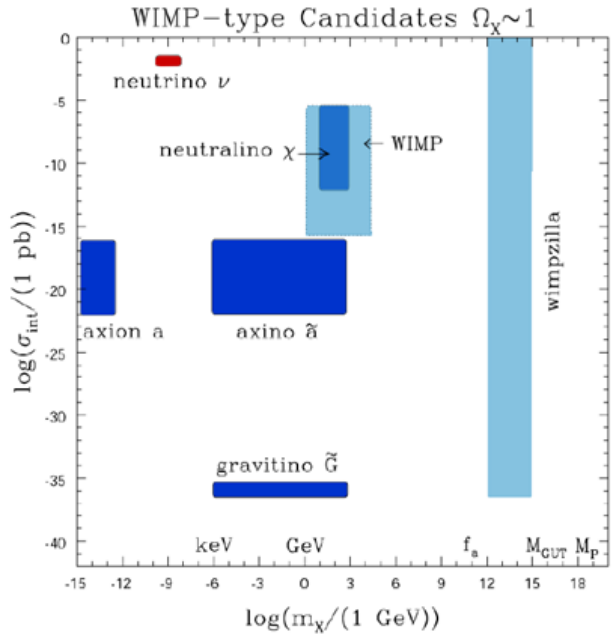

Figure 11.1: WIMP-type dark matter candidates with $\Omega_\chi = \Omega_{nbm}$ in the cross-section versus mass parameter space.

11.4 Direct WIMP searches

The direct detection of WIMPs or the constrains to its properties is based on the calculation of the expected counting rate in a detector. The comparison of all the experimental results requires the adoption of general hypothesis, whose uncertainties determine the accuracy on the expected counting rates and on the constrains on the parameters of the WIMP. The canonical calculation method is reviewed in this section, along with the distinctive features that could lead to a positive identification of the dark matter. The extremely low expected event rates and energy depositions impose the characteristics of any direct detection experiment. Finally, the experimental status and prospects are discussed.

11.4.1 Event rates

The WIMP direct detection rate depends on both astrophysical, particle and nuclear physics inputs. From the astrophysics side the inputs are the local WIMP density and velocity distribution in the detector frame. From particle and nuclear physics the inputs are the nuclear form factors and interaction cross-sections, which depend on the theoretical framework in which the WIMP candidate arises. Besides, experimental properties such as the *quenching* factor, energy resolution or energy threshold of the detector must be taken into account. Here, we review the parameters and assumptions (and therefore the uncertainties) in the calculation of the expected rate caused by a WIMP scattering elastically on the target material of a detector, focusing the discussion in the spin-independent coupling.

We start by assuming the existence of a WIMP halo in our galaxy of local density ρ_0. Given the neutral, weak-interacting and massive WIMPs nature we are forced to look for WIMP-nucleus elastic scattering as the most feasible technique for direct dark matter detection. The differential event rate, usually expressed in terms of counts/keV/kg/day, is proportional to the number of WIMPs per unit volume, $n = \rho_0/m_\chi$, to the WIMP-nucleus cross section, σ_{WN}, to the mean WIMP velocity, $< v >$, and normalized by the nuclear mass of the target element, m_N, being $N_T = M_{\rm det}/m_N$ the number of target nuclei in the detector. The differential rate for WIMP elastic scattering on nuclei is therefore:

$$\frac{dR}{dE_R} = \frac{\rho_0}{m_\chi m_N} \int_{v_{min}}^{v_{max}} v f(v) \frac{d\sigma_{\chi N}}{dE_R} dv \tag{11.2}$$

where $f(v)$ is the WIMP velocity distribution in the Earth frame and $d\sigma_{\chi N}/dE_R$ is the WIMP-nucleus differential cross-section. The WIMP-nucleus relative speed is non-relativistic (a few 100 km/s), and the WIMP energy is given by $E_\chi = m_\chi v^2/2$, while the energy transferred to the nucleus is

$$E_R = \frac{E_\chi \mu_r (1-\cos\theta)}{2} = \frac{\mu_r^2 v^2}{m_N}(1-\cos\theta) \tag{11.3}$$

where θ is the scattering angle in the WIMP-nucleus center of mass frame, and $\mu_r = m_\chi \cdot m_N/(m_\chi + m_N)$ is the WIMP-nucleus reduced mass. The minimum WIMP velocity to which the detector is sensitive

$$v_{min} = \left(\frac{m_N E_{th}}{2\mu_r^2}\right)^{1/2} \tag{11.4}$$

where E_{th} is the effective energy threshold of the detector. On the other hand, v_{max} is the maximum velocity at which WIMPs are gravitationally bounded to our galaxy, namely the escape velocity $v_{\rm esc}$.

The WIMP-nucleus cross-section can be separated into spin-dependent (SD) and spin-independent (SI) contributions, but for noble gases the SI independent process is enhanced. Encoding the momentum transfer dependency into the form factors $F(E_R)$, which represent the lost of coherence in the interaction as a result of the finite size of the nucleus, the cross-section is given by:

$$\frac{d\sigma_{\chi N}}{dE_R} = \left(\frac{d\sigma_{\chi N}}{dE_R}\right)_{SI} + \left(\frac{d\sigma_{\chi N}}{dE_R}\right)_{SD} = \frac{m_N}{2\mu_r^2 v^2}\left(\sigma_0^{SI} F_{SI}^2(E_R) + \sigma_0^{SD} F_{SD}^2(E_R)\right) \tag{11.5}$$

where σ_0 is the elastic cross-section for null momentum transfer. The SI and SD contributions arise from different couplings of the WIMPs with quarks. In the following, we will limit the discussion to the SI case. For this coupling, σ_0 is

$$\sigma_0 = \frac{4\mu_r^2}{\pi}\left[Z f_p + (A - Z) f_n\right] \tag{11.6}$$

where Z and A are the atomic and mass numbers, being f_p and f_n the effective coupling of the WIMPs with the protons and neutrons, respectively. Assuming $f_p \simeq f_n$, σ_0 can be written in terms of the WIMP cross-section with the nucleon, $\sigma_{\chi n}^0$, as

$$\sigma_0 = \left(\frac{1 + m_\chi/m_n}{1 + m_\chi/m_N}\right)^2 A^2 \sigma_{\chi n}^0 \tag{11.7}$$

where m_n is the mass of the nucleon in the approximation that the proton and neutron have equivalent mass. This expression allows to directly compare the cross-section on different target materials. The nuclear form factor is the Fourier transform of the nuclear density and it is parameterized as a function of the momentum transfer q. The analytic expression most widely used is:

$$F^2(q) = \left(\frac{3 j_1(qR_1)}{qR_1}\right)^2 \exp\left(-q^2 s^2\right) \tag{11.8}$$

where j_1 is the second spherical Bessel function, $s \simeq 1$ fm is an estimation of the nuclear skin thickness, and R_1 is related with the nuclear radius $R_1^2 = R^2 - 5s^2$, with $R \simeq 1.25 A^{1/3}$.

Under these assumptions, the calculation of the WIMP phenomenology in a detector has been reduced to the specific characteristics of the WIMP nature, its mass and cross section with the nucleon. Consequently, the results of any experiment will be interpreted in terms of these parameters, or more graphically, as regions in the parametric space (m_χ, $\sigma_{\chi n}$). The substitution of equation 11.5 into equation 11.2 results in a differential rate given by

$$\frac{dR}{dE_R} = \frac{\rho_0}{2 m_\chi \mu_N^2}\sigma_0 F^2(q) \int_{v_{min}}^{v_{esc}} \frac{f(v)}{v} dv \tag{11.9}$$

where σ_0 and $F^2(q)$ are those given in equations 11.7 and eq:ff, respectively. The main uncertainties in the determination of the expected event rate come from the astrophysical input, namely the halo model, and from the detector response to nuclear recoils. These factors are studied below.

Input from astrophysics. The existent uncertainties in the structure and distribution of a dark matter galactic halo translate into uncertainties in the event rate determination and in the inferred constraints on the scattering cross section. Most of this dependency is encoded in the WIMP local density ρ_0, which it is an overall multiplicative factor of the differential rate.

The distribution, structure and parameters of the galactic halo model are mainly (but not only) constrained from the observation of the galactic rotational curves. The shape of the halo distribution function presumably depends upon the details of the collapse process which formed the galaxy. However, general dynamic arguments suggest that the WIMP velocities were thermalized by fluctuations in the gravitational potential during collapse. The standard halo model (SHM) predicts an isothermal, spherical and isotropic halo, with density profile $\rho(r) \propto r^{-2}$ and Maxwellian velocity distribution:

$$f(v) = \frac{1}{\sqrt{2\pi}\sigma_v} \exp\left(-\frac{v^2}{2\sigma_v^2}\right) \tag{11.10}$$

where the dispersion in the velocities is related with the local circular velocity by $\sigma_v = \sqrt{3/2} v_c$, where in the SHM $v_c = (220 \pm 20)$ km/s, being $\sigma_v \simeq 270$ km/s. The WIMP distribution is

truncated at the local galactic escape velocity, $v_{esc} \sim$ 500-650 km/s. The velocity of the earth with respect to the local system (ignoring the motion of the earth around the sun) is around 12 km/s, so the velocity of the air with respect to the halo is $v_r = v_c + 12$ km/s $\simeq 232$ km/s. In the SHM the value for the local density is, within a factor 2, $\rho_0 = 0.3$ GeV/cm^3.

The SHM is a first approximation to the actual structure of the halo in the Milky Way that reproduces the rotational curves, but in principle, any other model that reproduces the observational parameters is acceptable. Indeed, there are some evidences of small substructures, such as streams or minihaloes, that would not change the local density significantly. There are also indications that the dark halo could be up to some extent triaxial and anisotropic.

Input from the detector response. A fraction of the nuclear recoil energy is not transformed into visible energy, namely ionization or scintillation. This means that an electron and nuclear recoil of the same energy do not produce the same amount of primary charges or light. Since direct detection detectors are usually calibrated with gamma sources it is necessary to correct the energy scale if one wants to express the WIMP rate in terms of visible energy, which is what an experiment actually will measure.

The fraction of energy of a nuclear recoil finally converted into ionization/scintillation respect to the signal that would produce an electronic interaction of the same energy, is an experimental parameter denominated *quenching* factor, $Q(E_R)$, that depends on the recoil energy and the detector material. It is defined as

$$Q(E_R) = \frac{\text{ionization/scintillation per unit energy for nuclear recoils}}{\text{ionization/scintillation per unit energy for electron recoils}} \tag{11.11}$$

There are different parameterizations of this factor. In this calculation we used [212]

$$Q(E_R) = \frac{g(E_R)}{1 + g(E_R)} \tag{11.12}$$

where the function $g(E_R)$ can be parameterized for different atoms as

$$g(E_R) \simeq 0.66 \left(\frac{Z^{5/18}}{A^{1/2}} \right) E_R^{1/6}(\text{keV}) \tag{11.13}$$

and alternatively [213]

$$Q(E_R) = \frac{\kappa g(\varepsilon)}{1 + \kappa g(\varepsilon)} \tag{11.14}$$

where $g(\varepsilon) = 3\varepsilon^{0.15} + 0.7\varepsilon^{0.6} + \varepsilon$, $\kappa = 0.133 Z^{1/12}/\sqrt{A}$, and $\varepsilon = 11.5 E_R(\text{keV})/Z^{7/3}$.

However, there are large uncertainties in the behaviour of the *quenching* factor at very low energies, where the experimental measures are extremely difficult. The uncertainty in $Q(E_R)$ is usually the main source of systematic uncertainty in determining the cross-section limits, specially for light WIMPs since the uncertainties at low energies are larger. Figure 11.2 shows the dependence of the *quenching* factor with the energy for some targets as computed with parameterization 11.13. On the right panel, the parameterization used here is compared for a germanium target with the data found in the literature [214] (Lindhard theoretical model and simulations done with TRIM [215] program).

There are two additional experimental factors that determine the expected rates, the exclusion limits and the regions of interest of an indication of positive signal: the energy threshold and energy resolution of the detector.

The energy threshold determines the minimum WIMP velocity to which the detector is sensitive, i.e., the lower is the energy threshold, the larger is the fraction of the WIMP velocity distribution to which the detector is sensitive (see equation 11.4). Again, this is critical for light WIMPs since a detector with a large energy threshold is only sensitive to the extreme tail of the spectral distribution. A reasonable constrain on the (m_χ,$\sigma^0_{\chi n}$) parametric space should be set only for WIMP masses for which at least 1% of the expected spectrum is above threshold. This is further discussed in next chapter, in the context of the TREX-DM project motivation.

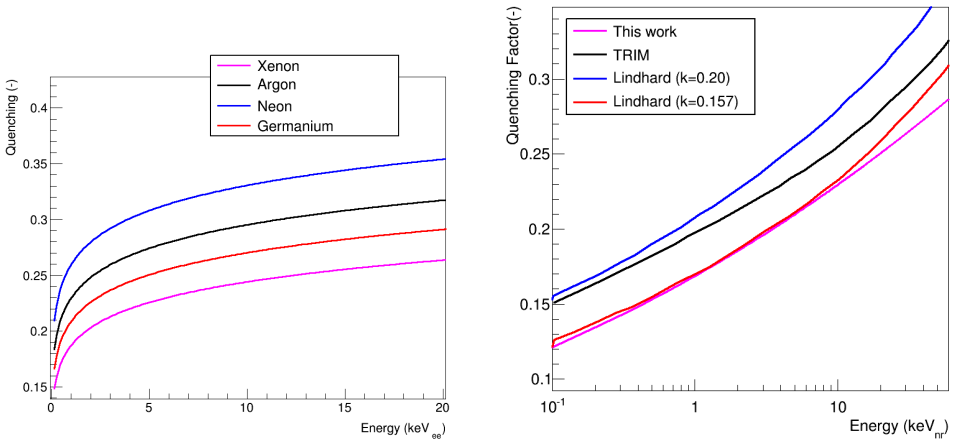

Figure 11.2: Dependence of the parameterization of the quenching factor with the energy for different target materials (left) and comparison between the parameterization used in this work and the values predicted by the Lindhard theory and TRIM code (values extracted from [214]) for a germanium target.

Finally, the energy resolution of the detector is included in the calculation as the convolution of the expected signal with a gaussian distribution whose width is determined by the energy resolution. The energy resolution of the detector at threshold has a non negligible importance because part of the expected WIMP-induced spectrum below effective threshold shifts above threshold. This effect is again especially relevant for light WIMPS for which the quasi-exponential spectrum is very steep. Indeed, this effect artificially makes an experiment sensitive to WIMPs to which would be completely insensitive in case of infinitely good energy resolution. A scientifically reasonable constrain on the (m_χ,$\sigma^0_{\chi n}$) parametric space should avoid setting limits below a mass where the increase of sensitivity due to this effect is not larger than a factor two.

The energy spectra induced by the spin-independent WIMP-nucleon elastic scattering in several target materials are shown in figures 11.3 and 11.4 for several axion masses under the assumptions described above. The spectra show a pseudo-exponential shape with mean value increasing with m_χ. From equation 11.7, the expected rate increases $\propto A^2$, so heavy nuclei are usually preferred; and it decreases $\propto 1/m_\chi$ since the flux of WIMPs does for a fixed ρ_0. This fact determines the typical shape of the exclusion curves: the best limit is achieved at $m_\chi \sim m_N$, increasing at low masses due to the energy threshold effect (for low masses the detector becomes insensitive to most of the signal) and linearly rising at high masses due to the WIMP flux reduction.

The featureless pseudo-exponential decreasing expected WIMP-induced spectrum makes it practically indistinguishable from radioactive backgrounds by observing only the spectral shape. This points to the need of observing distinctive signatures of the WIMP signals, which are discussed below.

11.4.2 Signatures

If a clear positive detection is aimed for, then more WIMP specific *smoking gun* signatures are needed. We have already mentioned that WIMPs interact differently (in rate as well as in spectral shape) with different target nuclei (see figures 11.3 and 11.4). This *A-dependence* signature is one of the goals of the large long-term dark matter projects. Besides, it provides complementary information to infer more accurately the WIMP properties, such as its mass. This technique however must face the important question of how to assure the background conditions of all targets are the same.

A second signature is the annual modulation of the WIMP signal, reflecting the periodical

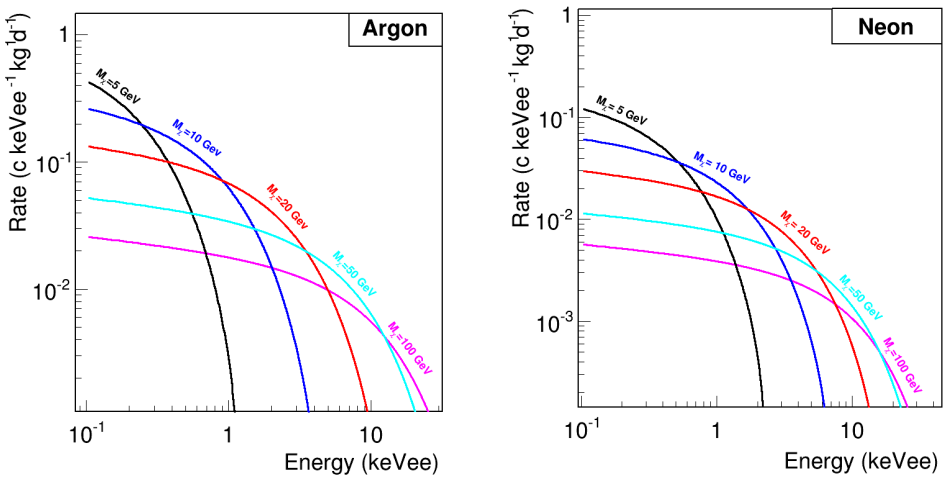

Figure 11.3: Expected WIMP-induced energy spectra in argon (left) and neon (right) detectors for different WIMP masses. The standard halo model is assumed with the parameters described in the text. Spin-independent WIMP-nucleon elastic scattering with coupling to neutrons equal to coupling to protons ($f_n = f_p$) is considered, with $\sigma^0_{\chi n} = 10^{-40}$ cm^2. The quenching factor used is shown in figure 11.2.

change of relative WIMP velocity due to the motion of the Earth around the Sun. The variation is only of a few % over the total WIMP signal, so even more sensitive detectors are needed. This signal may identify a WIMP in the data, provided a very good control of systematic effects is available, as backgrounds may also be subject to annual modulation. Due to the Earth's motion around the Sun, the rate of dark matter recoil events is predicted to vary throughout the year. The Sun moves around the galaxy at $v_\odot = 232 \pm 20$ km s^{-1}, and the Earth moves around the Sun at $v_\oplus = 30$ km s^{-1} in an orbit whose axis is tilted an angle $\theta = 30.7^0$ respect to the Sun's motion direction. Therefore, the Earth-halo relative velocity v_r oscillates as follows

$$v_r(t) = v_\odot + v_\oplus \sin\theta \cos(\omega(t - t_0)) \tag{11.15}$$

The time in which $t = t_0$, corresponds to June 2nd and v_r is a maximum, ~ 245 km s^{-1}, while in December reaches its minimum, ~ 215 km s^{-1}. In the same way oscillates the maximum energy that a WIMP of fixed mass releases in a detector.

The magnitude of modulation in the WIMP signal can be expressed as a cosenoidal variation added to a constant term plus the background

$$S(t) = B + S_0 + S_m \cos(\omega(t - t_0)) \tag{11.16}$$

where S_0 is the WIMP rate dR/dE calculated in equation 11.2 and all the prescriptions and parameters given in the previous section. S_m is the magnitude of the annual modulation, which is shown in figure 11.5 for a germanium target. Note that the amplitude of S_m varies with energy and below a given energy it becomes negative. The larger the WIMP mass, the higher is the recoil energy at which S_m changes its sign. This modulation is what DAMA/LIBRA collaboration claims to have observed over 1.17 t·y accumulated exposure. However, the lack of nuclear recoil identification of this experiment along with other methodological issues makes this claim controversial.

Finally, the directional detection of the nuclear recoil would allow to observe a daily asymmetry due to the rotation of the Earth. This technique requires the use of low-pressure gaseous detectors or anisotropic scintillators. However, the techniques are not yet sufficiently developed.

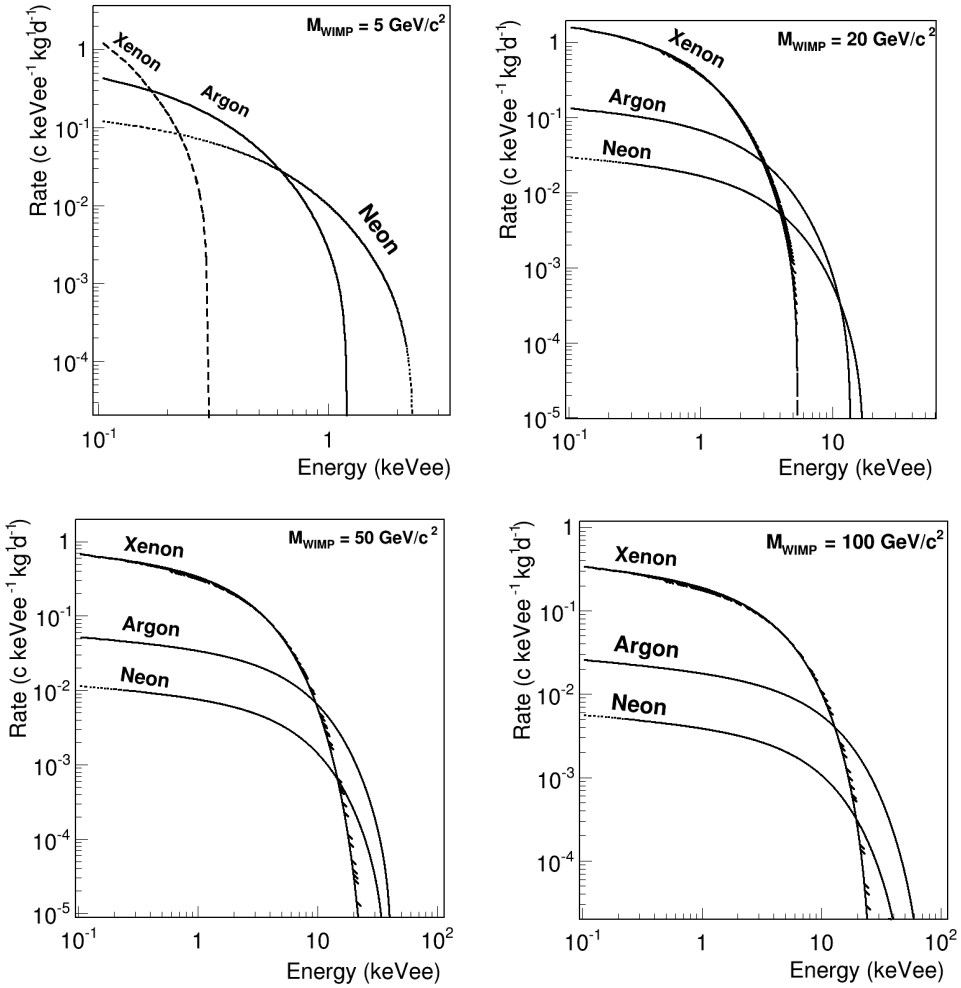

Figure 11.4: Expected WIMP-induced energy spectra in different targets for m_χ= 5, 20, 50 and 100 GeV. The same assumptions than those of figure 11.3 are applied.

11.4.3 Requirements for a WIMP direct detection experiment

As we have seen, a WIMP with a mass ranging from few to hundreds GeV produces a nuclear recoil with typical energies below 100 keV. The distribution of energy recoils shifts towards lower energies for lighter WIMPs and for heavy detector material nuclei. The expected event rates are typically below one count per kg detector material per day (see figure 11.3), much lower than radioactive and cosmic backgrounds. In brief, the small WIMP signal falls in a very low-energy region, where the background usually accumulates. Consequently, the generic characteristics that a direct detection experiment should have are:

1. a very low **energy threshold** in order to be sensitive to most of the signal,
2. a large **target mass** to gain sufficient statistics in a reasonable life-time of the experiment,
3. and a **background** level as low as possible.

Most of the background is produced by the interaction of electrons in the target material, either induced by photons or direct beta radiation. Contrarily, WIMPs and neutrons scatter elastically off a nucleus. A direct detection experiment must be located underground, using all the precautions of rare event searches: external γ and neutron shielding, anti-radon systems, muon vetoes, and

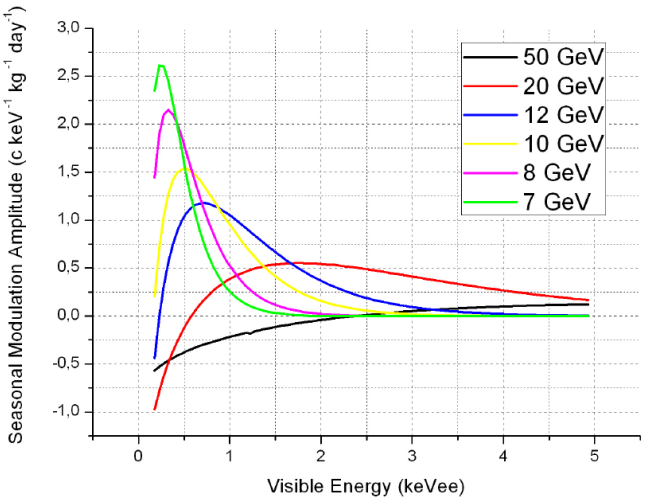

Figure 11.5: Spectral dependency of the S_m coefficient for different values of the WIMP mass in a germanium detector. The WIMP-nucleon cross section has been taken 10^{-40} cm^2 and the remaining galactic parameters are the ones explained in the text.

a careful screening and selection of the detector materials. On the other hand, it is critical to maximize the amount of information recorded by the detector to perform and active discrimination of neutron and e/γ-induced events. The energy released to the recoiling nucleus is transformed to a measurable signal in the form of ionization, scintillation light and phonons. The simultaneous observation of two of these measurable signals provides an important tool for the discrimination of electron or gamma induced backgrounds and nuclear recoils. This discrimination is based on the fact that nuclear recoil events produce less ionization/scintillation signal with respect to e/γ-induced events. The reduction in the signal for nuclear recoils is denominated *quenching*, and the energy calculated from γ sources in calibrations is called *electron equivalent energy* (expressed as keVee). In scintillator detectors, e/γ-induced events can also be distinguished from nuclear recoils because they produced different pulse features.

Furthermore, the access to the event position and topology allows to reject event with long electron tracks and select a fiducial volume, removing surface events, which are unlikely to be provoked by WIMPs. The access to the event timing allows to reject events with multiple scatters within the active detector volume. For the time being, the topological discrimination of low-energy x-rays and nuclear recoils is only viable in low-pressure gaseous detectors, which may be sensitive to the WIMP directionality.

11.4.4 Experimental status and prospects

The three main categories of WIMP detection techniques are based on solid-state semiconductor cryogenic detectors, noble liquid detectors and scintillating crystals. In this section, the status and prospects of the different technologies are reviewed. Other more unconventional techniques are also discussed because they can be competitive for some particular couplings or WIMP properties, and complement the knowledge about characteristics of the dark matter halo. Figures 11.6 and 11.7 show the current status of the direct detection searches in the parameter space of the WIMP-nucleon elastic scattering cross-section versus mass for spin-independent (SI) and spin-dependent (SD) couplings, respectively. Figure 11.8 shows the prospects of planned experiments for the SI interaction in the same parameter space.

Semiconductor cryogenic detectors. These detectors are operated at sub-Kelvin temperatures allowing to measure simultaneously the ionization yield and the phonons produce by a small energy depositions. Semiconductor (not cryogenic) detectors lead the field for many

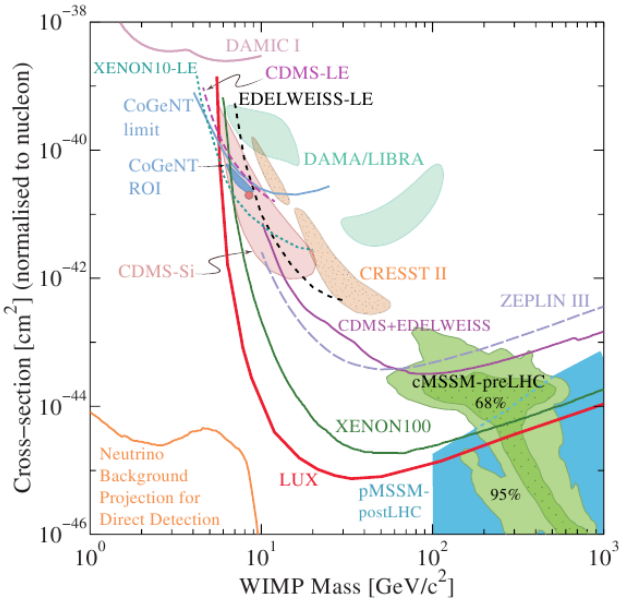

Figure 11.6: Limits (solid lines) on the WIMP-nucleon cross section for spin-independent coupling as a function of the mass. The enclosed regions represent hints for WIMP signals and the shadowed regions represent predictions from supersymmetric models. Extracted from [209].

years (Heidelberg-Moscow, IGEX, COSME-II) because of their excellent energy resolution (<10% FWHM at 10 keV) and relatively low energy threshold (<10 keV in recoil energy). Currently, the best implementations of this technique are the CDMS, CRESST and EDELWEISS experiments, operating respectively at Soudan Laboratory, at the Laboratori Nazionali di Gran Sasso (LNGS) and Laboratoire Souterraine de Modane (LSM).

In 2011 CDMS published results with an exposure of around 612 kd·d of Germanium detectors (around 300 kg·d fiducial), excluding SI WIMP-nucleon cross-sections above 3.8×10^{-44} cm^2 for a 70 GeV WIMP [216]. The combined analysis of EDELWEISS and CDMS has reached a sensitivity down to 3.3×10^{-44} cm^2 for a 90 GeV WIMP [217]. Both experiments have presented low energy analysis of their data, significantly improving their sensitivity for low-mass WIMPs. These analysis exclude part of the region of interest from possible signal events. Besides, CDMS has run a single Ge detector in a particular mode that allowed to achieve energy thresholds as low as 170 eVee, but without the ability to distinguish electronic and nuclear recoils. This experiment sets a very competitive limit for WIMP masses below 12 GeV, excluding also part of the hint regions. Finally, the re-analysis of the data obtained with the Silicon detectors of CMDS in a run of 140 kg·d exposure, shows an excess (3 events versus 0.7 expected). The best fit to the data produce a WIMP candidate with mass of 8 GeV and cross-section of 10^{-43} cm^2. However, this potential signal could most probably be attributed to an instrumental artifact since all the events are very close to the ionization energy threshold.

CRESST uses Ge detectors in combination with $CaWO_4$, whose scintillation light is used for background discrimination. In a run with 730 kg·d exposure they find an excess counting rate (67 events) respect to the expected background (40 events). Although the reliability of the signal is background model dependent, the excess can be explained by a dark matter signal implying WIMPs with 12 and 25 GeV masses and cross-sections of 3.7×10^{-41} cm^2 and 1.6×10^{-42} cm^2, respectively [218].

The recent development of low capacitance Germanium detectors has allowed CoGeNT, TEXONO (CDEX) and MALBEK collaborations to reach sub-keV energy thresholds, but without tools for electron/nuclear recoil discrimination. The CoGeNT collaboration [219] operated a 440 g Germanium detector with an energy threshold of 400 eVee, and claimed to find an irreducible excess

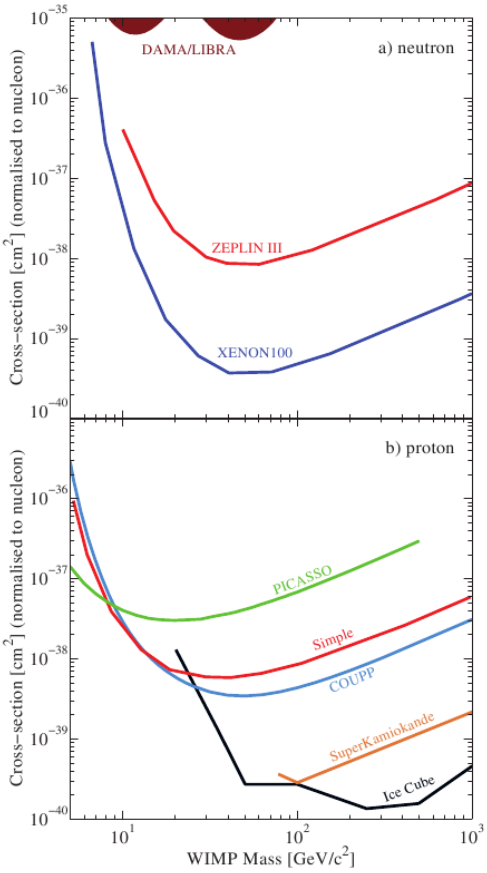

Figure 11.7: Limits on the WIMP-nucleon cross section for spin-dependent coupling as a function of the mass, for the interaction with the neutron (top) and proton (bottom). Extracted from [209].

of events below 4 keV, compatible with a WIMP of mass around 10 GeV and SI cross-section of around 3×10^{-41} cm^2. This result is derived by evaluating the pulses shape, particularly the risetime, whose distribution at energies around the keV overlaps for surface and bulk events. This fact makes the explanation by the WIMP hypothesis quite controversial. In the same way, the annual modulation observed by CoGeNT in one year of accumulated statistics is too large to be attributed to a WIMP, and the similarly sensitive CDMS experiment finds no modulation.

The next semiconductor cryogenic detectors will be: a) SuperCDMS [220], an evolution of CDMS with improved background and larger mass, plans to install 200 kg of germanium at SNOLAB with a projected sensitivity below 10^{-46} cm^2 for a WIMP mass of 60 GeV in a couple of years of science data, and very impressive limits in the low mass region; a medium-size detector of 9 kg is already operating at Soudan. b) EURECA [221], a joint effort between CRESST, EDELWEISS and ROSEBUD, aiming to operate a 150 kg detector. c) CDEX/TEXONO [222] project aims to operate germanium detectors with energy threshold as low as 100 eV in the Jinping laboratory.

Noble liquid detectors. Time projection chambers filled with noble gases such as argon or xenon are being intensively developed and are currently setting the most stringent limits to the WIMP-nucleon cross-sections for both SD and SI couplings. Dual phase (liquid an gas) detectors are excellent target materials since the liquid phase provides large mass, self-shielding and allow to measure both the primary scintillation and ionization caused by the radiation passing through it. The primary electrons are drifted towards the gaseous phase where they are amplified. The double detection of light and charge leads to a large discrimination power. Moreover, the measurement of

the drift time and pixelized readouts allows to determine the position and shape of the event with sub-mm resolution.

XENON100 (operated at LNGS) published results based on a run with 7650 kg·d fiducial exposure reaching a limit for the SI coupling of 2.0×10^{-45} cm^2 at a WIMP mass of 55 GeV [223], and the best limit in all the mass range for the SD WIMP-neutron interactions. However, the reliability of the SI limit below 12 GeV has been controversial because of the uncertainties in the relative light efficiency factor and the poor resolution at threshold. A low energy analysis of XENON10 dataset using only the ionization signal sets stringent limits below 12 GeV.

The ZEPLIN-III experiment [224] (operated at Boulby laboratory) published final results with an exposure of 1344 kg·d, setting limits comparable to those of CDMS and EDELWEISS for SI couplings, and the second best limit in the SD interaction with the neutron, although more than one order of magnitude above XENON100 limit.

The LUX experiment (operated at SURF laboratory) set the most stringent limit on the SI WIMP-nucleon elastic scattering cross-section so far, based on a dataset with an exposure of around 10000 kg·d. The minimum upper limit is 7.6×10^{-46} cm^2 at a WIMP mass of 33 GeV [225], and it is found to be between 100 and 1000 times lower than the low-mass candidate regions from other direct detection searches.

The future of noble liquid detectors typically involves ton mass scale detectors, being either upgrades of current experiments or newly designed projects. Regarding experiment with xenon as target material, XENON1t (3 t total mass, 1 t fiducial) is under construction at LNGS aiming to reach a sensitivity of a few 10^{-47} cm^2 in the SI coupling for a WIMP mass of some tens of GeV. The PandaX experiment (located at Jinping laboratory) is a double-phase xenon experiment designed to operate in two stages. The first phase, exploring the light WIMP region ($<$10 GeV) with low energy threshold, is already underway and taking science data. In the second phase, the detector will evolve to the ton-scale without changing the vessel of the TPC, with expected sensitivity down to 10^{-47} cm^2. XMASS collaboration plans to run a 5 t (1 t fiducial) single-phase xenon detector. The next phase of LUX will joint efforts with ZEPLIN in the so-called LZ experiment, aiming to operate a 7 t double-phase xenon detector. Regarding argon experiments, ArDM experiment is a double-phase $\sim$1 t experiment that will start physics data taking soon at the LSC. DarkSide is another double-phase argon experiment (using ^{39}Ar depleted argon from underground sources) project that will evolve from a run with 50 kg to the ton scale. Finally, MiniCLEAN (400 kg) and DEAP-3600 (3600 kg) are scintillation only LAr based experiments with spherical geometry.

Scintillating crystals. The DAMA/LIBRA experiment (operated at LGNS) has observed with an accumulated exposure of 1.17 t·y an annual modulation in the single-scatter rate in the NaI crystals between 2 and 6 keVee with the expected period and phase and statistical significance at the 8.9σ level [226]. This result has been interpreted as a positive signal induced by WIMPs of masses around 50 GeV and at low mass, around 8 GeV. These interpretations are however quite controversial and have been largely discussed by the community. Besides, the WIMP-induced interpretation of the signal is in strong disagreement with null results from other experiments. In particular, the KIMS experiment (which uses CsI crystasl and it is operated at CUNP laboratory) derives limits based on 24 t·d exposure that excludes the high-mass region and most of the low-mass DAMA/LIBRA regions of interest [227]. It is noteworthy that the results of both DAMA/LIBRA and KIMS are based on the WIMP interaction with the same nucleus (iodine).

There are active developments with the aim of further checking the DAMA/LIBRA interpretation with NaI crystals. The ANAIS project [228], currently working on the purity of the NaI crystals, aims to operate a 100 kg detector at the LSC. The DM-ice [229] is a 250 kg NaI-based detector to be installed within the frame defined by the IceCube arrays in the Antarctic icecap. On the other hand, DAMA/LIBRA will continue measuring with upgraded (lower energy threshold) photomultipliers.

In **superheated liquid detectors** an energy deposition leads to the formation of bubbles in the metastable liquid. By adjusting the pressure and temperature they can set the threshold for the phase transition in such a way that only nuclear recoils produce the formation of bubbles. These type of experiments are competitive in the WIMP SD coupling with protons, particularly with the

^{19}F isotope, whose unpaired proton carries most of the spin of the nucleus. SIMPLE (0.2 kg) [230], PICASSO (2.7 kg) [231], and COUPP (4.0 kg) [232] are the experiments developing this technique, the last of which achieved a lowest upper limit on the pronton SD cross-section of 3.0×10^{-9} cm^2 at a WIMP mass of 30 GeV [233]. If the WIMP detection is confirmed, the development of this technology could allow to determine the spin of the particle. In the future, PICASSO and COUPP are planning to combine into the PICO project.

The **directional detectors** aim to determine the direction and sense of the nuclear recoil in a low-pressure gaseous TPC. Since nuclear and electron recoils of the same energy have very different ranges, these detectors potentially have strong background suppression capabilities. Although more unconventional, directional detectors are very relevant because the directional sensitivity allows to prove unequivocally the galactic origin of the signal, complementing the *classic* experiments. Besides, if the evidence of a WIMP signal is established, these type of detectors (along with indirect searches) will be useful to determine some WIMP properties such as the local velocity profile of the dark matter halo. This technology is under development by some collaborations, such as DRIFT [234], MIMAC [235], DMTPC [236] or NewAge [237].

Other unconventional detectors have been lately developed aiming to explore the low-mas WIMP region, such as DAMIC [238], using CCDs; and NEWS [239], using a spherical proportional gaseous counter.

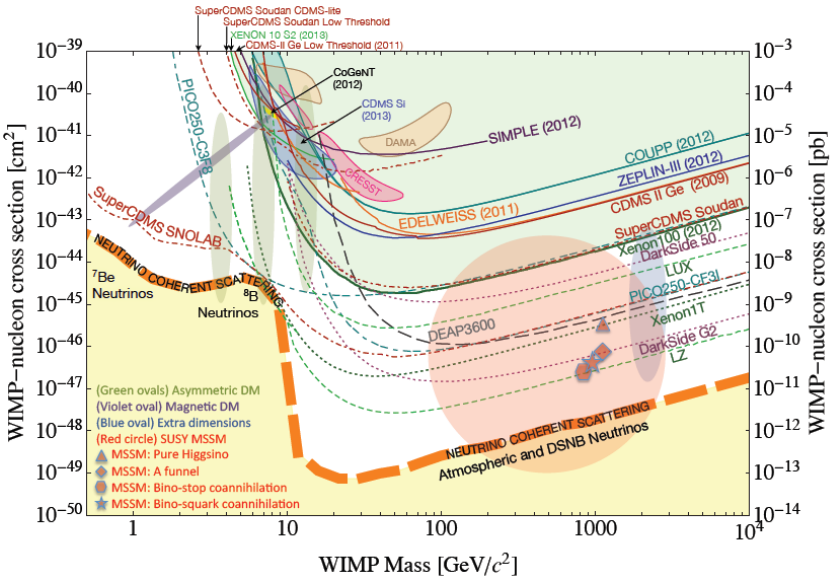

Figure 11.8: Limits on the WIMP-nucleon spin-independent cross section (solid curves), hints for WIMP signals (shaded closed contours) and projections (dot and dot-dashed curves) of direct detection experiments as in 2014. Also shown is a band where coherent scattering of neutrinos with nuclei will begin to limit the sensitivity of direct detection experiments to WIMPs. Finally, the shaded regions indicate a compilation of theoretical model predictions for the neutralino. Extracted from [240].

11.5 Indirect WIMP searches

Indirect WIMP searches complement direct searches since they can be sensitive to higher masses and different interaction models. WIMPs can annhilate in many channels producing a variety of detectable particles. For a full review on the indirect detection experiments and constrains, the reader is referred to [210]. Here, we will just mention the main detection channels and some intriguing observations.

WIMP annihilation in the Milky Way halo can produce charged cosmic rays, such as positrons, antiprotons and antinuclei. Positrons are the most interesting charged cosmic ray since measurements in the positron fraction $\phi(e^+)/(\phi(e^+)+\phi^-)$ by PAMELA [241] and AMS02 [242] show an unexpected rise above 10 GeV. Measurements of the total flux $\phi(e^+)+\phi^-$ above 300 GeV by ATIC [243], FERMI/LAT [244] and H.E.S.S [245] also exceed the spectrum predicted from secondary production by cosmic rays. These observations can be explained in terms of WIMP dark matter annihilation but it requires cross-sections that exceed the relic abundance. However, new standard astrophysical sources of electrons and positrons, like pulsars or supernova remnants, have been suggested as the responsibles of these excesses. Regarding the production of antiprotons, the best measurement is provided by PAMELA, whose results are in agreement with secondary production of antiprotons from cosmic rays.

WIMP annihilation in the galactic halo can also contribute to the gamma spectrum by continuous and monoenergetic photon distributions. H.E.S.S discovered a strong source of TeV photons near the central region of our galaxy, where the density of WIMPs is expected to be larger. Furthermore, FERMI/LAT found a extended source of GeV photons near the galactic center, around the galactic plane. These observations probably have astrophysical origin, contributing to the background for the search of WIMP annihilation in these channels. However, a characteristic feature in the spectrum measured by FERMI/LAT when all the known gamma sources were removed pointed to monenergetic photons of around 130 GeV, although the significance of the signal is not large enough and astrophysical sources or instrumental errors are not discarded. All other gamma ray observations by FERMI/LAT and Cherenkov telescope arrays agree with the predictions from standard astrophysical sources.

Finally, WIMP-induced neutrinos are also looked in the galactic halo. However, only the search for neutrinos from the annihilation of WIMPs trapped in the Sun (where they would be trapped, increasing its density and thus the annihilation probability) is competitive with direct searches in the spin-dependent coupling. Neutrinos are looked in experiments such as BAKSAN, SuperKamiokande, AMANDA, ANTARES or IceCube, setting stringent upper bounds in the interaction cross-section of WIMPs with protons, as figure 11.7 shows.

11.6 Accelerator WIMP searches

WIMP particles can be produced in the laboratory by high-energy proton-proton collisions. Their existence can be inferred either from the missing energy of the event or from the production of SM particles with large momentum imbalance in the transversal plane of the detector.

The most stringent limits are derived from the monojet channel since most of the collisions produce jets with multiple particles and the background of these channels is larger. The limits on the production of this channels is translated via an effective theory into WIMP-nucleon scattering cross-section. Even though the limits are model-dependent and a direct translation is somewhat difficult, accelerator searches are very competitive with direct and indirect searches in both SI and SD coupling, specially for light dark matter.

For the time being, the LHC has not found new physics beyond the SM and the absence of supersymmetric signals is constraining many models, although WIMPs are still viable in many supersymmetric models. Furthermore, the lack of positive signals in direct and indirect searches is driving some attention in other DM candidates, such as axions or axion-like particles.

Chapter 12

The TREX-DM detector

Contents

12.1 Introduction

In this chapter, the motivation and physics case for a low mass WIMP gaseous detector is discussed. The conceptual and technical design of the TREX-DM detector, a low background, low threshold TPC, is presented, entering into some detail in the different subsystems of the setup. The commissioning of the apparatus is described as the first stage for the detector characterization program at sea level (discussed in next chapter), which will be eventually followed by a physics run at an underground site. The main challenges of this project are reviewed along with the projected sensitivity of the experiment.

12.2 Low-mass WIMPs: motivation and physics case

As discussed in the previous chapter, the detection of Dark Matter (DM) is one of the open challenges of Astroparticle and Particle Physics for the next years. Evidence for DM (see section 11.2) is well founded in different observations like the anisotropies in the cosmic microwave background, the distribution of matter in our galaxy or its gravitational effect on visible matter. The nature of DM is still unknown, but its solution may involve new particles with masses and cross-sections characteristic of the electroweak scale. A generic type of DM are the so-called WIMPs, which appear in well-motivated extensions of the SM, in particular those including SuperSymmetry.

The extremely low rate and low energy of the nuclear recoils induced by WIMPs in underground terrestrial experiments poses formidable challenges in terms of background rate, threshold and target mass. During the last 30 years an ever growing experimental activity has been devoted to the development of detection techniques that have achieved increasingly larger target masses

and lower levels of background, in the quest of reaching higher sensitivity to DM WIMPs. At the moment, the leading experiments in the "WIMP race" are those using relatively heavy target nuclei (e.g. Xe or Ge) –to exploit the A^2-coherence (see equation 11.7) in the WIMP-nucleus interaction– and using detection techniques that provide nuclear recoil discrimination. This is the case, e.g. of liquid Xe double-phase detectors (e.g. LUX [264] or XENON [247]) or hybrid Ge bolometers (like CDMS [248]). These experiments are currently operating, or aiming at, target masses already at the few $\times$100 kg range, with background levels of a few counts per kilogram and year in their energy RoI. More specifically, and just as illustrative examples, LUX has already operated $\sim$118 kg of fiducial Xe mass with $\sim$3.1 mDRU$_{ee}$ (1 DRU = 1 event/kg/year/keV) [264]. Such impressive numbers are obtained thanks to the availability of discrimination techniques that allow distinguishing –with some efficiency– electron recoils (produced e.g. by gammas) from the signal-like nuclear recoils. This happens because the different ionization density of nuclear and electron types of events leads to a different yields-ratio in the detection medium (ionization/scintillation in the case of noble liquids, and ionization/phonon in case of hybrid Ge bolometers). Of course, this discrimination capability is energy-dependent and for low enough energies (typically few keV) it disappears, setting the effective threshold of the experiment.

Conventionally –and somewhat simplistically–, WIMP searches are expressed in the two-dimensional effective parameter space (σ_N, M_W), where σ_N is the WIMP-nucleon cross section and M_W is the WIMP mass. This representation usually comes with a number of additional over-simplifying assumptions, e.g., that the velocity distribution of WIMPs in the galactic halo follows a Maxwellian distribution, or that WIMPs interact exclusively (or mainly) with nuclei via elastic coherent spin-independent scattering. Although this conventional scenario is appealing to set a common ground for inter-comparison of experimental sensitivities, one has to keep in mind the implied assumptions, for many of which there is no real justification.

The large majority of the experimental effort so far has focused on the search for WIMPs of relatively large masses (of around 50 GeV and larger). This is due, in part, to theoretical considerations set in the early days of WIMP searches, that identified the WIMP with the neutralino of (simple) SUSY extensions of the Standard Model, and interpreted the early accelerator limits under the light of these models. The establishment of this "WIMP orthodoxy" was facilitated by the fact the the best WIMP detection techniques available were already well suited for this mass range. Indeed, mainstream experiments show the best sensitivity for $M_W \sim 50$ GeV, due in part to the kinematical matching between the WIMP and the nuclear mass. For higher masses the sensitivity to σ_N slowly decreases, while for lower masses it gets sharply reduced due to the effect of the energy threshold.

Despite the enormous progress in WIMP experiments during the last 10-15 years, that has witnessed an improvement in sensitivity to σ_N of more than 4 orders of magnitude, no convincing WIMP positive signal has been seen so far. This fact has triggered the revision of the mentioned assumptions and the study of more generic phenomenological WIMP frameworks (other WIMPs interactions, different WIMP velocity distributions, etc.). Besides, the non-observation of signals of SUSY in the last Run of the Large Hadron Collider (LHC) calls also for adopting more open-minded views of the possible theoretical frameworks behind the WIMP paradigm. With this attitude, recent theoretical and phenomenological efforts have focused on the study of less conventional SUSY models, or even non-SUSY WIMP models.

As part of this attitude of going beyond the WIMP orthodoxy, some recent experimental and phenomenological efforts have been focused on the study of WIMPs in the low mass range (i.e. $M_W < 10 - 20$GeV). The interest on this region of the parameter space, traditionally out of reach of mainstream experiments, was increased by the appearance of a number of hints that could be interpreted as due to low mass WIMPs (although those interpretations seem to have weakened over time). In addition, the well-known and persistent DAMA claim [226], despite having been excluded by many other experiments, might be reconciled only within very non-standard model assumptions, some of them invoking low mass WIMPs. Independently of the weight one gives to those hints, or to the theoretical motivation of low-mass WIMPs, it is clear that in the present situation of WIMP searches, as much as it is important to extent the current generic (σ_N, M_W) sensitivity frontline to lower σ_N values, so is it to extent it is to lower M_W values too.

On more experimental grounds, sensitivity to low mass WIMPs poses particular challenges. As mentioned above, mainstream experiments are severely limited at low masses due to the threshold effect of the nuclear recoil discrimination capabilities. Despite the impression that sensitivity lines may progress towards low masses as long as larger target masses are gathered this needs to be taken with a lot of caution. Low mass WIMPs leave energy deposits typically below the energy threshold of experiments based on heavy target nuclei like Xe or Ge. This means that the exclusion limits derived for low mass WIMPs by these experiments rely on a very small (1% or lower) fraction of the WIMP interactions in the detector, those corresponding to the high velocity tail of the distribution (with kinetic energies enough to produce a nuclear recoil visible in the detector). But precisely this part of the distribution is the most uncertain, and in some plausible galactic halo models it can altogether disappear (i.e. those with lower maximum WIMP velocity).

This fact is illustrated in figure 12.1 for a WIMP of mass 10 GeV assuming the standard halo model and the conventional parameters reviewed in the previous chapter. In a relatively light target nuclei such as argon or neon with very low detection threshold (0.4 keV electron scattering equivalent energy, keVee), most of the signal is above threshold, contrarily to a *classic* experimental approach (such as XENON-100), which is only sensitive to a very small fraction of the WIMP-induced nuclear recoils.

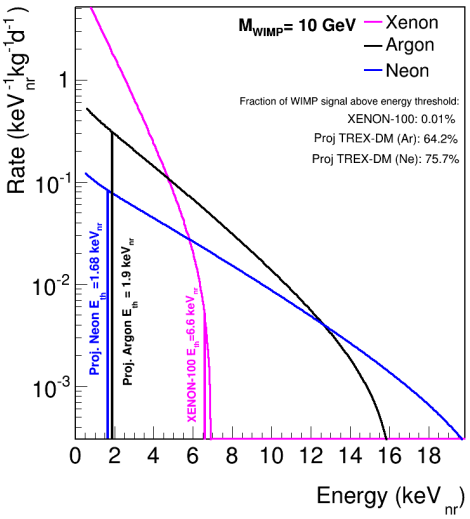

Figure 12.1: Event rate induced by 10 GeV WIMPs and arbitrary spin-independent WIMP-nucleon cross-section in xenon (pink), argon (black) and neon (blue). Standard halo model and parameters are used. The projected energy threshold of TREX-DM is shown as a vertical line in the argon and neon spectra. The XENON-100 energy threshold is shown for comparison. The fraction of the signal above threshold is also shown.

It is clear that to seriously tackle the low mass WIMP region, specific experiments optimized for this mass range are needed. A robust detection or exclusion must imply that a substantial fraction (order 50%) of the WIMP spectrum is over the experimental threshold. To achieve this the use of light target nuclei is preferred (to kinematically reach higher recoil energies), as well as techniques with intrinsically low energy detection threshold. These requirements are incompatible with the discrimination between nuclear and electron recoils, whose observable features become blurred at low energies. Some experimental efforts (still at modest scales) are already being carried out in this direction. Some conventional experiments, like e.g. CDMS [248] or XENON [247], have released "low energy" version of their analysis, bypassing their nuclear/electron discrimination and going to lower thresholds [249]. More relevantly, first experiments specifically focused on the new low-mass WIMP paradigm in the way exposed above are already appearing, like DAMIC [238], CDEX [265], or CDMSlite [263] among others. As the background levels in these experiments

must rely on more conventional handles like e.g. ultra-high levels of radiopurity of the detector components, the scale of these experiments remain so far at a relatively modest scale (still below the kg level of target mass).

12.2.1 High pressure TPCs to search for low-mass WIMPs

In the context described above, the TREX-DM experiment proposes another strategy based on the use of ionization gas TPCs at high pressure with novel Micromegas readouts to search for low mass WIMPs. Being gaseous detectors, gas TPCs scaling-up prospects are typically considered modest. However, advances in electronics and micro-pattern charge-amplification structures are changing this view. It is our claim that the charge amplification inherent to gaseous detectors (yielding correspondingly low energy threshold) and the flexibility in the choice of target gas (light nuclei are preferred, like argon, neon, helium) and pressure, together with the advances in radiopurity, scaling-up and general simplification and robustness of these detectors, make them very promising options for low-mass WIMP detection.

In such a detector, neutron/electron discrimination could be less effective, so radiopurity becomes even more important than in mainstream experiments. Furthermore, TREX-DM does not compete with those experiments in the target mass, although eventually one would like to extend the target mass from few hundreds of grams to few kilograms. The strength of this experimental approach is thus focused on the energy threshold, provided a low enough background level in the low energy range is obtained.

The TREX-DM prototype is part of the wider scope ERC-funded project called TREX (presented in section 1.7), that since 2009 is devoted to R&D on low background TPCs and their potential applications in axion, double beta decay and dark matter experiments. Work on the TREX-DM prototype started in 2012 with the first designs and it is now in the commissioning and detector characterization phase at the TREX laboratory at Zaragoza. Most of the components and sub-systems have been validated, as it shown in detail in the next section. The first signals were observed at the fall of 2014.

TREX-DM will profit from all developments made in Micromegas technology [44, 56, 57], as well as in the selection of radiopure materials [185, 251], specially in CAST [186] and NEXT-MM [252] projects. Its main goal is the operation of an active detection mass ∼0.300 kg (i.e., 100 times larger than CAST-MM TPCs) with an energy threshold of 0.4 keVee (as already observed in [186]) or lower, being fully built with previously selected radiopure materials.

Bulk Micromegas have barely been operated at high pressures and very limited literature exists about the subject. The first experimental step is thus the study of the detector performance in terms of electron transmission, absolute gain and energy resolution, as well as an analysis of low-energy x-ray charge cluster features at increasing pressures and with different argon and neon-based admixtures. These studies will constitute an important scientific result *per se*.

The construction of large radiopure bulk Micromegas detectors is in study. Alternatively, the detector could be segmented in smaller squared modules (current microbulk limitation is at ∼20×20 cm^2) made in a flexible PCB that would incorporate the flat cables feedthroughs, eliminating thus the need for multi-pin connectors. We have already explored the last alternative in a different context ($\beta\beta0\nu$ experiment).

The next, and most important, challenge is the demonstration of achievement of sub-keV energy threshold for large area detectors at high pressure, a crucial requirement whose satisfaction is a necessary prerequisite for any future development. This issue will require the use of low energy calibrations, such as the one used in NEWS based on a ^{37}Ar source [253]. The study of the energy threshold as a function of the gas pressure and the background expectation at a significant signal acceptance are the next critical points for the realization of the experiment. Finally, the measurement of the quenching factor requires, ideally, the calibration of the detector at a neutron spallation source since very limited literature about quenching factor exists at sub-keV energies, specially for gaseous detectors. The final goal is to perform a physics run at the LSC with the appropriate shielding.

Low-pressure gas TPCs could provide access to the imaging of the nuclear recoils, and therefore

to the WIMP incoming direction. However, this feature quickly degrade for long drift distances, which may limit the scalability of this type of experiments. WIMP directionality is considered the ultimate signature to identify unambiguously the extraterrestrial origin of the putative signal. The experimental challenge is large, due to the tiny size of nuclear recoils, and it requires working at very low pressures and with very high granularity readouts. Apart form the pioneer DRIFT experiment [234], a number of more recent initiatives are ongoing to demonstrate directional sensitivity with a number of different prototype of TPCs, like MIMAC [235], NEWAGE [237], DMTPC [236] and others. Although we acknowledge the importance of this goal as a motivation to develop gas TPCs for WIMP searches, TREX-DM is focused in the non-directional detection of WIMPs. This allows, among other things, to operate at higher pressure to increase sensitivity.

Other gas TPCs are also being considered as WIMP detectors. For example, NEWS [253] is a Spherical Proportional Counter filled with a neon-helium mixture at high pressure that has reported an energy threshold as low as 0.1 keVee.

12.2.2 Projected sensitivity

A first background model of the experiment in argon and neon-based mixtures an underground environment was developed by F. J. Iguaz in order to study the sensitivity of TREX-DM [254]. Two target materials at 10 bar were considered, Ar+2%iC$_4$H$_{10}$ and Ne+2%iC$_4$H$_{10}$; with an active mass of 0.3 and 0.16 kg respectively. Although these gases are good candidates for light WIMP detection, one of argon's isotope (^{39}Ar, produced by cosmogenic activation), is radioactive (β-decay, Q = 565 keV) with a long half-life (239 yr), and may limit the sensitivity of any argon-based experiment. However, low radioactivity argon from underground sources could help to overcome this limitation [255]. The radioactive chains of all the detector components were simulated considering their measured activities [185] as well as the muon flux at the Canfranc Underground Laboratory (LSC), at a depth of 2450 m.w.e. The activity of the Micromegas and Samtec connectors has been replaced by the one of their radiopure alternative. The external gamma flux has not been considered as its contribution may be fully suppressed by an adequate external shielding.

The simulation is based on the Decay0 and Geant4 simulation packages, for the particle decay, detector generation (see figure 12.2 left), and passage of radiation through matter; and on RestSoft, for the generation of electrons in the gas, the diffusion effects during the drift to readout plane, the charge amplification in the Micromegas gap and the signal generation both at mesh and strips, emulating the AFTER-based electronics.

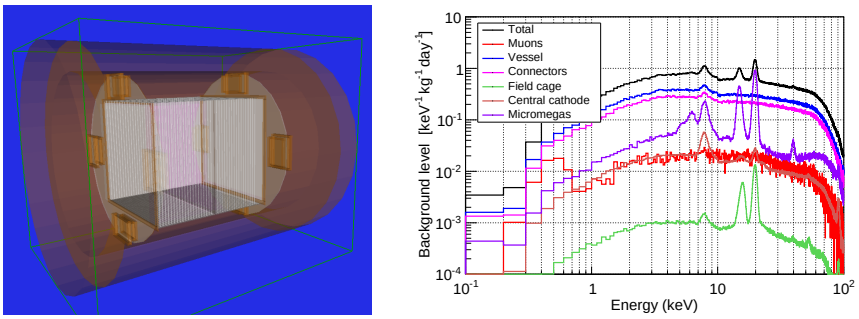

Figure 12.2: Left: a view of the TREX-DM geometry implemented in Geant4. The cylindrical copper vessel (orange volumes) contains a circular base with four shielded boxes (dark grey surface with four yellow boxes), the two active volumes (in light grey), the field cage and field shaper (white walls) and a central cathode. Right: background spectrum expected in TREX-DM experiment (black line) if operated in Ar+2%iC$_4$H$_{10}$ at 10 bar in absence of any ^{39}Ar isotope and installed in the LSC. The contribution of the different components is also plotted: external muon flux (red line), vessel contamination (blue line), connectors (magenta line), field cage (green line), central cathode (brown line) and Micromegas detector (purple line).

The resulting data is in the same format than DAQ data, so both real and simulated data are analyzed with the same routines. A modified version of the analysis done for the Micromegas detectors of CAST has been used. With a total 80% signal efficiency, the expected background level for the argon-based gas is around 2×10^2 keV^{1}kg^{-1}day^{-1}, dominated by the ^{39}Ar isotope. If this contribution could be eliminated by using depleted argon from underground sources, the background level would be reduced to ~ 2 keV^{1}kg^{-1}day^{-1} in both argon and neon, limited by the copper vessel and connectors (figure 12.2 right) [256]. A complete list of the contributions to the background is show in table 12.1.

Component	Material	Back. level (keV^{-1}kg^{-1}day^{-1}) Argon	Neon	Radioactivity Reference
Muons	–	0.019	0.026	LSC [267]
Cosmogenics	^{39}Ar	2.04	–	DarkSide Coll. [268]
Vessel	Copper	0.33	0.37	EXO-Coll. [269]
Connectors	Fujipoly	0.58	0.87	T-REX (unpublished)
Field cage	Teflon	1.0×10^{-3}	1.2×10^{-3}	EXO-Coll. [269]
Cathode	Copper	0.020	0.022	EXO-Coll. [269]
MM detectors	Cu-Kapton	0.099	0.084	BiPo (unpublished)
TOTAL		**3.09**	**1.38**	

Table 12.1: Summary of contributions to the TREX-DM background level in argon and neon mixtures obtained from simulations. The statistical errors are less than 10%. The muon flux and radioactivity of the components is taken from the references in the table.

Although x-rays are a potential background source of TREX-DM, in a gas at high pressure, the topology of x-rays and neutron/WIMP-induced events is difficult to distinguish. A preliminary neutron/electron discrimination method was also implemented in [256], achieving a modest improvement in background level of ∼44%.

Assuming that TREX-DM detector reaches an effective energy threshold of 0.4 keVee and a conservative background level of 10^2 keV^{-1}kg^{-1}day^{-1}, the experiment could be sensitive to a relevant fraction of the low-mass WIMP parameter space. Figure 12.3 shows the projected exclusion curve of TREX-DM at 90% confidence level with different hypothesis on background level, energy threshold and exposure. It is shown that with an exposure of 1 kg-year, the experiment could reach sensitivity to the low-mass "region of interest" invoked by some positive interpretations of a few dark matter experiments. The projected exclusion curves have been derived using a binned Poisson method with background suppression and energy binning of 100 eVee. This is a simple method that works well in case of large background cases, like ours. For our assumed flat background, the most significant bin is always the first above threshold. The Poissonian probability p of observing N or more events (where $N = s + b$, being s and b the signal and background events) given the background level b, is

$$p = \sum_{\mathrm{k=s+b}}^{\infty} \frac{e^{-b} b^k}{k!} \tag{12.1}$$

from which we can derive an exclusion contour at $1-\alpha$ confidence level by looping on the scattering cross-section σ_{W-n}, for each WIMP mass, until $p < \alpha$, being α set at 0.1. The input parameters we have used include the conservative quenching factor parameterization shown in figure 11.2, standard WIMP halo model with Maxwellian velocity distribution, conventional astrophysical parameters as well as WIMP coupling to neutrons equal to coupling to protons.

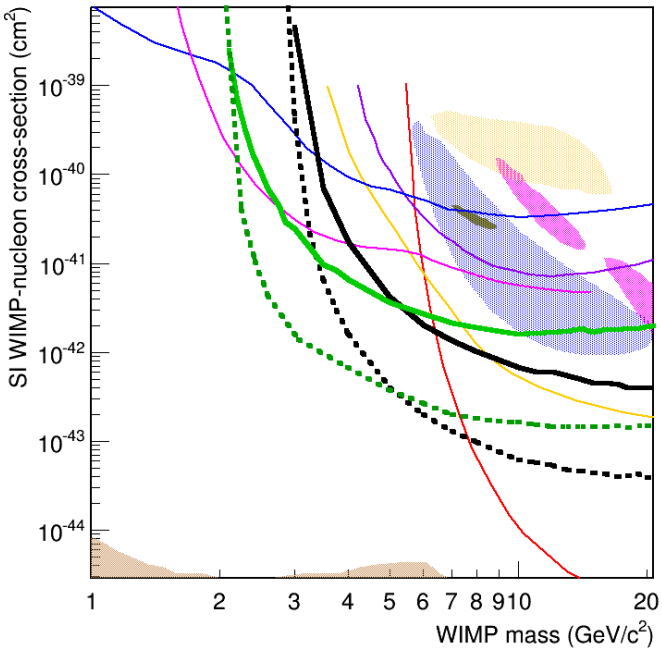

*Figure 12.3: 90% confidence level projected sensitivity of TREX-DM assuming an energy threshold of 0.4 keVee and a total exposure of 1 kg·y in argon (*black thick lines*) and neon (*green thick lines*) with a conservative (*solid*) and realistic (*dotted*) assumptions on the background levels of 100 and 1 keV^{-1}Kg^{-1}d^{-1}, respectively. Closed contours shown are CDMS II Si [257] (*blue*, 90% C.L.), CoGeNT [258] (*dark gray*, 90% C.L.), CRESST-II [259] (*magenta*, 95% C.L.), and DAMA/LIBRA [260, 261] (*tan*, 90% C.L.). For comparison we also show 90% C.L. exclusion limits from SuperCDMS [262] (orange), CDMSlite [263] (*magenta*), LUX [264] (*red*), and CDEX1 [265] (purple) and CRESST-II 2015 [266] (*blue*).*

12.3 Technical description and commisioning of TREX-DM

The TREX-DM vessel is conceived to host 0.3 kg of argon or 0.16 kg of neon at 10 bar. In some respects, it is an scaled-up version of the Micromegas detectors used in CAST, but with a 10^3 times larger active mass. In particular, they share the readout design, although the technology is different. While CAST detectors are fabricated with the microbulk technique, TREX-DM ones are produced with the bulk technology. The detector is built following radiopurity specifications. The only exceptions are the solder-less multi-pin signal SAMTEC connector made one liquid crystal polymer and the *bulk* Micromegas made on woven glass and epoxy laminates (FR-4), the usual materials in the PCB industry. The most readily available solution for the first problem was an *all-in-one* connector plus shielding structure, apparent on the left panel of figure 12.8, over the PCB. On the other hand, radiopure solutions for the *bulk* Micromegas are being designed based on kapton-copper foils only. The less radiopure itmes should be replaced for a science run in underground operation.

12.3.1 The TPC

The vessel is a 71 Nl solderless sleeve made of high purity copper (0.5 m diameter, 0.5 m length and 6 cm thick), closed by two 6 cm thick flat end caps. Its thickness is able to keep pressures

up to 20 bar and shield against external background radiation. An aluminum frame supports the vessel and allows the separation and rotation of the end caps, which allows to independently work on the Micromegas and on the drift vessel.

12.3.2 Active volume

The detector is assembled and read out as a symmetric TPC with two active volumes, a single central cathode and pixelated *bulk* Micromegas as anode. The symmetric design was elected with the aim of reducing the diffusion of the electron swarm and thus get more distinctive topological information. Besides, the required voltage to establish operative drift fields is also reduced. The TPC constituent materials are chosen to be radiopure: copper, polytetrafluoroethylene (PTFE) and polymide.

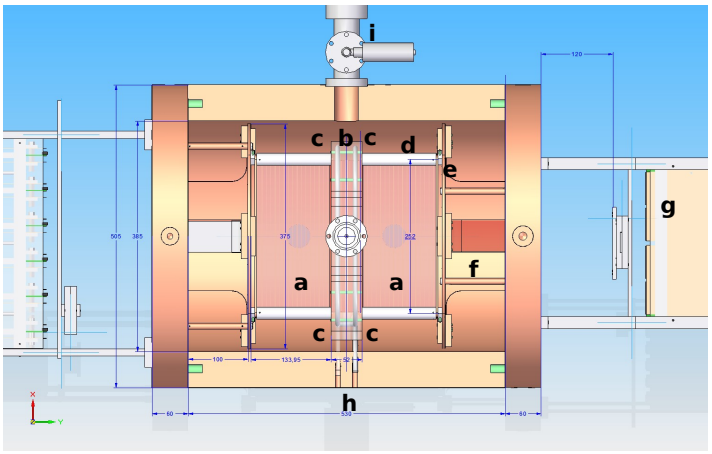

Figure 12.4: Left: Design of the TREX-DM detector. Its different parts are described in detail in the text: active volumes (a), central cathode (b), calibration points (c), field shaper (d), Micromegas detector and support base (e), flat cables (f), AFTER-based electronics (g), gas system (h) and pumping system (i).

A cross-section of the vessel is shown in figure 12.4. The vessel contains two parallelepiped active volumes (a in the figure) of 25.2×25.2×19 cm. The TPC is designed to house up to 300 g of argon in its active volume when operated at 10 bar. The two active volumes are separated by a 4 μm aluminized mylar foil glued on a copper frame, which acts as the cathode (b). It is biased by means of the central high voltage feedthrough shown in figure 12.5. Originally, the central cathode was designed in copper, but the aluminized mylar option was preferred because it is lighter (less radioactivity) and it allows to detect more events in coincidence between the two active volumes. Typical operational drift fields are of around 100 V/cm/bar, which requires setting voltages up to 50 kV in the most demanding (10 bar) situations. This voltage is provided by a Spellman SL30 power supply. The cathode is isolated from the vessel by a teflon gasket.

During the operation, it was noticed that this power supply induced some electronic noise in the mesh signal. With the aim of canceling this noise, a low-pass RC filter with characteristic cut-off frequency of 100 Hz was installed. The filter is composed of a 1.7 nF ultra-high voltage ceramic capacitor and a 1 MΩ resistor (see figure 12.5, right).

In each active volume there is a field shaper that makes uniform the drift field along the 19 cm between the cathodes and detectors. The field shaper consists on 22 copper strips spaced a distance $d = 7$ mm and connected through $R = 10$ MΩ resistors [1]. The strips are printed on a flexible polymide foil, which is mechanically attached to a PTFE structure. The last strip (i.e, the one closer to the readout plane) is driven outside the TPC vessel via the lateral feedthroughs shown

[1] Reference: SM5D resistor, produced by Finechem.

on figure 12.5, labeled as "last ring" feedtrhough. The voltage of the last ring is subsequently connected to an external variable resistor R_v (connected to ground) that allows to operate the TPC at different homogeneous drift field configurations independently of the applied voltage to the cathode and the Micromegas mesh. The variable resistance must be set according to

$$R_v = \frac{V_{\text{mesh}} + 3E_{\text{drift}}d}{E_{\text{drift}}d}R \tag{12.2}$$

where E_{drift} is the desired drift field, and V_{mesh} is the voltage applied at the mesh electrode.

The drift cage has been tested at high voltage (from nominal drift fields of 100 V/cm/bar to 200 V/cm/bar) in argon-based mixtures up to 10 bar. The difference between the expected and measured intensity slightly increases with the voltage applied, i.e., with the pressure, but it is always below 10%. Each Micromegas detector (e) is screwed to a copper base, which is then attached to the vessel's inner walls by means of four columns.

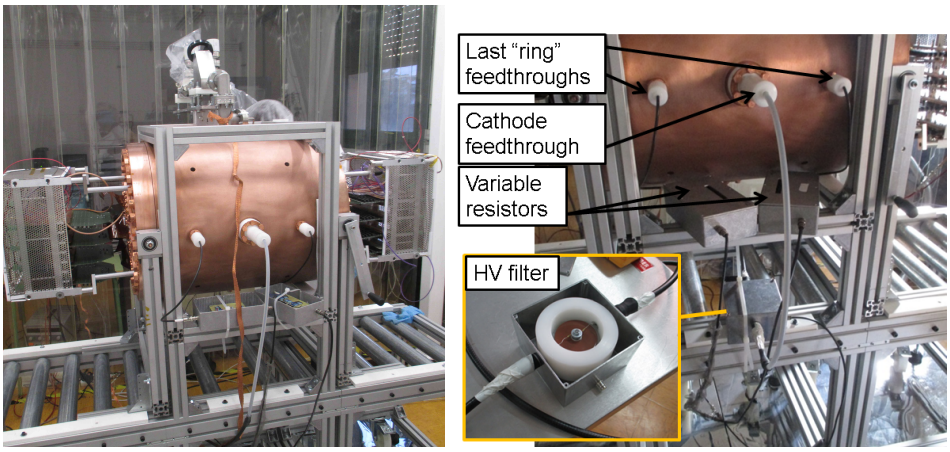

Figure 12.5: A view of the experiment during the comissioning (left) and detailed view of some high-voltage components: low-pass filter and feedthrough of the cathode, and feedthroughs of the last conductive ring *making the field shaper.*

12.3.3 Vacuum system

The experimental procedure starts with the bake-out of the TPC, done by means of a heating system based on thermal resistors. A several-day long pumping of the vessel follows in order to remove impurities, reduce the outgassing rate of the inner components and check for leaks. This is done by means of the vacuum system schematically shown in figure 12.6. It consist in a pumping unit (PU1 in the schema) made of a primary plus a turbomolecular pump connected to the vessel through a DN-40 ISO-CF flange (see figure 12.7). The vacuum line is composed of a vacuum valve (VV1), a high pressure valve (HPV1) and two full-range pressure gauges that allow to monitor the vacuum level and measure the leak and outgassing rate of the TPC. Besides, the line has additional free ports for auxiliary use, like ^{4}He leak detection.

The vacuum level inside the TPC is measured by gauge G1 and G2. The leak and/or outgassing rates are estimated by closing the vacuum valve VV1 and measuring the pressure evolution with gauge G1. The outgassing rate is simply

$$\text{Outgassing} = \frac{\Delta P \cdot V}{t} \tag{12.3}$$

where ΔP is the pressure variation, V is the pumping volume, and t is the time of the measurement.

The leak-tightness of all the vessel feedthroughs has been independently verified, and the vacuum level and leak rate has been measured individually in a dedicated test bench. Subsequently, once the TPC is closed all the unions are checked again, using a *SmarTest Helium Leak Detector*

HLT560 from *Pfeiffer* either in vacuum or sniffer mode. The final measured leak rates of some of the TPC feedthroughs are shown in table 12.2. The values have been measured with the helium leak detector in sniffer mode, after filling the TPC with ∼30 liters of helium and subsequently injecting N_2 up to 2 bar, or in vacuum mode, connecting the auxiliar port of the vacuum system to the helium leak detector.

All the leaks at the level of $\gtrsim 10^{-6}$ mbar·l/s have been sealed. It was found that the PTFE gaskets of 3 mm thickness reduced the leak rate with respect to the previous of 1.5 mm. Apparently, the flexibility of the gasket increases with its thickness, and hence the absorption of surface irregularities.

The lowest vacuum level of the full-equipped TPC is limited by the outgassing of the inner components. After ∼96 hours of continuous pumping, a level of $2.0{\cdot}10^{-4}$ mbar was achieved, while the outgassing/leak rate was below 10^{-5} mbar·l s^{-1}.

Union tested	Components	Leak rate (mbar·l s^{-1})
Gas inlet and source flange	copper gas tube	$8.0{\cdot}10^{-7}$
	calibration gasket	$<1.0{\cdot}10^{-7}$
	flange to vessel	$1.1{\cdot}10^{-7}$
Auxiliar flanges	side 1	$8.8{\cdot}10^{-8}$
	side 2	$9.0{\cdot}10^{-8}$
Electric connections	drift LV pin 1	$<3.0{\cdot}10^{-8}$
	drift LV pin 2	$<2.0{\cdot}10^{-8}$
	PTFE gasket 1	$3.3{\cdot}10^{-8}$
	PTFE gasket 2	$1.8{\cdot}10^{-8}$
	cathode HV pin	$3.5{\cdot}10^{-8}$
Outlet and vacuum	gas outlet	$<1.0{\cdot}10^{-8}$
	vessel PTFE flange	$<1.0{\cdot}10^{-8}$
End caps	big gasket 1	$5.0{\cdot}10^{-7}$
	big gasket 2	$7.0{\cdot}10^{-7}$
	Limandes	$\sim 2\text{–}3{\cdot}10^{-8}$

Table 12.2: Summary of leak rate levels achieved in TREX-DM feedthroughs and unions.

12.3.4 Gas system

Once the leak tightness of the vessel is verified, the gas is injected into the vessel by means of the gas system at an adjustable flow through the gas inlet on the bottom part (h) and comes out through the gas outlet at the top part (i). The schematic view of the gas system is shown in figure 12.6. The pressure of the premixed gas bottle is reduced in two steps by means of consecutive manometers (M1 and M2 in the schema) that determine the pressure in the gas line. The gas panel (see figure 12.7) incorporates a mass flow controller/meter from *Bronkhorst* that regulates the gas flow in the range of 1 to 10 l/h. This device is controlled and monitored through the slow-control system via RS232 protocol, and it can be bypassed through V1 valve for fast-filling of the chamber. A pressure transductor from *Swagelock* is installed downstream, just before the gas inlet, allowing to monitor the gas pressure inside the chamber. The gas outlet is driven to a back-pressure device (BP1) that allows to control and fix the pressure of the TPC. Finally, the gas is expelled to the atmosphere through a single-direction exhaust.

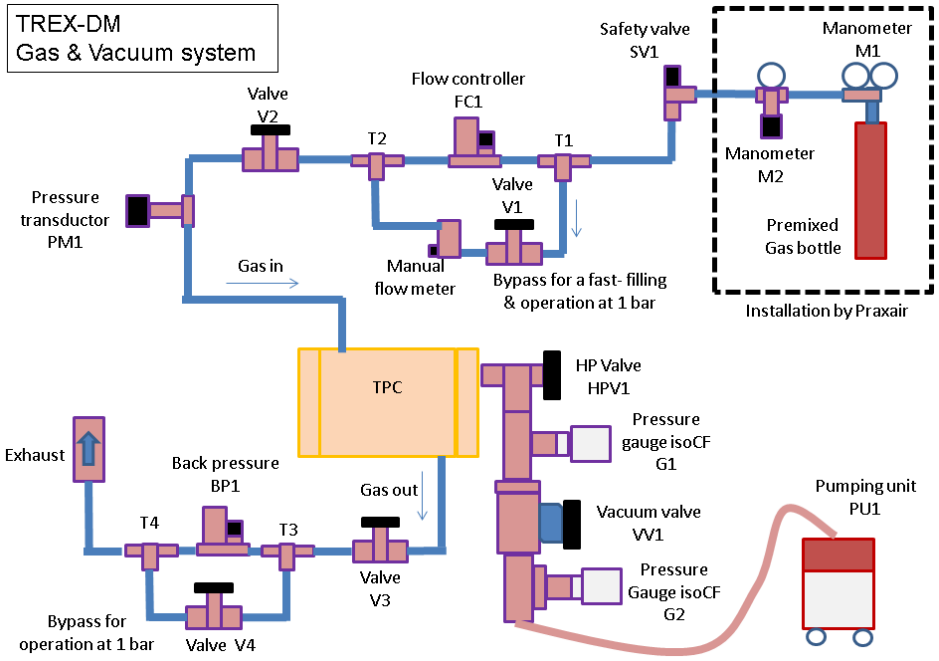

Figure 12.6: Simplified schematic view of the gas and vacuum system of TREX-DM.

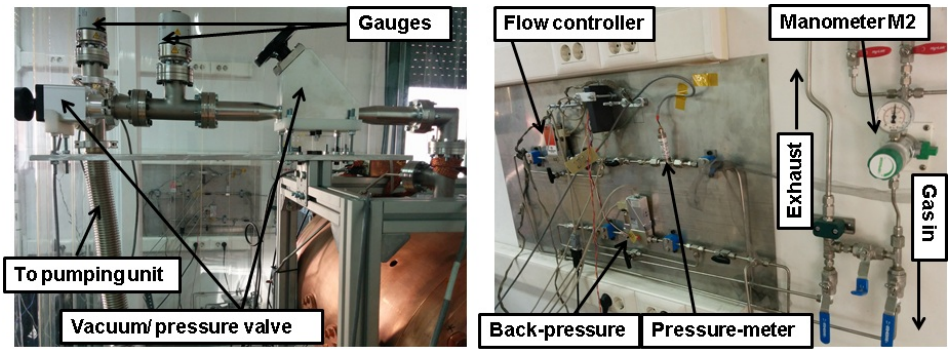

Figure 12.7: View of the vacuum (left) and gas (right) systems.

12.3.5 Calibration system

The calibration system consists on a very thin aluminum holder containing a deposition of ^{109}Cd. The holder is screwed to a plastic rod, which enters to the vessel through a leak tight port. The rod can be manually pushed to four calibration positions per active volume. The calibration points are situated at the corners of the region defined by the field shaper, where the source illuminates directly the active volume. The four calibration points guarantee that all the sectors of the Micromegas are uniformly illuminated, which becomes important at higher pressure, since few 22.1 (K_α) and 24.9 keV (K_β) x-rays would reach the opposite corners. A motor driven calibration system is well advanced and it will eventually substitute the manual procedure.

12.3.6 The bulk detectors and electronics

The design of the two *bulk* detectors is a modified version of the CAST-Micromegas one (see figure 12.8). Each detector is a 1.6 mm-thick, 37.5 cm-diameter Printed Circuit Board (PCB)

made on FR4/phenolic and copper. The active surface of25.2×25.2 cm^2 is divided in squared pads of 332 μm length and separated by a pitch of 582 μm. The detector PCB was produced by Somacis and a stainless steel mesh was laminated on it using the bulk technology in Saclay. The mesh defines a 128 μm-thick amplification gap. Pads are alternatively interconnected in x and y directions (432 strips per direction) through metalized holes, which are rooted into four connectors prints at the sides of the PCB. Instead of using a leak-tight PCB as in MIMAC detector [235], a flat cable, made on kapton-copper foils, is linked to each connector footprint by means of a commercial 300-pin solderless connector [2] . The connectivity is assured by four screws that assure the uniform pressure of the flat cable over the connector. At the same time, the screws also join two 1 cm thick lead pieces and two 1 cm thick copper containers, conceived to partially shield the intrinsic radioactivity of the connectors [251]. Each flat cable comes out from the vessel by means of a copper feedthrough, the leak tightness being guaranteed by PTFE seals and epoxy [3].

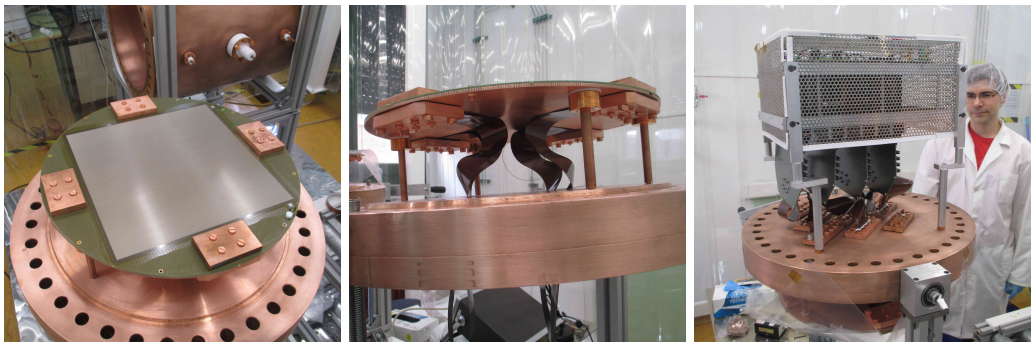

Figure 12.8: Three views of TREX-DM Micromegas detectors. Left: a bulk detector installed at its support base with its four flat cables already linked to it by four (shielded) Samtec connectors. Center: Flat cables come out from the vessel by their corresponding feedthroughs. Right: Flat cables are linked to their interface cards, which are then connected to the FEC boards.

The operation principle of the detector is the same as in any Micromegas-based TPC. A particle interacts in the active volume producing a swarm of free electrons, which drift towards the Micromegas plane. Charge multiplications takes then place in the amplification gap and the charge movement of the electron-ion pairs induces signals both at the mesh and the strips. A simplified schematic view of the electronics is shown in figure 12.9, while figure 12.10 shows the electronic modules used for the high-voltage biasing, strips triggering and mesh pulse processing of the TREX-DM detector. The mesh electrode is biased by a CAEN N470A power supply module through the high-voltage filter schematically shown on the right of figure 12.10. The characteristic RC constant is designed to reduce the recovery time after a current excursion, typically produced by sparks in the amplification gap. The mesh signal is extracted from the vessel by a low-voltage feedthrough and it is then consecutively amplified by a CANBERRA preamplifier and a spectroscopy amplifier and it is subsequently recorded by a Tektronix DS5054B oscilloscope or a Multichannel Analyzer MCA8000A. The mesh pulse could also be recorded using waveform digitizers for subsequent post-processing analysis. In parallel, strips pulses come out from the vessel by four flat cables. Each of them is linked to an interface card that distributes the signals to the entrance connectors of an AFTER (ASIC For TPC Electronics Readout)-based FEC board (described in chapter 5). Each board has four AFTER ASICs that collect and sample the strip signals continuously at 50 MHz in 512 samples per channel, recording a window of $\sim$10 μs, which is longer than the maximum drift time of charges created in the active volume. The readout electronics is triggered by the negative component of the mesh's amplified bipolar pulse. At that moment, the analog data from all channels is digitized by an ADC converter. Finally, a pure digital electronics card, the FEM board, gathers the ADC data of the four FEC boards, performs the pedestal subtraction and sends

[2] Reference: GFZ300, produced by SAMTEC
[3] Reference: Hysol RE2039, produced by Henkel.

it to a commercial Data Concentration Card (DCC) Xilinx ML405 via optical fiber. Finally, the data is gathered by the DAQ system by means of a standard network connection.

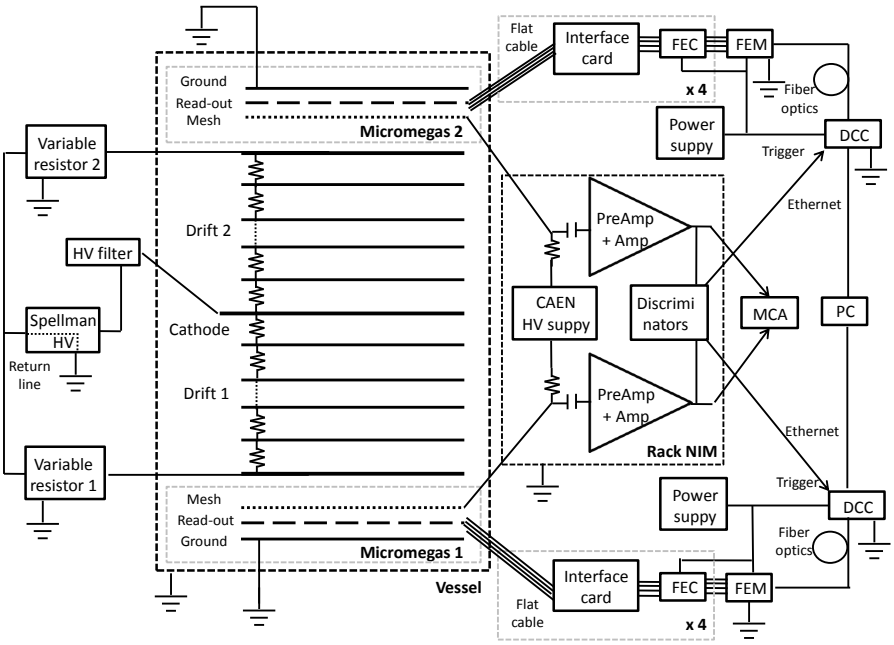

Figure 12.9: Simplified electric and readout scheme of the TREX-DM detector.

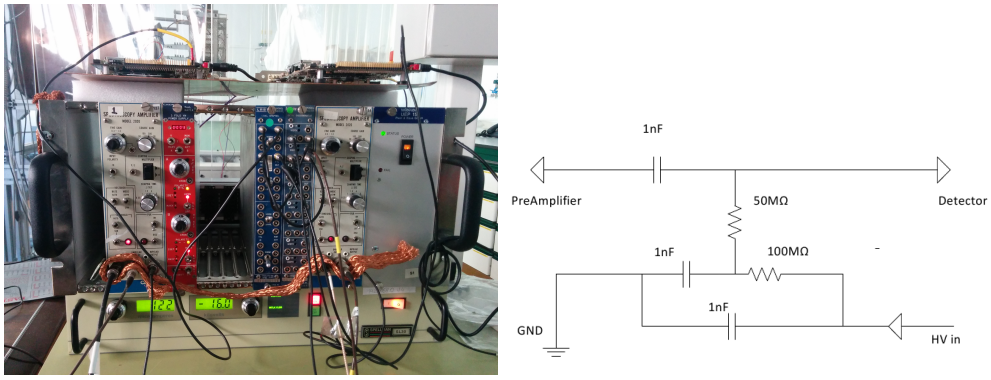

Figure 12.10: Left: electronic modules used for the high-voltage biasing, strips triggering and mesh pulse processing of the TREX-DM detector. From left to right: CANBERRA spectroscopy amplifier for Micromegas 1, CAEN N470A power supply, NIM-TTL converter, linear Fan-in/Fan-out and spectroscopy amplifier for Micromegas 2. On the bottom, the Spellman SL30 power supply. On the top part, the two DCCs for the strips acquisition. More details are given in the text. Right: schematics of the mesh signal filter/decoupler.

12.3.7 Detectors' quality test

Before the start of data-taking, the detectors' connectivity is verified. Firstly, the capacitance between each electronic channel (detector strip + PCB routing + flat cable routing) and the ground

is measured. This process allows to determine the electronic channels that, due to a manufacturing or assembling error, are not instrumented or are short-circuited. For example, figure 12.11 shows the measurements of one of the TREX-DM detectors, whose 2×432 channels are distributed in four connectors; it can be noticed that the connectivity is 100% with capacitance values in the 170–200 pF range.

Capacity of TREX-DM3 + 4 flat cables, full connectivity

NORTH	1	2	3	4	5	6	7	8	9	10	11	12	13	14	15	16	17	18	19	20	21	22	23	24	25	26	27	28	29	30
1	x	x	176	182	188	175	174	180	187	177	169	178	184	178	169	183	177	175	175	180	180	176	175	183	184	177	179	190	x	x
2	x	175	185	186	177	189	183	187	175	171	181	184	174	185	180	180	178	185	172	180	185	179	171	182	178	178	176	183	192	x
3	178	189	184	176	174	178	183	174	180	182	180	176	173	183	170	180	184	177	181	173	177	187	184	175	187	190	185	177	180	190
4	190	183	179	183	190	182	175	185	187	177	174	178	186	174	182	184	174	180	186	183	178	177	186	180	178	181	187	188	181	182
5	186	181	92	189	178	184	190	186	175	178	182	187	172	176	182	172	186	176	173	177	187	181	175	188	192	181	180	186	193	189
6	202	201	194	182	188	186	195	191	195	206	199	191	200	209	201	210	205	200	202	210	205	196	195	203	186	180	183	192	196	186
7	195	187	186	194	204	188	191	203	207	195	195	207	208	200	195	195	203	200	210	196	200	207	196	187	197	194	185	180	186	197
8	180	187	195	195	185	202	204	202	192	198	210	207	197	201	215	196	213	208	197	204	194	196	206	198	194	187	198	194	183	187
9	x	194	186	181	193	199	195	188	196	204	195	191	203	210	203	206	207	196	203	201	204	195	190	194	197	184	183	192	196	x
10	x	x	188	197	195	188	193	203	203	190	195	206	210	201	199	206	195	210	194	192	195	204	193	188	191	195	190	188	x	x

SOUTH	1	2	3	4	5	6	7	8	9	10	11	12	13	14	15	16	17	18	19	20	21	22	23	24	25	26	27	28	29	30
1	x	x	185	195	195	186	184	192	189	176	179	186	180	170	173	173	175	179	165	183	175	172	182	188	190	190	188	186	x	x
2	x	x	x	x	x	x	x	x	x	x	x	x	x	x	x	x	x	x	x	x	x	x	x	x	x	x	x	x	x	x
3	196	200	190	187	199	186	185	180	190	189	179	174	186	184	176	183	182	177	177	183	188	193	187	186	198	198	188	184	183	191
4	x	x	x	x	x	x	x	x	x	x	x	x	x	x	x	x	x	x	x	x	x	x	x	x	x	x	x	x	x	x
5	186	196	198	194	187	190	190	183	182	186	188	177	174	182	183	172	177	181	177	190	183	179	188	188	190	184	191	197	194	183
6	x	x	x	x	x	x	x	x	x	x	x	x	x	x	x	x	x	x	x	x	x	x	x	x	x	x	x	x	x	x
7	195	188	197	209	200	197	191	194	188	184	184	187	185	175	178	171	182	173	184	179	194	190	182	188	197	202	189	196	199	195
8	x	x	x	x	x	x	x	x	x	x	x	x	x	x	x	x	x	x	x	x	x	x	x	x	x	x	x	x	x	x
9	x	203	194	201	206	193	183	184	196	192	177	179	184	184	177	189	183	173	179	192	190	188	188	196	199	196	194	202	196	x
10	x	x	x	x	x	x	x	x	x	x	x	x	x	x	x	x	x	x	x	x	x	x	x	x	x	x	x	x	x	x

EAST	1	2	3	4	5	6	7	8	9	10	11	12	13	14	15	16	17	18	19	20	21	22	23	24	25	26	27	28	29	30
1	x	x	168	180	176	174	167	176	173	163	168	177	173	160	165	166	177	163	175	166	163	172	178	178	176	174	180	171	x	x
2	x	175	181	175	166	176	179	166	164	172	177	167	160	172	161	175	161	172	168	174	175	167	170	167	164	163	170	179	177	x
3	179	189	170	170	180	168	169	170	179	176	169	167	173	176	168	181	179	171	164	165	172	178	188	169	177	182	167	171	183	182
4	179	167	173	181	172	167	171	180	174	164	169	180	173	166	180	166	163	164	179	169	166	174	182	180	170	173	182	174	170	179
5	172	183	184	174	174	179	186	170	167	176	178	164	165	176	176	165	170	173	168	177	176	168	169	172	168	170	174	186	181	173
6	190	187	175	174	182	174	176	182	194	198	190	187	199	200	194	196	204	198	190	201	193	183	189	196	179	171	176	185	182	171
7	180	170	181	191	186	189	185	199	195	185	192	206	205	190	196	198	204	191	202	192	198	197	183	184	187	186	172	175	185	184
8	177	185	190	184	180	189	196	187	188	193	203	191	193	206	206	188	195	202	194	189	184	194	197	182	188	186	189	177	173	186
9	x	188	178	177	192	195	181	187	196	196	190	193	204	205	195	208	200	190	189	203	195	185	185	195	183	175	176	187	187	x
10	x	x	185	194	188	179	194	200	190	190	199	209	200	196	201	204	187	202	194	185	194	197	186	181	194	187	177	175	x	x

WEST	1	2	3	4	5	6	7	8	9	10	11	12	13	14	15	16	17	18	19	20	21	22	23	24	25	26	27	28	29	30
1	x	x	183	195	189	191	184	194	183	171	172	180	180	166	170	169	178	165	180	171	169	185	184	190	186	186	190	181	x	x
2	x	x	x	x	x	x	x	x	x	x	x	x	x	x	x	x	x	x	x	x	x	x	x	x	x	x	x	x	x	x
3	195	193	186	180	191	181	182	178	187	188	170	174	184	177	171	178	176	176	168	173	184	187	180	182	189	190	180	178	191	188
4	x	x	x	x	x	x	x	x	x	x	x	x	x	x	x	x	x	x	x	x	x	x	x	x	x	x	x	x	x	x
5	190	193	197	192	186	194	194	180	176	183	188	174	169	182	182	168	173	182	175	187	185	178	181	184	193	183	185	195	191	180
6	x	x	x	x	x	x	x	x	x	x	x	x	x	x	x	x	x	x	x	x	x	x	x	x	x	x	x	x	x	x
7	199	187	194	205	200	193	187	195	186	177	180	188	182	171	177	173	183	172	187	177	189	192	184	183	197	200	186	194	199	194
8	x	x	x	x	x	x	x	x	x	x	x	x	x	x	x	x	x	x	x	x	x	x	x	x	x	x	x	x	x	x
9	x	199	184	195	204	193	179	181	191	185	172	176	184	179	169	182	174	168	174	187	184	178	185	192	196	193	190	203	195	x
10	x	x	x	x	x	x	x	x	x	x	x	x	x	x	x	x	x	x	x	x	x	x	x	x	x	x	x	x	x	x

Figure 12.11: Capacitance measurements (in pF) of all the channels of the TREX-DM3 detector plus flat cables. The detector has four connectors (north, south, east, west); the connectivity is 100%, showing values of 170–200 pF per channel.

Once the connectivity is tested, the TPC vessel is closed and data-taking can proceed. Then, the detector performance is generically assessed by calibrating its surface and observing the number of hits in each channel. This process reveals the noisy channels, which can be turned off from the acquisition program, reducing the size of the data sets. Figure 12.12 the hits distribution in each electronic channel of the four Front End Cards (FECs) of one of the TREX-DM detectors. An approximately uniform distribution is expected, but instead, some noisy channels are observed: two in FEC0 (the red and yellow bins), three in FEC3 (in red). Besides, it was found that the non-instrumented channels were noisy, and they were disconnected from software (white rows in FEC3). Finally, the regular data-taking could start.

12.3.8 Slow control system

The TREX-DM slow-control is a flexible and modular data acquisition system based on sets of Raspberry-Pi [270] and Arduino [271] boards integrated in a single ethernet network. The software, developed in *Python* by A. Peiro, comprises the data acquisition programs and the graphical user interface [272], which allows the user to interact with the different devices of the system .

The key parameters of the experiment are continuously monitored and recorded in real time at a refreshing rate of typically ∼1 second. The gas flow and pressure, the vacuum levels, the temperature and the high voltage suppliers are continuously monitored. Besides, the system allows to: control the pressure in the TPC via the back-pressure; regulate the flow into the TPC via the flow-controller; move the calibration source to the different calibration positions or to garage position; set the high-voltage on the cathode and mesh.

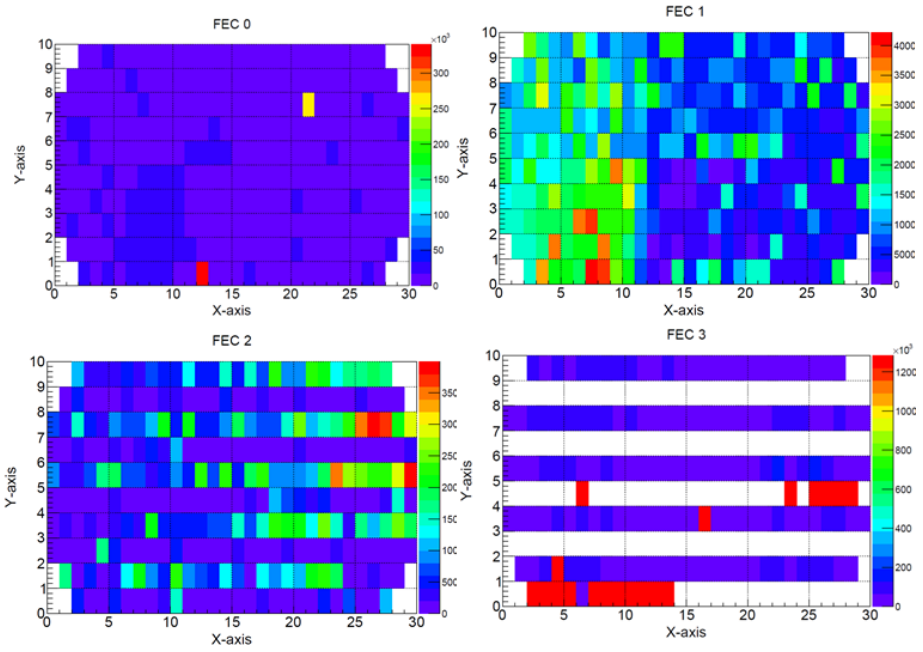

Figure 12.12: Number of hits in each electronic channel of the four Front End Cards (FEC). FEC0 presents two noisy channels (in red and yellow). The non-instrumented channels of FEC2 are slightly noisy, while most of those of FEC3 have been removed by software.

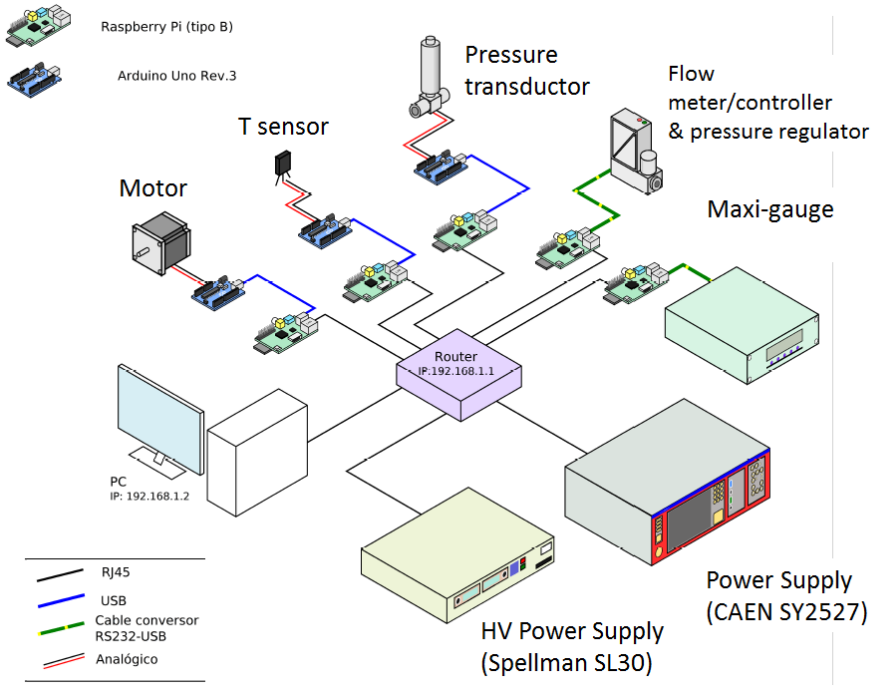

Figure 12.13: Sketch of the subsystems integrating the TREX-DM slow-control network.

12.3.9 Short-term upgrades

The non-radiopure components of the TPC (Micromegas PCB and Samtec multi-pin connectors) will be replaced in the short-term, and are only used to validate the experimental design. The PCB of the *bulk* Micromegas detectors will be replaced by a radiopure version made in four stack-up layers of polymide and copper from *Somacis*. The active area will be 246×246 mm^2 pixelated in pads of 344 μm, resulting in 410 channels per axis with a pitch of 600 μm. The fraction of the active area covered by pixels is around 66%. The cross-section view of the design is shown in figure 12.14, over which the mesh will be suspended following the usual *bulk* technique at Irfu CEA-Saclay.

Radiopure solutions to the multi-pin Samtec connectors are being looked for. A first attempt are the *Fujipoly gold 8000*, a high-density connector made of a silicon rubber core and flat metallic gold-plated conductors vulcanized in a row. Figure 12.15 (top) shows a figure of these connectors with their characteristic dimensions. The connectivity between the pads printed on a PCB and the strips of the Fujipoly connector has been measured. After a unsuccessful first attempt, the mechanical assembly was redesigned and full connectivity was achieved (see figure 12.15, bottom). The radioactivity of the connectors has been measured in HPGe detectors in the LSC. Although the contamination in ^{232}Th chain is reduced around a factor 10 with respect to the Samtec connector (from 62 to 6.8 μBq/channel), the activities of ^{238}U and ^{40}K are found to be similar (∼30 μBq/channel for ^{238}U) and 5 mBq/channel for ^{40}K).

On the detector instrumentation side, the current readout electronics based on the AFTER chip will be replaced by the self-triggered AGET chip [273], a crucial step for the achievement of the required low energy threshold.

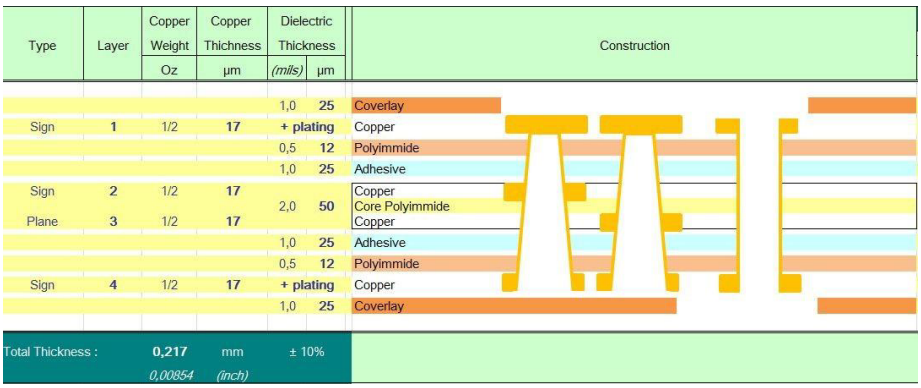

Figure 12.14: Schematic cross-section of the new radiopure bulk design.

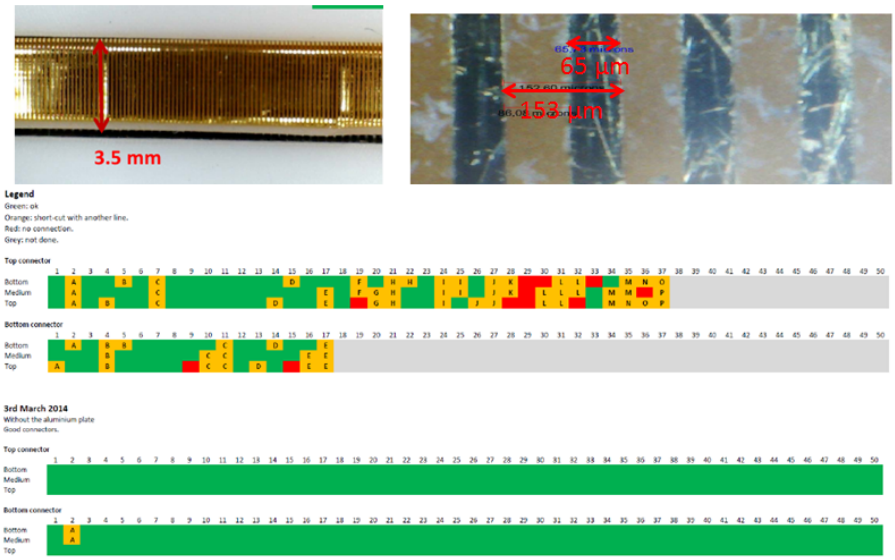

Figure 12.15: View of a Fujipoly Gold 8000 Connector and two connectivity tests performed. The first test (top) was not successful as many shortcircuited (in yellow) and not-connected (in red)channels were observed. However, in a second test (bottom) the connection mechanism was modified and the connectivity is 100%.

Chapter 13

TREX-DM characterization at surface

Contents

13.1 Introduction

The first proof-of-concept runs performed with TREX-DM aboveground are reported in this chapter, using a not fully radiopure setup.

First, we present the results of the detector performance up to 10 bar in Ar+2%iC$_4$H$_{10}$, in terms of electron transparency, gain level, gain uniformity and energy threshold.

Then, we describe the calibration procedure, along with the data analysis, event reconstruction and detector surface characterization. The background level of a first measurement at surface is also presented, and finally, the short-term prospects are discussed.

13.2 Characterization in Ar+2%iC$_4$H$_{10}$up to 10 bar

Two bulk Micromegas detectors, *MM1* and *MM2*, of 128 μm amplification gap have been characterized in Ar+2%iC$_4$H$_{10}$ from 1.2 to 10 bar in steps of 1 bar in order to study their general performance. The tests were performed from 21st April to 13th May 2015. This is the first systematic characterization of bulk Micromegas over atmospheric pressure. The measurements have been carried out in the TREX-DM vessel, establishing an initial gas flow 10 l/h of the argon-isobutane gas. The readouts are tested with a ^{109}Cd source (x-rays of 22 keV) keeping a gas flow of 3–5 l/h during the measurements. The mesh and drift voltages are changed in a wide range, from ∼300 V at 1.2 bar to ∼900 V at 10 bar, and from ∼1.5 kV to ∼30 kV, respectively. The signal induced in the mesh electrode was read out by a charge-sensitive preamplifier (ORTEC 142C and CANBERRA-2004 for MM1 and MM2, respectively), whose output fed a CANBERRA 2022 Spectroscopy Amplifier with an integration time of 1.5 μs. Subsequently, the unipolar output is connected to a multichannel analyzer AMPTEK MCA-8000A for spectra building.

Figures 13.2 and 13.1 show some calibration spectra acquired at different pressures. The spectrum is characterized by a peak at around 22 keV (K$_\alpha$ emissions) and by a fluorescence emission at around 6.4 and 8 keV from the copper and iron components. It can be noted how the intensity of this peak decreases with the pressure, since less photons are able to reach the components of

the TPC. An small peak around 3 keV can also be noticed on figure 13.1 (left), coming from the argon fluorescence.

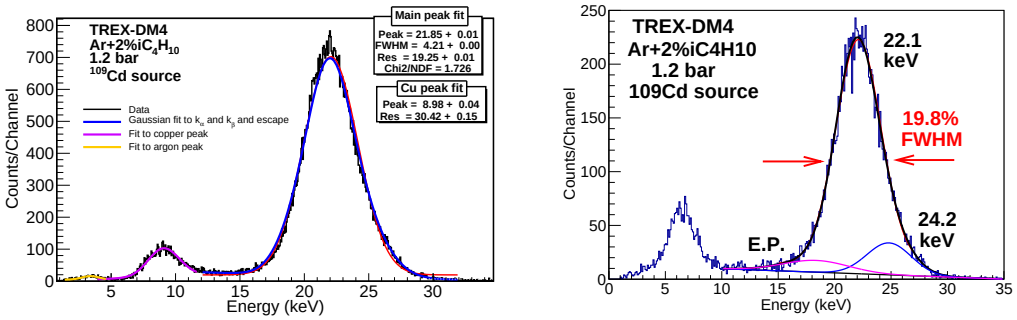

Figure 13.1: Energy spectrum respectively generated by the mesh (left) and strips signals (right) when one of the Micromegas detectors was irradiated by a ^{109}Cd source in $Ar+2\%iC_4H_{10}$ at 1.2 bar. The spectral parameters are defined through an iterative multi-Gaussian fit corresponding to the K_α and K_β emission lines of the source and their escape peaks (E.P.). The fluorescence lines of iron (at 6.4 keV, emitted from the mesh) and copper (8 keV, from the vessel) are also present in both spectra. The energy threshold is situated at around 1 keV.

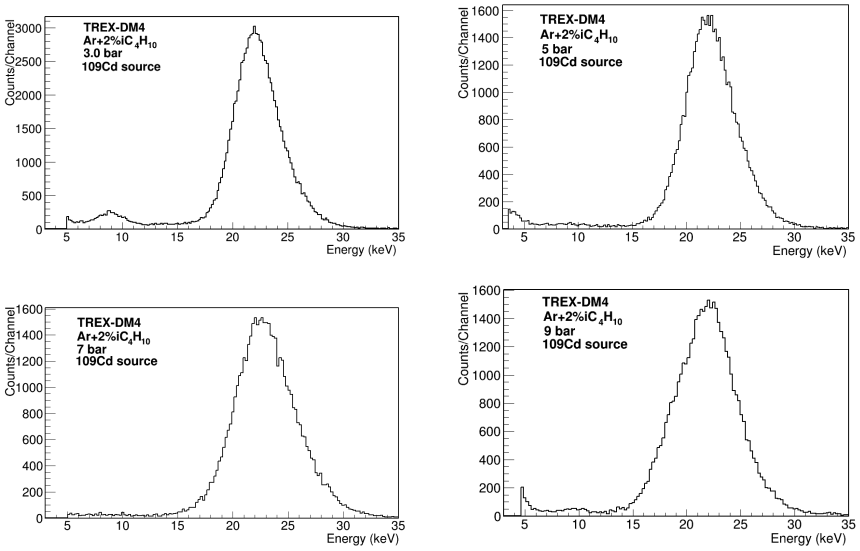

Figure 13.2: Calibration spectra at 3, 5, 7 and 9 bar in in $Ar+2\%iC_4H_{10}$. Note how the fluorescence peak is suppressed at higher pressures.

Firstly, the drift voltage is varied for a fixed mesh voltage to obtain the electron transmission curve at each pressure, shown in figure 13.3. The symmetric design of the TPC allowed to characterize both MM1 and MM2 simultaneously. The drift fields were varied typically from 30 to 300 V/cm/bar, with the bias voltages depending on the gas pressures, as table 13.1 shows. The detectors show a plateau of maximum electron transmission for a wide range of ratios of drift and amplification fields at all pressures. The electron transmission drops at very low drift fields ($\lesssim$50 V/cm/bar) due to electron attachment of the primary electrons generated in the conversion volume. For high drift fields, the mesh stops being transparent for primary electrons, and the energy resolution also degrades.

Pressure (bar)	V_{mesh} (V)	E_{amp} (kV/cm)	V_{cathode} (kV)	E_{drift} (V/cm/bar)	E_{drift} (V/cm)
1.2	360	28.1	1.6–5.2	60–240	72–288
2.0	430	33.6	1.7–10.5	40–300	80–600
3.0	500	39.1	2.0–16.1	30–310	90–930
4.0	560	43.8	2.6–20.0	30–290	120–1160
5.0	610	47.6	2.3–17.4	20–200	100–1000
6.0	690	53.9	2.7–23.8	20–230	120–1380
7.0	720	56.3	3.1–26.0	20–215	140–1505
8.0	780	60.9	3.5–27.7	20–200	160–1600
9.0	845	66.0	3.9–31.1	20–200	180–1800
10.0	895	69.9	3.9–31.1	18–180	180–1800

Table 13.1: Amplification and drift field ranges for the different pressure settings used during the electron transmission characterization of TREX-DM bulk Micromegas detectors in Ar+2%iC$_4$H$_{10}$.

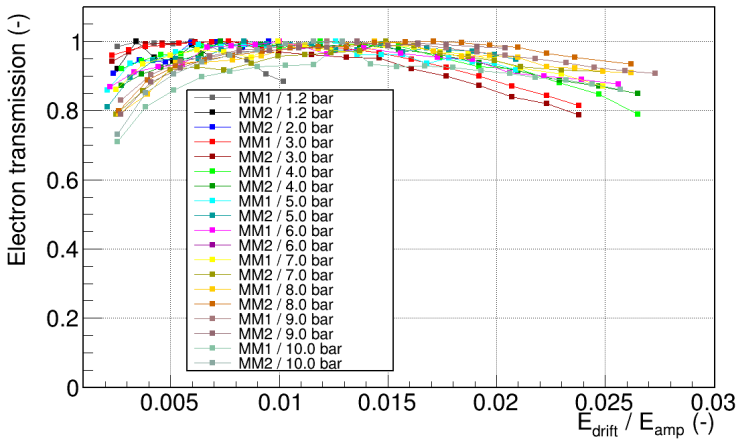

Figure 13.3: Dependence of the electron transmission with the ratio of drift and amplification fields in the bulk Micromegas of TREX-DM in Ar%iC$_4$H$_{10}$ at pressures from 1.2 to 10 bar. The peak positions have been normalized with he maximum of each series, assuming maximum electron transmission is always achieved.

After having studied the mesh transparency, the ratio of drift and amplification fields is fixed for every pressure at the point where the mesh shows the maximum electron transmission, typically at around 100 V/cm/bar. Then, the available range of mesh voltages is scanned, from very low amplification fields where the amplitude of the mesh waveform is just above threshold, up to the spark limit, where the sparking rate is too high for safe operation. The amplitude of the waveform increases with the applied amplification field and so does the peak position in the spectra. The peak position is used to calculate the absolute gain of the Micromegas detectors, defined as the ratio of the number of electrons after the avalanche n and the primary electrons,n_0: $G = \frac{n}{n_0}$. As explained in section 7.2.2, determining G requires the characterization of the electronic chain in order to obtain the conversion factor between the peak position registered by the multichannel analyzer (in arbitrary units) and the number of electrons before the preamplifier n, being n_0 a theoretical parameter given by 22.0 keV/W_{Ar}. Figure 13.4 (left) shows the characterization of the electronic chain with and without the signal filter, following in both cases an equivalent trend.

Figure 13.4 shows the gain curves obtained in Ar+2%iC$_4$H$_{10}$ between 1.2 and 10 bar. Both detectors present a similar gain and their maximum working gain before the spark limit decreases

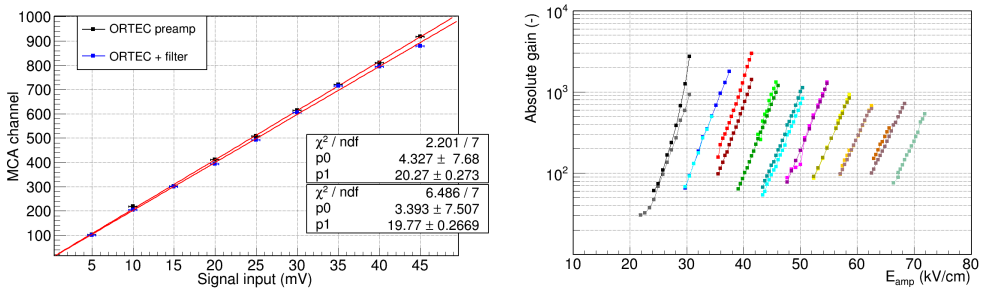

Figure 13.4: Left: gain calibration of the electronic chain. The signal input feds a 10 pF capacitance for its conversion in equivalent charge and subsequently into the charge-sensitive preamplifier and the rest of the electronic chain. The relation allows to determine the number of electrons n associated to any MCA channel. Right: dependence of the absolute gain with the amplification field in Ar+2%iC_4H_{10} between 1.2 and 10 bar. The maximum gain of each curve is obtained just before the spark limit.

with the gas pressure, from 3×10^3 at 1.2 bar down to 5×10^2 at 10 bar. Both detectors reach gains larger than 10^3 below ∼6 bar. The energy threshold achieved is related with the detector gain: the higher the gain, the lower the energy threshold because the signal becomes more and more separated from the electronic noise, as figure 13.5 (left) illustrates. The energy threshold of the mesh signal increases from 1 keV (at 1.2 bar) to 6 keV (at 10 bar).

The dependence of the energy resolution with the amplification field for the pressures settings in which we have operated is shown in figure 13.5, right. At each pressure there is a range of amplification fields for which the energy resolution is optimized. At low gains, the energy resolution degrades because the signal becomes comparable with noise. At high fields, the resolution degrades due to increase in the gain fluctuations by the UV photons generated in the avalanche. The worsening of the energy resolution as a function of the fraction of quencher has been studied in [274]. As can be noticed, the best energy resolution degrades with the pressure, being around 16% FWHM at 22.0 keV at 1.2 bar and above 25% FWHM at 10 bar; modest values for bulk detectors.

The low gain achieved may be explained by the low quantity of quencher (2%) in the gas. As shown in [275] for 50 μm-gap microbulk Micromegas, the gain loss with pressure becomes less significant with the increase in the quencher concentration. If this trend extrapolates to 128 μm-gap, higher gain could be achieved in gas mixtures with large isobutane mass ratio. A test with Ar+5%iC_4H_{10} was carried out to test this possibility.

On the other hand, the energy resolution and energy threshold are clearly affected by the noise conditions during the data-taking, due to the presence of a 1 MHz frequency noise both at the mesh and strips. A better detector grounding would probably result in better energy resolution and threshold levels. However, the critical point to achieve low enough energy thresholds is the availability of auto-trigger electronics. Observing the signal-to-noise ratio of the strip pulses (see as an example figure 13.6) or considering the value used for the zero-suppression we conclude that energy thresholds below 200 eVee are feasible.

13.3 Characterization in Ar+5%iC_4H_{10}

In the current phase, TREX-DM is planed to be tested at different gas mixtures. The goal is to evaluate if larger fractions of quencher or new base gases would allow to achieve larger gains and lower energy thresholds.

Both detectors were characterized following the procedure describe above for a mixture of Ar+5% iC_4H_{10}. For this mixture, the maximum drift velocity is reached at drift fields a factor 2 larger than in 2% isobutane mixtures (see figure 13.11), reducing the diffusion coefficients, a good

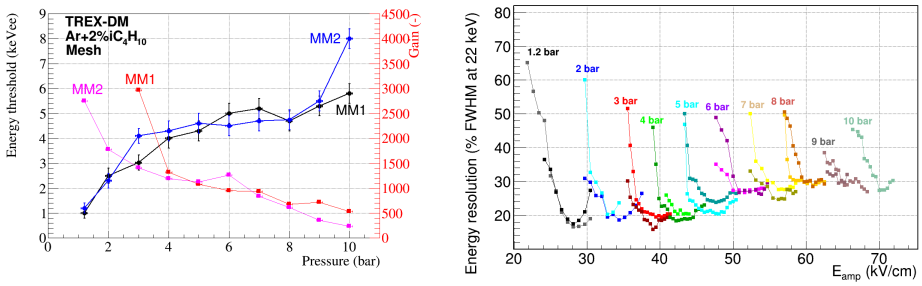

Figure 13.5: Left: energy threshold as a function of the detector pressure for the mesh signal of MM1 (black circles) and MM2 (blue circles). The gain at each pressure is also shown with the axis displayed on the right side. The correlation between gain and energy threshold is manifest. Right: dependence of the energy resolution at 22 keV with the amplification field for the bulk Micromegas of TREX-DM in Ar+2%iC$_4$H$_{10}$ between 1.2 and 10 bar. The best achievable energy resolution increases with pressure.

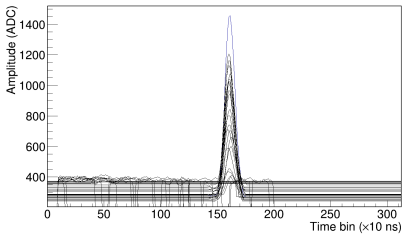

Figure 13.6: An example of a x-ray event with some noisy channels.

property for improving the resolution and the topological reconstruction. Before taking data, the vessel was pumped again reaching a worse value (1.4×10^{-3} mbar) than in previous cycles. Although two leak points (at the level of 4×10^{-5} mbar/l/s) were identified, we decided to continue with the measurements. Figure 13.7 shows the dependence of the absolute gain and energy resolution with the amplification field. Also in this mixture, it is observed a degradation of the maximum gain and energy resolution with pressure. However, the energy threshold does not seem to deteriorate too much from 1 to 3 bar, as the energy threshold evolves just from ∼1 keV to 1.5 keV (see figure 13.8), which is a smaller increase than the one observed in the 2% isobutane gas mixture. A comparison of the energy threshold and gain measured by the mesh in argon-based mixtures with an isobutane concentrations of 2% (black points) and 5% (red points) is shown in figure 13.9. A simple extrapolation shows that an energy threshold of 2.8 keV at 10 bar is feasible with the mesh signal.

Figure 13.10 shows the comparison between the energy resolution at 2% and 5% isobutane concentrations at 1.2, 2 and 3 bar. Although at low pressure energy resolution is better in the 5% iC$_4$H$_{10}$ mixture, it quickly degrades at higher pressures. The origin of this quick degradation observed at 2 and 3 bar is uncertain: could be due to an excess of quencher concentration for those pressures or due to attachment due to the gas leaks. Further tests with this mixture at higher pressures will elucidate which gas mixture is better in terms of gain, energy threshold and energy resolution.

13.4 Data taking at 2 bar

After having characterized the detector from the mesh signal, the next step was to study the electron tracks by means of γ-sources and background from the signal induced in the strips, which

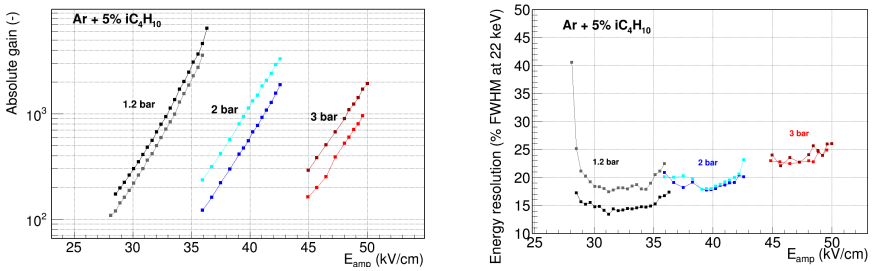

Figure 13.7: Left: dependence of the absolute gain with the amplification field in $Ar{+}5\%iC_4H_{10}$ between 1.2 and 3 bar for MM1 *&* MM2*. The maximum gain of each curve is obtained just before the spark limit. Right: dependence of the energy resolution at 22 keV with the amplification field in $Ar{+}5\%iC_4H_{10}$ between 1.2 and 3 bar. Energy resolution clearly degrades with pressure.*

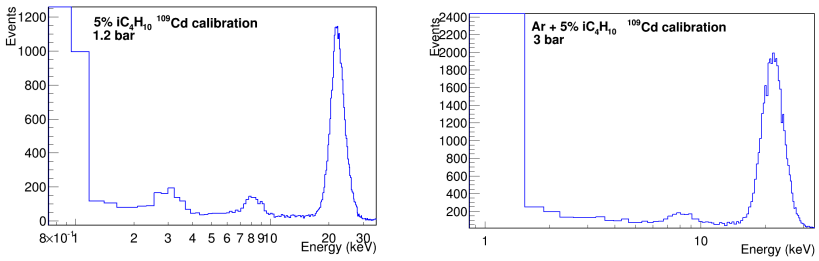

Figure 13.8: Calibration spectra (^{109}Cd source) in $Ar{+}5\%iC_4H_{10}$ at 1.2 and 3 bar at the maximum gain before spark limit. Energy threshold slightly degrades from ∼1 keV to 1.5 keV.

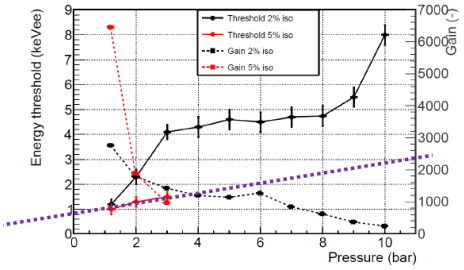

Figure 13.9: Comparison of energy threshold and gain measured by the mesh in argon-based mixtures with an isobutane concentrations of 2% (black points) and 5% (red points). A simple extrapolation (violet dotted line) shows the feasibility of an energy threshold of 2.8 keV at 10 bar.

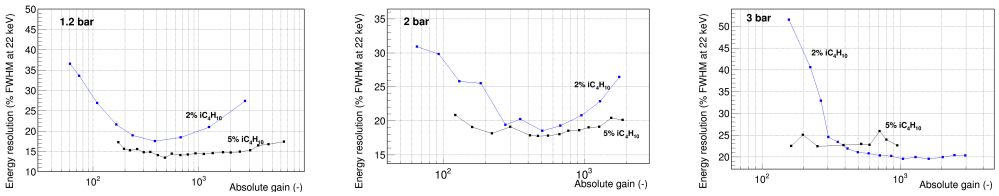

Figure 13.10: Energy resolution at 22 keV as a function of the absolute gain for Ar-based mixtures with 2% and 5% of isobutane from 1.2 bar (left) to 3 bar (right).

are recorded by sampling-ADC electronics, currently based on the AFTER chip. The sampling frequency was set to 50 MHz, recording 511 samples per channel, making a total time of 511×20 ns ≃10 μs. In the argon-isobutane mixture used at drift fields of 100 V/cm/bar, the electrons drift velocity is around 3 cm/μs, as figure 13.11 shows. For this field intensity, the electron drift velocity is maximized, corresponding to ionization tracks as long as ∼30 cm can be recorded, i.e., more than the total length of the TPC. The transversal and longitudinal diffusion coefficients are 134 and 221 μm/cm$^{1/2}$, respectively. On the other hand, the shaping time was set to 100 ns and the electronics gain to 240 pF. The readout response was studied in Ar+2%iC$_4$H$_{10}$ at 2 bar. Unfortunately, we could not extend this study to higher pressures as originally planned due to detector failure: a shortcircuit between mesh and ground appeared in a detector, which was impossible to solve without opening the vessel; the second detector suffered severe breakdown sparks, resulting in several (11) strips short-circuited in two days.

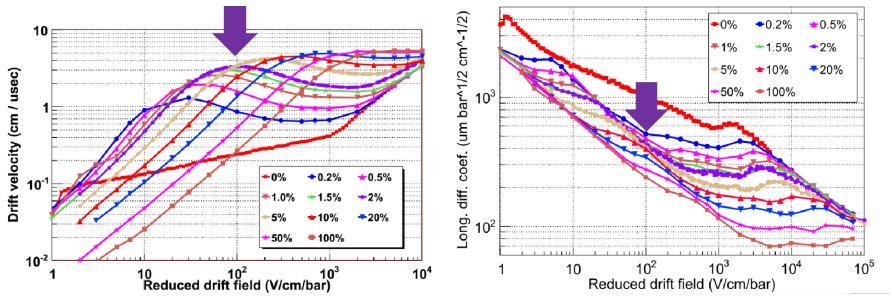

Figure 13.11: Left: drift velocity of electrons as a function of the reduced drift field for several argon-isobutane admixtures. Right: Longitudinal diffusion coefficient as a function of the reduced drift field for the same admixtures. The violet arrow represents the working field configuration in TREX-DM.

An event is a collection of waveforms of the triggered readout channels, defining a triggered channel as those whose waveform amplitude is larger than four times the standard deviation of the internal charge pedestal. The electron tracks can be reconstructed from the 511-point waveforms recorded by each of the 232×232 channels. The analysis chain resembles the one used in CAST (see section 6): a) zero-suppression to eliminate noisy channels, b) pulse shape analysis to determine the waveform parameters of the triggered readout channels, and c) identification of charge clusters in x, y and z directions.

13.4.1 Calibration

Firstly, the detector is calibrated by the ^{109}Cd γ-source. The primary electrons released drift towards the readout plane and the signal induced in the strips are recorded. The strip pulses are then combined and the event can be reconstructed: the temporal position determines the relative z position, while the decoding of the detector and the interface card is used to determine the x and y coordinates. Two examples of the recorded strips waveforms are shown in figure 13.12 for two calibration events, along with the reconstructed xz and yz views. X-rays produce symmetric, point-like energy depositions in the gas. In our examples, the first one is a mono-cluster event, while in the second two clusters are identified, relatively close in the z direction, but quite far away in the xy plane.

Each detector is calibrated from four points situated at the readout corners, a few cm away from the cathode, i.e., there are a total of eight calibration positions. This system allows for a full detector surface illumination even at high pressure. The calibration system is verified by studying the mean cluster position in the xy plane of the event population acquired during calibration runs (see figure 13.13). For each calibration run, an accumulation of events is observed close to the calibration position, as a result of the mean free path of 22 keV photons in the gas.

In order to study the gain uniformity of the detector plane, the detector surface is binned

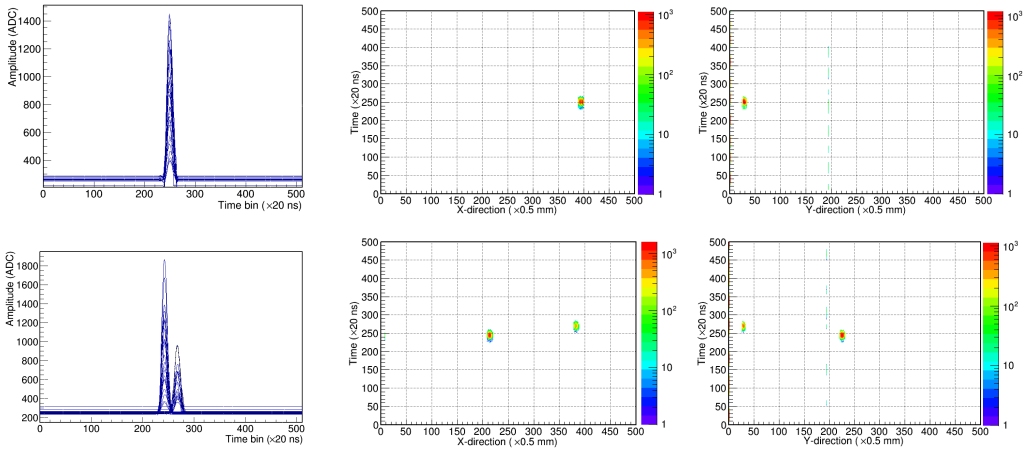

Figure 13.12: Strip pulses and 2D projections in the xz & yz planes of two calibration events (top: mono-cluster; bottom: double cluster) registered by TREX-DM in Ar+2%iC_4H_{10} at 2 bar.

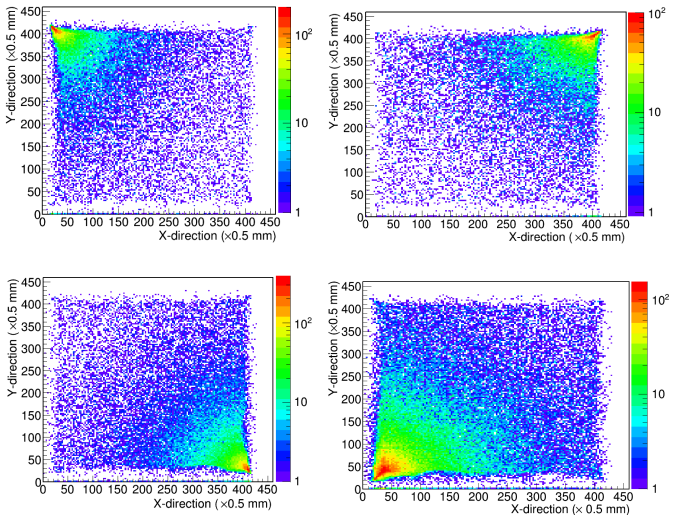

Figure 13.13: Event position distributions on the readout plane from the different calibration positions for typical ^{109}Cd runs in Ar+2%iC_4H_{10} at 2 bar.

into a 2D histogram of 216×216 cells (the readout has 432×432 strips). From the calibration runs, the mean energy-weighted position projected into the readout plane is used to fill the 2D histogram, each entry being weighted by the number of x-rays registered in that bin. The gain maps obtained for two detectors in TREX-DM in Ar+2%iC_4H_{10} at 2 bar are shown in figure 13.14, the first showing gain variations <10%, the second presenting regions without amplification at some positions within the fiducial area, and gain fluctuation around 20%.

The calibration energy spectrum of the detectors before and after the gain correction is shown in figure 13.15. The improvement in energy resolution is larger in the detector showing less gain homogeneity, although final energy resolutions at 22 keV are modest.

The detector relative gain is studied by pixelizing the detector in 216×216 cells, each cell containing 2×2 strips. The x-ray peak energy relative to the average value over the whole readout plane is shown in figure 13.16, each entry being weighted by the number of x-rays counted in that pixel.

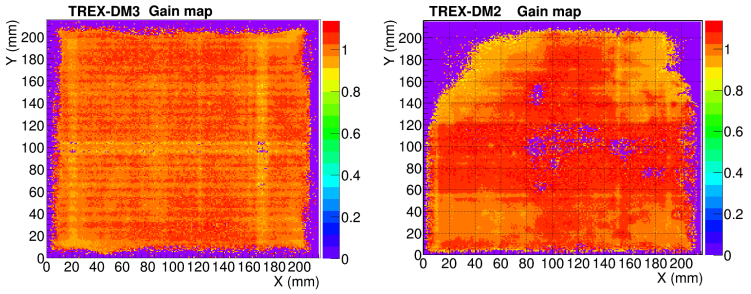

Figure 13.14: Relative gain over the over the TREX-DM3 (left) and TREX-DM2 (right) detector surface, which has been histogrammed in 216×216 bins, in Ar+2%iC$_4$H$_{10}$ at 2 bar.

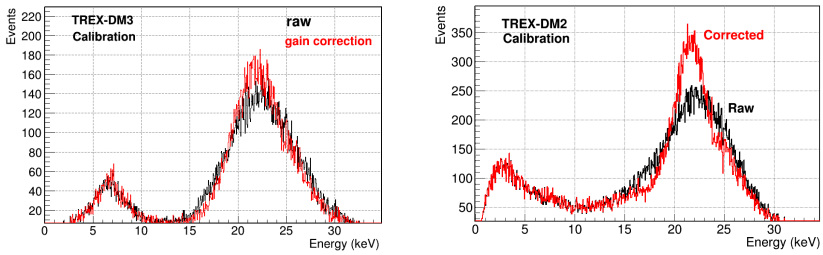

Figure 13.15: Energy spectrum before and after gain calibration. The improvement in energy resolution is modest in TREX-DM3, but considerable in TREX-DM2, due to the poorer gain uniformity of the later.

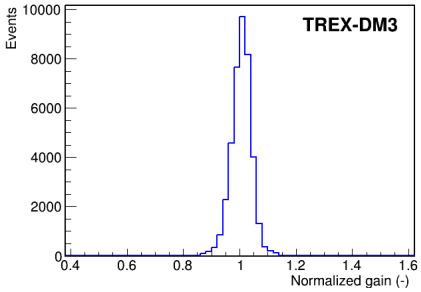

Figure 13.16: Relative gain weighted by the number of events per detector cell. The detector surface has been divided in 216×216 cells.

13.4.2 Background

Several background runs were taken in TREX-DM during the first months of 2015 in Ar+2%iC$_4$H$_{10}$ at 2 bar. The background trigger rate at surface is dominated by cosmic muons and environmental gamma rays. Several hand-picked examples of background events are shown in figure 13.17, where the xz and yz projections has been reconstructed using the collection of waveforms generated in the strips. Muons usually produce long straight ionization tracks, sometimes with a δ-ray at some point of the track. The tracks produced by δ-rays and γ-induced electrons are usually curved, presenting an increase in the ionization density towards the end of the track as a result of the Bethe-Bloch rise (Bragg peak).

The analysis method is an extension of the one used for the CAST Micromegas detectors. The ^{109}Cd calibrations are used as reference for defining the characteristics and parameters of

point-like events, and the cuts are generated from these data sets. In particular, two energy regions have been defined: the 8 keV and the 22 keV peaks are used to produce the cuts below and above 14 keV, respectively. Some calibration and background observables are compared in figure 13.18. Background events typically present larger and more asymmetric tracks in the three spatial directions.

The measured background spectrum acquired during 37.23 hours is shown in figure 13.19. The black line (raw) denotes all registered events that survived some preliminary quality cuts (4.05×10^5 events), the pink line represents a fiducialization that excludes the first 2 cm around the detector edges (defining an fiducial volume of (15 cm$\times$17.6$\times$17.6 cm^3)), and the blue line represents the population of events (2.5×10^4 events) surviving the discrimination cuts at a signal efficiency of 85%. The average background level in the 0-100 keV energy range is $(6.00\pm0.04)\times10^{-6}$ keV^{-1}cm^{-2}s^{-1}. The detector effective mass is 16 grams, so the background level is equivalent to $(1.004\pm0.007)\times10^4$ keV^{-1}kg^{-1}d^{-1}, a factor 100 larger than the conservative TREX-DM goal (see figure 12.3).

The main background contribution at surface and without shielding are μ– and γ–induced events. Muons leave typically a low-density ionization track with a possible δ–ray at some point along this track. If the main ionization track lies below threshold, only the δ–ray is detected, which is indistinguishable from an x-ray of the associated energy. Furthermore, muons excite the atoms of the TPC components producing fluorescence emissions that can reach the active volume. In the LSC, the muon flux is reduced by a factor 10^3–10^4, so in first approximation, its contribution should be reduced by that factor. This reduction could be enhanced by the use of active cosmic shielding. On the other hand, high energy environmental γ-rays can pass through the 6 cm-thick vessel and reach the active volume (or surrounding components), where they can be absorbed by virtue of photoelectric effect or they can interact via Compton scattering. The installation of a 10–15 cm-thick lead wall around the vessel will attenuate the external environmental γ of larger energy (2.6 MeV) to 0.6–0.04% of the flux without the lead shielding. Again, assuming a linear relation between flux and background level, the last will be reduced by more than a factor 100, showing good prospects for the achievement of the target levels.

The distribution of the background hits over the detector plane is shown in figure 13.20 before and after the application of the selection cuts. Background events tend to accumulate towards the detector edges before cuts. This is also true for the population of events that survive to the discrimination cuts in the 0-100 keV energy range, although it is a small effect. The background level in this energy region decreases monotonically towards the detector center, being reduced to $\sim 5\times10^{-6}$ in the 57.8 cm^2 squared area around the detector center.

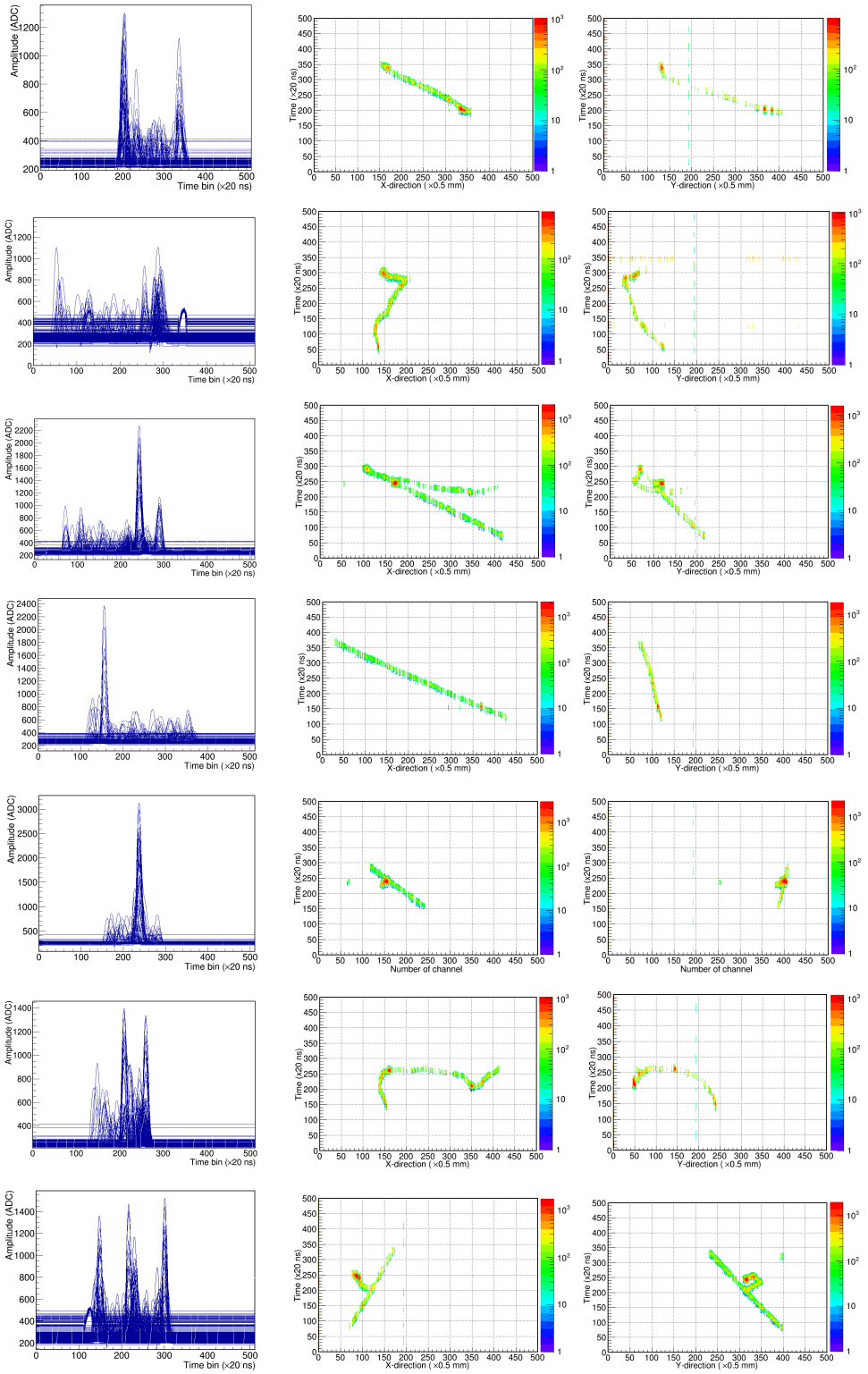

Figure 13.17: Strip pulses and 2D projections in the xz & yz planes of background events registered by TREX-DM in Ar+2%iC_4H_{10} at 2 bar.

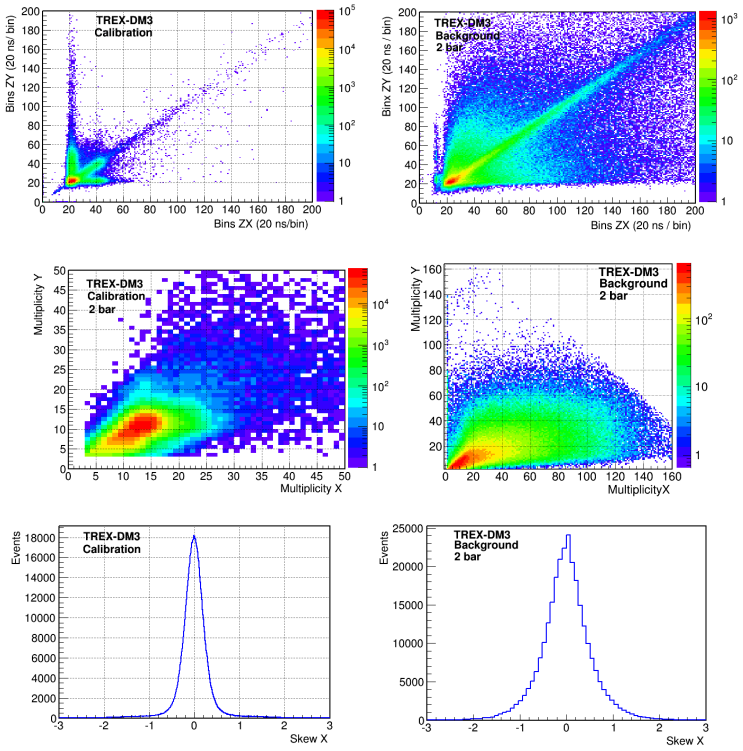

Figure 13.18: Comparison of some calibration and background observables.

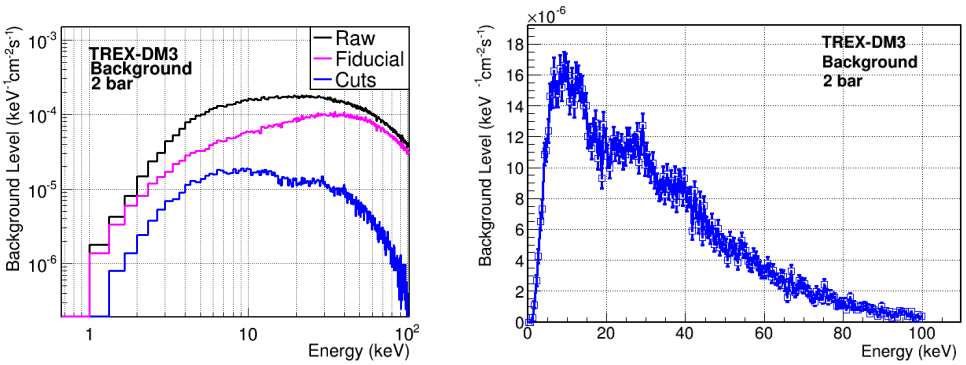

Figure 13.19: Background energy spectrum of TREX-DM in Ar+2%iC_4H_{10} at 2 bar before and after the application of the cuts.

13.5 Prospects

There are several upgrades, commissioning and characterization activities to take place in the near future. Firstly, a general characterization in argon-isobutane mixture at different mass ratios will be done, including the study of the charge cluster properties as a function of the TPC pressure. The performance in neon-based mixtures will also be studied, as larger gains and lower thresholds could be achieved in such mixtures as a result of a more efficient avalanche multiplication process (i.e., higher ionization yield) in lighter gases [276]. Works are being carried out in the detector and signal grounding in order to reduce the electronic noise level. Finally, we expect that the use of AGET-based electronics will allow to achieve the goal energy thresholds.

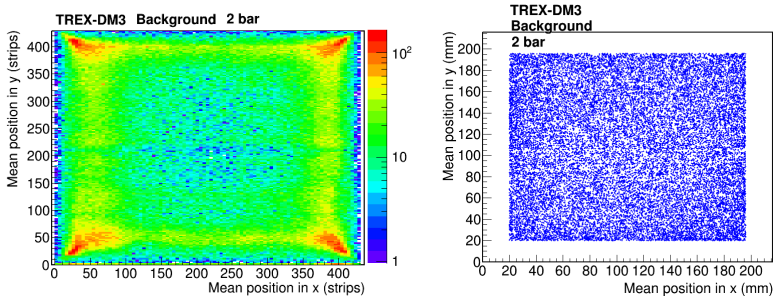

Figure 13.20: Background hitmap before (left) and after (right) the application of the cuts. Raw background events tend to concentrate towards the detector edges, while the final background distribution is more homogeneous.

In the short-term, some of the TREX-DM components will be replaced by radiopure ones, mainly, the Micromegas detectors, flat cables and multi-pin signal connectors (see section 12.3.9), after which all the components will be cleaned following underground prescriptions. Besides, the high-voltage cables inside the vessel will be replaced by radiopure ones, which will include better plastic isolation to avoid spark production. The automatic calibration system will be verified and a bake-out system will be fabricated to further reduce the outgassing rate. The setup will also be modified in order to leave room for a $\gtrsim$10 cm thick lead shielding. The possible installation at the LSC in 2016–17 for a physics run is still in study, and will strongly depend on the results achieved during the surface tests. The detection of WIMPs or, in the absence of a signal, the limits to the WIMP-nucleon cross-section will require a precise measurement of the quenching factor at keV energies, since few literature exists at these energies, specially for gases.

Appendix A

Electronic chain of Gassiplex and AFTER readout systems in CAST

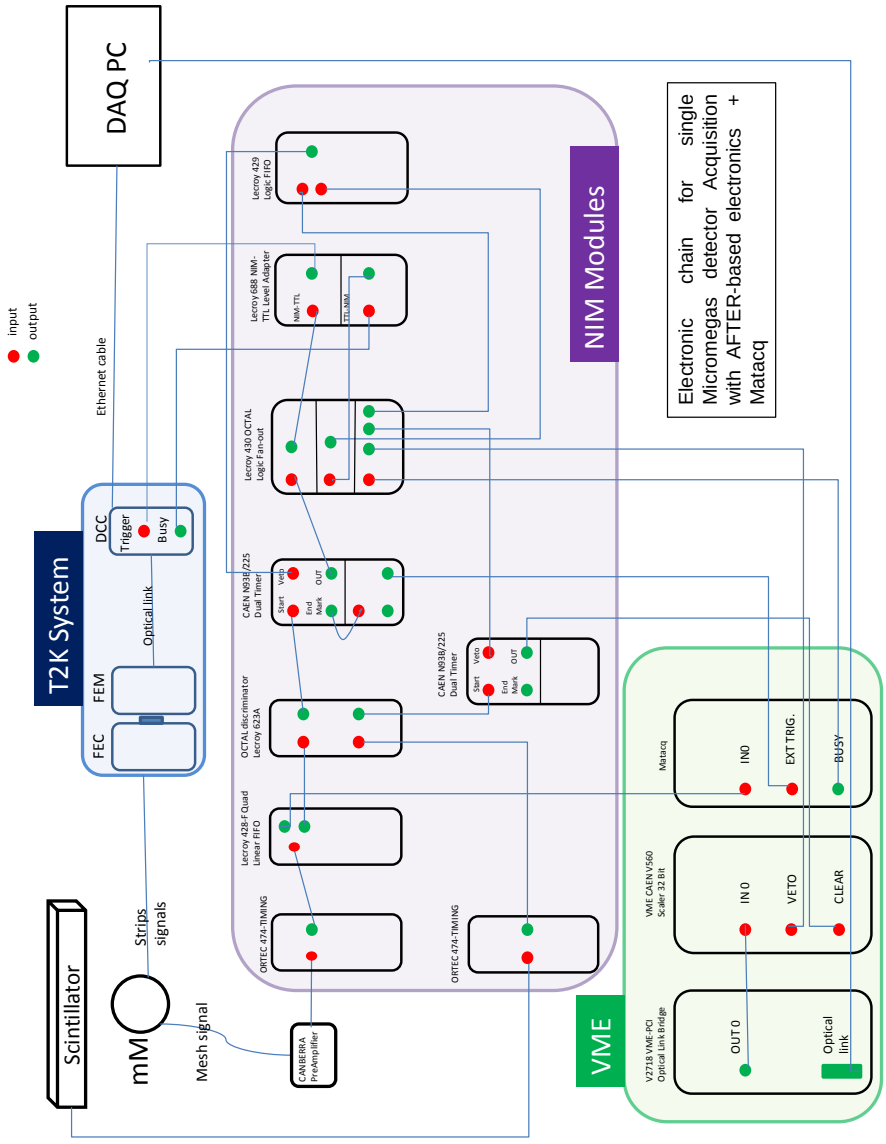

Figure A.1: The electronics chain of a Micromegas detector with AFTER-based electronics and a scintillator veto.

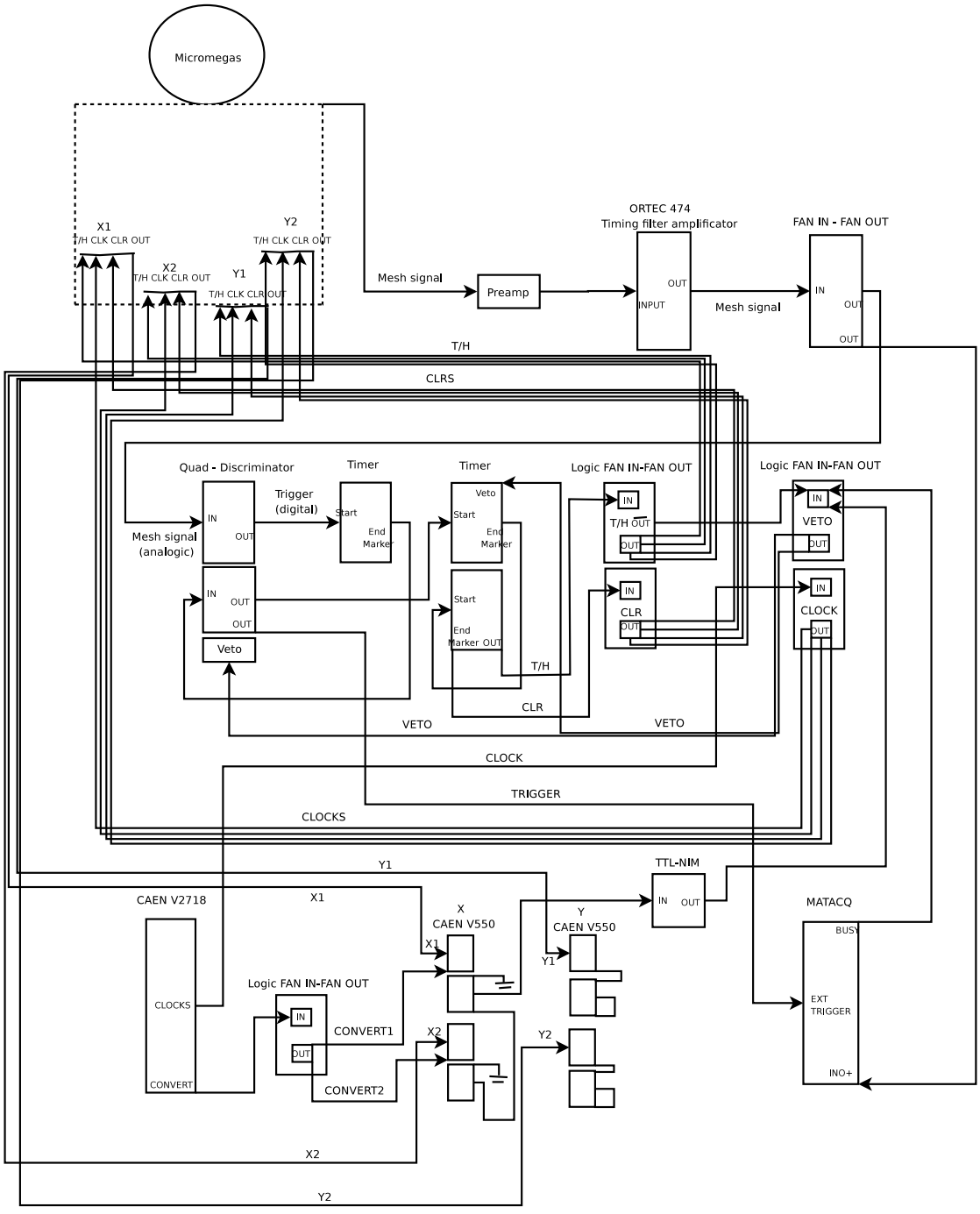

Figure A.2: The electronics chain of the sunset Micromegas with Gassiplex electronics.

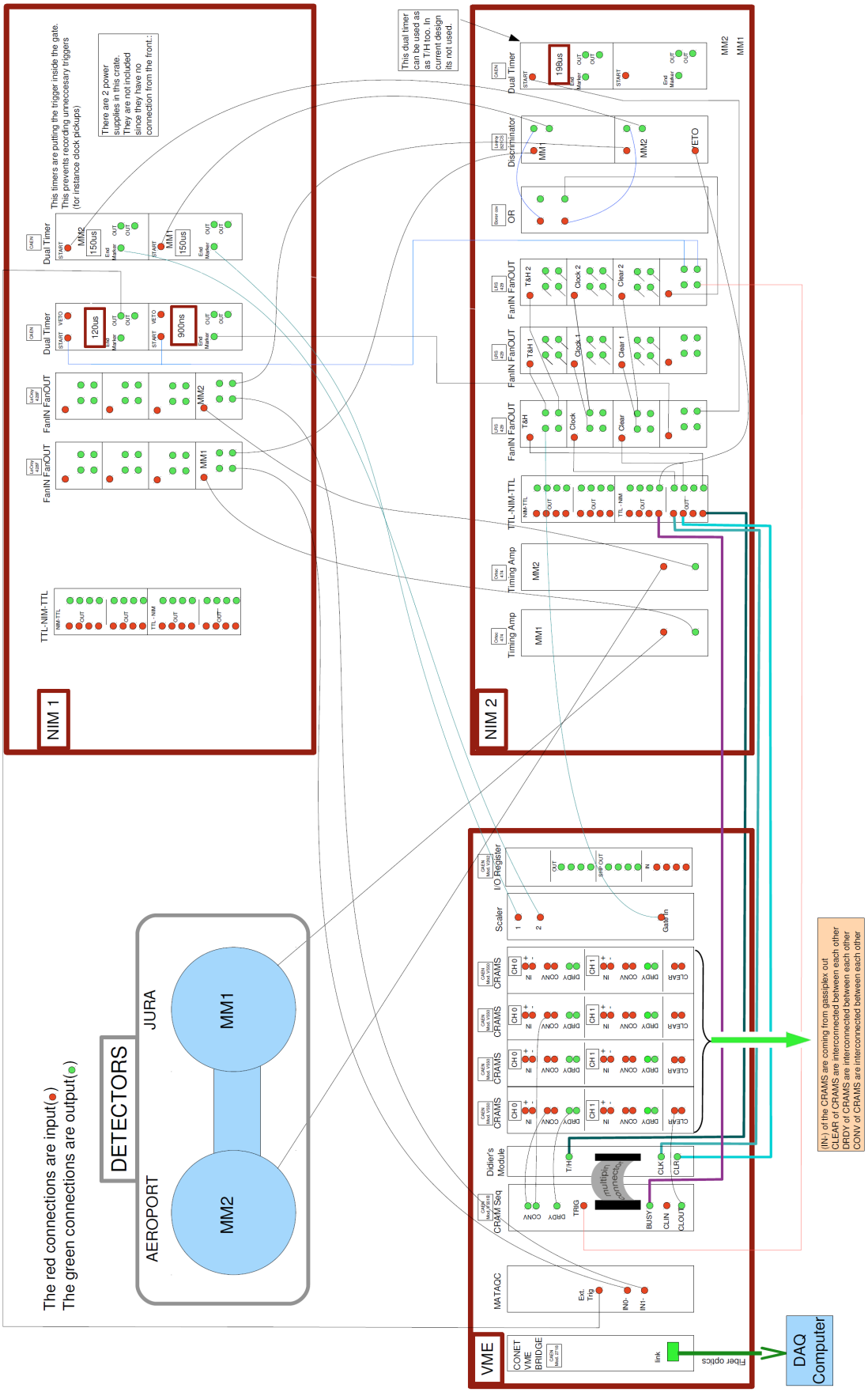

Figure A.3: The electronics chain of the sunset Micromegas with Gassiplex electronics.

Appendix B

Vacuum, leak tightness and pressure tests of x-ray windows

The x-ray windows of the vacuum system are 4 μm polypropylene foils. Since any tiny defect or imperfection in the foil itself or in the metallic surface (or in the strongback grid of the detector windows) where they are glued can produce the breakdown of the window, the are previously tested as part of the commissioning of the line. The requirements on the windows when pumped against atmospheric air are: a) reaching vacuum levels as low as 10^{-4} mbar b) leak rate (permeability to air) below 10^{-3} mbar·l/s.

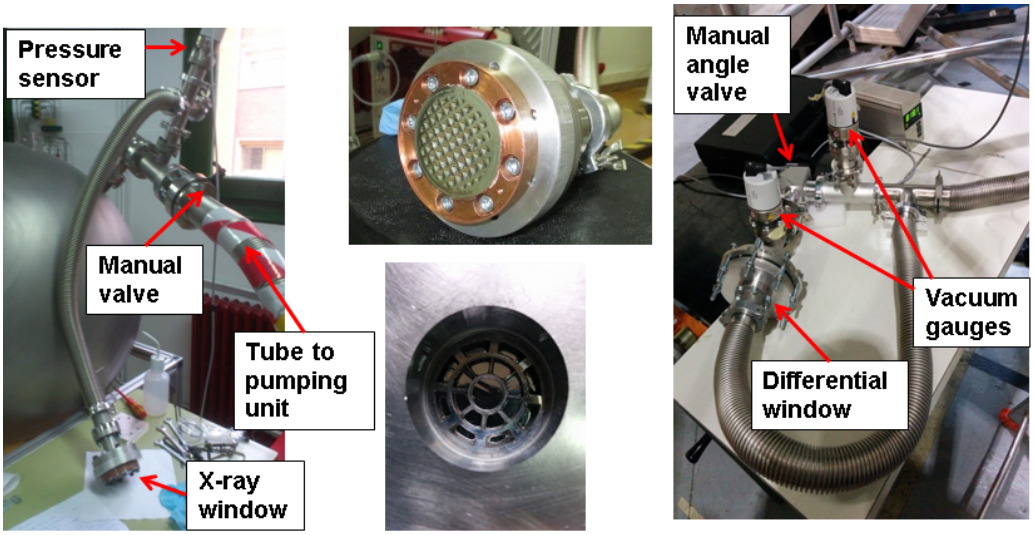

Figure B.1: Setup for the x-ray window leak tightness and vacuum studies (left), where both squared and spider-web *patterned windows (centre) have been tested. On the right, setup for the differential window test.*

Figure B.1 shows the experimental setup for the test of the x-ray windows. It consists in a *Pfeiffer* pumping unit (a primary and a turbomolecular pump) connected through a manual valve to the x-ray window to be tested. The pressure is monitored by a full-range vacuum gauge, and the leak rate can be measured by closing the manual valve present between the gauge and the pumping unit. Firstly, the system is characterized using a blank flange istead of a x-ray window. In this way, the vacuum and outgassing *background* vacuum levels are measured, resulting in $2.2{\cdot}10^{-6}$ mbar and $\lesssim 2{\cdot}10^{-5}$ mbar·l/s respectively. Then, the windows are tested in repeated pumping cycles to check any possible degradation with usage. In each cycle, the leak rate is measured by closing the manual valve that splits the pump and window volumes.

SRMM detector windows. Figures B.2 and B.3 show the permeability of two square and two *spider-web* patterned windows. The first ones routinely achieve vacuum levels as low as $4{\cdot}10^{-5}$ mbar after few minutes of pumping. The leak rate of *cathode-1* of figure B.2 increases

from $4{\cdot}10^{-4}$ mbar·l/s to $8{\cdot}10^{-4}$ mbar·l/s after the first pumping cycle, after which it stabilizes. In *cathode-2* a progressive increase in the leak rate is measured: from $6.6{\cdot}10^{-4}$ mbar·l/s to $1.2{\cdot}10^{-3}$ mbar·l/s.

The vacuum values and the leak rates measured are within the CAST specifications. However, the first window is selected for installation in a Micromegas chamber since the leak rate stabilizes after the first cycle. Meanwhile, the second x-ray window is kept as spare, since it is not clear whether it will continue degrading with more pumping cycles or the degradation will saturate at some point.

The *spider-web* windows were tested not only in vacuum but also in overpressure since windows with this innovative design had not been tested before. It was confirmed that both *cathode-1* and *cathode-2* can withstand more than the nominal CAST working pressures (i. e. 1.4 barg). The test consisted in putting 3 bara (2 barg) during some minutes into a gas buffer closed by the window and then bringing back the system to atmospheric pressure. The operation is repeated 4-5 times. Regarding the vacuum tests, the same procedure than for square-patterned grids is followed. Vacuum levels as good as $8.5{\cdot}10^{-6}$ mbar are achieved and leaking rates oscillating in the few 10^{-5} mbar·l/s range with no significant degradation. Therefore, CAST requirements are fulfilled.

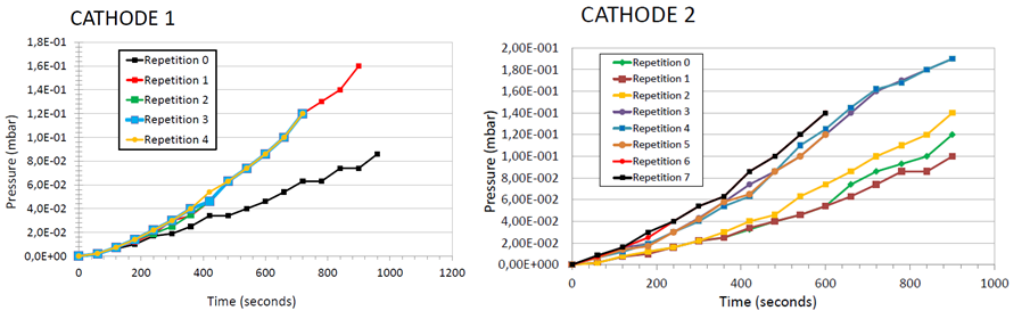

Figure B.2: Permeability to air of two SRMM square-patterned copper cathodes. Several vacuum-atmospheric cycles are performed in order to evaluate possible degradations with usage.

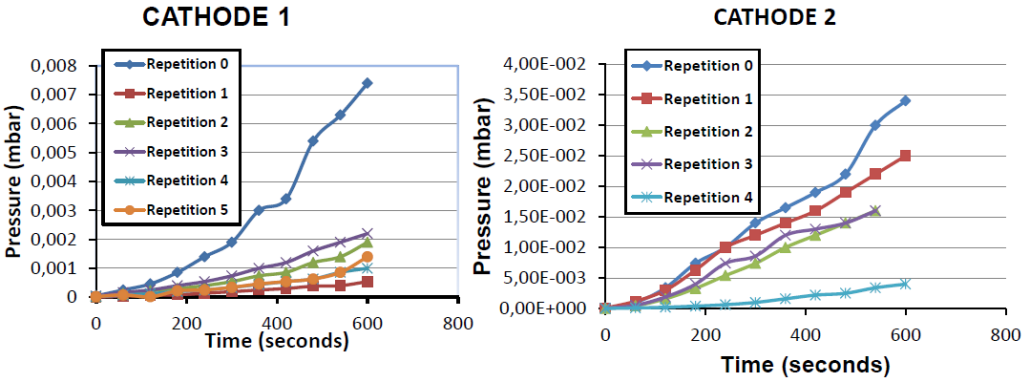

Figure B.3: Permeability to air of two SRMM spider-web *patterned cathodes. Several vacuum-atmospheric cycles are performed in order to evaluate possible degradations with usage.*

SSMM detector windows. The SSMM x-ray windows are tested following the same procedure described before for SRMM. Table B.1 summarizes the results of these tests. The table shows

Window	cycle	Time (min)	Pressure (mbar)	Permeability to air (mbar·l/s)
1	1	15	$1.4{\cdot}10^{-4}$	$7.3{\cdot}10^{-4}$
1	2	-	-	-
1	3	15	$1.3{\cdot}10^{-4}$	$6.3{\cdot}10^{-4}$
2	1	15	$1.2{\cdot}10^{-4}$	$5.3{\cdot}10^{-4}$
2	2	-	-	-
2	3	15	$1.1{\cdot}10^{-4}$	$4.3{\cdot}10^{-4}$
3	1	15	$1.7{\cdot}10^{-4}$	$3.0{\cdot}10^{-4}$
3	2	-	-	-
3	3	15	$1.6{\cdot}10^{-4}$	$2.0{\cdot}10^{-4}$

Table B.1: Vacuum test results of the SSMM x-ray windows.

that low enough vacuum levels are reached after short pumping periods, as well as low permeability to air.

Differential windows. The differential windows of the vacuum line enable the differential pumping of the volume close to the detector (affected by argon diffusion through the detector window) and the vacuum close to the gate valves and magnet. These windows do not have strongback as they do not support large pressure difference. However, they must withstand small pressure differences between good vacuum side ($\sim 10^{-6}$ mbar) and bad vacuum side ($\sim 10^{-6}$ mbar), and its permeation must be low ($\lesssim 10^{-4}$ mbar·l/s) to avoid cold-windows or contaminations The setup for testing these windows is shown on the right of figure B.1. The procedure consists in a) pumping both sides of the differential window at the same time (manual angle valve opened); b) isolating from the pump the small volume between the manual valve and one side of the differential window. The outgassing in this region produces a slow pressure increase, and thus a pressure difference between the sides of the window. Pressure differences up to 10^{-2} mbar were tested without window damage. The permeation is then measured by isolating the pump and monitoring the pressure increase in the *good vacuum side*. This value was quantified for two windows in $1.2{\cdot}10^{-5}$ mbar·l/s and $1.96{\cdot}10^{-6}$ mbar·l/s respectively.

Appendix C

The likelihood analysis method in CAST

Likelihood analysis methods need to be used in experiments with low statistics. In the second phase of CAST experiment the data taking was divided in density steps with very low statistics in each step. Here, we present the basic concepts of the binned likelihood method. The unbinned likelihood is derived from it and its mathematical equivalence is proved.

C.1 Binned likelihood analysis

First, we introduce some terminlogy and basic concpets that will be useful in the discussion of the analysis:

- In the following, the index k is used to denote density settings. The index i is reserved for the energy bins. n_{ik} is the total number of counts measured (i.e., detected) at density step k and energy bin i in axion-sensitive conditions. Note that n_{ik} may contain more than one solar tracking in case a density step k is repeated.
- The expected background level b_{ik} in the energy bin i and the density step k with which to feed the likelihood function is measured in-situ, contrarily to other rare event searches, e.g., WIMP direct detection experiments, which must estimate it from Montecarlo simulations. Here, b_{ik} is estimated from the full background data available. This can be done in several ways: average background over the full season, average background over some days before and after each solar tracking, the background of the day, tracking data at a pressure well away from the density step k, and others. The method here described does not fix this selection, so different background definitions can be checked for consistency and study of systematics.
- The expected signal for a given m_a is different at each density step. The analysis must differentiate the data taken at each step, but a single result from the full data set is wante: the exclusion curve $g_{a\gamma}(m_a)$ assuming absence of sigal. Likelihood functions provide an efficient way to account for the overlapping on the sensitivity of neighbouring density steps.

That said, for each density step k we build the likelihood function $\mathcal{L}_k$, assuming the counting rate follows poissonian statistics:

$$\mathcal{L}_k = \frac{1}{\mathcal{L}_{0k}} \prod_i e^{-\mu_{ik}} \frac{\mu_{ik}^{n_{ik}}}{n_{ik}!} \tag{C.1}$$

where $\mathcal{L}_{0k} = \prod_i e^{-n_{ik}} \frac{n_{ik}^{n_{ik}}}{n_{ik}!}$ is the appropriate normalization of the likelihood function in order to get goodness-of-fit information. This is, $\log \mathcal{L}$ behaves asymptotically as $-1/2\chi^2$.

μ_{ik} is the expected number of counts for the densitity step k and energy bin i, i.e., is the sum of the expected backround b_{ik} plus the theoretical axion signal s_{ik}, which depends on the theory parameters, m_a and $g_{a\gamma}$:

$$\mu_{ik} = b_{ik} + s_{ik}(g_{a\gamma}, m_a) \tag{C.2}$$

Note that the definition of the likelihood function reflects the proabability of measuring n_{ik} counts when the expected value is μ_{ik}. The theoretical signal s_{ik} is calculated as

$$s_{ik} = \int_{E_i}^{E_i+\Delta E} \frac{d\Phi_a}{dE} P_{a\to\gamma} A\ \varepsilon_d\ \Delta t_k\ dE \tag{C.3}$$

where $\frac{d\Phi_a}{dE}$ is the differential axion flux (see equation 3.10), $P_{a\to\gamma}$ is the conversion probability (see equation 3.13), A is the magnet bore area, ε_d is the detector efficiency curve, Δt_k is the exposures of the density step k and ΔE is the energy bin size.

Once $\mathcal{L}_k(g_{a\gamma}, m_a)$ is built, a partial result of step k can be obtained as follows. For a fix value of m_a, we maximize $\mathcal{L}_k(g_{a\gamma}, m_a)$ (or $\log \mathcal{L}_k = -1/2\chi^2_{m_a}$), and we get the best fit value for the coupling constant for that mass value, $(g^4_{a\gamma})_{\min}$. The confidence interval can be estimated as

$$\log \mathcal{L}_k(g_{\text{interval}}) = \log \mathcal{L}_{k,\max} - 1/2 \tag{C.4}$$

Assuming no signal is found, the upper limit can be estimated by integrating the Bayesian probability on g^4 over the physical region (positive values) till getting the 95% of it:

$$\frac{\int_0^{g^4_{95}} P(g^4) dg^4}{\int_0^{\infty} P(g^4) dg^4} = 0.95 \tag{C.5}$$

Here, the Bayesian probability is identified as the likelihood function, which implies that a prior probability flat on g^4 has been assumed. A single value g^4_{95} is obtained for each m_a. By looping on m_a one gets the full contour exclusion line $g_{a\gamma}(m_a)$. This contour line is obtained for each $\mathcal{L}_k$ so it would have a resonance at the axion mass corresponding to the density step ρ_k.

Although one could simply take the envelope of the individual contour lines in order to combine two or more density steps, a much more appropriate approach to combine all data consist in building the overall likelihood function by simply multiplying all $\mathcal{L}_k$:

$$\mathcal{L} = \prod_k \mathcal{L}_k \tag{C.6}$$

The maximization and integration method described above can be skipped for each L_k and done directly on L. The final upper limit contour is thus obtained and takes automatically into account the fact the neighbouring steps contribute partially to the same axion mass.

The data from the different detectors d can be commined following the same philosophy:

$$\mathcal{L}_{\text{total}} = \prod_d \mathcal{L}_d \tag{C.7}$$

C.2 Unbinned likelihood analysis

The unbinned likelihood method is motivated by the low statistics in each density steps and because it better takes into account the density variations within a density step k. The method relies then in the continuous monitorization of the pressure and temperature of the magnet cold bore.

Here, instead of calculating the likelihood function for each density step, it is calculated for infinitesimal time bins, in which one may detect eihter zero or one tracking counts ($n = 0, n = 1$). The likelihood can be written as

$$\mathcal{L} = \prod_k \mathcal{L}_k(n=0) \prod_l \mathcal{L}_l(n=1) \tag{C.8}$$

where k and l run over the event counts with zero and one count, respectively. Recalling our definition of the likelihood function in equation C.1, the expected number of counts in equation C.2 and letting apart constant terms that won't contribute to the final result (they would be cancelled in equation C.5), the log-likelihood function is expressed as:

$$\log \mathcal{L} = -\sum_i \sum_{k'} b_{ik'} - \sum_i \sum_{k'} s_{ik'}(g_{a\gamma}, m_a) + \sum_i \sum_l \log\left(b_{il} + s_{il}(g_{a\gamma,m_a})\right) \tag{C.9}$$

where k' runs over all the time bins and l over all the trackgin counts. The first term can be disregarded as it does not depend on $g_{a\gamma}$ and it is cancelled in the obention of the 95% of the Bayesina probability (see equation C.5). The second termn I_1 can be simply written as

$$I_2 = -\sum_{k'}\sum_{i}\int_{E_i}^{E_i+\Delta E}\frac{d\Phi_a}{dE}P_{a\to\gamma}A\;\varepsilon_d\;\Delta t_{k'}\;dE \tag{C.10}$$

which in the limit $\Delta t_{k'} \to 0$ it is the total number of expected counts from axion to photon conversion over all exposure time (i.e, tracking time) and energy (R_T):

$$I_2 = R_T = -\int_t\int_E\frac{d\Phi_a}{dE}P_{a\to\gamma}A\;\varepsilon_d\;dt\;dE \tag{C.11}$$

On the other hand, the third term in equation C.9 I_3 is:

$$I_3 = \sum_{i}\sum_{l}\left(\log\left[\frac{\Delta b_{il}}{\Delta t_l}+\frac{s_{il}}{\Delta t_l}\right]+\log\Delta t_l\right) \tag{C.12}$$

Here, the last term can be disregarded, while the first is written as the sum over the l detected tracking counts for an expected rate $R(t,E)$ as a function of the event time and energy:

$$I_3 = \sum_{l}\log R(t_l,E_l) = \sum_{l}\log\int_{E_i}^{E_i+\Delta E}\left(\frac{db_{il}}{dt_l}+\frac{d\Phi_a}{dEdt_l}P_{a\to\gamma}A\;\varepsilon_d\;dt_l\right)dE \tag{C.13}$$

Finally, combining equations C.11 and C.13 we get the overall likelihood function

$$\log\mathcal{L} \propto -R_T + \sum_{l}\log R(t_l,E_l) \tag{C.14}$$

which is used in chapters 8 and 9for the extraction of the 95% confidence level exclusion curve $g_{a\gamma}(m_a)$ with the ^{4}He 2012 and vacuum 2013 data sets.

Bibliography

[1] M. J. Berger *et al.*, XCOM: Photon Cross Sections Database, National Institute of Standarts and Technology (NIST). 4, 7

[2] Center for X-ray Optics and Advanced Light Source, Lawrence Berkeley National Laboratory, X-ray data booklet, http://xdb.lbl.gov. 4

[3] W. F. Frey *et al.*, K-Series Fluorescence Yields of Vanadium, Manganese, and Neon, *Phys. Rev.* **113** (1959) 1057. 5

[4] M. Hribar *et al.*, The determination of the K-shell fluorescence yield of xenon by use of the proportional counter method, *Zeitschrift fur Physik A: Atoms and Nuclei* **280** (1977) 227. 5

[5] M. Hribar *et al.*, The study of the L-shell fluorescence yields of xenon, *Physica B+C* **92** (1977) 143. 5

[6] C. Amsler *et al.* (Particle Data Group Collaboration), Review of Particle Physics, 2008-2009. Review of Particle Properties *Phys. Lett. B* **667** (2008). 8, 9, 10, 11, 13

[7] M. Lindhard *et al.*, *Mat. Fys. Medd.* **33** (1963). 8

[8] M. Chefdeville, Development of Micromegas-like gaseous detectors using a pixel readout chip as collecting anode, PhD Thesis, University of Amsterdam, 2009. 9, 13

[9] Wikipedia encyclopedy, Sopping power (particle radiation), http://en.wikipedia.org. 9

[10] I. B. Smirnov, Modeling of ionization produced by fast charged particles in gases, *Nucl. Instrum. Meth. A* **554** (2005) 474. 11

[11] S. N. Ahmed, Physics and Engineering of Radiation Detection, Elsevier (2007). 11

[12] H. J. Hilke, Time projection chambers, *Reports on Progress in Physics* **73** (2010) 116201. 12, 13, 15

[13] U. Fano, Ionization Yield of Radiations. The Fluctuations of the Number of Ions *Phys. Rev.* **72** (1947) 26. 13

[14] H. Schindler *et al.*, Calculation of gas gain fluctuations in uniform fields, *Nucl. Instrum. Meth. A* **624** (2010) 78. 14

[15] A. Andronic *et al.*, Drift velocity and gain in argon- and xenon-based mixtures, *Nucl. Instrum. Meth. A* **523** (2004) 302. 15

[16] P. Colas *et al.*, Electron drift velocity measurements at high electric fields, *Nucl. Instrum. Meth. A***478** (2002) 215. 15

[17] J. C. Bowe, Drift Velocity of Electrons in Nitrogen, Helium, Neon, Argon, Krypton, and Xenon, *Phys. Rev.* **117** (1960) 1411. 15

[18] D. C. Herrera, Development of a Micromegas Time Projection Chamber in Xe-based Penning Mixtures for Rare Event Searches, PhD Thesis, Universidad de Zaragoza, 2014. 15, 22

[19] F. Iguaz, Development of a Time Projection Chamber prototype with Micromegas technology for the search of the Double Beta Decay of ^{136}Xe, PhD Thesis, Universidad de Zaragoza, 2010. 22, 163

[20] T. Dafni *et al.*, Energy resolution of alpha particles in a microbulk Micromegas detector at high pressure Argon and Xenon mixtures, *Nucl. Instrum. Meth. A***608** (2009) 259. 22

[21] L. G. Christophorou *et al.*, Electron-attachment processes in Electron-Molecule interactions and their applications, Academic Press (1984). 16

[22] D. L. McCorkle *et al.*, Electron attachment rate constants and cross-sections for halocarbons, Proc. Second International Swarm Seminar, Oak Ridge (USA), 1981. 16

[23] H. Shimamori and H. Hotta, Mechanism of thermal electron attachment to O_2 : Isotope effect studies with $^{18}O_2$ in rare gases and some hydrocarbons, *J. Chem Phys.* **81** (1984). 16

[24] M. Huk *et al.*, Electron attachment to oxygen, water and methanol in various drift chamber gas mixtures, *Nucl. Instrum. Meth. A***267** (1988). 16

[25] M. E. Rose *et al.*, An Investigation of the Properties of Proportional Counters, *Phys. Rev.* **59** (1941) 850. 17, 109

[26] W. Diethorn, A methan proportional counter system for natural radiocarbon measurements, UASEC Report NY06628, 1956. 17

[27] A. Tomas, Development of Time Projection Chambers with Micromegas for Rare Event Searches, PhD Thesis, Universidad de Zaragoza, 2013. 17, 158, 163

[28] J. Derre *et al.*, Fast signals and single electron detection with a MICROMEGAS photodetector, *Nucl. Instrum. Meth. A***449** (2000) 314. 18

[29] J. Byrne, Statistics of the electron multiplication process in proportional counters, Proc. R. Soc. Edinburgh, XVI A 33, 1962. 18

[30] G. D. Alkhazov, Statistics of electron avalanches and ultimate resolution of proportional counters, *Nucl. Instrum. Meth. A***89** (1970) 155. 18

[31] S. Cebrian *et al.*, Micromegas readouts for double beta decay searches, *JCAP* **1010** (2010) 010. 18

[32] F. J. Iguaz *et al.*, New developments in Micromegas Microbulk detectors, *Phys. Procedia* **37** (2012) 448. 18, 214

[33] W. Shockley, Currents to Conductors Induced by a Moving Point Charge, *J. Appl. Phys.* **91** (1938). 19

[34] S. Ramo, Currents Induced by Electron Motion, *Proc, IRE* **27** (1939). 19

[35] Wikipedia encyclopedy, Micromegas detector, http://en.wikipedia.org. 19

[36] W. Riegler, Induced signals in resistive plate chambers, *Nucl. Instrum. Meth. A***491** (2002) 258. 20

[37] G. Charpak *et al.*, The use of multiwire proportional counters to select and localize charged particles, *Nucl. Instrum. Meth. A***62** (1968) 262. 20

[38] W. Blum *et al.*, Particle detectors with drift chambers, Springer, 2008. 20

[39] D. R. Nygren and J. N. Marx. The Time Projection Chamber, *Phys. Today* **31N10** (1978) 46. 20

[40] A. Oed, Position sensitive detector with microstrip anode for electron multiplication with gases, *Nucl. Instrum. Meth. A***263** (1988) 351. 20

[41] D. Mattern *et al.*, A New approach for constructing sensitive surfaces: The gaseous Pixel chamber, *Nucl. Instrum. Meth. A***300** (1991) 275. 20

[42] S. F. Biagi and T. J. Jones, The microdot gas avalanche chamber: an investigation of new geometries, *Nucl. Instrum. Meth. A***361** (1995) 72. 20

[43] F. Sauli, GEM: A new concept for electron amplification in gas detectors, *Nucl. Instrum. Meth.* **A386** (1997) 531. 20

[44] Y. Giomataris *et al.*, MICROMEGAS: A high-granularity position-sensitive gaseous detector for high particle-flux environments, *Nucl. Instrum. Meth. A***376** (1996) 29. 20, 21, 196

[45] M. Chefdeville *et al.*, An electron-multiplying Micromegas grid made in silicon wafer post-processing technology, *Nucl. Instrum. Meth. A***556** (2006) 490. 20

[46] A. Di Mauro *et al.*, Development of innovative micro-pattern gaseous detectors with resistive electrodes and first results of their applications, *Nucl. Instrum. Meth. A***581** (2007) 225. 20

[47] RD51 Collaboration, http://rd51-public.web.cern.ch. 21

[48] T. Franke and V. Peskov, Innovative applications and developments of Micro-Pattern gaseous detectors, Engineering Science Reference, IGI Global, 2014. 21, 24

[49] D. Neyret *et al.*, New pixelized Micromegas detector for the COMPASS experiment, *JINST* **4** (2009) 12004. 21

[50] B. Peyaud *et al.*, KABES: A novel beam spectrometer for NA48, *Nucl. Instrum. Meth.* *A***535** (2004) 247. 21

[51] S. Andriamonje *et al.* (N-TOF Collaboration), The MICROMEGAS neutron detector for CERN n-TOF, *Nucl. Phys. B* (2002). 21

[52] G. Vasseur *et al.*, Operation of the T2K time projection chambers *JINST* **7** (2012) C02040. 21

[53] G. Charles *et al.*, Micromegas detectors for CLAS12, *Nucl. Instrum. Meth.* *A***718** (2013) 414. 21

[54] A. Zibell *et al.*, Micromegas detectors for the upgrade of the ATLAS muon spectrometer, *JINST* **9** (2014) C08013. 21

[55] A. Delbart *et al.*, New developments of Micromegas detector, *Nucl. Instrum. Meth.* *A***461** (2001) 84. 21

[56] I. Giomataris *et al.*, Micromegas in a bulk, *Nucl. Instrum. Meth.* *A***560** (2006) 405. 21, 23, 196

[57] S. Andriamonje *et al.*, Development and performance of Microbulk Micromegas detectors, *JINST* **5** (2010) P02001. 21, 22, 196

[58] Y. Giomataris, Development and prospects of the new gaseous detector Micromegas, *Nucl. Instrum. Meth.* *A***419** (1998) 239. 23

[59] T. Alexopoulos *et al.*, The ATLAS muon Micromegas R&D project: towards large-size chambers for the s-LHC, *JINST* **4** (2009) P12015. 24

[60] I. G. Irastorza *et al.*, Status of R&D on Micromegas for Rare Event Searches : The T-REX project, *EAS Publications Series* /bf 53 (2012) 147. 24

[61] R. D. Peccei and H. R. Quinn, CP conservation in the Presence of Instantons, *Phys. Rev. Lett.* **38** (1977) 1440. 28, 31

[62] R. D. Peccei and H. R. Quinn, Constraints imposed by CP conservation in the presence of instantons, *Phys. Rev. D* **16** (1977) 1791. 28, 31

[63] S. Weinberg, A New Light Boson?, *Phys. Rev. Lett.* **40** (1978) 223. 28, 31, 34

[64] F. Wilczek, Problem of Strong P and T Invariance in the Presence of Instantons, *Phys. Rev. Lett.* **40** (1978) 279. 28, 31, 34

[65] P. Svrcek and E. Witten, Axions in string theory, *JHEP* **06** (2006) 051. 28, 35

[66] M. Gell-Mann, Symmetries of baryons and mesons, *Phys. Rev.* **125** (1962) 1067. 28

[67] R. P. Feynman, The Behavior of Hadron Collisions at Extreme Energies, High Energy Collisions: Third International Conference at Stony Brook, 1969. 28

[68] D. Gross and F. Wilczek, Ultraviolet behavior of non-abelian gauge theories, *Phys. Rev. Let* **30** (1973) 1343. 28

[69] S. Weinberg, The U(1) Problem, *Phys. Rev. D* **11** (1975) 3583. 29

[70] G. 't Hooft, Computation of the Quantum Effects Due to a Four-Dimensional Pseudoparticle, *Phys. Rev. D* **14** (1976) 3423. 29

[71] G. 't Hooft, Symmetry Breaking Through Bell-Jackiw Anomalies, *Phys. Rev. Lett.* **37** (1976) 8. 29

[72] J. Beringer *et al.* (Particle Data Group Collaboration), Review of Particle Physics, *Phys. Rev. D* **86** (2012) 010001. 30

[73] J. S. Schwinger, The Theory of quantized fields, *Phys. Rev.* **91** (1953) 713. 30

[74] G. Luders, On the Equivalence of Invariance under Time Reversal and under Particle-Antiparticle Conjugation for Relativistic Field Theories, *Kong. Dan.Vid. Sel. Mat. Fys. Med.* **28N5** (1954) 1. 30

[75] V. Baluni, The Status of CPT, *Phys. Rev. D* **19** (1969) 2227. 30

[76] R. Crewthter *et al.*, Chiral estimate of the electric dipole moment of the neutron in quantum chromodynamics *Phys. Lett. B* **88** (1979) 123. 30

[77] M. Pospelov and A. Ritz, Electric dipole moments as probes of new physics, *Annals Phys.* **318** (2005) 119. 30

[78] C. Baker *et al.*, Improved Experimental Limit on the Electric Dipole Moment of the Neutron, *Phys. Rev. Lett.* **97** (2006) 131801. 30

[79] H. Leutwyler, The ratios of the light quark masses *Phys. Lett. B* **378** (1996). 32

[80] J. Gasses and H. Leutwyler , Quark masses, *Phys. Rept.* **87** (1984). 32

[81] J. E. Kim, Weak-Interaction Singlet and Strong CP Invariance, *Phys. Rev. Lett.* **43** (1979) 103. 32, 34

[82] A. R. Zhitnitsky, On Possible Suppression of the Axion Hadron Interactions, *Sov. J. Nucl. Phys.* **31** (1980) 260. 32, 35

[83] M. Dine *et al.*, A Simple Solution to the Strong CP Problem with a Harmless Axion, *Phys. Lett. B* **104** (1981) 199. 32, 35

[84] S. L. Cheng *et al.*, Axion-photon couplings in invisible axion models, *Phys. Rev. D* **52** (1995) 3132. 32

[85] G. Raffelt, Astrophysical axion bounds, *Lect. Notes Phys.* **741** (2008) 51. 32, 37, 39

[86] S. M. Turner, Windows on the Axion, *Phys. Rept.* **197** (1990) 67. 33

[87] W. A. Bardeen *et al.*, Constraints on variant axion models, *Nucl. Phys. B* **279** (1987) 401. 34

[88] Y. Asano *et al.*, Search for a Heavy Neutrino Emitted in $K^+ \to \mu^+$ Neutrino Decay, *Phys. Lett. B* **104** (1981) 84. 34

[89] M. A. Shifman *et al.*, Can Confinement Ensure Natural CP Invariance of Strong Interactions?, *Nucl. Phys. B* **166** (1980) 493. 34, 133

[90] Y. Chikashige *et al.*, Are There Real Goldstone Bosons Associated with Broken Lepton Number?, *Phys. Lett. B* **98** (1981) 265. 35

[91] A. E. Nelson and N. Seiberg, R symmetry breaking versus supersymmetry breaking, *Nucl. Phys. B* **416** (1994) 46. 35

[92] J. Jaeckel and A. Ringwald, The Low-Energy Frontier of Particle Physics, *Ann. Rev. Nucl. Part. Sci.* **60** (2010) 405. 35, 37

[93] R. Essig *et al.*, Working Group Report: New Light Weakly Coupled Particles, Community Summer Study 2013: Snowmass on the Mississippi (CSS2013) Minneapolis, USA, 2013. 36

[94] S. Hannestad *et al.*, Neutrino and axion hot dark matter bounds after WMAP-7 *JCAP* **8** (2010) 1. 36

[95] D. Cadamuro *et al.*, Cosmological bounds on sub-MeV mass axions, *JCAP* **1102** (2011) 3. 36

[96] D. Cadamuro *et al.*, Cosmological bounds on sub-MeV mass axions, *JCAP* **1102** (2011) 003. 36

[97] P. Arias *et al.*, WISPy Cold Dark Matter *JCAP* **1206** (2012) 013. 37

[98] R. Adam *et al.* Planck 2015 results. Overview of products and scientific results, arXiv:1502.01582, 2015. 37, 178

[99] O. Wantz and E. P. S. Shellard, Axion Cosmology Revisited, *Phys. Rev. D* **82** (2010) 123508. 37

[100] P. Sikivie, Axion cosmology, Lect. Notes Phys. **741** (2008) 19. 37

[101] L. Visinelli and P. Gondolo, Axion cold dark matter in view of BICEP2 results, *Phys. Rev. Lett.* **113** (2014) 011802. 37

[102] H. Schlattl *et al.*, Helioseismological constraint on solar axion emission, *Astropart. Phys.* **10** (1999) 353. 37

[103] J. N. Bahcall *et al.*, New solar opacities, abundances, helioseismology, and neutrino fluxes, *Astrophys. J.* **621** (2005) L85. 38

[104] G. Raffelt and D. S. P. Dearborn, Bounds on Weakly Interacting Particles From Observational Lifetimes of Helium Burning Stars, *Phys. Rev. D* **37** (1988) 549. 38

[105] A. Ayala *et al.*, Revisiting the Bound on Axion-Photon Coupling from Globular Clusters, *Phys. Rev. Lett.* **113** (2014) 191302. 38, 136

[106] A. Ayala *et al.*, Revisiting the Bound on Axion-Photon Coupling from Globular Clusters, *Phys. Rev. Lett.* **113** (2014) 191302. 38, 40

[107] G. Raffelt, Particle Physics from Stars, *Ann. Rev. Nucl. Part. Sci.* **49** (1999) 163. 38

[108] A. H. Corsico *et al.*, The Potential of the variable DA white dwarf G117 - B15A as a tool for fundamental physics, *New Astron.* **6** (2001) 197. 38

[109] A. Payez *et al.*, Revisiting the SN1987A gamma-ray limit on ultralight axion-like particles, *JCAP* **1502** (2015) 006. 39

[110] A. Friedland *et al.*, Constraining the Axion-Photon Coupling with Massive Stars, *Phys. Rev. Lett.* **110** (2013) 061101. 39, 55

[111] J. M. Overduin and P. S. Wesson, Dark matter and background light, *Phys. Rept.* **402** (2004) 267. 39

[112] D. Grin *et al.*, A Telescope Search for Decaying Relic Axions, *Phys. Rev. D.* **75** (2007) 105018. 39

[113] A. Boyarsky *et al.*, The Role of sterile neutrinos in cosmology and astrophysics, *Ann. Rev. Nucl. Part. Sci.* **59** (2009) 191. 39

[114] J. Isern *et al.*, Axions and the cooling of white dwarf stars, *Astrophys. J* **682** (2012) L109. 40

[115] B. Melendez *et al.*, Revisiting the Impact of Axions in the Cooling of White Dwarfs, 18th European White Dwarf Workshop (EUROWD 12) Krakow, Poland, 2012. 40

[116] A. H. Corsico *et al.*, The rate of cooling of the pulsating white dwarf star G117-B15A: a new asteroseismological inference of the axion mass, *MNRAS* **424** (2012) 2792. 40

[117] A. H. Corsico *et al.*, An independent limit on the axion mass from the variable white dwarf star R548, *JCAP* **12** (2012) 10. 40

[118] N. Viaux *et al.*, Neutrino and axion bounds from the globular cluster M5 (NGC 5904), *Phys. Rev. Lett.* **111** (2013) 231301. 40

[119] L. B. Leinson, Axion mass limit from observations of the neutron star in Cassiopeia A, *JCAP* **1408** (2014) 031. 40

[120] A. Abramowski *et al.*, Constraints on axionlike particles with H.E.S.S. from the irregularity of the PKS 2155-304 energy spectrum, *Phys. Rev. D* **88** (2013) 102003. 41

[121] J. P. Conlon *et al.*, Searching for a 0.1-1 keV Cosmic Axion Background, *Phys. Rev. Lett.* **111** (2013) 151301. 41

[122] S. Angus *et al.*, Soft X-ray Excess in the Coma Cluster from a Cosmic Axion Background, *JCAP* **1409** (2014) 026. 41

[123] P. Sikivie, Evidence for ring caustics in the Milky Way, *Phys. Lett. B* **567** (2003) 1. 41

[124] O. Erken *et al.*, Cosmic axion thermalization, *Phys. Rev. D* **85** (2012) 063520. 41

[125] J. Jaeckel *et al.*, A 3.55 keV hint for decaying axion-like particle dark matter, *Phys. Rev. D* **89** (2014) 103511. 41

[126] J. Redondo and A. Ringwald, Light shining through walls, *Contemp. Phys.* **52** (2011) 211. 41

[127] K. Ehret *et al.*, New ALPS Results on Hidden-Sector Lightweights, *Phys. Lett. B* **689** (2010) 149. 42

[128] R. Ballou *et al.*, Latest Results of the OSQAR Photon Regeneration Experiment for Axion-Like Particle Search, 10th Patras Workshop on Axions, WIMPs & WISPs (AXION-WIMP 2014), Geneva, Switzerland, 2014. 42

[129] P. Sikivie *et al.*, Resonantly enhanced axion-photon regeneration, *Phys. Rev. Lett.* **98** (2007) 172002. 42

[130] S. J. Asztalos *et al.*, An Improved RF Cavity Search for Halo Axions, *Phys. Rev. D* **69** (2004) 011101. 42

[131] A. Malagon *et al.*, Yale Microwave Cavity Experiment, 9th Patras Workshop on Axions, WIMPs, and WISPs, Mainz, Germany, 2013. 42

[132] D. Horns *et al.*, WISPers from the Dark Side: Radio Probes of Axions and Hidden Photons, 9th Patras Workshop on Axions, WIMPs & WISPs, Mainz, Germany, 2013. 43

[133] P. Sikivie *et al.*, Axion Dark Matter Detection using an LC Circuit, *Phys. Rev. Lett.* **112** (2014) 131301. 43

[134] J. Jaeckel and J. Redondo, An Antenna for Directional Detection of WISPy Dark Matter, *JCAP* **1311** (2013) 016. 43

[135] P. Sikivie, Experimental tests of the invisible axion, *Phys. Rev. Lett.* **51** (1983) 1415. 43

[136] K. vanBibber *et al.*, Design for a practical laboratory detector for solar axions, *Phys. Rev. D* **39** (1989) 2089. 43, 49

[137] D. M. Lazarus *et al.* A Search for solar axions, *Phys. Rev. Lett.* **69** (1992) 2333. 43

[138] S. Moriyama *et al.* (CAST Collaboration), Direct search for solar axions by using strong magnetic field and X-ray detectors, *Phys. Lett. B* **434** (1998) 147. 43, 55

[139] K. Zioutas *et al.*, A decommissioned LHC model magnet as an axion telescope, *Nucl. Instrum. Meth. A* **425** (1999) 480. 43, 53, 55

[140] K. Zioutas *et al.* (CAST Collaboration), First results from the CERN Axion Solar Telescope (CAST), *Phys. Rev. Lett.* **94** (2005) 121301. 44

[141] S. Andriamonje *et al.* (CAST Collaboration), Probing eV-scale axions with CAST, *JCAP* **0902** (2009) 008. 44, 47, 48

[142] E. Arik *et al.* (CAST Collaboration), Probing eV-scale axions with CAST *JCAP* **0902** (2009) 008. 44, 55

[143] S. Aune *et al.* (CAST Collaboration), CAST search for sub-eV mass solar axions with 3He buffer gas, *Phys. Rev. Lett.* **107** (2011) 261302. 44, 55

[144] M. Arik *et al.* (CAST Collaboration), CAST solar axion search with ^{3}He buffer gas: Closing the hot dark matter gap, *Phys. Rev. Lett.* **112** (2014) 091302. 44, 55

[145] M. Ahlers *et al.*, Light from the hidden sector, *Phys. Rev. D* **76** (2007) 115005. 44

[146] H. Gies *et al.*, Polarized Light Propagating in a Magnetic Field as a Probe of Millicharged Fermions, *Phys. Rev. Lett.* **97** (2006) 140402. 44

[147] E. Zavattini *et al.* (PVLAS Collaboration), Experimental observation of optical rotation generated in vacuum by a magnetic field, *Phys. Rev. Lett.* **96** (2006) 110406. 44

[148] Z. Ahmed *et al.* (CDMS Collaboration), Search for Axions with the CDMS Experiment, *Phys. Rev. Lett.* **103** (2009) 141802. 44

[149] R. Bernabei *et al.* (DAMA/LIBRA Collaboration), Search for solar axions by Primakoff effect in NaI crystals, *Phys. Lett. B* **515** (2001) 6. 44

[150] F. T. Avignone *et al.* (SOLAX Collaboration), *Phys. Rev. Lett.* **81** (1998) 5068. 44

[151] A. Morales *et al.* (COSME Collaboration), Particle Dark Matter and Solar Axion Searches with a small germanium detector at the Canfranc Underground Laboratory, *Astropart. Phys.* **16** (2002) 325. 44

[152] E. A. Paschos *et al.*, A Proposal for solar axion detection via Bragg scattering, *Phys. Lett. B* **323** (1994) 367. 44

[153] E. Aprile *et al.* (XENON100 Collaboration), First Axion Results from the XENON100 Experiment, *Phys. Rev. D* **90** (2014) 062009. 44

[154] K. Aber *et al.*, Search for solar axions in XMASS, a large liquid-xenon detector, *Phys. Lett. B* **724** (2013) 46. 44

[155] R. Essig *et al.*, Discovering New Light States at Neutrino Experiments *Phys. Rev. D* **82** (2010) 113008. 44

[156] S. Moriyama, A Proposal to search for a monochromatic component of solar axions using Fe-57, *Phys. Rev. Lett.* **75** (1995) 3222. 44

[157] D. Budker *et al.*, Proposal for a Cosmic Axion Spin Precession Experiment (CASPEr), *Phys. Rev. X* **4** (2014) 021030. 44

[158] A. Geraci *et al.* (Ariadne Collaboration), The Axion Resonant InterAction Detection Experiment (ARIADNE), APS April Meeting Abstracts, 6009, 2015. 44

[159] J. Redondo, Solar axion flux from the axion-electron coupling, *JCAP* **1312** (2013) 008. 46

[160] G. G. Raffelt, Astrophysical axion bounds diminished by screening effects, *Phys. Rev. D* **33** (1985) 897. 46, 47

[161] G. G. Raffelt, Plasmon Decay Into Low Mass Bosons in Stars, *Phys. Rev. D* **37** (1988) 1356. 47

[162] G. G. Raffelt and L. Stodolsky, Mixing of the Photon with Low Mass Particles, *Phys. Rev. D* **37** (1988) 1237. 48

[163] I. G. Irastorza *et al.*, Towards a new generation axion helioscope *JCAP* **1106** (2011) 013. 51, 52, 143

[164] I. G. Irastorza *et al.*, The International Axion Observatory IAXO. Letter of Intent to the CERN SPS committee. CERN-SPSC-2013-022. SPSC-I-242 (2013). 52

[165] I. Shilon *et al.*, Conceptual Design of a New Large Superconducting Toroid for IAXO, the New International AXion Observatory, *IEEE Trans. Appl. Supercond.* **22** (2012). 52

[166] M. Kuster *et al.*, The X-ray Telescope of CAST, *New. J. Phys.* **9** (2007) 170. 54, 68, 69, 70

[167] Y. Inoue *et al.*, Search for sub-electronvolt solar axions using coherent conversion of axions into photons in magnetic field and gas helium, *Phys. Lett. B* **536** (2002) 18. 55

[168] Y. Inoue *et al.*, Search for solar axions with mass around 1 eV using coherent conversion of axions into photons, *Phys. Lett. B* **668** (2008) 93. 55

[169] K. Barth *et al.* (CAST Collaboration), CAST constraints on the axion-electron coupling, *JCAP* **1305** (2013) 010. 56, 57

[170] S. Andriamonje *et al.* (CAST Collaboration), Search for solar axion emission from ^{7}Li and D(p,γ)^{3}He nuclear decays with the CAST gamma-ray calorimeter, *JCAP* **1003** (2010) 032. 56, 57

[171] T. Vafeiadis, Status of CAST and Solar Chameleon searches, Proceedings of 10th PATRAS Workshop on Axions, WIMPs and WISPs, CERN, Switzerland, 2014. 56, 72

[172] T. O. Niinikosi *et al.*, Thin Cryogenic X-ray Windows, CERN-AT-2008-034, 2008. 58

[173] Naval Observatory Vector Astrometry Software, http://aa.usno.navy.mil/software/novas/. 63

[174] I. Ortega and M. Karuza, Update on Sun filming results, Talk given at 50th CAST Collaboration Meeting, CERN, Switzerland, 2013. 65

[175] I. Ortega and M. Karuza, September 2013 Sun filming, Talk given at 52nd CAST Collaboration Meeting, CERN, Switzerland, 2013. 66

[176] J. Altmann *et al.*, Mirror system for the German x-ray satellite ABRIXAS: I. Flight mirror fabrication, integration, and testing, *Proc. SPIE* **3444** (1998) 350. 68

[177] L. Struder *et al.*, The European Photon Imaging Camera on XMM-Newton: The pn-CCD camera, *Astron. Astrophysics* **365** (2001) L18. 68

[178] S. Cebrian *et al.*, Background study for the pn-CCD detector of CERN Axion Solar Telescope, *Astroparticle Astrophysics* **28** (2007) 205. 69

[179] D. Autiero *et al.*, The CAST time projection chamber, *New J. Phys.* **9** (2007) 171. 69, 71

[180] M. Chefdeville *et al.*, An electron-multiplying 'Micromegas' grid made in silicon wafer post-processing technology, *Nucl. Instrum. Meth. A* **556** (2006) 490. 71

[181] M. Campbell *et al.*, Detection of single electrons by means of a Micromegas-covered MediPix2 pixel CMOS readout circuit, *Nucl. Instrum. Meth. A* **540** (2005) 540. 71

[182] C. Krieger *et al.*, An InGrid based Low Energy X-ray Detector, Talk given at 10th PATRAS Workshop on Axions, WIMPs and WISPs, CERN, Switzerland, 2014. 71, 73

[183] X. Llopart *et al.*, Timepix, a 65k programmable pixel readout chip for arrival time, energy and/or photon counting measurements, *Nucl. Instrum. Meth. A* **581** (2007) 485. 72

[184] G. Cantatore, Recent bounds on solar Hidden Photons obtained at CAST, Talk given at 9th PATRAS Workshop on Axions, WIMPs and WISPs, Mainz, Germany, 2013. 72

[185] S. Cebrian *et al.*, Radiopurity of Micromegas readout planes, *Astropart. Phys.* **34** (2011) 354. 75, 196, 197

[186] S. Aune *et al.*, Low background x-ray detection with Micromegas for axion research, *JINST* **9** (2014) P01001. 76, 157, 158, 196

[187] ELJEN Technology, EJ-200, http://www.eljentechnology.com. 82

[188] HAMAMATSU Photonics, http://www.hamamatsu.com. 82

[189] D. Breton *et al.*, Very high dynamic range and high sampling rate VME digitizing boards for physics experiments, *IEEE Trans. Nucl. Sci.* **52** (2005). 82

[190] J. C. Santiard *et al.*, Gasplex: A Low noise analog signal processor for readout of gaseous detectors, CERN-ECP-94-17, C94-05-22.2, 1994. 82

[191] P. Baron *et al.*, AFTER, an ASIC for the readout of the large T2K time projection chambers, *IEEE Trans. Nucl. Sci.* **55** (2008) 1744. 82

[192] P. Baron *et al.*, Architecture and Implementation of the Front-End Electronics of the Time Projection Chambers in the T2K Experiment, *IEEE Trans. Nucl. Sci.* **57** (2010) 406. 82

[193] D. Calvet, A New Versatile and Cost Effective Readout System for Small to Medium Scale Gaseous and Silicon Detectors, Nuclear Science Symposium and Medical Imaging Conference (NSS/MIC), 2013 IEEE. 84

[194] J. Galan, Probing eV-mass scale axions with a Micromegas detector in the CAST experiment, PhD Thesis, Universidad de Zaragoza, 2011. 98

[195] I. K. Bronic and B. Grosswendt, Gas amplification and ionization coefficients in isobutane and argon-isobutane mixtures at low gas pressures, *Nucl. Instrum. Meth. A* **142** (1998) 219. 109

[196] F. J. Iguaz *et al.*, Characterization of microbulk detectors in argon- and neon-based mixtures, *JINST* **7** (2012) P04007. 110

[197] M. Arik *et al.* (CAST Collaboration), New solar axion search in CAST with ^{4}He filling, *Phys. Rev. D* **92** (2015) 021101. 120

[198] J. E. Kim, Weak Interaction Singlet and Strong CP Invariance, *Phys Rev. Lett.* **43** (1979) 103. 133

[199] M. A. Shifman *et al.*, Can Confinement Ensure Natural CP Invariance of Strong Interactions?, *Nucl. Phys. B* **166** (1980) 493. 34, 133

[200] F. Aznar *et al.*, A Micromegas-based low-background x-ray detector coupled to a slumped-glass telescope for axion research, *Submitted to: JCAP*, arXiv:1509.06190

[201] S. Aune *et al.*, X-ray detection with Micromegas with background levels below 10^{-6} keV^{-1}cm^{-2}s^{-1}, *JINST* **8** (2013) C12042. 155

[202] G. Luzon *et al.*, Characterization of the Canfranc underground laboratory: Status and future plans, Proceedings, 6th International Workshop on The identification of dark matter (IDM 2006). 157

[203] AlphaGUARD Radon Monitor, http://www.genitron.de. 158

[204] S. Agostinelli *et al.*, Geant4–a simulation toolkit, *Nucl. Instrum. Meth. A* **506** (2003) 250. 161

[205] J. Allison *et al.*, Geant4 developments and applications, *Nucl. Sci.* **53** (2006) 270. 161

[206] R. Brun and F. Rademakers, ROOT - An Object Oriented Data Analysis Framework, *Nucl. Inst. Meth. in Phys. Res. A* **389** (1997) 81. 163

[207] F. Iguaz and J. G. Garza, TREX-DM a low background Micromegas-based TPC for low mass WIMP detection, *TAUP2015*, Torino, Italy, 2015.

[208] http://radiopurity.in2p3.fr/ 168

[209] K. A. Olive *et al.* (Particle Data Group Collaboration), 2014 Review of Particle Physics, Chin. Phys. C **38** (2014). 163, 177, 187, 188

[210] G. Bertone *et al.*, Particle dark matter: Evidence, candidates and constraints, *Phys. Rept.* **405** (2005) 279. 177, 179, 190

[211] F. Zwicky, Die Rotverschiebung von extragalaktischen Nebeln, *Helv. Phyus. Acta* **6** 110. 178

[212] P. F. Smith and J. D. Lewin, Dark matter detection, *Phys. Rept.* **187** (1990) 203. 182

[213] H. Chagani *et al.*, Measurement of the quenching factor of Na recoils in NaI(Tl), *JINST* **3** (2008) 6003. 182

[214] S. T. Lin *et al.* (TEXONO Collaboration), New limits on spin-independent and spin-dependent couplings of low-mass WIMP dark matter with a germanium detector at a threshold of 220 eV, *Phys. Rev. D* **79** (2009) 061101. 182, 183

[215] J. F. Ziegler *et al.*, SRIM/TRIM, http://www.srim.org. 182

[216] Z. Ahmed *et al.* (CDMS), Dark Matter Search Results from the CDMS II Experiment, *Science* **327** (2010) 1619. 187

[217] Z. Ahmed *et al.*, Combined limits on WIMPs from the CDMS and EDELWEISS experiments, *Phys. Rev. D* **84** (2011) 011102. 187

[218] G. Angloher *et al.* (CRESST Collaboration), Results from 730 kg days of the CRESST-II Dark Matter Search, *Eur. Phys. J. C* **72** (2012) 1971. 187

[219] C. E. Aalseth *et al.*, Search for an Annual Modulation in a p-type Point Contact Germanium Dark Matter Detector, *Phys. Rev. Lett.* **107** (2011) 141301. 187

[220] R. Agnese *et al.* (SuperCDMS Collaboration), Search for Low-Mass Weakly Interacting Massive Particles with SuperCDMS, *Phys. Rev. Lett.* **112** (2014) 241302. 188

[221] H. Kraus *et al.*, EURECA - the European future of cryogenic dark matter searches, *J. Phys Conf. Series* **39** (2006) 139. 188

[222] W. Zhao *et al.* (CDEX Collaboration), First results on low-mass WIMPs from the CDEX-1 experiment at the China Jinping underground laboratory, *Phys Rev. D* **88** (2013) 052004. 188

[223] E. Aprile *et al.* (XENON100 Collaboration), Dark Matter Results from 225 Live Days of XENON100 Data, *Phys. Rev. Lett.* **109** (2012) 181301. 189

[224] D. Akimov *et al.*, WIMP-nucleon cross-section results from the second science run of ZEPLIN-III, *Phys. Lett. B* **709** (2012) 14. 189

[225] D. S. Akerib *et al.* (LUX Collaboration), First results from the LUX dark matter experiment at the Sanford Underground Research Facility, *Phys. Rev. Lett.* **112** (2014) 091303. 189

[226] R. Bernabei *et al.* (DAMA/LIBRA Collaboration), New results from DAMA/LIBRA *Eur. Phys. J. C* **67** (2010) 39. 189, 194

[227] S. C. Kim *et al.*, New Limits on Interactions between Weakly Interacting Massive Particles and Nucleons Obtained with CsI(Tl) Crystal Detectors, *Phys. Rev. Lett.* **108** (2012) 181301. 189

[228] J. Amare *et al.*, ANAIS: Status and prospects, 5th Roma International Conference on Astroparticle physics (RICAP 14), Sicily, Italy, 2014. 189

[229] , J. Cherwinka *et al.* A search for the dark matter annual modulation in South Pole ice, *Astrop. Phys.* **35** (2012) 749. 189

[230] T. A. Girard *et al.*, SIMPLE Dark Matter Search Results, *Phys. Lett. B* **621** (2005) 233. 190

[231] M. Barnabe-Heider *et al.*, Improved Spin Dependent Limits from the PICASSO Dark Matter Search Experiment, *Phys. Lett. B* **624** (2005) 186. 190

[232] E. Behnke *et al.*, Improved Spin-Dependent WIMP Limits from a Bubble Chamber, *Science* **319** (2008) 933. 190

[233] E. Behnke *et al.*, Improved Limits on Spin-Dependent WIMP-Proton Interactions from a Two Liter CF3I Bubble Chamber, *Phys. Rev. Lett.* **106** (2011) 021303. 190

[234] E. Daw *et al.*, The DRIFT Dark Matter Experiments, arXiv:1110.0222 190, 197

[235] D. Santos *et al.*, MIMAC: A Micro-TPC Matrix of Chambers for direct detection of Wimps, *J. Phys Conf. Series* **65** (2007) 012012. 190, 197, 204

[236] C. Deaconu *et al.*, Track Reconstruction Progress from the DMTPC Directional Dark Matter Experiment, *Phys Procedia* **61** (2015) 39. 190, 197

[237] K. Nakamura *et al.*, NEWAGE - Direction-sensitive Dark Matter Search Experiment, *Phys Procedia* **61** (2015) 737. 190, 197

[238] A. A. Aguilar-Arevalo *et al.* (DAMIC Collaboration), DAMIC: a novel dark matter experiment, arXiv:1310.6688 190, 195

[239] G. Gerbier *et al.*, NEWS : a new spherical gas detector for very low mass WIMP detection, arXiv:1401.7902 190

[240] P. Cushman *et al.*, Working Group Report: WIMP Dark Matter Direct Detection Community Summer Study 2013: Snowmass on the Mississippi (CSS2013) Minneapolis, USA, 2013. 190

[241] O. Adriani *et al.* (PAMELLA Collaboration), Cosmic-Ray Positron Energy Spectrum Measured by PAMELA *Phys. Rev. Lett.* **106** (2011) 021303. 191

[242] M. Aguilar *et al.*, First Result from the Alpha Magnetic Spectrometer on the International Space Station: Precision Measurement of the Positron Fraction in Primary Cosmic Rays of 0.5-350 GeV, *Phys. Rev. Lett.* **110** (2013) 141102. 191

[243] J. Chang *et al.* (ATTIC Collaboration), An excess of cosmic ray electrons at energies of 300-800 GeV, *Nature* **456** (2008) 362. 191

[244] A. A. Abdo *et al.* (FERMI collaboration), Measurement of the Cosmic Ray $e^+ + e^-$ Spectrum from 20GeV to 1TeV with the Fermi Large Area Telescope, *Phys. Rev. Lett.* **102** (2009) 181101. 191

[245] F. Aharonian *et al.* (HESS Collaboration), Probing the ATIC peak in the cosmic-ray electron spectrum with H.E.S.S., *Astron. Astrophys.* **508** (2009) 561. 191

[246] D. S. Akerib *et al.* (LUX Collaboration), First results from the LUX dark matter experiment at the Sanford Underground Research Facility, *Phys. Rev. Lett.* **112** (2014) 091303. 194, 199

[247] E. Aprile *et al.* (XENON Collaboration), Dark Matter Results from 225 Live Days of XENON100 Data, *Phys. Rev. Lett.* **109** (2012) 181301. 194, 195

[248] R. Agnese *et al.* (SuperCDMS Collaboration), Search for Low-Mass Weakly Interacting Massive Particles with SuperCDMS, *Phys. Rev. Lett.* **112** (2014) 241302. 194, 195

[249] R. Agnese *et al.* (SuperCDMS Collaboration), Maximum Likelihood Analysis of Low Energy CDMS II Germanium Data, *Phys. Rev. D* **91** (2014) 052021. 195

[250] R. Agnese *et al.* (SuperCDMS Collaboration), Search for Low-Mass Weakly Interacting Massive Particles Using Voltage-Assisted Calorimetric Ionization Detection in the SuperCDMS Experiment, *Phys. Rev. Lett.* **112** (2014) 041302. 195, 199

[251] F. Aznar *et al.*, Assessment of material radiopurity for Rare Event experiments using Micromegas, *JINST* **8** (2013) C1012. 196, 204

[252] V. Alvarez *et al.* (NEXT Collaboration), Description and commissioning of NEXT-MM prototype: first results from operation in a Xenon-Trimethylamine gas mixture, *JINST* **9** (2014) P03010. 196

[253] G. Gerbier *et al.*, NEWS : a new spherical gas detector for very low mass WIMP detection, arXiv:1401.7902. 196, 197

[254] F. J. Iguaz *et al.*, TREX-DM: a low background Micromegas-based TPC for low mass WIMP detection, 7th Symposium on large TPCs for low-energy rare event detection Paris, France, 2014. 197

[255] H. O. Back *et al.*, First Large Scale Production of Low Radioactivity Argon From Underground Sources, arXiv:1204.6024. 197

[256] F. J. Iguaz *et al.*, Comissioning of TREX-DM, a low background Micromegas-based TPC for low mass WIMP detection, 11th AxionWIMP Conference , Zaragzoza, Spain, 2015. 198

[257] R. Agnese *et al.*, (CDMS Collaboration), Phys. Rev. Lett., **111**, 251301 (2013) 199

[258] C. E. Aalseth *et al.*, (CoGeNT Collaboration), Phys. Rev. D, **88**, 012002 (2013) 199

[259] G. Angloher *et al.*, (CRESST Collaboration), Eur. Phys. J. C, **72**, 1971 (2012) 199

[260] R. Bernabei *et al.*, Eur. Phys. J. C, **67**, 39 (2010) 199

[261] C. Savage *et al.*, JCAP, **0904**, 010 (2009) 199

[262] R. Agnese *et al.*, (SuperCDMS Collaboration), Phys. Rev. Lett., **112**, 241302 (2014) 199

[263] R. Agnese *et al.*, (SuperCDMS Collaboration), Submitted to: Phys. Rev. Lett., 2015. 195, 199

[264] D. Akerib *et al.*, (LUX Collaboration), Phys. Rev. Lett., **112**, 091303 (2014) 194, 199

[265] Q. Yue *et al.*, (CDEX Collaboration), Phys. Rev. D, **90**, 091701 (2014) 195, 199

[266] G. Angloher *et al.*,(CRESST Collaboration), arXiv:1509.01515, 2015. 199

[267] G. Luzon *et al.*, 6th Workshop on the Identification of Dark Matter (IDM2008), Stockholm, Sweden, 2008. 198

[268] J. Xu *et al.*, A Study of the Residual ^{39}Ar Content in Argon from Underground Sources, 198

[269] D. S. Leonard . *et al.*, Systematic study of trace radioactive impurities in candidate construction materials for EXO-200, *Nucl. Instrum. Meth. A* **591** (2008) 591. 198

[270] Raspberry Pi, https://www.raspberrypi.org. 206

[271] Arduino, http://www.arduino.cc. 206

[272] A. Peiro, Desarrollo e implantacion de un sistema de adquisicion de datos y monitorizacionn para un sistema de deteccion de materia oscura, http://zaguan.unizar.es/record/12149. 206

[273] P. Baron *et al.*, AGET, the Get Front-End ASIC, for the readout of the Time Projection Chambers used in Nuclear Physic Experiments, Nuclear Science Symposium Conference Record, 2011. 102, 172, 208

[274] F. J. Iguaz *et al.*, New developments in Micromegas Microbulk detectors *Phys Procedia* **37** (2012) 448. 18, 214

[275] F. J. Iguaz *et al.*, New results of microbulk detectores, 5th RD-51 collaboration meeting, Freiburg, Germany, 2010. 214

[276] H. Schindler, Microscopic Simulation of Particle Detectors PhD Thesis, University of Wien, 2012. 222